University of Exeter
Department of Physics and Astronomy

Methods and Trends in 2D van der Waals Heterostructures

Francis Huw Davies

Submitted by Francis Huw Davies, to the University of Exeter as a thesis for the degree of Doctor of Philosophy in Physics, March, 2021.

I certify that all material in this thesis which is not my own work has been identified and that any material that has previously been submitted and approved for the award of a degree by this or any other University has been acknowledged.

Signed: .....

Abstract

The research here will identify both thermal and electronic trends in 2D heterostructures and develop rigorous methodologies for calculating interface structures. A link will be made between common devices and the materials and interfaces from which they are constructed. A comprehensive presentation of the theories used throughout the thesis will be given, defining density functional theory, the Frozen phonon method and thermal conductivity via the Boltzmann transport equation.

The failure of Anderson's rule in 2D heterostructures will be demonstrated and explained. Also demonstrated, will be, how 2D heterostructure bandgap predictions can be improved using two physically based corrections to Anderson's rule ΔE_{Γ} and ΔE_{IF}. We will show that ΔE_{Γ} affects the bandstructure such that for any constructed heterostructure the effective mass will always decrease and will likely exhibit an indirect bandgap. Furthermore, we will provide expressions to give the band alignments in terms of knowable material properties. It is then discussed how theory could be readily extended to other 2D heterostructures by adjustments to corrective terms ΔE_{Γ} and ΔE_{IF}. This insight allows for a method which avoids the need for advanced calculation when estimating the properties of TMDC heterostructures. This in turn will expand the possibilities for exploring the optoelectronic properties of various heterostructures to the broader research community.

We will follow on by showing that the thermal conductivity of a TMDC heterostructure will be lower than either of its constituents. We will show that this is consistent even when considering a wide range of possible conductivities. Generous parameter allocation will be used to define maximum bounding conductivity values. Such an approach will improve the confidence in the results. This is expected to provide a route for artificially reducing heat flow in 2D layered materials and will demonstrate a clear trend in the thermal transport of 2D heterostructure interfaces.

To facilitate methods for heterostructures and interfaces A program, ARTEMIS, well be developed. This software allows for the generation of interfaces by identifying lattice matches between two parent crystal structures. To allow for further exploration of the energetic space of the interface, multiple surface terminations parallel to the Miller plane and interface alignments are used to generate sets of potential interfaces for each lattice match. These interface structures can then be used in atomic simulations to determine the most energetically favourable interface. The software here can help to both drastically reduce the work of generating and exploring interfaces, as well as aid in understanding of how the interface structure influences subsequent properties. Using several test cases, we will demonstrate how ARTEMIS can both identify the location of an interface in existing structures, and also predict an optimum interface separation based upon the parents' atomic structures, which aims to accelerate and inform the study of interface science.

The electronic and mechanical properties of $Ba_2TiSi_2O_8$, an inter-grain material, will be obtained and compared using the generalised gradient approximation and hybrid functional methods. This will define procedures and limitations for the investigation of inter-grain materials. With no need to adhere to the stoichiometry of the parent crystals procedural generation of inter-grain materials cannot be achived by ARTEMIS. It will be demonstrated that for insulating inter-grain materials hybrid functionals can result in significant change. The hybrid functional corrects the bandgap from 3.79 eV to 5.72 eV and shows overall stronger ionic bonding and weaker covalent bonding within the structure. The calculated value of 131.73 GPa for the bulk modulus sits between the values of its two parent crystals ($BaTiO_3$ and SiO_2). Using the HSE06 functional, will give a better understanding of the optical and electron transport properties and provide better understanding of the chemical structure making this investigation helpful for further work on similar inter-grain systems. This body of work serves the purpose of identifying general trends across heterostructures and interfaces and developing sound methodologies

for the investigation of these structures.

Acknowledgements

This thesis has been years in making and months in the writing. Many people have contributed to it in ways both large and small. Here I give thanks to as many of them as I can.

I would first like to thank my coworkers, each of whom I would also consider a friend. This includes Ned Thaddeus Taylor, Shane Graham Davies, Conor Price, Joe Pitfield, Edward Baker and Edmund Chan. In particular I would like to give special acknowledgements to Ned Thaddeus Taylor who has provided continued support and friendship throughout the course of my PhD.

I give great thanks to, my supervisor, Dr. Steven Paul Hepplestone who has provided guidance and has had more influence on my research and development than any other person. Further thanks are given to Saverio Russo and Gyaneshwar Srivastava for their guidance and advice.

For preserving my sanity, I give thanks to my friends, the ostriches: Rosamund Herapath, Milo Baraclough, Lizzie Martin, Ned Taylor and Austin. Their friendship has been both welcome and necessary over these past years. I also thank Ian Jones, my housemate, who has stoically endured my presence for three years.

Lastly, I give thanks to my Family. Both for there fierce support and also for their help. Due to current circumstances I have, unexpectedly, written much of this thesis in my family home. I must therefore give further acknowledgements to my family for how willingly they have embraced my presence and how generously they have facilitated my requirements.

Frank

List of Notation

Presented below is a list of the symbols and notation used within this thesis. The list shown is not exhaustive as the meaning of symbols is normally clear from their context. Here the meanings of the most important and frequently occurring symbols contained within this thesis are presented for clarity and ease of reference.

$a^\dagger$	Creation operator
a	Annihilation operator
$A^{\alpha\beta\gamma}_{l\sigma l'\sigma' l''\sigma''}$	third order force constants
b	Orthogonal basis function
c	Basis coefficient
$\bar{c}$	Average acoustic phonon speed
C_V	Specific heat capacity
$D_{\alpha\beta}(\sigma\sigma'\|\mathbf{q})$	Dynamical matrix, defined at arbitrary $\mathbf{q}$-value
$\hat{e}$	Polarisation vector
E	Energy
E_H	Hartree energy
f_i	Fraction of the ith isotope of atomic an species
F	Force
E_{xc}	Exchange correlation functional
F_{HK}	Hohenberg-Kohn functional
g	Mass defect scaling parameter
$\mathcal{G}_{md}$	The isotropic mass factor
$\mathcal{G}_2$	The species specific isotropic mass factor
$\hbar$	The reduced Planks constant

$\hat{H}$	Hamiltonian operator
$\hat{H}_{KS}$	Kohn-Sham Hamiltonian
k_B	Boltzmann constant
l	Unit cell index
L	Scattering length
$\mathbf{L}$	Lattice matrix
M	Mass
m	Atomic mass
$\bar{m}$	Average atomic mass
$n(\mathbf{r})$	Particle density
$n_0(\mathbf{r})$	Ground state particle density
$\bar{n}(\mathbf{q}s)$	Bose-Einstein distribution, for state with wavevector $\mathbf{q}$ and mode s
N	Number of unit cells
P_i^f	Transition probability from initial state, i, to final state, f
$\mathbf{q}$	Phonon wavevector
$\mathbf{r}, \mathbf{R}$	Position vectors
s	Band/mode index
S	Seebeck coefficient
$\mathcal{S}$	Variational functional
T	Temperature
$\mathbf{T}$	Transformation matrix
$\hat{T}$	Kinetic energy operator
$\vec{u}$	Atomic displacement vector
$u_\alpha(l\sigma)$	Atomic displacement element, in direction α for atom σ in unit cell l
$\hat{U}$	Total potential energy operator
V	Volume
$\hat{V}$	Potential energy operator
V_{ext}	External potential

$\mathcal{V}$	Crystal potential energy
Z	Atomic charge number
ZT	Dimensionless thermoelectric figure of merit
γ	The Grüneisen constant
ϵ	Energy eigenvalue
ε	Efficiency
κ	Thermal conductivity
ν	Group velocity
ρ	Mass density
σ	Electrical conductivity
σ	Index over atoms within unit cell
τ	Relaxation time
φ	Electronic wavefunction
ψ	A many body eigenstate
Φ	Second order inter-atomic force constants
Ψ	Full coupled molecular wavefunction
χ	Coupled ionic & electronic wavefunction
ω	Phonon frequency
∇	Vector differential operator
$A[b]$	A functional, A of function, b
δ_{ij}	Kronecker delta
$\delta(x-a)$	Dirac delta function

List of Publications

Chapter 4

- Francis H. Davies, Conor J. Price, Ned T. Taylor, Shane G. Davies, and Steven P. Hepplestone, *Band alignment of transition metal dichalcogenide heterostructures*, Phys. Rev. B 103, 045417. (2021)

Chapter 6

- Ned T. Taylor, Francis H. Davies, Isiah E. M. Rudkin, Conor J. Price, Tsz H. Chan and Steven P. Hepplestone, *ARTEMIS: Ab initio restructuring tool enabling the modelling of interface structures*, Comp. Phys. Commun., 257, p. 107515. (2020)

Chapter 7

- Ned T. Taylor, Francis H. Davies, and Steven P. Hepplestone, *First principles electronic and elastic properties of fresnoite* $Ba_2TiSi_2O_8$, Mater. Res. Express 4 125904. (2017)

Contents

List of Figures

List of Tables

Chapter 1

Introduction

"As far as he can achieve it, readability is as important for the scientific writer as it is for the novelist."

— Donald O. Hebb

'Scientific Writing and the General Problem of Communication', 1968

1.1 The Needs of The Modern World

The modern world is teeming with technology. Within the space of a lifetime computers have changed from huge, room filling machines, to pocket-sized appliances. This trend is codified by Moore's law [1] and has helped make computers an everyday item. According to the Office of National Statistics [2] 99% of people between the age of 25-34 in the UK use a smartphone. This fact is emblematic of the wide spread usage of electronics and digital media, which will only have been increased by the ongoing COVID-19 pandemic [3].

The tools and devices of the modern world can overheat as a result of their basic operations, even when functioning as intended [4]. Such considerations force

us to examine thermal properties alongside electronic ones. Furthermore, displays and touch screens, alongside countless other practical applications, are governed by a sub-field within the field of electronics called optoelectronics. These three considerations, the thermal, electrical and optical properties, are vital for the construction of materials for device applications.

All the work in this thesis is concerned with the modelling and predicting of material properties. Indeed, it is the ability to predict, from *ab initio*/first principles, the properties of "new materials" that is of primary concern in this work. So called new or meta-materials are constructed by constraining their structure to unnatural configurations, such as in 2D graphene. This principle can be taken further here, to the merging of materials into heterostructures with new properties characteristic of the interface. These properties, thermal, thermoelectric and optoelectronic, can be defined as follows. Optoelectronics, the sub-field of technology which concerns the interaction of light and electronics. Thermoelectrics, characteristics governing the thermoelectric effect, in which a heat differential may be converted into accessible electrical energy. Lastly, thermal properties, are those properties that relate to the storage and transport of heat.

1.1.1 Optoelectronics

The field of optoelectronics is a sub-field of electronics (or sometimes photonics). It is the branch of electronics engaged with studying how electronic devices can manipulate, emit or detect light. Optoelectronics, is at some point a feature of most devices since light emission is the primary way humans draw information from those devices.

Electrons interact with photons through transitions within their bandstructures. The process of photon absorption is shown figure 1.1 with an electron in

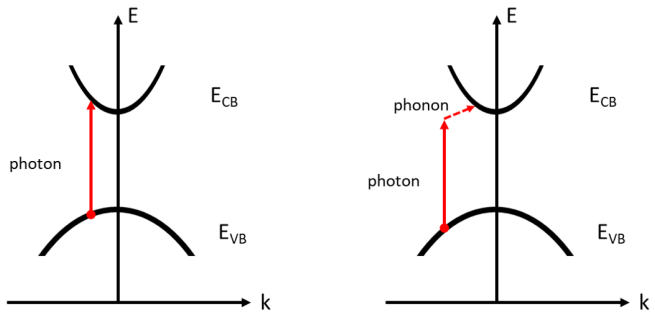

Figure 1.1. A diagram showing direct and indirect photon absorption.

the valence band absorbing a photon and rising to the conduction band. Photon absorption can also occur indirectly, where an electron transition is mediated by a phonon. By definition then, indirect photon absorption causes heating of the device.

The following is an elementary account of some common place optoelectronic devices that have practical daily uses.

Light-Emitting Diode

An LED or light-emitting diode is a simple P-N junction that has been specially fine-tuned such that recombination of the electron-hole pairs, results in emission of optical frequency light. Because LEDs are dependent on the materials they are made from, tailoring an LED to output a specific frequency is difficult and requires dedicated materials engineering. Work on producing a blue LED led to the awarding of the 2014 Nobel prize in Physics [5].

Photodetectors

Photodetectors are useful electronic components. They are likewise built from a P-N junction, although the structure is usually more complex, incorporating an intrinsic semiconductor layer between the P and N layers. This is often called a *pin* diode. The basic mechanism involves the absorption of photons within the depletion region of a P-N junction. The newly created electron and hole naturally flow along their respective energy gradients. This produces a small current. Photodetectors typically have a reverse bias which is useful since it will widen the depletion region

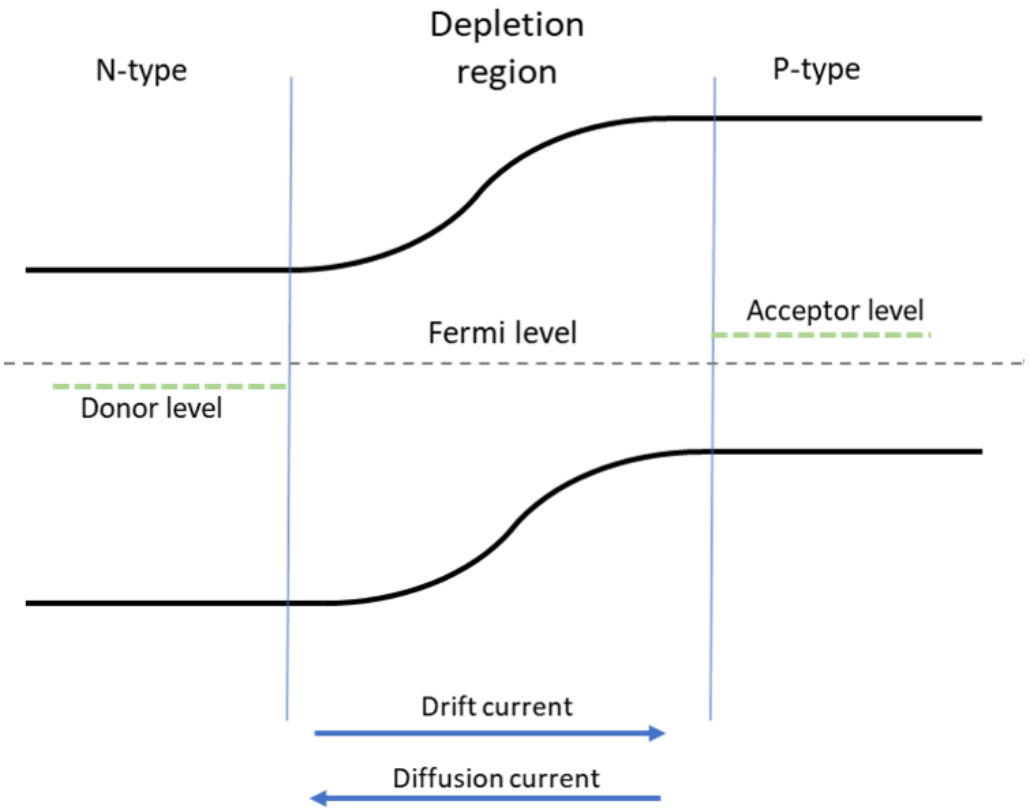

Figure 1.2. Band diagram of a P-N junction in the unbiased condition.

and produce clear and detectable change from saturation current.

Photovoltaics

A photovoltaic is a P-N junction with a reverse bias which helps to enhance the drift current of minority charge carriers. Photovoltaics are very often constructed in a similar manner to photodetectors. However, where a photodetector is concerned with the detection of small current changes due to photon excitations, the photovoltaic is concerned with the capturing of electrical gain induced by the optical absorption.

Each of the described devices are built upon the physics of the P-N junctions; an important part of optoelectonics and electronics in general. The P-N junction is, in a fundamental way, an interface between two materials and is therefore an example of the emergent properties that may spring from the interaction between materials.

A simple band diagram of the an unbiased P-N junction is shown in figure 1.2. A P-N junction is an interface between an n-type doped and a p-type doped semiconductor. At the interface, electrons diffuse from the n-type side into the p-type side. The same process happens in reverse with holes defusing from the p-type to n-type sides. These electrons and holes recombine depleting the region of charge carriers. At this point diffusion of majority charges (against the gradient) and drift of minority charges (with the gradient) balance with no net conduction.

There is a set of material properties that determine the operation of optoelectronic devices. However, those properties that describe the individual materials are insufficient to describe optoelectronics that incorporate interface physics. Therefore, when determining the properties which govern the majority of optoelectronic devices one must consider both electron-phonon interactions and interface interaction.

The material property of most importance, in optoelectronics, is the band gap. However, understanding of both the direct and indirect bandgap is important as this will affect transition probabilities and device heating. Additionally, dopant states and the Fermi level position and band alignments are crucial to determining features of the semiconductor interfaces.

1.1.2 Thermoelectrics

Nothing is one hundred percent efficient. Whenever work is done, some energy will always be given off in the form of heat. Such heat obstructs the efficient running of most devices and must be drawn out of the system. This waste is ubiquitous throughout modern technology and therefore accounts for a significant amount of the energy produced by mankind. A very promising solution to the problem of thermal management is given in the form of thermoelectric (TE) materials.

TE devices (see fig. 1.3) offer a means of converting a thermal gradient directly

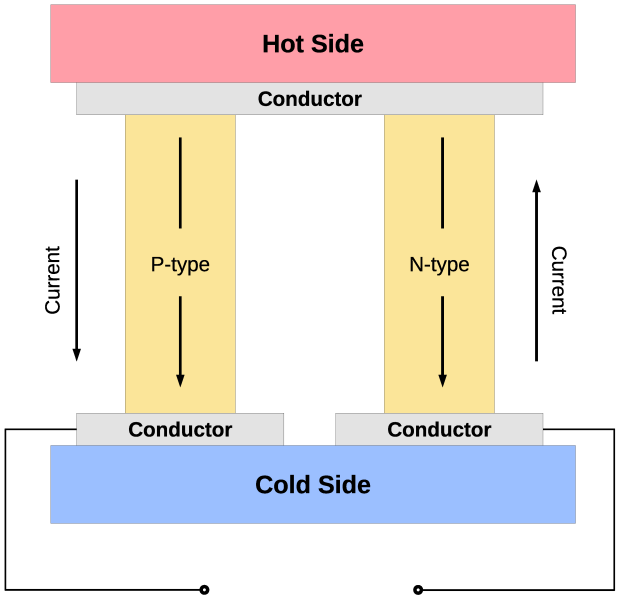

Figure 1.3. A diagram of a thermoelectric generator, composed of a P-type and an N-type leg.

into electrical power. Unlike most conversion methods a thermoelectric generator (TEG) has no intermediate steps, it converts heat energy into electrical energy directly. Unlike other generators, this mechanism utilises a solid-state property of the material. This means that it requires no moving parts and hence no maintenance and therefore, that all of the costs of producing a TEG are upfront. This critical feature of TEGs ensures that it would have a long lifetime demonstrated by its use (and continued function) on spacecrafts such as VOYAGER I and II [6]. Devices utilising a TEG can be cooled noiselessly. Again this is due to the mechanism by which a TEG converts heat.

There are many factors that affect performance of a TEG. To understand these it is first necessary to define the dimensionless figure of merit ZT.

$$ZT = \frac{\sigma S^2}{\kappa} T, \tag{1.1}$$

where σ is the electrical conductivity, κ is the thermal conductivity and S is the

Seebeck coefficient. Some attempts have been made to improve on ZT by removing the explicit temperature dependence [7]. However, it is ZT, the dimensionless thermoelectric figure of merit which is used, almost exclusively, to determine the quality of a TE material. It is useful to explain why this is the case. It is because the value of ZT directly influences operational efficiency of TEGs according to [8],

$$\varepsilon = \frac{T_H - T_C}{T_H} \frac{\sqrt{1+ZT}-1}{\sqrt{1+ZT}+\frac{T_C}{T_H}}, \tag{1.2}$$

where T_H and T_C are the hot side and cold side temperatures. The thermoelectric is assumed to operate at the average temperature between the hot (T_H) and the cold (T_C) sides. It is the value of the thermoelectric dimensionless figure of merit ZT that is the focus of most materials research within the field of thermoelectrics [8, 9, 10]. It can be seen from the expression for TEG efficiency that for $ZT = 0$ the efficiency will equal zero and as ZT tends to infinity, the efficiency tends to the Carnot efficiency.

In a TE device the current is produced by the thermal excitation of charge carriers causing electrons and holes to diffuse from the hot to the cold side of the device. In actuality the situation is more complicated. Hot electrons do diffuse from the hot side of the device to the cold side. However, holes cannot be considered as hot carriers. Instead it is necessary to consider that electrons below the chemical potential are cold and hence will diffuse from the cold side to the hot side.

The current of hot electrons and the current of cold electrons in a TEG occur in opposing directions so as to negate each other. However, these carriers do not possess the same mobility within the electronic structure of the material. This asymmetry of mobilities leads to a net current. It follows that a highly doped P-type or N-type semiconductor will show optimal thermoelectric performance.

Assessing the important properties for thermoelectric construction is made

easy by the definition of the figure of merit (eq. 1.1). A TEG is made more efficient by enhancing the electrical conductivity and to a greater extent the Seebeck coefficient. Efficiency may be further enhanced by reducing the thermal conductivity. There are, however, two contributions to thermal conductivity; the lattice thermal conductivity and the electron thermal conductivity ($\kappa = \kappa_L + \kappa_e$). The relationship between the electrical conductivity and electron thermal conductivity ($\kappa_e/\sigma \propto T$) is known as the Wiedermann-Franz law and serves to demonstrate the difficulty in tailoring these material properties. Although the individual properties (σ, κ & S) contributing to ZT may each vary by orders of magnitude, ZT itself rarely achieves a value greater than 2 [10].

1.1.3 Thermal Management

Thermal management is the third issue and it is important for all modern electronic devices. It's importance is often overlooked; a report by the US Air Force found that over 50% of equipment malfunction was due to poor temperature control [11]. The growing relevance of thermal management to the electronics industry is driven even further by the desire for minimization of electronic devices, such as phones and computers[1]. Any electronic device will have an inevitable waste heat output. This waste must be managed effectively if we are to continue improving computers and hand held devices[4].

There are two effective methods for limiting thermal failure. First is to improve the base efficiency of a device and the second is to dissipate or harvest the waste heat. There is often a compromise between performance and efficiency. Usually, this is because if a device can be made more efficient, it will be made more efficient, unless there is some drawback of the high efficiency version. For instance, one could consider the electric car which is more then twice as energy efficient [12] as any combustion engine car. However, there are notable draw backs to performance

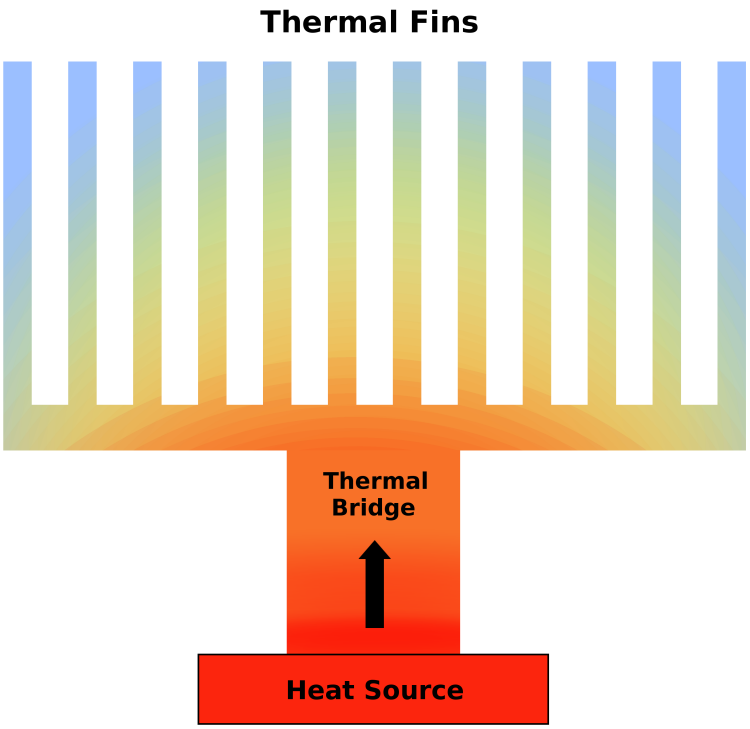

Figure 1.4. A diagram of a thermal management device. It shows a thermal bridge that draws heat from a source to a drain (shown as thermal fins).

making any future transition from combustion engine to electric cars uncertain. This stands to illustrate the point that simply improving the base efficiency of a device will typically lead to a compromise (be it performance, upfront cost or even comfort) and therefore a wide proportion of the population would not elect to change.

TEGs have so far been reviewed in the context of energy harvesting. The Peltier effect describes how thermoelectric materials may also be used for cooling. When a current is passed through a device the disparity between the mobilities of hot and cold electrons causes a heat flux to accompany the electronic current. This will result in one side getting cooler as the other side heats up. Unlike with thermoelectric power generation, the thermoelectric cooling does not depend of ZT, instead it is only dependent on the "power factor" PF. A definition for the power factor can be given as, $PF = \sigma S^2$.

Thermal management also involves heat flow control, such as shown in figure 1.4. Low conductivity materials will transfer heat very slowly, where as a high thermal conductivity material will dissipate that same heat quickly. Careful construction can allow two points to be in thermal contact, via high conductivity materials, while being effectively thermally isolated from other points separated by low conductivity materials. It is such design principles that allow ovens to contain the majority of their heat, and computers to channel heat into thermal sinks [13].

Tailoring materials to have better or worse thermal transport involves understanding the mechanisms behind thermal conductivity. Phonons, excitations of the periodic crystal lattice, determine the thermal transport properties of a material. A full theory of thermal transport is presented in chapter 3. Many of the properties that govern the thermal conductivity, phonon group velocity, the density of states, specific heat capacity, sample size, defect concentration and scattering rates are interlinked and changing any one cannot be achieved without changing at least one other. Even changing the material sample size will effect the phonon scattering rate.

1.2 Materials Design: Changing The Focus

Historically the goals of materials science have been to model and predict the properties of existing materials. Through detailed and careful parameterisation the nature of one material may be extended to new scenarios in which predictions of its behaviour may be made. Modern materials science has a growing focus on developing new materials. Under lab conditions advanced fabrication methods such as molecular beam epitaxy and epitaxial growth have allowed for the manipulation of the material structure down to the atomic scale [14, 15].

Metamaterials, nanostructures, and heterostructures are all examples of new materials with new emergent material properties. What makes something a material is somewhat context dependent. A useful definition would be; A material is the matter from which a device is made. From this definition any solid or combination of solids or even an arrangement of solids may be a component material. This has always been true, graphite and diamond are both comprised of the same components differing only by their arrangement.

In device manufacturing, materials play a special role. It is the characteristics of the materials that determine the properties and function of the device. The, earlier discussed, efficiency of a TEG (eq. 1.2) is determined by properties of its materials. In short, designing an ideal device relies on the existence of a material that provides the ideal properties. Many devices are built upon interface interactions (such as P-N junctions) and they derive all their characteristics from their materials. The pursuance of the optimal design for interface devices depends, to some degree, on serendipity to provide appropriate material combinations.

The problem of device limitation due to poor material options can be overcome by designing the optimal material. The construction of heterostructures is one way to design a material with novel properties. Another method of material design is

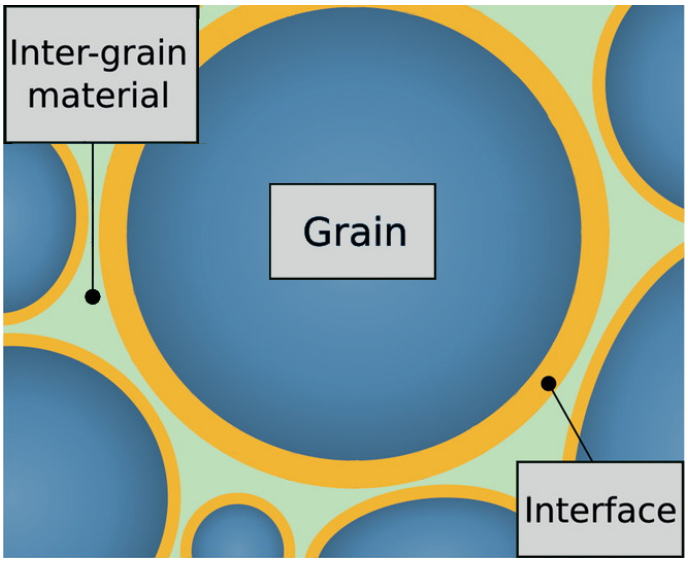

Figure 1.5. Schematic of the microscopic grain boundary. The image displays an exaggerated interface and inter-grain mater among the host crystal grains.

to form a nano-structure of the original material. This would include 2D materials and 1D materials such as carbon nanotubes. A third way of generating emergent material properties is simply by the assembly of interfaces.

1.2.1 Material Interfaces

Interfaces are common, both in devices and in the materials themselves. An interface is a boundary region between two different materials. These interfaces form as a natural part of the crystal growth. Alternatively, interfaces are deliberate structures carefully constructed out of a pair of materials. It could even be an unwanted but inevitable result of fabrication. Despite the origin of an interface its properties are often hard to predict and can give rise to unusual phenomena [16, 17].

Natural interfaces are a consequence of crystal growth. Crystallization starts with nucleation, small groups of molecules bind into a solid forming the first nucleation sites from which crystal grains can grow. These have no guarantee of being aligned and, as such, a single crystal cannot be maintained from one grain to another. This results in the formation of grain boundaries; the interfaces formed

between separate grains. A great variety of growth conditions can effect the formation of the grains, and some of those conditions can lead to entirely new materials being formed in the grain boundary region. Such a material may be thought of as an inter-grain material since strictly, the grain boundary would form between it and the host crystal [17]. It is possible to remove or at least limit the formation of grain boundaries within a material but the process of device fabrication makes some interfaces inevitable anyway. Electrical devices will have interfaces between the device components and the metallic contacts or the substrate. These interfaces must be accounted for since they will affect the function of any manufactured device [18].

Many interfaces in devices are also intentional. In these cases the interface properties give the device its function. Here, great care must be taken to ensure that the interface is clean to ensure that the intended properties of the interface are realised.

1.2.2 2D materials

2D materials are typically constructed by isolating individual layers of a bulk layered material bound by weak van der Waals forces [19]. However, some 2D materials are formed from materials that are not layered in their bulk phase, such is the case for 2D tellurium [20] and germanene [21]. These 2D materials require a great effort to make, which reflects the unusual condition 2D materials exist in. The unique dimensional constraint leads to drastically different material properties.

There are a vast number of 2D materials, a great number of which were laid out by Novoselov *et al.* the same research group [19] as published the now famous paper on the electronic properties of graphene [22]. While the research attention that graphene has received is fully merited there are many other 2D materials, such

as: transition metal dichalcogenides (TMDCs), hexagonal boron nitride (hBN) and phosphorene.

Here, crystal structures will be defined by the principal vectors and angles of the lattice. The vectors $\vec{a}$, $\vec{b}$ and $\vec{c}$ along with there angles α, β and γ, where each angle applies to the two vectors that it is not corresponded to, hence α is the angle between $\vec{b}$ & $\vec{c}$, β is the angle between $\vec{a}$ & $\vec{c}$ and γ is the angle between $\vec{a}$ & $\vec{b}$.

1.2.2.1 Graphene

Graphene has many impressive properties but the most renowned is its unique electronic structure. Novoselov *et al.* [22] demonstrated that the metallic dispersion of graphene becomes linear close to the Fermi level. This dispersion characteristic removes graphene from the regime of the non-relativistic Schrödinger equation. Graphene represents a regime in which electron transport is governed by the relativistic Dirac equation for massless fermions. The dispersion pattern, known as the Dirac cone, is formed from the out of plain p_Z orbitals. This creates a platform for the discovery and investigation of fundamental physics. This, as much as any practical application, has helped increase the research interest in graphene. The concept of using novel materials to investigate fundamental physics is one that we continue in this thesis.

Graphene is an allotrope of carbon, consisting of a single atomic layer arranged into an hexagonal honeycomb lattice that can be directly observed by scanning tunneling microscope [23]. It's structure (see fig. 1.6b) is that of a single layer of graphite (see fig. 1.6a). Graphene has a lattice constant of 2.464 Å and the cell can be defined by its angles and edge lengths $\vec{a} = 2.464\hat{a}$, $\vec{b} = 2.464\hat{b}$ with angle $\gamma = 60°$. Graphene has a two atom basis, the atoms may sit at any two of the three possible sites in the crystal. In direct coordinates the three possible sites are $[0, 0]$, $[1/3, 1/3]$ and $[2/3, 2/3]$, when any two sites have an atom the hexagonal crystal is formed.

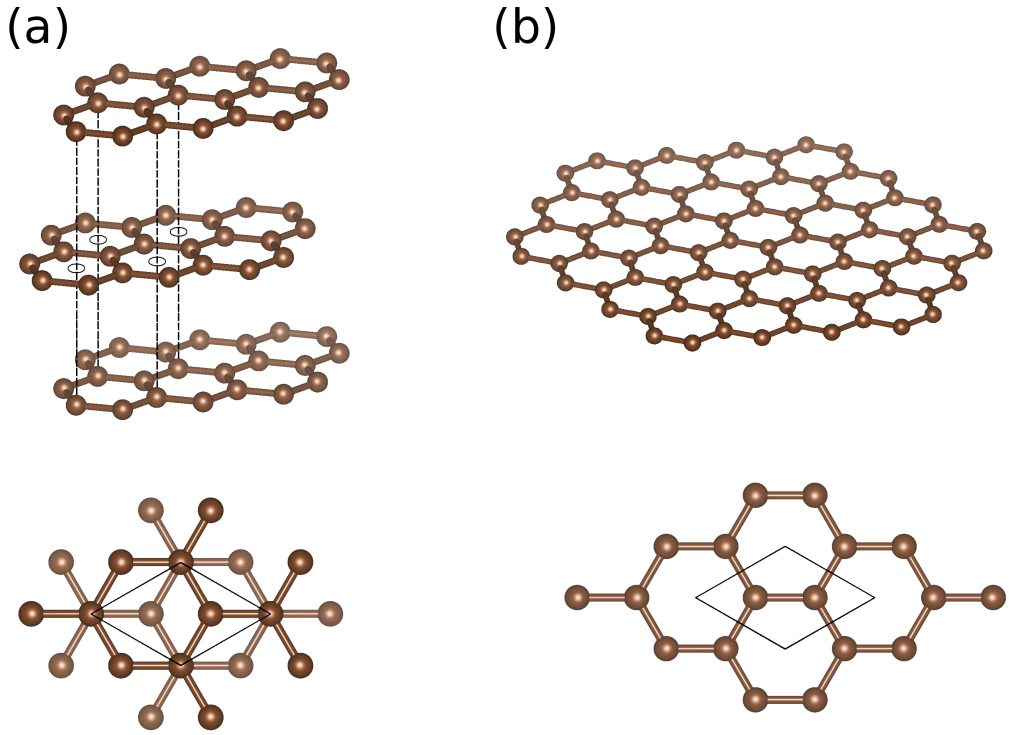

Figure 1.6. (a) The structure of graphite and a top-down view of its primitive cell. (b) The structure of graphene and a top-down view of its primitive cell.

Graphene has the space group (191) P6/mmm.

Many of graphene's primary applications are in the lab setting. The commercialisation of graphene has been slow due to economic and engineering barriers [24]. Commercial adoption of graphene has been compared to that of carbon fibre [25] which can now be found in cars, sports equipment, even in phone cases. Just as carbon fibre took time to become commercial, graphene can be expected to make its way into everyday technology, but it could take several decades. Among the many useful properties of graphene is its ultra high thermal conductivity [26] shared by other allotropes of carbon. In the lab setting graphene makes excellent electrical contacts for other 2D materials [18]. It also has impressive optical properties with an exceptionally high optical absorption (for a single atomic layer) of over 2%[27]. Furthermore, specific patterning of defected graphene can lead to 100% absorption [28]. Finally, it is emphasised that there is considerable interest in graphene for its

ability to be used as a platform for investigating fundamental physics.

1.2.2.2 Hexagonal Boron Nitride

Whereas graphene is conducting hexagonal boron nitride is insulating with a 5.8 eV band-gap, meaning that, for the purposes of electronics, it fills a unique niche separate from graphene. Boron nitride can exist in a number of different phases, including cubic phase, an amorphous phase and, of course, the hexagonal phase, shown in figure 1.7. The stoichiometry of all these phases is the same, with one boron to one nitrogen atom. Unlike graphene hexagonal boron nitride has strong ionisation between its a-site and b-site atoms. When multilayered, Hexagonal boron nitride can be arranged into a number of different stacking configurations. Here, AA' stacking indicates that each layer sits directly above the other but with the opposite atoms occupying the same sites from one layer to the next. The AA' stacking (see fig 1.7) is the preferable configuration for hexagonal boron nitride.

The crystal structure of monolayer hexagonal boron nitride, shown in figure 1.7a & 1.7b, is similar to that of graphene and forms the same honeycomb lattice. Its lattice can be described the same way, by two vectors of the same length separated by an angle of 60°. The lattice constant of hexagonal boron nitride is 2.512 Å. In describing the basis, one of the atoms set at a potential site , $[0, 0]$, $[1/3, 1/3]$ or $[2/3, 2/3]$, must be boron and on either of the two remaining sites will sit a nitrogen. The symmetry of hexagonal boron nitride gives it the space group (194) $P6_3/mmc$, just the same as graphene.

Hexagonal boron nitride is considered to be one of the best substrate choices for 2D materials fabrication. Due to its atomically smooth surface a clean interface can be easily made with hexagonal boron nitride [29] and because of its wide bandgap it remains electrically isolated from the components built on it [30]. Furthermore hexagonal boron nitride has high chemical stability, mechanical strength and thermal

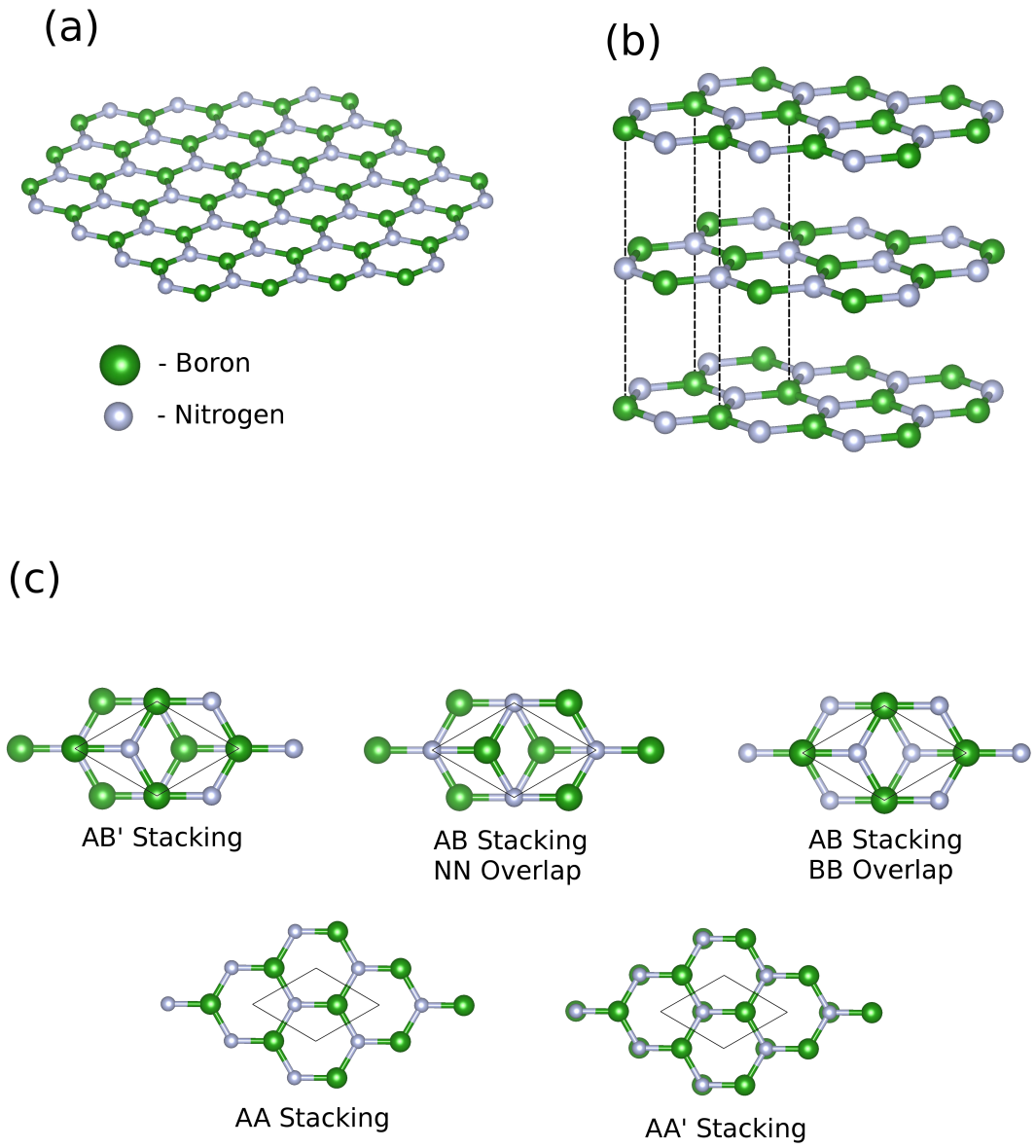

Figure 1.7. (a) The structure of monolayer hexagonal boron nitride with a legend for atomic spices. (b) The structure of mulitlayer hexagonal boron nitride in favorable AA' stacking. (c) Shows the different stacking orders hexagonal boron nitride can adopt

conductivity and has been proposed as a new dielectric medium [31].

1.2.2.3 Transition Metal Dichalcogenides

While graphene is metallic (often described as a zero bandgap semiconductor) and hexagonal boron nitride is insulating transition metal dichalcogenides (TMDCs) are typically semiconducting. TMDCs (sometimes abbreviated to TMDs) are unlike graphene and hexagonal boron nitride in that the TMDCs are a family of many different 2D materials[32]. A single TMDC is formed from a transition metal (the M atom) and two chalcogen atoms (the X atoms) of the same species. The chalcogen atoms for TMDCs are usually restricted to sulphur, selenium and tellurium, since oxygen compounds usually do not form layered structures [33]. While TMDCs are often seen as semiconducting this is not necessarily the case, with 3 chalcogen atoms and 29 transition metals there are in principle 87 TMDCs, each with unique properties. We choose to neglect the heaviest row of transition metals from this count due to their rarity and instability. Experimentally, much focus has been placed on MoS_2 due to its convenient semiconducting bandgap of 1.9 eV [34, 35] and its high stability, making it relatively easy to fabricate. Numerous investigations into TMDCs are performed first or only ever on MoS_2 [36, 37]. Considerable research interest has also been cast at WS_2, $MoSe_2$ and WSe_2.

The crystal structure of the TMDCs is very different to hexagonal boron nitride and graphene, in that, not all atoms are centred on a 2D plane. The lattice however is made from the same 2D hexagonal cell with just three potential atomic sites. The three sites are, as before, at $[0, 0, \pm\Delta]$, $[1/3, 1/3, \pm\Delta]$ or $[2/3, 2/3, \pm\Delta]$. Here, the three vectors include a displacement in the z-axis normal to the Bessel plane. This shift applies to the chalcogen atoms that sit just above and below the plane, while for transition metal, M atoms $\Delta = 0$. It could therefore be considered that a TMDC is not a true 2D material. If, however, this argument were

extended it could also apply to graphene since each atom has a three dimensional physical extent. While symmetry and periodicity play a crucial role in determining two dimensionality, practical considerations are often more useful. A material can reasonably be described as 2D when there is significant quantisation of energy levels along this direction i.e. greater than $\sim KT$.The lattice for the TMDCs is still 2D with a lattice constant dependent on the specific compound.

There are two phases of TMDC, the H phase and T phase. In both the H and T structures the chemical formula is the same with one transition metal and two chalcogen atoms. However, the structure is such that in both cases a single M atom will be bonded to three X atoms above the plane and to three below the plane. Figure 1.8 shows that the 3 bonded X atoms form an equilateral triangle (when in their respective unstained structures [38]). For a TMDC in the H structure, each X atom occupies a site directly above or below another X atom. The X atom triangles overlay each other in this structure . A T structure monolayer has X atom triangles above and below the plane which are rotated by 60°. The H phase is more commonly denoted 2H since TMDCs with a 2H structure have an AA' stacking. The T phase has AA stacking and correspondingly it is frequently called the 1T phase.

The electronic features of a great many TMDCs are well investigated [39, 40]. Among the most notable H phase TMDCs (MoS_2, WS_2, $MoSe_2$ and WSe_2) the bandgap is indirect in the bulk structure, but becomes direct when reduced to the 2D structure. Some of the 2H-TMDC's have been found to exhibit a spin splitting at the K point, driven by spin orbit coupling [41, 42]. TMDCs demonstrate vastly different thermal properties to either graphene or hBN. This is in part due to the out of plane bonding leading to unique phonon behaviour. Furthermore, phonon bandgaps may be induced in TMDCs as a result of their differing atomic masses. TMDCs have also been examined for their application to water splitting [43], energy storage [44, 45] thermoelectrics, optoelectronics, thermal management tribo eclectics and piezo electricity.

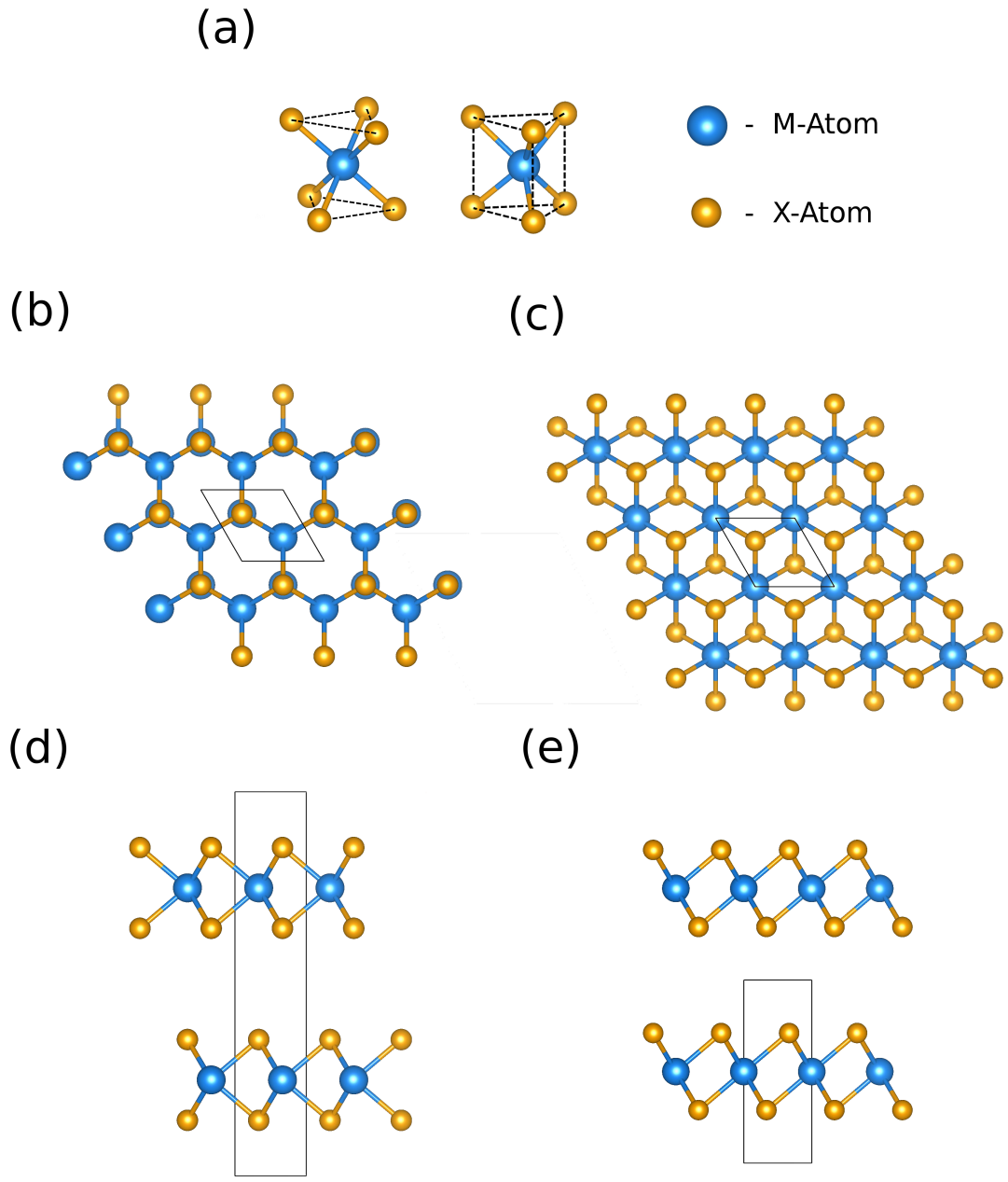

Figure 1.8. (a) Shows the local coordination about the M atoms for the 1H and 1T phases. Subfigures (b) & (c) show the unit 2H & 1T unit cells respectively, each embedded within there crystal structures. (d) shows the layer structure of the 2H cell and (e) shows the layer structure of the 1T cell.

1.2.3 2D Heterostructures

2D heterostructures or van der Waals heterostructures are repeating structures conforming to alternating layers of material 1 and material 2. In the case of 2D (van der Waals) materials this means stacking heterostructure pairs by switching materials across the van der Waals gap. Other terminology employed includes heterobilayers and heterojunctions, A heterobilayer is a heterostructure in which only one layer of each material constitutes the structure, making it non-periodic in the out of plane direction. A heterojunction is where focus is laid on electrical transport through material 1 into material 2 or vice versa.

2D materials are an artificial phase of matter with altered physical properties from their bulk counterparts. However, while 2D materials represent a significant step forward in terms of materials design, it is a small step compared to the wealth of variation provided by 2D heterostructures. For n 2D materials there are $n(n-1)/2$ possible heterostructure pairs and even more permutations exist for more layers. High throughput computational studies have estimated the number of possible 2D materials at $5,619$ which would put the number of possible 2D heterostructures at $15,783,771$, almost 16 million. This is is before a consideration has been made for stacking order. As demonstrated in figure 1.7 relatively simple van der Waals heterostructures can have many stacking arrangements. When the van der Waals layers differ from each other and become more complicated the variation in stacking arrangements will increase. As one considers supercells and Moiré lattices the variety of stacking orders approaches a continuum.

The properties and applications of 2D heterostructures have as much variety as there are heterostructure combinations. 2D heterostructures have been applied to the fabrication of field-effect tunneling transistor [46] by sandwiching a semiconducting or insulating 2D layer between sheets of graphene. There have been studies on 2D heterostructures for their application to thermoelectrics [47]. Studies have inves-

tigated using heterostructuring to enhance electrical conductivity, whilst exploiting interface scattering to reduce thermal transport. 2D heterostructures should also have the effect of increasing the asymmetry of the density of states, which will improve the Seebeck coefficient thus further enhancing thermoelectric performance. Heterostructures of MoS_2 and graphene have been explored for nonvolatile memory [48]. Photovoltaic cells employing heterostructures have also been developed [49]. Relevant to photovoltaics and other optoelectronic applications, electron hole separation can be driven by the band alignment due to conduction and valence bands in adjacent material layers [50]. Water splitting has also seen innovation through 2D heterostuctures since a key requirement in their design is the efficient separation of electron hole pairs [51]. Additionally ultrathin Sensing Devices have been constructed using 2D heterostructures [52] based on the charge sensitivity of photoluminescence.

1.2.3.1 Heterostucture Modelling

Despite the huge potential of heterostructures much of the possible research space remains relatively unexplored. This is in part due to the broad scope of heterostructure research but also because of the inherent difficulties involved. Understanding the electronics and phononics of interfaces and heterostructures requires atomic scale modelling. In the case of electronics this further requires methods of calculating the electronic structure of the interface. One approach to is to use first principles methods, that directly solve the Schröedinger equation for a given set of approximations. These methods require no parameterisation to calculate an electronic structure. This makes them predictive in any variety of situations. First principles methods include density functional theory, DFT, which is detailed in chapter 2.

Non-*ab initio* electronic modelling techniques require comparison to analogous scenarios and detailed parameterisation or they can be limited to non-specific broad

statements. The investigation of systems in unique and/or unusual conditions requires such parameterisation or an approach that can be considered parameterless. All heterostructures represent a unique material condition including stress, charge transfer and interface bonding. Additionally, any previously unstudied heterostructure will have no data to parameterise against. These structures force one to consider parameterless methods, like DFT.

In the context of *ab initio* methods there are many complications that must be considered for heterostructure calculations to be trusted. The first is commensurability; no two materials are going to have a perfect ratio relationship between there lattice constants. Both in real systems and in models two materials of a heterostructure will strain to fit each other. This makes lattice matching a key problem. This leads on to the coincidence of the different basis. The rotation and strain are determined by the lattice matching, however, the in plane alignment can also change. In terms of 2D heterostructures this would correspond to the stacking order. Just as the layers can shift in plane, so can they shift in the interface direction. This is to say that an optimal layer separation must be found. Finally, surface terminations and interface reconstruction are of vital importance in 3D heterostructures but this issue is somewhat avoided in the van der Waals case.

The calculation of heterostructures or interfaces, frequently requires the use of super cell structures. Supercells can play a vital part in the calculation of lattice matching, phonons, defects and geometry optimisation. A supercell is a legitimate unit cell for the crystal. Upon periodic replication of the supercell the original crystal is returned. Diagonal expansion of the unit cell is the simplest. A unit cell described by three lattice vectors $\vec{a}$, $\vec{b}$ and $\vec{c}$ may be expanded in those same directions. Where a primitive cell may be described $\mathbf{L} = (i\vec{a}, j\vec{b}, k\vec{c})$ for $i = j = k = 1$, with $\mathbf{L}$ being the lattice, a diagonal supercell may be described by i, j and k taking integer values greater than unity. These diagonal supercells are given using the notation $i \times j \times k$ and an example is shown in 2D in figure 1.9b. More complicated expansions can be

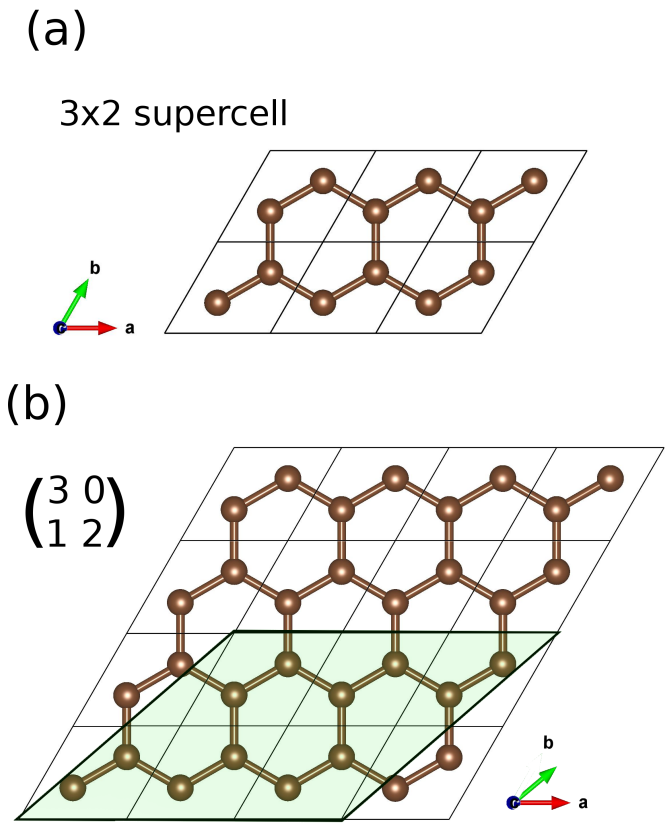

Figure 1.9. Example supercells of 2D graphene. (a) Shows a diagonal 3×2 supercell while (b) shows, in the highlighted region, a non-diagonal supercell of graphene with the given 2D transformation matrix.

made by linear combinations of the primitive cell vectors to form three new vectors. These are non-diagonal supercells and can be written as

$$\mathbf{L} = (T_{11}\vec{a} + T_{12}\vec{b} + T_{13}\vec{c}\ ,\ T_{21}\vec{a} + T_{22}\vec{b} + T_{23}\vec{c}\ ,\ T_{31}\vec{a} + T_{32}\vec{b} + T_{33}\vec{c}). \tag{1.3}$$

The notation used intentionally indicates that $\mathbf{T}$ is a transformation matrix. A supercell is formed by any transformation matrix with integer elements and a determinant greater than one ($det(\mathbf{T}) > 1$). This process creates a cell with lattice vectors that are linear combinations of primitive cell vectors and the requirement for the determinant to be greater than one ensures that the supercell will be larger than the primitive (an example is shown in 2D in figure 1.9c).

1.2.3.2 Constituent Interactions

There are a number of important physical features of the interface that need to be explored in order to understand the behaviour of a heterostructure. Some of the most important for thermal, electronic, optoelectronic and thermoelectric are band alignment, phonon transport and interface reconstruction.

Band alignment is an important property of the interface. By understanding the relative placement of the valence and conduction bands across the two materials, we understand, to some extent how the interface will behave. The optoelectronic (along with the just the electronic) are strongly controlled by the band alignment. Type I band alignments are incorporated into light-emitting diodes. Type II band alignments help create highly efficient photovoltaic cells. Finally, type III are rarely helpful but nearly type III alignments are valuable for interlayer tunneling field effect transistors [53].

While band alignments determine many optoelectronic properties, thermal properties are governed by the phonons. This makes understanding the properties

of phonon transport both along and across the interface vitally important. High conductivity materials are wanted for crucial electrical components that can overheat, so that they can dissipate that heat more effectively. However, materials with low thermal conductivity are just as important. Thermoelectric materials benefit from low thermal conductivity, additionally two dimensional confinement will enhance the Seebeck coefficient [54]. This makes 2D heterostructures a promising new meta-material for thermoelectric devices.

At the interface, chemical reactions and intermixing can lead to the formation of amorphous interfacial materials. In some cases this material can grow large enough and be favorable enough to crystallise into a new interface material. A general approach to predicting the properties of an unknown material which may or may not form are beyond *ab initio* methods. However, careful surface defect analysis and random structure searches may yield considerable insights. Confidence in these results still calls for experimental justification [17, 55].

1.3 Outline

In this thesis the concept of heterostructures will be investigated. This investigation will be conducted with two primary goals; to identify trends in 2D heterostructures and to establish a rigorous methodology for calculation of interface structures such as heterostructures and their properties. The investigation into trends in 2D heterostructures is conducted on the TMDCs, while the development of methodologies for interface calculations are established for the general case, with continuing exceptions, such as reconstruction, accounted for by case study. This chapter, (Chapter 1) acts as an introduction to the main body of the thesis

The fundamental theory of both *ab initio* electronic and phononic structure calculation is detailed in chapter 2. Here, are derived the theories that form the

basis of density functional theory (DFT). The principles of DFT are extended to the understanding of phonons in atomic matter. Hence, are derived, the fundamentals of the frozen phonon method. These theories and methods are used throughout the work of this thesis. A separate theoretical discussion takes place in chapter 3. The aims of this chapter are to derive the lattice thermal conductivity. In doing so, the boundary, isotope and three phonon scattering rates are derived, along with a quasi-anharmonic model of thermal conductivity. These derivations support the work presented on thermal transport in chapter 5.

Chapter 4 explores trends in band alignment for TMDCs. This provides valuable insight into the nature of band alignments and interface interaction. The many trends are consolidated into a simple rule that shows a marked improvement over Anderson's rule. In this chapter a trend in the band alignments of TMDC heterostructures is explored, developed and explained. In chapter 5 the thermal properties of TMDCs are examined. The thermal conductivity of a TMDC heterostructure will in general be reduced from either constituent. This establishes a trend in the conductivities of TMDC heterostructures.

In chapter 6, the fundamental theory of interfaces is explored and an extensive, rigorous methodology is developed for *ab initio* calculation. Uses and applications of this methodology are presented for wider application. These methods do not yet include a systematic procedure for identifying, generating and modelling new interface materials. Due to this limitation the case study of fresnoite is examined in chapter 7. Fresnoite is a non-stoichiometric interface material that forms between SiO_2 and $BaTiO_3$, its chemical formula is $BaTiSi_2O_3$. This provides an understanding of interface materials and represents a methodology for investigating them.

1.4 Summary

We introduce the pressures of modern technology that we wish, in the long term, to alleviate through our work. As part of this, a brief review of the technology is given, exploring optoelectronics, thermoelectrics and thermal management. Recent years and decades have seen an increase in materials design within the field of materials research. This and current trends in the field of material research are discussed. Furthermore, we discuss the intrinsic promise of 2D materials, heterostructures and 2D heterostructures in particular. The difficulties of working with these materials and the key interface interactions are clearly defined. Lastly, a concise outline of the thesis structure and content is explained. The following chapters present in depth theory which provides the background physics that underpins the work presented in this thesis.

Chapter 2

Theory of Electron and Phonon Structure

"Truth... is much too complicated to allow anything but approximations."

— John von Neumann,

"The Mathematician" in 'The Works of the Mind', 1947

2.1 Introduction

The research presented in this body of work will be predominantly theoretical and from first principles. The theory behind first principles Density Functional Theory (DFT) is both deep and broad. In order to preserve the fluidity of this work the extensive background theory is reported here as part of a dedicated theory section.

The majority of work presented, in this thesis, is be underpinned by DFT. A review of the basic operations of DFT is presented in this chapter. In addition the specifics of *ab initio* phonon calculations are also presented here. Such phonon calculations lead naturally on to thermal conductivity calculations described in the

following chapter.

2.2 Density Functional Theory

Density functional theory or DFT is today the premier tool for the calculation of electronic structure, both crystals and molecules. DFT is a first principles theoretical approach also called *ab initio*. The Latin expression *ab initio* means "*ab*"-"from" and "*initio*"-"beginning". In the world of physics and quantum chemistry this means to apply theory with the fewest number of possible assumptions. In DFT the only input assumptions are fundamental constants, electromagnetism and quantum mechanics.

A basic principle of DFT was outlined in 1927 by Llewellyn Thomas in 1927[56]. He described that electrons within the crystal would respond to an effective potential, V, determined by the ionic positions and the distribution of electrons within the solid. This theory is also used and developed by Fermi in 1928[57] and Dirac in 1930[58] who incorporated exchange into the method. However, a modern theory of DFT begins with Hohenberg and Kohn's work on density functionals in 1964[59]. It is the modern formalism of DFT that will be reviewed here with special reference to the lecture notes of Paolo Giannozzi[60].

Modern DFT has become a widely used tool for many reasons. In its current form it is immensely versatile and can be used to calculate far more than electronic structure. Through the application of DFT one can find material properties such as: atomic structure, bulks modulus, formation and binding energies, magnetic polarisation, dielectric response[61], phonon dispersions[62] and, with perturbation theory both electrical[63] and heat transmission[64]. In fact, as we shall see from the Hohenberg-Kohn theorem, any material property can in principal be determined by a functional of the electron density[59].

When describing DFT we are sometimes faced with the problem that, while the core theories are relatively simple, any practical applications of the theory grow rapidly in complexity. This is because there are many, physical and numerical, theories and proofs, that are entirely necessary for practical computation, but are generally superfluous for a detailed understanding of the theory. DFT can sometime be described as "A few good ideas and a books worth of appendices".

In the description presented here we will use Hartree atomic units ($\hbar = m_e = e = 4\pi/\epsilon_0 = 1$). The problem will be broken down into the a set of questions each corresponding to a section or subsection of the DFT theory:

- section **2.2.1 Many Body Problem:** "Why do we need DFT?",
- section **2.2.2 Born-Oppenheimer Approximation:** "Why & How can we solve for just electrons and ignore ionic motion?",
- section **2.2.3 Hohenberg-Kohn Theorem**: "Is a description based on functionals valid?",
- section **2.2.4 Kohn-Sham Auxiliary System** "How can we handle interacting electrons?" and subsection **2.2.4.1 Kohn-Sham Eigenvalues** "Given our assumptions, are the results still meaningful?",
- section **2.2.5 The Secular Equation**: "What equation are we solving?" and subsection **2.2.5.1 Orthogonal Basis Set** "How do we solve it?"

2.2.1 Many Body Problem

In quantum mechanics any system can be described by the Schrödinger equation[65]. For a system of electrons in equilibrium the time independent Schrödinger equation

is appropriate and can be written generically as,

$$\hat{H}\left|\psi_s\right\rangle = E_s\left|\psi_s\right\rangle, \tag{2.1}$$

where $|\psi_s\rangle$ is eigenstate s and E_s is the corresponding energy eigenvalue. Here $|\psi_s\rangle$ is clearly defined as a coupled system of electrons and nuclei,

$$\left|\psi_s\right\rangle = \left|\psi_s(\mathbf{r}_1, \mathbf{R}_1, ...\mathbf{r}_{N_i}, \mathbf{R}_{N_n})\right\rangle. \tag{2.2}$$

Here $\mathbf{r}_i$ is the i'th electron's position vector and $\mathbf{R}_n$ is the position vector of ion n. The values N_i and N_n are the total number of electrons and ions respectively.

The Hamiltonian of a quantum solid, a system of interacting nuclei and electrons, can be written as

$$\begin{aligned}\hat{H} =& \hat{T}_n + \hat{T}_e + \hat{U} \\ =& \hat{T}_n + \hat{T}_e + \hat{V}_{ee} + \hat{V}_{en} + \hat{V}_{nn},\end{aligned} \tag{2.3}$$

where $\hat{T}$ is a kinetic energy operator for the subscripts n and e denoting ions and electrons respectively. $\hat{V}_{ee}$ is the potential energy operator describing the electron-electron interactions while $\hat{V}_{en}$ and $\hat{V}_{nn}$ are the electron-ion and the ion-ion interactions respectively. Expanding out the Hamiltonian gives us

$$\hat{H} = -\sum_n \frac{1}{2M_n}\nabla_n^2 - \frac{1}{2}\sum_i \nabla_i^2 + \frac{1}{2}\sum_{i\neq i'} \frac{1}{|\mathbf{r}_i - \mathbf{r}_{i'}|} - \sum_{ni} \frac{Z_n}{|\mathbf{R}_n - \mathbf{r}_i|} + \frac{1}{2}\sum_{n\neq n'} \frac{Z_n Z_{n'}}{|\mathbf{R}_n - \mathbf{R}_{n'}|}. \tag{2.4}$$

Here, the ion n has Z_n as its atomic number and M_n as its mass. The ∇ operator is constructed from derivatives with respect to either ionic position, ∇_n, or electronic positions, ∇_i. There is no general solution to equation 2.4, neither are there any trivial simplifications that can be made.

In order to make this soluble we can separate the ionic and electronic com-

ponents. One may then, with an appropriate choice of base states, and a means of determining the potential $\hat{U}$, solve for the eigenstates of a quantum solid.

2.2.2 Born-Oppenheimer Approximation

The Born-Oppenheimer approximation is often defined very loosely, stating that as electrons are much less massive than ions, any perturbation in the crystal will be compensated for by the motion of electrons before the ions have a chance to react. This implies that for any given displacement of the ions, due to there motion, the electrons will be in there equilibrium state. One may then say that even if a vibration is excited in the lattice the electrons will always occupy their ground state and therefore may be treated as separable.

Here is given a rigorous demonstration of the adiabatic approximation (Born Oppenheimer Approximation to second order[66]). First we define the exact Hamiltonian for a crystal or of molecule as

$$\hat{H} = \hat{T}_e + \hat{T}_n + \hat{V}_{ee} + \hat{V}_{en} + \hat{V}_{nn} \tag{2.5}$$

We can separate the ionic kinetic energy from the electronic and potential terms to give,

$$\hat{H}\Psi_s = \hat{H}_e\Psi_s + \hat{T}_n\Psi_s = E_s\Psi_s \tag{2.6}$$

Now we may let the full coupled molecular/crystal wavefunction, Ψ_s, have separable coupled $\chi_{si}(\mathbf{R})$ and electronic $\varphi_i(\mathbf{r};\mathbf{R})$ contributions. This does not assume separability, if the states are always coupled $\varphi_i(\mathbf{r};\mathbf{R})$ will go to unity when,

$$\Psi_s = \sum_i \varphi_i(\mathbf{r};\mathbf{R})\chi_{si}(\mathbf{R}). \tag{2.7}$$

Here the electron wavefunction is determined by r which itself has a parametric

dependence on R. Meaning that φ_i has a functional dependence on $\mathbf{R}$.

Now using the definition in equation 2.7 the Schrödinger equation may be rewritten as,

$$\left(\hat{H}_e + \hat{T}_n\right) \sum_i \varphi_i(\mathbf{r};\mathbf{R})\chi_{si}(\mathbf{R}) = E_s \sum_i \varphi_i(\mathbf{r};\mathbf{R})\chi_{si}(\mathbf{R}) \tag{2.8}$$

If under the adiabatic approximation the coupled wavefunctions are determined by a potential derived from only the electronic wavefunctions then it is valid (or at least consistent) to neglect the coupling and interpret the coupled wavefunctions as ionic wavefunctions. The ionic contribution can then also be neglected when calculating the electron wavefunctions.

In order to derive an ionic Schrödinger equation we evaluate the integrals of the electronic wavefunctions over r. We define this inner-product using Dirac notation as

$$\begin{aligned} \int_{\mathbf{r}} \varphi^*_{i''}(\mathbf{r};\mathbf{R})\left(\hat{H}_e + \hat{T}_n\right) \sum_i \varphi_i(\mathbf{r};\mathbf{R})\chi_{si}(\mathbf{R})\ dr &= \int_{\mathbf{r}} \varphi^*_{i''}(\mathbf{r};\mathbf{R}) \sum_{i'} \varphi_{i'}(\mathbf{r};\mathbf{R})\chi_{si'}(\mathbf{R})\ d\mathbf{r}, \\ \sum_i \left\langle i'' \middle| \hat{H}_e + \hat{T}_n \middle| i \right\rangle |\chi_{si}\rangle &= \sum_{i'} E_s \langle i''|i'\rangle |\chi_{si'}\rangle , \end{aligned} \tag{2.9}$$

where we allow ourselves to express the electronic wavefunction by only its index.

We can observe that the summation drops out of the right hand side of equation 2.9 leaving $E_s |\chi_{si''}\rangle$. Now we evaluate the first term on the left hand side

giving

$$\begin{aligned}\sum_i \left(\left\langle i''\middle|\hat{H}_e\middle|i\right\rangle + \left\langle i''\middle|\hat{T}_n\middle|i\right\rangle\right)|\chi_{si}\rangle &= E_s\,|\chi_{si''}\rangle \\ \sum_i \left(E_i\,\langle i''|i\rangle + \left\langle i''\middle|\hat{T}_n\middle|i\right\rangle\right)|\chi_{si}\rangle &= E_s\,|\chi_{si''}\rangle \\ E_{i''}\,|\chi_{si''}\rangle + \sum_i \left\langle i''\middle|\hat{T}_n\middle|i\right\rangle|\chi_{si}\rangle &= E_s\,|\chi_{si''}\rangle\,,\end{aligned} \tag{2.10}$$

where the two terms on the left account for the electronic energy and for the electronic transitions due to ionic motion.

We may now rearrange the equation,

$$(E_{i''} - E_s)\,|\chi_{si''}\rangle = -\sum_i \left\langle i''\middle|\hat{T}_n\middle|i\right\rangle|\chi_{si}\rangle\,. \tag{2.11}$$

This demonstrates that the difference between the complete coupled energy of the system and the electronic energy is entirely described by the interaction between the ionic kinetic energy operator and the electronic wavefunctions.

To evaluate the right-hand side of equation 2.11 we use the definition

$$\hat{T}_n = -\sum_\sigma \frac{1}{2M_\sigma}\nabla_\sigma^2. \tag{2.12}$$

We now evaluate the to get

$$\sum_\sigma \left\langle i''\middle|\hat{T}_n\middle|i\right\rangle|\chi_{si}\rangle = \hat{T}_n\,|\chi_{si''}\rangle + \sum_i (B_{i''i} + A_{i''i})\,|\chi_{si}\rangle\,, \tag{2.13}$$

where two expressions are convenient to define, from the product rule, $A_{i''i}$ and $B_{i''i}$ corresponding to terms in ∇ and ∇^2 respectively. These terms are defined,

$$A_{ii'} = \sum_\sigma \frac{-1}{M_\sigma}\,\langle i|\nabla_\sigma|i'\rangle\,, \tag{2.14}$$

and

$$B_{ii'} = \sum_{\sigma} \frac{-1}{2M_\sigma} \left\langle i \middle| \nabla_\sigma^2 \middle| i' \right\rangle . \tag{2.15}$$

We now substitute back into equation 2.11 to get

$$\left(E_{i''} + \hat{T}_n - E_s\right) |\chi_{si''}\rangle = \sum_i \left(B_{i''i} + A_{i''i}\right) |\chi_{si}\rangle \tag{2.16}$$

The terms in the remaining summation can be separated into $i = i''$ and $i \neq i''$. This separates the interactions into those which leave the electron state unchanged and those which do not. Applying this separation gives,

$$\left(E_{i''} + \hat{T}_n - E_s\right) |\chi_{si''}\rangle = -\left(B_{i''i''} + A_{i''i''}\right) |\chi_{si''}\rangle - \sum_{i \neq i''} \left(B_{i''i} + A_{i''i}\right) |\chi_{si}\rangle . \tag{2.17}$$

At this point we can impose the adiabatic condition. This is done by imposing the condition that ionic motion cannot excite an electronic state, hence all terms in which the initial and final states are different ($i \neq i''$) go to zero. This expresses the notion that ionic motion is slow compared to electronic relaxation rate and so the electrons effectively remain in the ground state in spite of ionic vibration.

We can also remove A_{ii} since it goes to zero. $\nabla \langle i|i\rangle = \nabla[1] = 0$, but by product rule we can say

$$\begin{aligned} \nabla \langle i|i\rangle &= \langle \nabla i|i\rangle + \langle i|\nabla i\rangle \\ \langle \nabla i|i\rangle &= -\langle i|\nabla i\rangle \\ \langle i|\nabla i\rangle^\dagger &= -\langle i|\nabla i\rangle \end{aligned} \tag{2.18}$$

The inner product must return a real value, therefore we know that $\langle i|\nabla i\rangle^\dagger = \langle i|\nabla i\rangle$ and hence

$$\begin{aligned} \langle i|\nabla i\rangle &= -\langle i|\nabla i\rangle \\ \langle i|\nabla i\rangle &= \langle i|\nabla|i\rangle = 0 \end{aligned} \tag{2.19}$$

Now we rewrite 2.17 and rearrange to obtain

$$\left(\hat{T}_n + E_i + B_{ii}\right)|\chi_{si}\rangle = E_s\,|\chi_{si}\rangle \tag{2.20}$$

Here the term B_{ii} is the Diagonal Born Oppenheimer Correction. At this point the subscripts must be evaluated. The term B_{ii} and E_i can be combined into an effective electronic potential $U_i = B_{ii} + E_i$. This allows us to define an ionic motion equation for each electronic state i,

$$\left(\hat{T}_n + U_i\right)|\chi_{si}\rangle = E_s\,|\chi_{si}\rangle \tag{2.21}$$

In reaching this point we have demonstrated that the electronic wavefunctions are separable from the coupled wavefunction, hence demonstrating that under the adiabatic approximation there is no coupling and we can reformulate equation 2.21 as

$$\left(\hat{T}_n + U_i\right)|\chi_{ji}\rangle = E_{ji}\,|\chi_{ji}\rangle\,, \tag{2.22}$$

and

$$\left(\hat{T}_n + \mathcal{V}\right)|\chi_j\rangle = E_j\,|\chi_j\rangle \tag{2.23}$$

where the index j counts over ionic states, thus proving that electronic and ionic states are separable under the adiabatic approximation . We can define the electronic state i that will evolve adiabatically with ionic motion.

It has been demonstrated that, under the adiabatic approximation, the separable electronic states may be defined,

$$\hat{H}_e\,|\varphi_i\rangle = \left(\hat{T}_e + \hat{V}_{ee} + \hat{V}_{en}\right)|\varphi_i\rangle\,, \tag{2.24}$$

allowing calculations of electronic energies and eigenvalues independently of ionic motion. We note that here the ion-ion interaction is dropped since it only has the

effect of applying a static shift to the energies. This term can therefore be neglected without consequence.

2.2.3 Hohenberg-Kohn Theorem

The Hohenberg-Kohn theorem is actually two theories, both central to the concept of DFT. The first Hohenberg-Kohn theorem establishes that the Hamiltonian may be exactly and uniquely determined by an external potential which in turn is determined by a ground state density of interacting particles. Second, it shows that a functional for energy, with a global minimum corresponding to the ground state density, always exists for an external potential.

These two Theorems are stated clearly and without ambiguity by R.Martin[61].

Theorem 1

For any system of interacting particles in an external potential $V_{ext}(\mathbf{r})$, the potential $V_{ext}(\mathbf{r})$ is determined uniquely, except for a constant, by the ground state particle density $n_0(\mathbf{r})$.

and

Theorem 2

A universal function for the energy $E[n]$ in terms of the density $n(\mathbf{r})$ can be defined valid for any external potential $V_{ext}(\mathbf{r})$. For any particular $V_{ext}(\mathbf{r})$, the exact ground state energy of the system is the global minimum value of this functional, and the density $n(\mathbf{r})$ that minimizes the functional is the exact ground state density $n_0(\mathbf{r})$.

We now expand on these rules.

Theorem 1:

We will now provide the proof for the first Hohenberg-Kohn theorem by contradiction[59]. To achieve this we evoke the variational principle, which states that, for any Hamiltonian $\hat{H}^{(1)}$ there is a corresponding ground state $|1\rangle$ which gives the global minimum of $\langle 1|\hat{H}^{(1)}|1\rangle$. Now suppose that we have two external potentials ($V_{ext}^{(1)}(\mathbf{r})$ and $V_{ext}^{(2)}(\mathbf{r})$) that both return the same ground state density $n_0(\mathbf{r})$. Having two external potentials leads to two Hamiltonians, $\hat{H}^{(1)}$ and $\hat{H}^{(2)}$, each with a corresponding ground state $|1\rangle$ and $|2\rangle$. Remember it is only the ground state density $n_0(\mathbf{r})$ that is chosen to be the same.

We may now state explicitly,

$$E^{(1)} = \left\langle 1\middle|\hat{H}^{(1)}\middle|1\right\rangle < \left\langle 2\middle|\hat{H}^{(1)}\middle|2\right\rangle. \tag{2.25}$$

It is important to see that we could make an equivalent expression for $E^{(2)}$ by swapping all the state indices ($1 \rightleftharpoons 2$).

$$E^{(2)} = \left\langle 2\middle|\hat{H}^{(2)}\middle|2\right\rangle < \left\langle 1\middle|\hat{H}^{(2)}\middle|1\right\rangle. \tag{2.26}$$

This inversion of states can be applied at any stage of the derivation.

We may freely define

$$\hat{H}^{(1)} = \hat{H}^{(1)} + \hat{H}^{(2)} - \hat{H}^{(2)} \tag{2.27}$$

and hence

$$\begin{aligned}\left\langle 2\middle|\hat{H}^{(1)}\middle|2\right\rangle &= \left\langle 2\middle|\hat{H}^{(2)}\middle|2\right\rangle + \left\langle 2\middle|\hat{H}^{(1)} - \hat{H}^{(2)}\middle|2\right\rangle \\ &= E^{(2)} + \int \left(V_{ext}^{(1)}(\mathbf{r}) - V_{ext}^{(2)}(\mathbf{r})\right) n_0(\mathbf{r})\, d^3\mathbf{r}\end{aligned} \tag{2.28}$$

The only terms of the two Hamiltonians which do not cancel out are the external

potential terms. Further, because the external potential is not an operator, the state vectors may form an inner product and go to unity.

We may now substitute this expression into equation 2.25 to give

$$E^{(1)} < E^{(2)} + \int \Big(V_{ext}^{(1)}(\mathbf{r}) - V_{ext}^{(2)}(\mathbf{r})\Big) n_0(\mathbf{r})\ d^3\mathbf{r}, \tag{2.29}$$

We may again enact the inversion of states performed for equation 2.26 to give

$$E^{(2)} < E^{(1)} + \int \Big(V_{ext}^{(2)}(\mathbf{r}) - V_{ext}^{(1)}(\mathbf{r})\Big) n_0(\mathbf{r})\ d^3\mathbf{r}, \tag{2.30}$$

Now if we simply add together equations 2.29 & 2.30 we obtain a contradiction.

$$E^{(2)} + E^{(1)} < E^{(1)} + E^{(2)} \tag{2.31}$$

where, clearly the integral terms cancel out. This contradiction demonstrates that for any given ground state density there is a single unique external potential (excluding a constant value difference) associated with it. This shows that it is the particle density that defines the external potential (to within a static shift).

It follows that since the Hamiltonian may be defined in terms of the external potential and the external potential is defined by the particle density, so can the ground state wavefunction be defined in terms of the ground state particle density.

Theorem 2:

The second Hohenberg-Kohn theorem proof proceeds as follows. First we will express the electron-electron (or particle-particle) interaction and the kinetic energy as functionals and define the Hohenberg-Kohn functional,

$$F_{HK}[n] = T[n] + E_{int}[n], \tag{2.32}$$

where $T[n]$ is the kinetic energy functional and $E_{int}[n]$ is the particle-particle interaction functional.

We can now define a functional for the total energy as,

$$E_{HK} = F_{HK} + \int V_{ext}(\mathbf{r})n(\mathbf{r})\ d^3\mathbf{r}. \tag{2.33}$$

As before we neglect the ion-ion interaction. The first Hohenberg-Kohn theorem shows that an external potential can be determined, with the exception of a constant shift. Because, the ion-ion interaction is, for any system, only a constant shift to the energies, it can be neglected with no consequence to the applicability of the theory.

We put this formulation to the test by considering a specific state $n^{(1)}(\mathbf{r})$ which corresponds to a distinct ground state, energy and wavefunction. We may now write

$$E^{(1)} = E_{HK}[n^{(1)}] = \langle 1|\hat{H}^{(1)}|1\rangle\,, \tag{2.34}$$

and if we define the energy of state $|2\rangle$ for the same Hamiltonian

$$E^{(2)} = \langle 2|\hat{H}^{(1)}|2\rangle\,, \tag{2.35}$$

we can say

$$\begin{aligned} \langle 1|\hat{H}^{(1)}|1\rangle &< \langle 2|\hat{H}^{(1)}|2\rangle \\ E^{(1)} &< E^{(2)} \\ E_{HK}[n^{(1)}] &< E_{HK}[n^{(2)}]. \end{aligned} \tag{2.36}$$

Here we have demonstrated that a functional, defined by a particular ground state density, will return a greater energy when acting on a particle density that is not the ground state. This can be restated as having its global minimum when it acts on the ground state density.

2.2.4 Kohn-Sham Auxiliary System

The transformation of the Hohenberg-Kohn theorem from a curiosity into a useful tool takes place via the Kohn-Sham approach. The objective of the Kohn-Sham auxiliary system is to replace the many body system of interacting electrons with an artificial "auxiliary" system of non-interacting electron-like particles. The auxiliary system is built on the assumption that the ground state density of the electron system is the same as the ground state density of the Kohn-Sham particles.

$$n(\mathbf{r}) = \sum_k |\psi_k(\mathbf{r})|^2, \tag{2.37}$$

where each Kohn-Sham orbital ψ_k acts as a single-electron wavefunction. The Hohenberg-Kohn energy functional has already been shown to give the exact ground state energy (in principle). Therefore the requirement that the ground-state particle density is exactly replicated is enough to ensure that the ground-state energy is also replicated.

If we wanted to include spin in the description, a simple sum over spin states would be incorporated into equation 2.37. The Kohn-Sham orbitals are defined according to the condition that E_{HK} is minimized. We now define the energy functional

$$E_{KS}[n] = T_s[n] + \int V_{ext}(\mathbf{r}) n(\mathbf{r})\ d^3\mathbf{r} + E_H[n] + E_{xc}[n] \tag{2.38}$$

where $T_s[n]$ is the independent particle kinetic energy, E_H is the Hartree energy and $E_{xc}[n]$ is the exchange correlation functional.

We define the independent particle kinetic energy, $T_s[n]$ as,

$$-\frac{1}{2}\sum_k \int \psi_k^*(\mathbf{r}) \nabla^2 \psi_k(\mathbf{r})\ d^3\mathbf{r}, \tag{2.39}$$

and the Hartree energy, $E_H[n]$ as,

$$\frac{1}{2}\int \frac{n(\mathbf{r})n(\mathbf{r}')}{|\mathbf{r}-\mathbf{r}'|}\, d^3\mathbf{r}d^3\mathbf{r}' \tag{2.40}$$

While this is sufficient to define the energy we cannot define a Kohn-Sham Hamiltonian without potential defined by the functionals.

$$\hat{H}_{KS} = -\frac{1}{2}\nabla^2 + V_{KS}[n], \tag{2.41}$$

Here $V_{KS}[n]$, is defined such that Kohn-Sham Hamiltonian should return the same energy as the energy functional and that it must obey the same variational principle, such that the ground state wavefunction gives the lowest energy.

We have demonstrated, already, that the Kohn-Sham energy is at a minimum when evaluated at the ground state density and/or wavefunction. We can impose this condition mathematically by setting the differential of the Kohn-Sham energy functional to zero. It is necessary however to include the normalisation condition by Lagrange multiplier technique.

$$\epsilon[\langle\psi|\psi\rangle - 1] = 0, \tag{2.42}$$

where ϵ is, for now, a Lagrange multiplier but, we will soon see, becomes the energy eigenvalue. For this reason we have conveniently selected to represent it using ϵ. The derivative of the Kohn-Sham energy functional is already defined as zero at the ground state, hence we set the derivative of the left hand side of equation 2.38 equal to our Lagrange multiplier condition,

$$\frac{\delta T_s}{\delta\psi_k^*} + \left[\frac{\delta E_{ext}}{\delta n(\mathbf{r})} + \frac{\delta E_H}{\delta n(\mathbf{r})} + \frac{\delta E_{xc}}{\delta n(\mathbf{r})}\right]\frac{\delta n(\mathbf{r})}{\delta\psi_k^*} = \frac{\delta}{\delta\psi_k^*}\epsilon[\langle\psi|\psi\rangle - 1] \tag{2.43}$$

using their definitions (eq. 2.39 & 2.40) we can evaluate the derivatives of T_s and

$n(\mathbf{r})$ as,

$$\frac{\delta T_s}{\delta \psi_k^*} = -\frac{1}{2}\nabla^2 |\psi_k\rangle \,, \tag{2.44}$$

$$\frac{\delta n(\mathbf{r})}{\delta \psi_k^*} = |\psi_k\rangle \,, \tag{2.45}$$

and, lastly, the derivative of Lagrange multiplier condition gives,

$$\frac{\delta}{\delta \psi_k^*}\epsilon[\langle\psi|\psi\rangle - 1] = \epsilon\,|\psi_k\rangle \,. \tag{2.46}$$

Now, if we recognise the three derivatives with respect to $n(\mathbf{r})$ (eq. 2.43) as potentials and apply the three evaluations (eq. 2.44, 2.45 and 2.46) we can rewrite equation 2.43 as,

$$-\frac{1}{2}\nabla^2 |\psi_k\rangle + V_{ext}(\mathbf{r})\,|\psi_k\rangle + V_H(\mathbf{r})\,|\psi_k\rangle + V_{xc}(\mathbf{r})\,|\psi_k\rangle = \epsilon\,|\psi_k\rangle \tag{2.47}$$

$$-\frac{1}{2}\nabla^2 |\psi_k\rangle + V_{KS}(\mathbf{r})\,|\psi_k\rangle = \epsilon_k\,|\psi_k\rangle \,. \tag{2.48}$$

It can be recognised that equation 2.48 is a Schrödinger equation, with a Hamiltonian defined as

$$\hat{H}_{KS} = -\frac{1}{2}\nabla^2 + V_{KS}(\mathbf{r}) \tag{2.49}$$

We have now expressed the Hamiltonian of the Kohn-Sham auxiliary system in terms of calculable quantities (given the existence of an exchange-correlation functional). However, it is unclear how helpful this auxiliary system is for describing true electronic features of the solid.

2.2.4.1 Kohn-Sham Eigenvalues

It is easy to think that the Kohn-Sham eigenvalues have no physical meaning and while this is true to some degree, the Kohn-Sham eigenvalues are not intrinsically the energies required to add or subtract electrons from an interacting many body

system. This being the case there are two items of research that demonstrate the usefulness of the Kohn-Sham eigenvalues.

First we look at the work of Janak in 1978[67]. In this work, Janak derives an expression for the rate of change of energy of the system with particle number. This is done within the DFT formalism. It is demonstrated that the $\partial E/\partial n_i = \epsilon_i$, thus clearly showing that eigenvalues properly correspond to addition and subtraction energies for the fictitious Kohn-Sham electron-like particles. This is commonly known as the Slater-Janak theorem[61]. It can further be stated that the exact functional energy derivative ($\partial E/\partial n_i = \epsilon_i$) is discontinuous between electrons. The total energy of electrons $E(N)$ may be viewed as a series of straight-line segments intersecting a curve at integer values of electron number. It is the absence of the potential discontinuity (among other factors) that leads the failure of GGA and LDA methods in predicting the bandgaps of Mott insulators; reintroducing this discontinuity is goal of the Hubbard +U correction[68].

In relation to the Slater-Janak theorem it must be noted that part of the exchange correlation potential, $V_{xc}(\mathbf{r})$, depends on the derivative of $E_{xc}[n]$ with respect to $n(\mathbf{r})$ which can change discontinuously between states. This is the "band-gap discontinuity"[69]. It follows that in principle the band-gap is not accurately predicted, however many effective potentials and extended tools exist for correcting this, including hybrid functionals[70] and GW quasiparticle methods[71].

The Slater-Janak theorem establishes a rigorous connection between N and $N+1$ particles systems. Next we review the work of Levy, Perdew and Sahni[72]. They demonstrate that at asymptotically long-range, the charge density is governed by the occupied state with the highest eigenvalue. If we allow for the existence of an exact exchange correlation functional then we can say, as Levy *et al.* do, that since the particle density is exact then so should the ground-state ionisation energy be exact.

In summary the work of Levy *et al.*[72] lets us state that (for an exact V_{xc}) the highest occupied molecular orbital has the genuine electronic energy eigenvalue. Further, through the work of Janak[67] we can extend this trust somewhat, to nearby occupied states. Some work has also been done to establish DFT as providing well-defined approximations for excitation energies[73]. However, accurate band-gap prediction requires methods beyond DFT[69, 70, 71].

2.2.5 The Secular Equation

The variational principle can be utilised in the construction of an equation which allows us to reduce the many body Shrödinger equation to linear algebra. We must expand the wavefunctions into a finite basis set. The variational principle can then be used to find the optimal coefficients of the expansion. The procedure is very simple, first we express the expectation value as,

$$\langle\psi|\hat{H}|\psi\rangle = \epsilon\,\langle\psi|\psi\rangle \tag{2.50}$$

We then describe a function equal to the variation in energy as you move away from optimal wavefunction.

$$\mathcal{S}[\psi] = \langle\psi|\hat{H}|\psi\rangle - \epsilon\,\langle\psi|\psi\rangle \tag{2.51}$$

This is not yet the secular equation, but rather a variational functional.

At this point, we can, by expanding the wavefunctions as a sum of basis sets, differentiate with respect to basis coefficients. Then to identify the minimum energy condition we expand at the turning point where the derivative is equal to zero.

2.2.5.1 Orthogonal Basis Set

The Schrödinger equation for the Kohn-Sham auxiliary system can be written as

$$\hat{H}_{KS} \left|\psi_k\right\rangle = -\frac{1}{2}\nabla^2 \left|\psi_k\right\rangle + V_{KS}(\mathbf{r}) \left|\psi_k\right\rangle = \epsilon_k \tag{2.52}$$

for each Kohn-Sham equation, which is to say, for each value of k a solution can be obtained providing there is a known electron density (strictly it is an electron-like particle density). From this point onward we drop the k index since we will only be concerned with solving any single Kohn-Sham equation.

A Kohn-Sham wavefunction can be defined in terms of a finite basis set,

$$\left|\psi\right\rangle = \sum_{i}^{N} c_i b_i, \tag{2.53}$$

where b_i is an orthogonal basis function, c_i is the coefficient and N is the total number of base states.

We can now use the definition from equation 2.53 and substitute it into our variational functional (eq. 2.51). This is written

$$\mathcal{S} = \int \sum_i c_i^* b_i^* \ \hat{H}_{KS} \ \sum_j c_j b_j \ d^3\mathbf{r} - \epsilon \sum_{ij} c_i^* c_j \left\langle b_i | b_j \right\rangle \tag{2.54}$$

for brevity of notation we allow ourselves to define

$$H_{ij} = \left\langle b_i | \hat{H}_{KS} | b_j \right\rangle . \tag{2.55}$$

Assuming the a Kohn-Sham potential can be calculated through means of an exchange correlation functional and using a plain wave basis set (plain waves are orthonormal) the evaluation of each matrix element H_{ij} is now trivial. Each of element of H_{ij} should, for this point onwards, be considered a known quantity.

We can substitute equation 2.55 back into equation 2.54 to get,

$$\begin{aligned}\mathcal{S} &= \sum_{ij} c_i^* c_j H_{ij} - \epsilon \sum_{ij} c_i^* c_j \langle b_i | b_j \rangle \\ &= \sum_{ij} c_i^* c_j \Big(H_{ij} - \epsilon \langle b_i | b_j \rangle \Big)\end{aligned} \tag{2.56}$$

It is by the differentiation of the variational functional that the minimum energy condition is revealed.

$$\frac{\partial \mathcal{S}}{\partial c_i^*} = 0 \tag{2.57}$$

The turning point of the equation gives

$$0 = \sum_{ij} c_j \Big(H_{ij} - \epsilon \delta_{ij} \Big) \tag{2.58}$$

However, the equation 2.58 is not generally solvable (beyond trivial the case $\vec{c} = 0$). So it is here that we define the secular equation.

$$det|H_{ij} - \epsilon \delta_{ij}| = 0 \tag{2.59}$$

It is an algebraic equation, that admits N roots, each root returning a different eigenvalue. Reformulating this as a matrix equation we have

$$\mathbf{H}\vec{c} = \epsilon \vec{c} \tag{2.60}$$

This is now a standard eigenvector/eigenvalue problem. However, there is a problem, we are seeking the set of coefficients that define a Kohn-Sham state but we have N solutions. This corresponds to an $N \times N$ matrix $\mathbf{H}$.

This leaves us with N eigenvectors, each one we denote with λ up to a value of N.

$$\psi_\lambda = \sum_i C_{i\lambda} b_i \tag{2.61}$$

we can then define,

$$\hat{H}\psi_\lambda = \epsilon_\lambda \psi_\lambda \tag{2.62}$$

We can now define a Kohn-Sham eigenstate and eigenvalue as

$$\psi_k = \sum_\lambda \psi_\lambda \tag{2.63}$$

$$\epsilon_k = \sum_\lambda \epsilon_\lambda \tag{2.64}$$

It is these values, ϵ_k, that are the energy eigenvalues obtained from DFT. The total energy of the system is found by summing across all the energy eigenvalues of the Kohn-Sham orbitals.

The equation 2.60 is a very common problem in mathematics and computer science; the process of solving such an equation is called diagonalisation.

2.2.6 DFT Summary

This section has derived and defined the theorems and approximations that coalesce to form the fundamental theory of DFT. Section 2.2.1 explored why many body *ab initio* methods are needed and to express the potential benefit they have. The adiabatic approximation is shown, in section 2.2.2, to be sufficient to decouple the electronic and ionic wavefunctions. This establishes the necessary electron Hamiltonian to derive the first and second Hohenberg-Kohn theorems (sec. 2.2.3) which prove that (1st) a functional approach is, in principle, valid and that (2nd) it obeys the variational principle. Section 2.2.4 explores the Kohn-Sham auxiliary system and derives the Kohn-Sham equations. Then are derived the general quantum mechanical principles of solving for the optimal coefficients of a basis set. Section 2.2.5 introduces the secular equation, in which the variational method is reduced to an algebraic problem, and orthogonal basis sets are explored as a method of solving a

Hamiltonian of known or calculable terms (sec. 2.2.5.1). Thus, do we derive the fundamentals of density functional theory and explore the means by which it is solved.

2.3 Functional Choice

Much of the theory of DFT is built upon the assumption of a exact (or at least suitable) exchange correlation functional $E_{xc}[n]$. The Hohenberg-Kohn theorems demonstrate that there exists a functional that describes the physical properties of a set of interacting particles. The Kohn-Sham theorem shows how one may replace the true system of interacting particles with a non-interacting auxiliary system of the same ground state charge density. These foundational theories do not provide a clear indication as to the form of $E_{xc}[n]$. There are many different functionals used in DFT however the majority can be classified as local density approximation (LDA), generalised gradient approximation (GGA) or hybrid functionals. Each method represents a different balance between computational cost and chemical accuracy.

Each functional gives two important physical properties of the system. The first is the total exchange correlation energy. This value is minimised to give optimal charge density of the system. The second is the exchange correlation potential, $V_{xc}(\mathbf{r})$, expressed in equations 2.43 and 2.47. Here are explored three formulations of density functional theory: LDA, GGA and hybrid functionals.

2.3.1 Local Density Approximation

The local density approximation (or local spin density approximation (LSDA) more generally) considers a solid to be a close to the limit of the homogeneous electron gas. As such it depends on the local charge density at each point in space to determine

the exchange correlation energy ($E_{xc}^{LDA}[n]$). Despite the fact that the energy of each point is unchanged by it's environment this approach yields some reasonable results.

The exchange correlation energy may be stated explicitly as,

$$E_{xc}^{LDA}[n(\mathbf{r})] = \int \epsilon_{xc}^{LDA}\ n(\mathbf{r})\ d\mathbf{r}, \tag{2.65}$$

where $\epsilon_{xc}^{LDA} \equiv \epsilon_{xc}^{LDA}(n(\mathbf{r}))$ and is the exchange-correlation energy per particle (in the case of LDA, this is the exchange-correlation energy of a homogeneous electron gas). This gives the corresponding exchange correlation potential,

$$V_{xc}^{LDA}(\mathbf{r}) = \frac{\delta E_{xc}^{LDA}[n(\mathbf{r})]}{\delta n(\mathbf{r})} = \epsilon_{xc}^{LDA} + n(\mathbf{r})\frac{\partial \epsilon_{xc}^{LDA}}{\partial n(\mathbf{r})} \tag{2.66}$$

The LDA class of functionals are widely considered the least accurate of the three discussed here. The local approximation depends heavily on the assumption that exchange and correlation are very short range. This assumption has no formal justification[61]. This functional can be expected to be most suitable for systems which resemble the homogeneous electron gas (such as nearly free electron like metals). Two common LDA functionals are the PZ (Perdew-Zunger)[74] and the PW92 (Perdew-Wang 1992)[75].

2.3.2 Generalised Gradient Approximation

The generalised gradient approximation is a clear attempt to improve upon LDA by incorporating pseudo non-local effects. In the generalised gradient approximation both the local density and the local gradient of that density are used to determine the exchange correlation energy. This means that while GGA is still a truly local approximation each point inherently carries information about its surroundings. This allows GGA to outperform LDA in most cases with minimal enhancement to the computational cost.

The exchange correlation energy for the GGA functional can be given as,

$$E_{xc}^{GGA}[n(\mathbf{r})] = \int \epsilon_{xc}^{GGA}\ n(\mathbf{r})\ d\mathbf{r}. \tag{2.67}$$

The crutial difference from the LDA is the definition of $\epsilon_{xc}^{GGA} \equiv \epsilon_{xc}^{GGA}(n(\mathbf{r}), |\nabla n(\mathbf{r})|)$. This principle can be taken further with higher order derivatives constituting the class of meta-GGA functionals[76]. The GGA exchange-correlation potential can be written as

$$V_{xc}^{GGA}(\mathbf{r}) = \frac{\delta E_{xc}^{GGA}[n(\mathbf{r})]}{\delta n(\mathbf{r})} = \epsilon_{xc}^{GGA} + n(\mathbf{r})\frac{\partial \epsilon_{xc}^{GGA}}{\partial n(\mathbf{r})} + \nabla\left(n(\mathbf{r})\frac{\partial \epsilon_{xc}^{GGA}}{\partial \nabla n(\mathbf{r})}\right) \tag{2.68}$$

Methods for incorporating the gradient effect into the energy are far more varied than for LDA leading to a great many different functional forms. The most widely used GGA functional is PBE (Perdew, Burke and Ernzerhof)[77]. The PBE functional is used for the majority of calculations presented throughout this body of work. The improvements offered by GGA over LDA come at a relatively small cost due to the fact that the diagonalisation (the most time consuming part of the calculation) is unaffected. GGA is however known to under perform compared to LDA in the prediction of lattice constants and the van der Waals gaps. This is often attributed to the cancellation of errors in LDA.

2.3.3 Hybrids

Hybrid functionals are, as the name suggests, a hybrid between the methods of density functional theory and Hartree-Fock. A critical problem of DFT is an underestimation of the exchange, leading to an underestimation of the bandgap. This problem can be severe in cases where the bandgap is of importance. The hybrid functional represents a method for overcoming this obstacle by incorporating the exact exchange. This allows hybrid functionals to be far more accurate for bandgap

prediction than GGA functionals.

The hybrid mixing can be defined as

$$E_{xc}^{hyb} = \lambda E_x^{HF} + (1-\lambda)E_x^{DFT} + E_c^{DFT}, \tag{2.69}$$

where E_x^{DFT} and E_c^{DFT} are the exchange and correlation of the DFT functional and E_x^{HF} is the exchange energy calculated through Hartree-Fock. Most methodologies fix the mixing parameter, λ, such that it's value is determined by the choice of hybrid functional.

Hybrid functionals offer improvements over the GGA functionals in predicting bandgaps, lattice constants and phonon frequencies[78]. The enhancements due to hybridisation incur a significant computational cost. This is because of the requirement to calculate the Hartree-Fock exchange and because this in turn effects the diagonalization the cost is much more significant for plainwave calculations. Some of the most common hybrid functionals are PBE0 [79], HSE06 [70] and B3LYP [80, 81]. In this body of work the only hybrid functional utilised is HSE06. This is because HSE is a screened hybrid functional, where long range exchange interaction is truncated, vastly improving performance in large supercells.

2.3.4 Functional Summary

Density functional theory and its predictions are dependent on the quality of the functional used. Ultimately DFT lives or dies on how well it agrees with experiment. While it is easy to recognise that the GGA functional, in principle, represents an improvement over LDA, this will not hold for all crystals. For this reason no functional can be said to be a universal improvement on any other, however, it can be recognised that for the vast majority of cases hybrids represent an improvement over GGA, just as GGA is an improvement over LDA. Further *ab initio* methods

exist, providing improvements over DFT at the cost of ever more computational requirements. Such methods include the quasi-particle GW method [82] and the Quantum Monte Carlo [83].

2.4 Phonons

Phonons are lattice vibrations in the harmonic limit. It is a wave of motion carried by the atoms of a crystal, even its name "phonon" is demonstrative of this property. The word phonon, like the word phonics, indicates that it is a quantised sound wave but it is probably best described as a quasi-particle existing in a specific mode of the lattice with a specific frequency and momentum.

Crucially, phonons are the only modes of vibration permitted within a harmonic crystal and this fact carries many consequences. For instance, consider a frozen crystal in which only a single atom is displaced from equilibrium. When the crystal is released the displaced atom will pull, and be pulled, on, and by, neighbouring atoms. Each of these vibrations is a phonon and will propagate through the crystal. Displacement of a single atom is therefore a linear combination of phonons; more than this, any possible deformation of the lattice must be a linear combination of phonons.

While a phonon is often described as a particle of sound it is more interesting to consider that it can also be described as "a particle of heat". Heat energy is expressed as the random vibration of atoms in a solid but since the only permitted vibrations are phonons, then heat in harmonic solids is in the form of phonons distributed according to the Bose-Einstein distribution.

2.4.1 The harmonic lattice

In this section we must apply the Adiabatic condition examined in section 2.2.2. This condition is required in order to separate the electronic and ionic wavefunctions. The Hamiltonian for lattice vibration can be extracted from equation 2.23 to give,

$$\hat{H} = T_n + \mathcal{V}. \tag{2.70}$$

In this expression T_n is the ionic kinetic energy operator and $\mathcal{V}$ is the crystal potential energy, which is determined by the electron density. In the absence of ionic motion the system total energy would be determined entirely by the potential $\mathcal{V}$. This energy would be the ground-state total energy calculated by the solution of the Kohn-Sham equations.

The crystal potential is now expanded with respect to the atomic displacements vector

$$\begin{aligned}\mathcal{V} = \mathcal{V}_0 + \sum_{l\sigma}\sum_{\alpha} \frac{\partial \mathcal{V}}{\partial \vec{u}_\alpha(l\sigma)} \vec{u}_\alpha(l\sigma) \\ + \frac{1}{2}\sum_{l\sigma l'\sigma'}\sum_{\alpha\beta} \frac{\partial^2 \mathcal{V}}{\partial \vec{u}_\alpha(l\sigma)\partial \vec{u}_\beta(l'\sigma')} \vec{u}_\alpha(l\sigma)\vec{u}_\beta(l'\sigma'),\end{aligned} \tag{2.71}$$

here $\vec{u}_\alpha(l\sigma)$ is the atomic displacement vector of atom σ in unit cell l with polarisation α. The first term in the expansion is the equilibrium potential, the second term goes to zero, by definition, since equilibrium is a natural turning point. It is the third term, the harmonic potential, that is of most interest here.

We may define the elements of a matrix of second order inter-atomic force constants as

$$\Phi_{\alpha\beta}(l\sigma l'\sigma') = \frac{\partial^2 \mathcal{V}}{\partial \vec{u}_\alpha(l\sigma)\partial \vec{u}_\beta(l'\sigma')}. \tag{2.72}$$

However, the force constants themselves are not of interest. Lattice dynamics and phonon calculations are predominantly concerned with calculation of phonon fre-

quencies.

To find the phonon dispersion in the harmonic approximation we solve the classical equation of motion,

$$M_\sigma \ddot{u}_\alpha(l\sigma) = -\sum_{l'\sigma'\beta} \Phi_{\alpha\beta}(l\sigma l'\sigma')\vec{u}_\beta(l'\sigma'). \tag{2.73}$$

This equation of motion can be solved by using the phonon displacement vector[84]

$$\vec{u}_\alpha(l\sigma) = \frac{1}{\sqrt{M_\sigma}} \sum_{\mathbf{q}} U_\alpha(\mathbf{q}\sigma) e^{\mathrm{i}(\mathbf{q}\cdot\mathbf{r}(l)-\omega t)} \tag{2.74}$$

where $\mathbf{r}(l)$ is the position vector to the unit cell l and t is time. $U_\alpha(\mathbf{q}\sigma)$ is an arbitrary function or operator independent of l.

Substituting equation 2.74 into equation 2.73 and dropping the summation over $\mathbf{q}$, such that $\mathbf{q} = \mathbf{q}'$, yields

$$\omega^2 U_\alpha(\mathbf{q}\sigma) = \sum_{\sigma'\beta} U_\alpha(\mathbf{q}\sigma) \frac{1}{\sqrt{M_\sigma M_{\sigma'}}} \sum_{l'} \Phi_{\alpha\beta}(l\sigma l'\sigma') e^{\mathrm{i}\mathbf{q}\cdot(r(l')-r(l))} \tag{2.75}$$

Now it is convenient to apply lattice transitional symmetry to reduce the problem. The symmetry of the lattice means that $\Phi_{\alpha\beta}(l\sigma l'\sigma')$ is unchanged upon lattice translation, therefore if we choose to translate by $-l$ then we show

$$\Phi_{\alpha\beta}(l\sigma l'\sigma') = \Phi_{\alpha\beta}(0\sigma(l'-l)\sigma') \tag{2.76}$$

We now let $l' - l$ be represented by l'. Applying this symmetry to equation 2.75, gives

$$\omega^2 U_\alpha(\mathbf{q}\sigma) = \sum_{\sigma'\beta} D_{\alpha\beta}(\sigma\sigma'|\mathbf{q}) U_\beta(\mathbf{q}\sigma') \tag{2.77}$$

where we include the dynamical matrix, $D_{\alpha\beta}(\sigma\sigma'|\mathbf{q})$. We use the vertical bar notation to indicate that the dynamical matrix is set for a fixed value of $\mathbf{q}$. The

dynamical matrix is defined as

$$D_{\alpha\beta}(\sigma\sigma'|\mathbf{q}) = \frac{1}{\sqrt{M_\sigma M_{\sigma'}}} \sum_{l'} \Phi_{\alpha\beta}(0\sigma l'\sigma') e^{\mathrm{i}\mathbf{q}\cdot r(l')} \tag{2.78}$$

As with the secular equation we can determine non-trivial solutions using the determinant,

$$det\big|D_{\alpha\beta}(\sigma\sigma'|\mathbf{q}) - \omega^2\delta_{\alpha\beta}\delta_{\sigma\sigma'}\big| = 0. \tag{2.79}$$

If we consolidate the directional index and the atomic index, we can easily represent this as a matrix equation. Since α can only be $1, 2, 3$ or x, y, z it is straight forward then to change to an index over σ_α.

$$\vec{U}(\mathbf{q}) = \Big(U(\mathbf{q}\sigma_x),\ U(\mathbf{q}\sigma_y),\ U(\mathbf{q}\sigma_z),\ U(\mathbf{q}(\sigma+1)_x),\ U(\mathbf{q}(\sigma+1)_y),\ U(\mathbf{q}(\sigma+1)_z)\dots\Big) \tag{2.80}$$

Using this vector across atomic directions, equation 2.79 can be represented in matrix form, as

$$\vec{U}(\mathbf{q})\mathbf{D}(\mathbf{q}) = \vec{U}(\mathbf{q})\omega^2 \tag{2.81}$$

It is clear from this that to find the phonon frequencies of a structure, described by a set of force constants, one must diagonalise the dynamical matrix. The eigenvalues of the dynamical matrix are the squared angular frequencies. A negative eigenvalue would indicate an atomic directions vector, $\vec{U}(\mathbf{q})$, that returns a positive force i.e. one that does not push the atoms back to the equilibrium positions and therefore fulfills the conditions of an unstable crystal structure.

The difficulty in calculating a phononic structure lies in determining the interatomic force constants, $\Phi_{\alpha\beta}(0\sigma l'\sigma')$.

2.4.2 Phonon *ab initio* Calculation Methods

There are three typical *ab initio* methods for the calculation of phonon modes. They are: the frozen phonon method, the planar force constant method and the linear response method also called density functional perturbation theory (DFPT).

The frozen phonon method involves taking static atomic arrangements at small displacements away from equilibrium. Each small displacement corresponds to a "frozen" vibrational mode. Either by calculating second order changes in energy or more easily calculating the inter-atomic force constants matrix. This can then be used to determine the dynamical matrix. This methodology is adopted, for calculations within this work and is described in detail in section 2.4.3.2.

A simplified approach to the problem is offered by the planar force constant model. If we consider a q-vector, then we may define a series of atomic plains perpendicular to that vector (let there be N plains). A vibrational mode corresponding to the considered q-vector will excite either perpendicular or parallel displacements within those plains. This means that the plains are acting as single rigid bodies, each connected to it's neighbors by inter-planar force constants. A force equation can therefore be written for the n'th plain,

$$-\vec{F}(n) = k_n \vec{U}_0, \tag{2.82}$$

where $\vec{U}_0$ is the displacement of the zeroth plain and k_n is the force constant between plain 0and n. A more detailed description of the planar force constant model is provided by Srivastava 1990[84].

The linear response method is described breffly here following the method of Giannozzi *et al.*[85]. In this approach a distortion, u to the lattice can be seen as a static perturbation acting on the electrons. By consideration of the Hellmann-Feynman theorem (see 2.4.3.1) linear variation of the electron density (due to a

static perturbation) determines the second order variation in energy. The electronic energy may be written,

$$E(\mathbf{u}) = E(0) + \delta E(\mathbf{u}\Delta n) \tag{2.83}$$

where Δn is the static change in the charge density. This change in the total energy will lead to a change in the force constants matrix which is entirely determined by the ionic cores and electron density. The ionic component may be determined trivially however the electronic component requires the carefully application of the Hellmann-Feynman theorem an can be given as

$$\Phi_{\alpha\sigma\beta\sigma'}(l-l') = \int \frac{\partial n(\mathbf{r})}{\partial u_{\alpha\sigma}(l)} \frac{\partial \mathcal{V}(\mathbf{r})}{\partial u_{\alpha\sigma'}(l')} + n_0(\mathbf{r}) \frac{\partial^2 \mathcal{V}(\mathbf{r})}{\partial u_{\alpha\sigma}(l) \partial u_{\alpha\sigma'}(l')} d\mathbf{r}. \tag{2.84}$$

Here n_0 is the electron density of the unperturbed system and $\partial n/\partial u$ is the electronic response. This provides a means to calculate the force constants matrix. Within the framework of DFT the electronic potential $\mathcal{V}(\mathbf{r}) = V_{KS}(\mathbf{r})$. The self consistent Kohn-Sham potential can be written

$$V_{KS}(\mathbf{r}) = V_{ps}(\mathbf{r}) + \frac{e^2}{4\pi\epsilon_0} \int \frac{n(\mathbf{r}')}{|\mathbf{r}-\mathbf{r}'|} d\mathbf{r}' + V_{xc}(n(\mathbf{r})), \tag{2.85}$$

Where V_{ps} is the ionic potential (derived from the pseudopotentials), the second term is the the electronic potential and the third term, $V_{xc}(n(\mathbf{r}))$, is the exchange correlation potential. Using density functional perturbation theory one can define the Kohn-Sham potential response to a perturbation as $V_{KS} \rightarrow V_{KS} + \Delta V_{KS}$. To evaluate diferent elements of the harmonic force constants matrix two values must be found; they are $\Delta n(\mathbf{r})$ and $\Delta V_{KS}(\mathbf{r})$. The Fourier components of $\Delta n(\mathbf{r})$ can be expressed as

$$\Delta n(\mathbf{q}+\mathbf{G}) = \frac{4}{N_0 \Omega} \sum_{\mathbf{k}} \sum_{v,c} \left[\frac{\left\langle \psi_{v,\mathbf{k}} \middle| e^{-\mathrm{i}(\mathbf{q}+\mathbf{G})\cdot\mathbf{r}} \middle| \psi_{c,\mathbf{k}+\mathbf{q}} \right\rangle \langle \psi_{c,\mathbf{k}+\mathbf{q}} | \Delta V_{KS} | \psi_{v,\mathbf{k}} \rangle}{\varepsilon_{v,\mathbf{k}} - \varepsilon_{c,\mathbf{k}+\mathbf{q}}} \right], \tag{2.86}$$

where Ω is the unit cell volume, N_0 is the number of unit cells, G is a reciprocal lattice

vector and ε is the energy eigenvalue at k-point $\mathbf{k}$ and of either the conduction (c) or valence band (v). The perturbation induced change in the electronic Kohn-Sham potential can be written,

$$\Delta V_{KS}(\mathbf{r}) = \Delta V_{ps}(\mathbf{r}) + \frac{e^2}{4\pi\epsilon_0}\int \frac{\Delta n(\mathbf{r}')}{|\mathbf{r}-\mathbf{r}'|}d\mathbf{r}' + \Delta n(\mathbf{q})\left[\frac{dV_{xc}(n(\mathbf{r}))}{dn}\right]_{n=n_0} \tag{2.87}$$

These equations are generated from density functional linear response theory[85]. The equations for $\Delta n(\mathbf{r})$ and $\Delta V_{KS}(\mathbf{r})$ solved iteratively. This provides the input values necessary for the calculation of the elements of the dynamical matrix.

2.4.3 Calculating Inter-atomic Force Constants

When calculating the inter-atomic force constants matrix, it is important to understand the inherent symmetries the matrix contains. This understanding reduces the number of terms that must be explicitly calculated (alternatively, it could be used to as an error check). Hence it is important to understand the self term.

$$\Phi_{\alpha\beta}(0\sigma l'\sigma') = -\sum_{l'\sigma'\neq 0\sigma} \Phi_{\alpha\beta}(0\sigma l'\sigma') \tag{2.88}$$

Here, i the condition that the force on an atom due to a displacement x must be equal to the force on all other atoms displaced $-x$.

Another useful property of the inter-atomic force constants is that they remain unchanged under an exchange of indices

$$\Phi_{\alpha\beta}(0\sigma l'\sigma') = \Phi_{\alpha\beta}(l'\sigma' 0\sigma), \tag{2.89}$$

This naturally extends to the dynamical matrix $[\mathbf{D}(q)]^T = \mathbf{D}(q)$, which informs the diagonalisation routine.

2.4.3.1 Hellmann Feynman Forces

In order to calculate the force constants on atoms it is useful to have a method for force calculation from DFT. To do this we examine the Hellmann-Feynman forces[86].

In a quantum system, energy is well defined.

$$\langle E \rangle = \int \varphi^*(\mathbf{r}) \hat{H} \varphi(\mathbf{r}) \; d^3r \tag{2.90}$$

However, to establish a clear, well defined , quantum version of force we can look at the classical definition. Ehrenfest's theorem defines force in a time dependent system[87] but here we explore precisely a molecular systems of atoms, in the time independent case.

Classically,

$$F_\lambda = -\frac{d\mathcal{V}}{d\lambda} \tag{2.91}$$

where $\mathcal{V}$ is the crystal potential energy, λ is just one of any number of parameters which specify nuclear positions. A force F_λ corresponds with λ such that $F_\lambda d\lambda$ measures the work done in displacing the nuclei by $d\lambda$

As has been stated, energy in a quantum system is well defined. In order to move from the classical frame, we replace the variable for energy with the Hamiltonian.

$$F_\lambda = -\left\langle \varphi \left| \frac{\partial \hat{H}}{\partial \lambda} \right| \varphi \right\rangle \tag{2.92}$$

Alternatively, we might take $\langle E \rangle$ as the average energy and describe force as,

$$F_\lambda = -\frac{\partial \langle E \rangle}{\partial \lambda} \tag{2.93}$$

We shall follow the method of Feynman[86] and show that each of these definitions

of force is the same, and so demonstrate that all forces on atoms can be treated as classical interactions via the Coulomb law.

Employing the product rule to expand equation 2.93, returns

$$\frac{\partial\langle E\rangle}{\partial\lambda} = \left\langle \varphi \middle| \frac{\partial\hat{H}}{\partial\lambda} \middle| \varphi \right\rangle + \left\langle \frac{\partial\varphi}{\partial\lambda} \middle| \hat{H} \middle| \varphi \right\rangle + \left\langle \varphi \middle| \hat{H} \middle| \frac{\partial\varphi}{\partial\lambda} \right\rangle . \tag{2.94}$$

In accordance with our objectives, we wish to show that the final two terms go to zero. The Hamiltonian is a self adjoint,

$$\left\langle \varphi \middle| \hat{H} \middle| \frac{\partial\varphi}{\partial\lambda} \right\rangle^{\dagger} = \left\langle \frac{\partial\varphi^*}{\partial\lambda} \middle| \hat{H} \middle| \varphi^* \right\rangle \tag{2.95}$$

we may also use the fact that $\hat{H}\,|\varphi^*\rangle = E\,|\varphi^*\rangle$ to show

$$\frac{\partial\langle E\rangle}{\partial\lambda} = \left\langle \varphi \middle| \frac{\partial\hat{H}}{\partial\lambda} \middle| \varphi \right\rangle + E\left[\left\langle \frac{\partial\varphi}{\partial\lambda} \middle| \varphi \right\rangle + \left\langle \varphi \middle| \frac{\partial\varphi}{\partial\lambda} \right\rangle \right] \tag{2.96}$$

Now a simple inverse product rule shows,

$$\begin{aligned} \frac{\partial\langle E\rangle}{\partial\lambda} &= \left\langle \varphi \middle| \frac{\partial\hat{H}}{\partial\lambda} \middle| \varphi \right\rangle + E\frac{\partial}{\partial\lambda}[\langle\varphi|\varphi\rangle] \\ \frac{\partial\langle E\rangle}{\partial\lambda} &= \left\langle \varphi \middle| \frac{\partial\hat{H}}{\partial\lambda} \middle| \varphi \right\rangle \end{aligned} \tag{2.97}$$

We can now define a consistent quantum mechanical force using equation 2.23

$$\frac{\partial\hat{H}}{\partial\lambda} = \frac{\partial\mathcal{V}(\lambda)}{\partial\lambda} = -F_\lambda \tag{2.98}$$

This justifies us in using classical Coulombic charge interaction to find the interatomic force constants.

In the context of DFT the Hellmann-Feynman forces represent a viable method for the calculating of atomic forces. The principle that forces can be properly calculated as a classical Coulomb interaction enables us to calculate atomic forces from

the charge density and ionic cores. Because charge density is exact, in principle, so will the atomic forces be exact.

2.4.3.2 Frozen Phonon Method

The frozen phonon method is built upon the application of the Hellmann-Feynman forces. In a crystal structure the force on an atom may be written,

$$F_\alpha(l\sigma) = -\frac{\partial \mathcal{V}}{\partial u_\alpha(l\sigma)}, \tag{2.99}$$

hence,

$$\Phi_{\alpha\beta}(0\sigma l'\sigma') = \frac{\partial^2 \mathcal{V}}{\partial u_\alpha(0\sigma)\partial u_\beta(l'\sigma')} = \frac{\partial F_\beta(l'\sigma')}{\partial u_\alpha(0\sigma)}. \tag{2.100}$$

Here, we are able to determine the forces on atoms by displacements of atoms, only, within the primitive cell. We then apply a finite difference method to solve the derivative.

$$\Phi_{\alpha\beta}(0\sigma l'\sigma') = \frac{F_\beta(l'\sigma'; \Delta u_\alpha(0\sigma)) - F_\beta(l'\sigma'; 0)}{\Delta u_\alpha(0\sigma)} \tag{2.101}$$

where we define $F_\beta(l'\sigma'; \Delta u_\alpha(0\sigma))$ as the force in the β direction, on atom σ', in unit cell l', evaluated at the displacement $u_\alpha(0\sigma)$, of atom σ in direction α. For a system with a perfectly relaxed atomic geometry $F_\beta(l'\sigma'; 0)$ would have a zero value.

2.4.4 Phonon Summary

It has been shown that the Hellmann-Feynman forces can be extracted from a DFT calculation. It has further been demonstrated that the frozen phonon method may utilise the Hellmann-Feynman forces to determine the interatomic force constants matrix. An exploration of the harmonic lattice gives the relationship between interatomic force constants and the dynamical matrix. For any given $\mathbf{q}$ vector within the Brillouin zone the dynamical matrix may be diagonalised to obtain the squared

angular frequencies and associated atomic displacements. Hence, from the theories presented here, can a full phononic dispersion relation can be calculated.

Chapter 3

Thermal Transport Theory

"What'd ya got there? Numbers?"

- Bender Bending Rodríguez

Futurama: Benders Big Score, 2007

3.1 Introduction

A comprehensive exploration of thermal transport and scattering mechanisms is necessary to support the discussion of thermal transport in 2D heterostructures (Ch. 5). The discussion of *ab initio* thermal transport theory relies on and builds upon the contents of the previous chapter(Ch. 2).

In this thesis the author develops their own model for thermal transport. The model described throughout this chapter is an adaptation to Thomas *et al.*[88]. Specifically it follows the theories of Srivastava[84] in it's application of the Grüneisen constant and Ziman [89] in it's treatment of momentum conservation, making it uniquely distinct from either transport model. Initially thermal transport and its dependence on scattering rate is described. The different transport mechanisms are

then explored in detail.

3.2 Thermal Transport

The study of thermal transport in crystals is governed by the phonons. With sufficiently accurate phonon dispersion relations a calculation method for the thermal conductivity may be developed. The greatest difficulty in calculating this lies in calculating appropriate scattering rates.

Throughout this thesis the lattice thermal conductivity is computed by solving the linearised Boltzmann transport equation (see Appendix A) using the single mode relaxation time approximation. The thermal conductivity tensor can be written as a sum over the bands (s) and q-points ($\mathbf{q}$)[64, 84, 90]

$$\kappa_{ij} = \frac{1}{NV_0} \sum_{\mathbf{q},s} C_V(\mathbf{q}s)\nu_i(\mathbf{q}s)\nu_j(\mathbf{q}s)\tau(\mathbf{q}s), \tag{3.1}$$

where N and V_0 are the number of unit cells and the unit cell volume respectively, $\nu(\mathbf{qs})$ are group velocities and $\tau(\mathbf{qs})$ is the relaxation time. Further, C_V is specific heat capacity which in turn can be written as

$$C_V(\mathbf{q}s) = \frac{\hbar^2\omega^2(\mathbf{q}s)}{k_B T^2}\bar{n}(\mathbf{q}s)[\bar{n}(\mathbf{q}s)+1], \tag{3.2}$$

with $\omega(\mathbf{q}s)$ being frequency and $\bar{n}$, the Bose-Einstein distribution, all other symbols have their usual meaning.

Thermal conductivity calculations require phonon frequencies and group velocities to be summed over special q-points schemes[91]. This presents little difficulty for computation, however, the methods for deriving the scattering rates are more difficult. A system has more than one possible source of scattering. When the total

scattering of a system is comprised of many different sources the scattering contributions can be treated as additive. Specifically, it is the scattering rate (inverse relaxation times) that can be summed to find a total scattering rate. In the context of electrical conductivity this is known as Matthiessen's rule[84].

Here three contributions to the scattering rate are considered, hence the total scattering rate is defined as,

$$\tau^{-1} = \tau_{BS}^{-1} + \tau_{MD}^{-1} + \tau_{PP}^{-1}, \tag{3.3}$$

where the three contributions to the scattering rate are, boundary scattering (τ_{BS}^{-1}), isotope or mass defect scattering (τ_{MD}^{-1}) and three phonon scattering (τ_{PP}^{-1}). Only these three scattering mechanisms will be be used in thermal conductivity calculations throughout this work.

Four-phonon processes are neglected due to their rarity. Just as three-phonon processes are rare at low temperature, due to the low density of phonons within the crystal, four-phonon processes are even more uncommon. Work by Thomas *et al.*[88] show that Four-phonon contribution to the thermal conductivity is negligible until $\sim$ 600 Kelvin. Electron-phonon coupling is also neglected. At high temperature, the thermal conductivity is governed by the three phonon process while at low temperatures boundary scattering is dominant. In semiconductors electron-phonon coupling is closely linked to mass defect scattering. This is because it is the charge carriers, both electrons and holes, that scatter phonons. The number of charge carriers is, especially at low temperature, determined by the impurity defects. In this theory we concern ourselves with the lightly doped systems. In a lightly doped system one can afford to neglect the weak electron-phonon coupling. It is worthy of note that the mass defect scattering only derives isotope scattering (see section 3.2.2) and accounts for impurity scattering through a simple scaling parameter, most appropriate for lightly doped systems.

Three phonon interactions are either normal or Umklapp processes and which is which depends on there momentum interaction. Phonons are quasi-particles and can be described as having a quasi-momentum. This is because when the momentum changes by an amount $\hbar\mathbf{G}$ then (where $\mathbf{G}$ is a reciprocal lattice vector) Bragg reflection occurs and the momentum is transferred to the crystal as a whole and leaving the phonon momentum unchanged. This is an example of an Umklapp process, where the phonon "quasi-momentum" extends beyond the Brillouin zone and so the phonon momentum is transformed back into the Brillouin zone by a reciprocal lattice vector. Normal processes do not exchange momentum with the lattice; there "quasi-momentum" never extends beyond the Brillouin zone edge. In terms of scattering both Umklapp and normal processes can be accounted for together by constraining the momentum to any reciporical lattice vector ($\delta_{\mathbf{G},\mathbf{q}+\mathbf{q}'+\mathbf{q}''}$). Here normal processes correspond to $\mathbf{G} = 0$ and Umklapp processes to $\mathbf{G} \neq 0$.

3.2.1 Boundary Scattering

Boundary scattering is the simplest scattering rate contribution. Peierls developed the first theory of heat transfer based on phonon scattering in 1929[92]. However, this model led to asymptotic growth of the conductivity at low temperatures, which was not found in experiments[93]. Peierls was then the first to suggest that scattering of phonons at the boundaries of the crystal may contribute to thermal resistance. The consequences of this suggestion were developed by Casimir in 1938[94] and the balisttic boundary scattering model was developed by Callaway in 1959[95].

Here, boundary scattering is implemented following the methodology of Hepplestone[96] and Srivastava[84]. The boundary scattering rate is governed by the scattering length and can, for a given phonon state, be given as

$$\tau_{BS}^{-1} = |\nu|/L, \tag{3.4}$$

where L is the scattering length. This is an extremely intuitive representation of the boundary scattering phenomena. However some complicating factors are obscured. A material grain of given radius will have an effective boundary mean free path, L_0, equal to the radius. However, due to specular reflection (determined by surface smoothness) this will not exactly represent the actual scattering length.

Let us assume probability p of a phonon reflecting at the boundary. Then let us assume that the average starting point of a phonon is the grain center. We can now say that $(1-p)L_0$ is the proportion of phonons that travel only one path length before scattering. However some number of phonons will have traveled from the zone center to the edge and back (a length of $2L_0$) any number of times before now. Including them we find $L = (1-p)[L_0 + p(3L_0) + p^2(5L_0)...]$. Evaluating this infinite sum[84] gives $L = L_0(1+p)/(1-p)$ where the parameter L is the same as from equation 3.4.

The scattering length may in some regards be treated as a parameter, however, it is one that can in most cases be closely attributed to measurable physical quantities. The two physical features that determine the scattering length are the physical dimensions of a single crystal and, in large structures of many grains, the typical grain size. In both cases this represents the mean free path of phonons in the material.

3.2.2 Mass Defect Scattering

Few theoretical works looked into defect scattering[93] prior to Klemens in 1951[97] and 1955[98]. It has since then, been approached many times (see Skoug *et al.*[99]) and we shall follow a combination of the treatments given by Srivastava [84] and Tamura [100] focusing on the role of isotope scattering.

First, let us consider the crystal Hamiltonian within the harmonic approxima-

tion, with isotopic atom substitutions

$$H = \frac{1}{2}\sum_{\alpha l\sigma} m(l\sigma)\dot{u}^2_\alpha(l\sigma) + \mathcal{V}_2, \tag{3.5}$$

where, α is the polarisation index, l, is the unit cell index and σ is the index over the atoms within a single unit cell. The Crystal potential in the harmonic limit is denoted $\mathcal{V}_2$. It is possible to separate the Hamiltonian into two components one representing the default crystal and one representing the perturbation due to isotope or mass defects.

$$H = H_0 + H_{md} \tag{3.6}$$

where H_0 and H_{md} can be easily defined as

$$H_0 = \frac{1}{2}\sum_{\alpha l\sigma} \bar{m}(\sigma)\dot{u}^2_\alpha(l\sigma) + \mathcal{V}_2, \tag{3.7}$$

$$\begin{aligned} H_{md} =& \frac{1}{2}\sum_{\alpha l\sigma}[m(l\sigma) - \bar{m}(\sigma)]\dot{u}^2_\alpha(l\sigma) \\ H_{md} =& \frac{1}{2}\sum_{\alpha l\sigma}\Delta m(l\sigma)\dot{u}^2_\alpha(l\sigma) \end{aligned} \tag{3.8}$$

Thus we have defined a perturbation Hamiltonian describing the isotope or mass defect scattering.

The perturbation Hamiltonian is defined in terms of the average mass of atom σ. The average mass is defined as,

$$\bar{m}(\sigma) = \frac{1}{N_0}\sum_{l} m(l\sigma), \tag{3.9}$$

furthermore, when we consider an isotope driven scattering we may also define the average mass as

$$\bar{m}(\sigma) = \sum_{i} f_i(\sigma)m_i(\sigma), \tag{3.10}$$

where N_0 is the number of unit cells in the solid and $f_i(\sigma)$ is the fraction of the ith

isotope of atom σ having mass m_i. The values of f_i can be determined by global isotope abundances[101].

The perturbation Hamiltonian can be utilised in a Fermi golden rule approach to determine scattering probabilities. The perturbation method holds validity while the perturbation Hamiltonian represents only a weak disturbance to the system. Here we see that H_{md} represents only kinetic energy and even then only a portion of the total kinetic energy. While the kinetic energy of the unperturbed Hamiltonian is composed of the average atomic mass the perturbation Hamiltonian uses the mass difference. This makes the perturbation method highly appropriate for the case of isotope mass differences. However, vacancies or defects of significantly different masses will result in large perturbations that potentially fall outside the regime of validity. However, because this methodology examines changes in average mass across many atoms even vacancies can be accounted for at low concentrations.

To calculate the transition probabilities we must expand the perturbation Hamiltonian. First we express the lattice displacement vector in second quantised form

$$\vec{u}_\alpha(l\sigma) = -\mathrm{i}\sqrt{\frac{\hbar}{2N\bar{m}(\sigma)}}\sum_{\mathbf{q}s}\frac{1}{\sqrt{\omega(\mathbf{q},s)}}\hat{\mathbf{e}}_\alpha(\mathbf{q}s)[a^\dagger_{\mathbf{q}s} - a_{-\mathbf{q}s}]e^{\mathrm{i}(\mathbf{q}\cdot\mathbf{r}(l))} \tag{3.11}$$

and substitute into equation 3.8 to get

$$\begin{aligned} H_{md} = \frac{\hbar}{4N\bar{m}(\sigma)}\sum_{\mathbf{q}s\mathbf{q}'s'}\sqrt{\omega(\mathbf{q}s)\omega(\mathbf{q}'s')}[a^\dagger_{\mathbf{q}s} - a_{-\mathbf{q}s}][a^\dagger_{\mathbf{q}'s'} - a_{-\mathbf{q}'s'}] \\ \sum_{l\sigma}\hat{\mathbf{e}}^\dagger(\mathbf{q}s)\cdot\hat{\mathbf{e}}(\mathbf{q}'s')\Delta m(l\sigma)e^{\mathrm{i}(\mathbf{q}-\mathbf{q}')\cdot\mathbf{r}(l)}, \end{aligned} \tag{3.12}$$

Here, $\omega(\mathbf{qs})$ is the angular frequency of a phonon in mode s and at q-point $\mathbf{q}$, the annihilation and creation operators are $a_{\mathbf{q}s}$ and its Hermitian conjugate $a^\dagger_{\mathbf{q}s}$, $\hat{\mathbf{e}}(\mathbf{q}'s')$ is the polarisation vector and its conjugate $\hat{\mathbf{e}}^\dagger(\mathbf{q}s)$ and lastly $\mathbf{r}(l)$ is the position vector of cell l.

In order to evaluate scattering probability we need to look at the transition probability of a phonon scattering from one phonon state $n_{\mathbf{q}s}$ to another $n_{\mathbf{q}'s'}$. This corresponds to the initial state $|i\rangle = |n_{\mathbf{q}s}, n_{\mathbf{q}'s'}\rangle$ to a final state $|f\rangle = |n_{\mathbf{q}s} - 1, n_{\mathbf{q}'s'} + 1\rangle$. The transition probability can be given as

$$P_{\mathbf{q}s}^{\mathbf{q}'s'} = \frac{2\pi}{\hbar}|\langle f| H_{md} |i\rangle|^2 \delta(E_f - E_i), \tag{3.13}$$

substituting in the expression for the perturbation Hamiltonian

$$\begin{aligned} P_{\mathbf{q}s}^{\mathbf{q}'s'} =& \frac{2\pi}{\hbar}| \langle f| \frac{\hbar}{4N\bar{m}(\sigma)} \\ & \sum_{\mathbf{q}s\mathbf{q}'s'} \sqrt{\omega(\mathbf{q}s)\omega(\mathbf{q}'s')}[a_{\mathbf{q}s}^\dagger - a_{-\mathbf{q}s}][a_{\mathbf{q}'s'}^\dagger - a_{-\mathbf{q}'s'}] \\ & M_{qq'} |i\rangle |^2 \delta(E_f - E_i), \end{aligned} \tag{3.14}$$

for simplicity we define

$$M_{qq'} = \sum_{l\sigma} \hat{\mathbf{e}}^\dagger(\mathbf{q}s) \cdot \hat{\mathbf{e}}(\mathbf{q}'s') \Delta m(l\sigma) e^{\mathrm{i}(\mathbf{q}-\mathbf{q}')\cdot\mathbf{r}(l)}. \tag{3.15}$$

Now expand the ladder operators and convert the delta function to angular frequency with $E = \hbar\omega$, and hence $\delta(E_f - E_i) = \frac{1}{\hbar}\delta(\omega_f - \omega_i)$

$$\begin{aligned} P_{\mathbf{q}s}^{\mathbf{q}'s'} =& \frac{2\pi}{\hbar^2}\Big| \langle f| \frac{\hbar}{4N\bar{m}(\sigma)} \sum_{\mathbf{q}s\mathbf{q}'s'} \sqrt{\omega(-\mathbf{q}s)\omega(\mathbf{q}'s')} \\ & [a_{\mathbf{q}s}^\dagger a_{\mathbf{q}'s'}^\dagger + a_{-\mathbf{q}s} a_{-\mathbf{q}'s'} - a_{\mathbf{q}s}^\dagger a_{-\mathbf{q}'s'} - a_{\mathbf{q}'s'}^\dagger a_{-\mathbf{q}s}] \\ & M_{qq'} |i\rangle \Big|^2 \delta(\omega_{\mathbf{q}'s'} - \omega_{\mathbf{q}s}), \end{aligned} \tag{3.16}$$

it can be seen that only two elements of the sum across phonon states in H_{md} will return a *ket* that matches the final state. Letting λ be an arbitrary phonon state in the summation, one can consider the two interactions, $a_\lambda^\dagger a_{-\lambda'} |n_{\mathbf{q}s}, n_{\mathbf{q}'s'}\rangle$ and $a_{\lambda'}^\dagger a_{-\lambda} |n_{\mathbf{q}s}, n_{\mathbf{q}'s'}\rangle$. Clearly, the only valid summation terms are $\lambda = \mathbf{q}s$ & $\lambda' = -\mathbf{q}'s'$ for $a_\lambda^\dagger a_{-\lambda'} |n_{\mathbf{q}s}, n_{\mathbf{q}'s'}\rangle$, and $\lambda' = \mathbf{q}s$ & $\lambda = -\mathbf{q}'s'$ for $a_{\lambda'}^\dagger a_{-\lambda} |n_{\mathbf{q}s}, n_{\mathbf{q}'s'}\rangle$. More than

this knowing the condition of our final state it is clear that only the last 2 terms of the expanded ladder operators will give a non-orthogonal results. We may therefore simplify and evaluate the operators.

$$\begin{aligned} P_{\mathbf{q}s}^{\mathbf{q}'s'} =& \frac{2\pi}{\hbar^2}\left|\left\langle f\left|\frac{-\hbar}{4N\bar{m}(\sigma)}\sqrt{\omega(\mathbf{q}'s')\omega(-\mathbf{q}s)}a^{\dagger}_{\mathbf{q}'s'}a_{\mathbf{q}s}M_{q'-q}\right|i\right\rangle\right|^2\delta(\omega_{\mathbf{q}'s'}-\omega_{\mathbf{q}s}), \\ &+\frac{2\pi}{\hbar^2}\left|\left\langle f\left|\frac{-\hbar}{4N\bar{m}(\sigma)}\sqrt{\omega(-\mathbf{q}s)\omega(\mathbf{q}'s')}a^{\dagger}_{\mathbf{q}'s'}a_{\mathbf{q}s}M_{-\mathbf{q}\mathbf{q}'}\right|i\right\rangle\right|^2\delta(\omega_{\mathbf{q}'s'}-\omega_{\mathbf{q}s}), \end{aligned} \tag{3.17}$$

$$\begin{aligned} P_{\mathbf{q}s}^{\mathbf{q}'s'} =& \frac{\pi}{2N^2\bar{m}^2(\sigma)}\omega(\mathbf{q}s)\omega(\mathbf{q}'s')n_{\mathbf{q}s}(n_{\mathbf{q}'s'}+1)|M_{qq'}|^2\delta(\omega_{\mathbf{q}'s'}-\omega_{\mathbf{q}s}) \\ =& \frac{\pi}{2N^2\bar{m}^2(\sigma)}\omega^2(\mathbf{q}s)n_{\mathbf{q}s}(n_{\mathbf{q}'s'}+1)|M_{qq'}|^2\delta(\omega_{\mathbf{q}'s'}-\omega_{\mathbf{q}s}) \end{aligned} \tag{3.18}$$

in this final expression, we apply the condition imposed by the delta function and collect the frequencies.

The mass terms $|M_{qq'}|^2$ contains the mass difference $\Delta m(l\sigma)$, which has a unique value for each atom. These terms must be reduced to evaluate the transition probability.

$$|M_{qq'}|^2 = \left|\sum_{l\sigma}\hat{\mathbf{e}}^{\dagger}(\mathbf{q}s)\cdot\hat{\mathbf{e}}(\mathbf{q}'s')\Delta m(l\sigma)e^{\mathrm{i}(\mathbf{q}-\mathbf{q}')\cdot\mathbf{r}(l)}\right|^2, \tag{3.19}$$

here the polarisation vectors are generalised for isotropic media using a factor of $(\hat{\mathbf{e}}^{\dagger}(\mathbf{q}s)\cdot\hat{\mathbf{e}}(\mathbf{q}'s'))^2 = 1/3$[84]. This can be included, more rigorously, by a dot product of the phonon eigenvectors[100] which are obtained by diagonalisation of the dynamical matrix. Utilising equation 3.19 the mass terms can be expressed as,

$$|M_{qq'}|^2 = \frac{1}{3}\sum_{ll'\sigma\sigma'}\Delta m(l\sigma)\Delta m(l'\sigma')e^{\mathrm{i}(-\mathbf{q}-\mathbf{q}')\cdot(\mathbf{r}(l)-\mathbf{r}(l'))}, \tag{3.20}$$

which allows us to separate the special condition where the exponential vanishes,

$l = l', \sigma = \sigma'$ from $l \neq l', \sigma \neq \sigma'$ giving

$$|M_{qq'}|^2 = \frac{1}{3}\sum_{l\sigma}\big(\Delta m(l\sigma)\big)^2 + \frac{1}{3}\sum_{l\neq l'}\sum_{\sigma\sigma'}\Delta m(l\sigma)\Delta m(l'\sigma')e^{\mathrm{i}(\mathbf{q}-\mathbf{q}')\cdot(\mathbf{r}(l)-\mathbf{r}(l'))} \tag{3.21}$$

for any positionally identical atoms within two unit cells the mass difference can be partially evaluated by considering a random distribution of isotopes in the structure. For this random case the local mass can be expected to have as strong a negative deviation from the mean as it does a positive one. As such, when summing across the full structure, this value can be expected to approach zero. Only the term where the same positional atom in the same unit cell is summed over do the values not cancel out, in a manner analogous to a statistical variance. Hence the mass term becomes

$$|M_{qq'}|^2 = \frac{1}{3}\sum_{l\sigma}\big(\Delta m(l\sigma)\big)^2 \tag{3.22}$$

Previously, we defined the average mass (eq. 3.9 & 3.10) and the mass difference (Δm) can now be expressed in the same manner

$$|M_{qq'}|^2 = \frac{1}{3}\sum_{\sigma} N \sum_{i} f_i(\sigma)\big(\Delta m_i(\sigma)\big)^2 \tag{3.23}$$

substituting this back into equation 3.18 we can collect the mass variables together giving

$$P_{\mathbf{q}s}^{\mathbf{q}'s'} = \frac{\pi\mathcal{G}_{md}}{6N}\omega^2(\mathbf{q}s)n_{\mathbf{q}s}(n_{\mathbf{q}'s'}+1)\delta(\omega_{\mathbf{q}'s'}-\omega_{\mathbf{q}s}) \tag{3.24}$$

where

$$\mathcal{G}_{md} = \sum_{\sigma}\mathcal{G}_2(\sigma) \;=\; \sum_{\sigma}\sum_{i} f_i(\sigma)\left(\frac{\Delta m_i(\sigma)}{\bar{m}(\sigma)}\right)^2 \tag{3.25}$$

with the transition probability established we can use the formalism of the phonon

Boltzmann transport[84, 89, 100] equation to calculate a scattering rate.

$$\tau_{\mathbf{q}s}^{-1} = \frac{\pi \mathcal{G}_{md}}{6N} \omega^2(\mathbf{q}s) \sum_{\mathbf{q}'s'} \frac{\bar{n}_{\mathbf{q}'s'} + 1}{\bar{n}_{\mathbf{q}s} + 1} \delta(\omega_{\mathbf{q}'s'} - \omega_{\mathbf{q}s}). \tag{3.26}$$

We can again impose the condition on the delta function and change to a representation in terms of state degeneracy, $g(\omega)$

$$\begin{aligned} \tau_{\mathbf{q}s}^{-1} &= \frac{\pi \mathcal{G}_{md}}{6N} \omega^2(\mathbf{q}s) \sum_{\mathbf{q}'s'} \delta(\omega_{\mathbf{q}'s'} - \omega_{\mathbf{q}s}) \\ &= \frac{\pi \mathcal{G}_{md}}{6N} \omega^2(\mathbf{q}s) \int_0^\infty g(\omega_{\mathbf{q}'s'}) \delta(\omega_{\mathbf{q}'s'} - \omega_{\mathbf{q}s}) \, d\omega_{\mathbf{q}'s'} \\ &= \frac{\pi \mathcal{G}_{md}}{6N} \omega^2(\mathbf{q}s) g(\omega_{\mathbf{q}s}). \end{aligned} \tag{3.27}$$

The scattering rate is now expressed in terms of readily available quantities.

Equation 3.27 is an optimal representation of the mass defect scattering rate for computational methods DFT. To further impose simplifications would be to impose assumptions about the nature of the phonon dispersion and would be antithetical to aims of this derivation. Computational methods and highly accurate DFT phonon calculations obviate the need for further simplification.

In addition to the phonon dispersion the variation in number and masses of the atomic isotopes is a vital component of the mass defect scattering rate. The isotropic mass factor $\mathcal{G}_{md}$, expresses the contribution of the isotopes to the scattering rate(eq. 3.25). This factor is entirely governed by the atomic species and their earth isotope abundances. Each element $\mathcal{G}_2(\sigma)$ is calculated by summing over the isotopes of that element, it therefore has a unique value that depends only on the atomic species.

In reality there are more point defects than just isotopic mass defects. There are vacancies and substitutional atoms with different binding forces as well as masses. This can to some degree be incorporated by simple parameterisation to experimental

data, guided by theory. A parameter g is placed into the definition of $\mathcal{G}_{md}$, altering equation 3.25 to give

$$\mathcal{G}_{md} = g \sum_{\sigma} \mathcal{G}_2(\sigma) \tag{3.28}$$

It is important to note that the mass defect scaling parameter is required to be greater than one ($g \geq 1$) since isotope scattering can reasonably be expected to be the minimum influence of mass defect scattering.

3.2.3 Three Phonon Scattering

The phonon-phonon interaction was the first scattering mechanism to be explored and was done so (as mentioned previously) by Peierls[92]. It is clear, intuitively, that ballistic heat transfer mechanisms that do not involve scattering of heat carriers would not replicate diffusive heat transfer we observe in true solids.

Heat transfer based on three phonon scattering is the natural starting place from an analytical, non-computational perspective. Three phonon interactions do not depend on lattice imperfections or on limiting the infinite periodicity of the crystal. However, from a computational perspective three phonon scattering is extremely demanding due to the necessity to loop over the square of the number of q-points. Even that expense is dwarfed by computational requirements for calculating the third order force constants tensor.

In order to evaluate a three phonon scattering rate we need to examine the anharmonic crystal potential. First, the crystal potential is expanded, as a Taylor

series,

$$\begin{aligned}\mathcal{V} = \mathcal{V}_0 &+ \sum_{l\sigma}\sum_{\alpha}\frac{\partial\mathcal{V}}{\partial\vec{u}_\alpha(l\sigma)}\vec{u}_\alpha(l\sigma) \\ &+ \frac{1}{2}\sum_{l\sigma l'\sigma'}\sum_{\alpha\beta}\frac{\partial^2\mathcal{V}}{\partial\vec{u}_\alpha(l\sigma)\partial\vec{u}_\beta(l'\sigma')}\vec{u}_\alpha(l\sigma)\vec{u}_\beta(l'\sigma') \\ &+ \frac{1}{3!}\sum_{l\sigma l'\sigma' l''\sigma''}\sum_{\alpha\beta\gamma}\frac{\partial^3\mathcal{V}}{\partial\vec{u}_\alpha(l\sigma)\partial\vec{u}_\beta(l'\sigma')\partial\vec{u}_\gamma(l''\sigma'')}\vec{u}_\alpha(l\sigma)\vec{u}_\beta(l'\sigma')\vec{u}_\gamma(l''\sigma'')\end{aligned} \tag{3.29}$$

here $\vec{u}_\alpha(l\sigma)$ is the atomic displacement vector of atom σ in unit cell l and in the direction α. By expanding the Taylor series about the equilibrium position the system is by definition at a natural turning point hence the second term of the expansion vanishes. The third term is the harmonic condition used to derive phonons. The fourth term is the first anharmonic potential that drives the phonon-phonon interaction. This anharmonic potential is far weaker than harmonic potentials. This is a natural consequence of the thermodynamic stability of crystal structures. Because each atom sits at the bottom of a local potential well, it is closely modeled by a harmonic potential. It is therefore safe to say that the anharmonic potential is small compared to the full harmonic Hamiltonian. This places the anharmonic potential well within the perturbative limit. It is the anharmonic term that is responsible for thermal expansion and as this is small compared to the crystal volume $\sim 5\%$ then the perturbation associated is also small.

We can rewrite the anharmonic potential term as

$$\mathcal{V}_3 = \frac{1}{3!}\sum_{l\sigma l'\sigma' l''\sigma''}\sum_{\alpha\beta\gamma}A^{\alpha\beta\gamma}_{l\sigma l'\sigma' l''\sigma''}\vec{u}_\alpha(l\sigma)\vec{u}_\beta(l'\sigma')\vec{u}_\gamma(l''\sigma''), \tag{3.30}$$

the third order force constants $A^{\alpha\beta\gamma}_{l\sigma l'\sigma' l''\sigma''}$ is a third rank tensor with 3^3 elements per atom.

In order to, further, examine the effects of the anharmonic potential on phonon interaction, we are going to want to express the potential in terms of the second

quantisation displacement vectors given above in equation 3.11. For convenience we will use λ for all combinations of phonon states ($\lambda = qs$).

$$\begin{aligned}\mathcal{V}_3 = \mathrm{i}\frac{1}{3!}\sqrt{\frac{\hbar^3}{8N^3}}\sum_{\lambda\lambda'\lambda''}\sum_{\sigma\sigma'\sigma''}&\frac{1}{\sqrt{\omega(\lambda)\omega(\lambda')\omega(\lambda'')}\sqrt{m(\sigma)m(\sigma')m(\sigma'')}}\\ &[a^\dagger_\lambda - a_{-\lambda}][a^\dagger_{\lambda'} - a_{-\lambda'}][a^\dagger_{\lambda''} - a_{-\lambda''}]\\ &\sum_{ll'l''} e^{\mathrm{i}\mathbf{q}\cdot r(l)}e^{\mathrm{i}\mathbf{q}'\cdot r(l')}e^{\mathrm{i}\mathbf{q}''\cdot r(l'')}\sum_{\alpha\beta\gamma}A^{\alpha\beta\gamma}_{l\sigma l'\sigma' l''\sigma''}\hat{\mathbf{e}}_\alpha(\lambda)\hat{\mathbf{e}}_\beta(\lambda')\hat{\mathbf{e}}_\gamma(\lambda'').\end{aligned} \tag{3.31}$$

To make use of the crystal periodic symmetry we now redefine our summation over unit cells

$$l' = l + h', \qquad l'' = l + h'', \tag{3.32}$$

incorporating this change of index gives

$$\begin{aligned}\mathcal{V}_3 = \mathrm{i}\frac{1}{3!}\sqrt{\frac{\hbar^3}{8N^3}}\sum_{\lambda\lambda'\lambda''}\sum_{\sigma\sigma'\sigma''}&\frac{1}{\sqrt{\omega(\lambda)\omega(\lambda')\omega(\lambda'')}\sqrt{m(\sigma)m(\sigma')m(\sigma'')}}\\ &[a^\dagger_\lambda - a_{-\lambda}][a^\dagger_{\lambda'} - a_{-\lambda'}][a^\dagger_{\lambda''} - a_{-\lambda''}]\\ &\sum_{l}\sum_{h'h''} e^{\mathrm{i}(\mathbf{q}+\mathbf{q}'+\mathbf{q}'')\cdot r(l)}e^{\mathrm{i}\mathbf{q}\cdot r(h')}e^{\mathrm{i}\mathbf{q}\cdot r(h'')}\\ &\sum_{\alpha\beta\gamma}A^{\alpha\beta\gamma}_{l\sigma(l+h')\sigma'(l+h'')\sigma''}\hat{\mathbf{e}}_\alpha(\lambda)\hat{\mathbf{e}}_\beta(\lambda')\hat{\mathbf{e}}_\gamma(\lambda'').\end{aligned} \tag{3.33}$$

Due to our change of index we have made it possible to evaluate the sum over l. This is because the transformed third order force constants tensor is defined relative to a single unit cell. It is a fundamental part of the nature of crystals that properties of the unit cell are replicated across all unit cells. For the system to adhere to this basic law of crystals it would require that the third order force constants for one cell $l = x$ must be the same as for another cell $l = y$. This means that $A^{\alpha\beta\gamma}_{l\sigma(l+h')\sigma'(l+h'')\sigma''}$ is independent of l and the summation can proceed.

By utilising the crystal symmetry to change the index we have also created a

summation over l of the form [89]

$$\sum_l e^{\mathrm{i}\mathbf{Q}\cdot r(l)} = \sum_l e^{\mathrm{i}(\mathbf{q}+\mathbf{q}'+\mathbf{q}'')\cdot r(l)} = NV\delta_{G,q+q'+q''}. \tag{3.34}$$

In order to evaluate this, it is necessary to remember that $\mathbf{q}$ is not continuous. The number of $\mathbf{q}$ vectors that a crystal can support is limited by the number of wavelengths that crystal can support. The supported $\mathbf{q}$ vectors of a crystal may be defined by Bloch's theorem [89] applied to a finite structure, giving

$$\mathbf{q} = \left(\frac{n}{N}\mathbf{a}^*, \frac{m}{M}\mathbf{b}^*, \frac{l}{L}\mathbf{c}^*\right). \tag{3.35}$$

Here N, M and L are the integer number of unit cells contained within the full crystal (in their respective directions). The allowed values of n, m and l are integers smaller than the corresponding number of unit cells (i.e. $n < N$). The reciprocal lattice vectors can be defined by matrix inversion (which is well defined for 2D as well as 3D)

$$[\mathbf{a}^*\mathbf{b}^*\mathbf{c}^*] = 2\pi[\mathbf{a}\ \mathbf{b}\ \mathbf{c}]^{-1}, \tag{3.36}$$

where each vector is treated as a column vector which fills out a 3×3 matrix and $\mathbf{a}$, $\mathbf{b}$ & $\mathbf{c}$ are the periodic lattice vectors.

We now also define

$$\phi^{\alpha\beta\gamma}_{\mathbf{q}\sigma\mathbf{q}'\sigma'\mathbf{q}''\sigma''} = \sum_{h'h''} e^{\mathrm{i}\mathbf{q}\cdot r(h')} e^{\mathrm{i}\mathbf{q}\cdot r(h'')} A^{\alpha\beta\gamma}_{l\sigma(l+h')\sigma'(l+h'')\sigma''} \tag{3.37}$$

with that the anharmonic potential can be written as

$$\begin{aligned}\mathcal{V}_3 = \mathrm{i}\frac{1}{3!}\sqrt{\frac{V^2\hbar^3}{8N}} \sum_{\lambda\lambda'\lambda''}\sum_{\sigma\sigma'\sigma''} &\frac{1}{\sqrt{\omega(\lambda)\omega(\lambda')\omega(\lambda'')}\sqrt{m(\sigma)m(\sigma')m(\sigma'')}} \\ &[a^\dagger_\lambda - a_{-\lambda}][a^\dagger_{\lambda'} - a_{-\lambda'}][a^\dagger_{\lambda''} - a_{-\lambda''}]\delta_{G,q+q'+q''} \\ &\sum_{\alpha\beta\gamma} \phi^{\alpha\beta\gamma}_{\mathbf{q}\sigma\mathbf{q}'\sigma'\mathbf{q}''\sigma''} \hat{\mathbf{e}}_\alpha(\lambda)\hat{\mathbf{e}}_\beta(\lambda')\hat{\mathbf{e}}_\gamma(\lambda'').\end{aligned} \tag{3.38}$$

This can be simplified further by using the density in place of mass. This is valid over many unit cells and takes the form[88]

$$\begin{aligned}\mathcal{V}_3 = \mathrm{i}\frac{1}{3!}\sqrt{\frac{\hbar^3}{8NV\rho^3}}\sum_{\lambda\lambda'\lambda''}\frac{1}{\sqrt{\omega(\lambda)\omega(\lambda')\omega(\lambda'')}} \\ [a^\dagger_\lambda - a_{-\lambda}][a^\dagger_{\lambda'} - a_{-\lambda'}][a^\dagger_{\lambda''} - a_{-\lambda''}]\delta_{G,q+q'+q''} \\ \sum_{\alpha\beta\gamma}\sum_{\sigma\sigma'\sigma''}\phi^{\alpha\beta\gamma}_{\mathbf{q}\sigma\mathbf{q}'\sigma'\mathbf{q}''\sigma''}\hat{\mathbf{e}}_\alpha(\lambda)\hat{\mathbf{e}}_\beta(\lambda')\hat{\mathbf{e}}_\gamma(\lambda'').\end{aligned} \tag{3.39}$$

Now we will drop the use of λ and return to $\mathbf{q}s$. we may also simplify the reading of this equation significantly by defining

$$\begin{aligned}\Phi_{\mathbf{q}s\mathbf{q}'s'\mathbf{q}''s''} = \mathrm{i}\sqrt{\frac{\hbar^3}{8NV\rho^3\sqrt{\omega(\mathbf{q}s)\omega(\mathbf{q}'s')\omega(\mathbf{q}'s')}}} \\ \sum_{\alpha\beta\gamma}\sum_{\sigma\sigma'\sigma''}\phi^{\alpha\beta\gamma}_{\mathbf{q}\sigma\mathbf{q}'\sigma'\mathbf{q}''\sigma''}\hat{\mathbf{e}}_\alpha(\mathbf{q}s)\hat{\mathbf{e}}_\beta(\mathbf{q}'s')\hat{\mathbf{e}}_\gamma(\mathbf{q}''s'').\end{aligned} \tag{3.40}$$

The anharmonic potential can now be expressed as

$$\mathcal{V}_3 = \frac{1}{3!}\sum_{\mathbf{q}s\mathbf{q}'s'\mathbf{q}''s''}[a^\dagger_{\mathbf{q}s} - a_{-\mathbf{q}s}][a^\dagger_{\mathbf{q}'s'} - a_{-\mathbf{q}'s'}][a^\dagger_{\mathbf{q}''s''} - a_{-\mathbf{q}''s''}]\Phi_{\mathbf{q}s\mathbf{q}'s'\mathbf{q}''s''}\delta_{G,q+q'+q''} \tag{3.41}$$

Before we can proceed with a Fermi golden rule calculated transition probability we must consider the set of possible interactions.

To evaluate transitions we must be able to define both an initial and final state. Let us begin with the system in the initial state $|i\rangle = |n_{\mathbf{q}s}, n_{\mathbf{q}'s'}, n_{\mathbf{q}''s''}\rangle$. We can let this be our initial state for all transitions considered. We can see from equation 3.30 that the inclusion of anharmonic scattering will involve the interaction of three phonons. It is possible to visualise a three phonon interaction in which two phonons collide to form a third. This interaction is a class 1 event[84] and will give a final state of $|f\rangle = |n_{\mathbf{q}s} - 1, n_{\mathbf{q}'s'} - 1, n_{\mathbf{q}''s''} + 1\rangle$. A Feynman diagram of this phonon interaction (3.1) reveals that we should consider the opposite interaction, with one phonon decaying into two others. The second three phonon interaction is

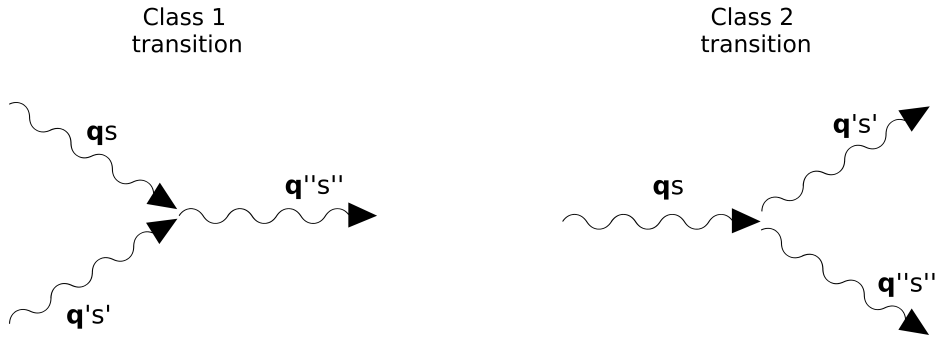

$$|i\rangle = |n_{\mathbf{q}s}, n_{\mathbf{q}'s'}, n_{\mathbf{q}''s''}\rangle \qquad |i\rangle = |n_{\mathbf{q}s}, n_{\mathbf{q}'s'}, n_{\mathbf{q}''s''}\rangle$$
$$|f\rangle = |n_{\mathbf{q}s} - 1, n_{\mathbf{q}'s'} - 1, n_{\mathbf{q}''s''} + 1\rangle \qquad |f\rangle = |n_{\mathbf{q}s} - 1, n_{\mathbf{q}'s'} + 1, n_{\mathbf{q}''s''} + 1\rangle$$

Figure 3.1. Three phonon Feynman diagrams showing class 1 and class 2 events.

(unsurprisingly) called a class 2[84] event. Class 2 events result in a final state of $|f\rangle = |n_{\mathbf{q}s} - 1, n_{\mathbf{q}'s'} + 1, n_{\mathbf{q}''s''} + 1\rangle$.

Now let us consider the Fermi golden rule for anharmonic scattering probability.

$$\frac{2\pi}{\hbar} \langle f| \frac{1}{3!} \sum_{\mathbf{q}s\mathbf{q}'s'\mathbf{q}''s''} [a^\dagger_{\mathbf{q}s} - a_{-\mathbf{q}s}][a^\dagger_{\mathbf{q}'s'} - a_{-\mathbf{q}'s'}] \\ [a^\dagger_{\mathbf{q}''s''} - a_{-\mathbf{q}''s''}]\Phi_{\mathbf{q}s\mathbf{q}'s'\mathbf{q}''s''}\delta_{G,q+q'+q''} |i\rangle \, \delta(E_f - E_i). \tag{3.42}$$

In this equation there are two transition constraints, one imposing energy conservation and one momentum conservation. These two constraints take different forms depending on which three phonon matrix element is being considered and on whether it is a transition of class 1 or class 2. When we expand out the ladder operators we will get 8 permutations consisting of 3 creation and annihilation operators. It is trivial to dismiss the case of $a^\dagger_{\mathbf{q}s}a^\dagger_{\mathbf{q}'s'}a^\dagger_{\mathbf{q}''s''}$ and $a_{\mathbf{q}s}a_{\mathbf{q}'s'}a_{\mathbf{q}''s''}$ since nether can conserve energy. In both cases either 3 phonons are created or 3 phonons are annihilated resulting in a change in energy. Ultimately, the energy conservation must hold for the change from the initial state ($|i\rangle$) to the final state ($|f\rangle$). The Energy conservation

can therefore be defined for each class of scattering event. For class 1 the energy conservation takes the form

$$\delta(E_f - E_i) = \frac{1}{\hbar}\delta(\omega(\mathbf{q}s) + \omega(\mathbf{q}'s') - \omega(\mathbf{q}''s'')), \tag{3.43}$$

and for class 2

$$\delta(E_f - E_i) = \frac{1}{\hbar}\delta(\omega(\mathbf{q}s) - \omega(\mathbf{q}'s') - \omega(\mathbf{q}''s'')). \tag{3.44}$$

The momentum conservation is slightly more subtle. It is important to note that creation and annihilation operators for the same state do not carry the same index. The creation operators carry a positive index and the annihilation operators carry a negative one. The q-points will sum over both positive and negative values allowing each to operate for a particular value of q. This, however, has a consequence on the momentum conservation as the Kronecker delta is effected. Effectively, we can say that whenever an annihilation operator appears in the matrix element it will cause the corresponding q-value to become negative. Hence, summing over a matrix element of $a_{-\mathbf{q}s}a_{-\mathbf{q}'s'}a^{\dagger}_{\mathbf{q}''s''}$ will result in a momentum conservation of $\delta_{G,-q-q'+q''}$ corresponding to the condition of $q + q' = q'' + G$.

Through careful consideration of the final state we can identify a matrix element for class 1 and class 2:

$$\Phi_{\mathbf{q}s\mathbf{q}'s'\mathbf{q}''s''}\delta_{G,-q-q'+q''}\left\langle n_{\mathbf{q}s}-1, n_{\mathbf{q}'s'}-1, n_{\mathbf{q}''s''}+1\middle|a_{-\mathbf{q}s}a_{-\mathbf{q}'s'}a^{\dagger}_{\mathbf{q}''s''}\middle|n_{\mathbf{q}s}, n_{\mathbf{q}'s'}, n_{\mathbf{q}''s''}\right\rangle \tag{3.45}$$

$$\Phi_{\mathbf{q}s\mathbf{q}'s'\mathbf{q}''s''}\delta_{G,-q+q'+q''}\left\langle n_{\mathbf{q}s}-1, n_{\mathbf{q}'s'}+1, n_{\mathbf{q}''s''}+1\middle|a_{-\mathbf{q}s}a^{\dagger}_{\mathbf{q}'s'}a^{\dagger}_{\mathbf{q}''s''}\middle|n_{\mathbf{q}s}, n_{\mathbf{q}'s'}, n_{\mathbf{q}''s''}\right\rangle \tag{3.46}$$

Here the momentum condition has been updated to account for the summation. Across the summation for both class 1 and class 2 there are 3! equivalent terms that

come from the permutation of phonon states. Using the λ notation we can define the phonon states that produce non-vanishing terms. For class 1 they are

$$\begin{aligned}(\lambda,\lambda',\lambda'') =&(-\mathbf{q}s,-\mathbf{q}'s',\mathbf{q}''s''),(-\mathbf{q}''s'',-\mathbf{q}s,\mathbf{q}'s'),(-\mathbf{q}'s',-\mathbf{q}''s'',\mathbf{q}s),\\ &(-\mathbf{q}s,-\mathbf{q}''s'',\mathbf{q}'s'),(-\mathbf{q}'s',-\mathbf{q}s,\mathbf{q}''s''),(-\mathbf{q}''s'',-\mathbf{q}'s',\mathbf{q}s)\end{aligned} \tag{3.47}$$

Likewise there is such a set of states for class 2

$$\begin{aligned}(\lambda,\lambda',\lambda'') =&(-\mathbf{q}s,\mathbf{q}'s',\mathbf{q}''s''),(-\mathbf{q}''s'',\mathbf{q}s,\mathbf{q}'s'),(-\mathbf{q}'s',\mathbf{q}''s'',\mathbf{q}s),\\ &(-\mathbf{q}s,\mathbf{q}''s'',\mathbf{q}'s'),(-\mathbf{q}'s',\mathbf{q}s,\mathbf{q}''s''),(-\mathbf{q}''s'',\mathbf{q}'s',\mathbf{q}s)\end{aligned} \tag{3.48}$$

With this we can cancel out the 1/3! term in equation 3.42.

Together we can combine energy conditions in equation 3.43 & 3.44 with the elements 3.45 & 3.46 and accounting for the equivalent summation terms in equations 3.47 & 3.48 one can incorporate it into equation 3.42 to give

$$\begin{aligned}P^{\mathbf{q}''s''}_{\mathbf{q}s\mathbf{q}'s'} = &\frac{2\pi}{\hbar^2}\Phi_{\mathbf{q}s\mathbf{q}'s'\mathbf{q}''s''}n_{\mathbf{q}s}n_{\mathbf{q}'s'}(n_{\mathbf{q}''s''}+1)\\ &\delta_{G,-q-q'+q''}\delta(\omega(\mathbf{q}s)+\omega(\mathbf{q}'s')-\omega(\mathbf{q}''s'')).\end{aligned} \tag{3.49}$$

and

$$\begin{aligned}P^{\mathbf{q}'s'\mathbf{q}''s''}_{\mathbf{q}s} = &\frac{2\pi}{\hbar^2}\Phi_{\mathbf{q}s\mathbf{q}'s'\mathbf{q}''s''}(n_{\mathbf{q}s}+1)n_{\mathbf{q}'s'}n_{\mathbf{q}''s''}\\ &\delta_{G,-q+q'+q''}\delta(\omega(\mathbf{q}s)-\omega(\mathbf{q}'s')-\omega(\mathbf{q}''s'')).\end{aligned} \tag{3.50}$$

Now we have the transition probabilities, the scattering rate can be calculated. There is, however, a complication to the SMRT LBTE methodology that we must define. For three phonon scattering the inverse relaxation time is given as

$$\tau^{-1}_{\mathbf{q}s} = \frac{1}{\bar{n}_{\mathbf{q}s}(\bar{n}_{\mathbf{q}s}+1)}\sum_{\mathbf{q}'s'\mathbf{q}''s''}\bar{P}^{\mathbf{q}''s''}_{\mathbf{q}s\mathbf{q}'s'}+\frac{1}{2}\bar{P}^{\mathbf{q}'s'\mathbf{q}''s''}_{\mathbf{q}s}, \tag{3.51}$$

or expanded, as

$$\begin{aligned}\tau_{\mathbf{q}s}^{-1} =& \frac{2\pi}{\hbar^2} \sum_{\mathbf{q}'s'\mathbf{q}''s''} \Phi_{\mathbf{q}s\mathbf{q}'s'\mathbf{q}''s''} \\ & \left[\frac{\bar{n}_{\mathbf{q}'s'}(\bar{n}_{\mathbf{q}''s''}+1)}{(\bar{n}_{\mathbf{q}s}+1)} \delta_{G,-q-q'+q''} \delta(\omega(\mathbf{q}s)+\omega(\mathbf{q}'s')-\omega(\mathbf{q}''s'')) \right. \\ & \left. + \frac{1}{2} \frac{\bar{n}_{\mathbf{q}'s'}\bar{n}_{\mathbf{q}''s''}}{\bar{n}_{\mathbf{q}s}} \delta_{G,-q+q'+q''} \delta(\omega(\mathbf{q}s)-\omega(\mathbf{q}'s')-\omega(\mathbf{q}''s'')) \right],\end{aligned} \tag{3.52}$$

where we have $\bar{P}$ defined by setting all $n_{\mathbf{q}s}$ to $\bar{n}_{\mathbf{q}s}$. It is necessary to include a factor of $1/2$ to the second probability term so as to avoid errors from over counting. This over counting occurs because, a state described as $\mathbf{q}s$ scattering into the states $\mathbf{q}'s'$ and $\mathbf{q}''s''$, should be indistinguishable from, the state $\mathbf{q}s$ scattering into the states $\mathbf{q}''s''$ and $\mathbf{q}'s'$. An analogous rule applies when scattering from the states $\mathbf{q}'s'$ and $\mathbf{q}''s''$. One could instead incorporate this law into equation 3.48 or even into the summation routine, providing an optimal route for computation.

3.2.3.1 Quasi Anharmonic Approximation

At this point we have the inverse relaxation time in terms of the anharmonic force constants tensor. Performing *ab initio* calculations to determine the third order force constants is computationally exhaustive. The high demand on computational resources is to this day prohibitive. While these methods are appropriate for single crystals and small scale systems[102, 103, 104], they are not useful when applied to large or complicated structures. When developing a theory to investigate heterostructures we choose to reside in the quasi-anharmonic approximation[84, 88, 96, 105].

Here we follow the methodology of Thomas *et al.*[88] with the exception that we employ an improved momentum constraint and we neglect the temperature dependence of the Grüneisen constant, γ. By consideration of the elastic continuum

model one can redefine the phonon coupling strengths. Through this approach one can say[88]

$$\mathcal{V}_3 = \frac{1}{3}\sqrt{\frac{\hbar^3}{8\rho NV}} \sum_{\mathbf{q}s\mathbf{q}'s'\mathbf{q}''s''} \frac{\mathbf{q}\mathbf{q}'\mathbf{q}''}{\sqrt{\omega(\mathbf{q}s)\omega(\mathbf{q}'s')\omega(\mathbf{q}''s'')}} A^{ss's''}_{\mathbf{q}\mathbf{q}'\mathbf{q}''} \\ [a^\dagger_{\mathbf{q}s} - a_{-\mathbf{q}s}][a^\dagger_{\mathbf{q}'s'} - a_{-\mathbf{q}'s'}][a^\dagger_{\mathbf{q}''s''} - a_{-\mathbf{q}''s''}]\delta_{G,q+q'+q''} \tag{3.53}$$

an exactly analogous procedure as detailed previously from equations 3.39 to 3.52 can be used to derive a scattering rate from the crystal potential of an anharmonic elastic continuum. In order to remove the necessity for calculation of the full three phonon coupling strengths tensor ($A^{ss's''}_{\mathbf{q}\mathbf{q}'\mathbf{q}''}$) we assume homogeneity in there interactions. To achieve this we use the dimensionless Grüneisen parameter which provides a link between the macroscopic and the micromechanical. It can be defined macroscopically as,

$$\gamma = V\frac{dP}{dE}\bigg|_V, \tag{3.54}$$

where E is the Internal energy and P is the pressure. The Grüneisen parameter represents an effective pressure due to the thermal vibration of atoms, enhancing the volume thermal expansion,

$$\beta = \frac{\gamma C_V}{VK_T}, \tag{3.55}$$

where K_T is the isothermal bulk modulus[84]. However, a mode dependent Grüneisen parameter is defined micromechanically as,

$$\frac{\partial\omega(\mathbf{q}s)}{\partial V} = -\gamma(\mathbf{q}s)\frac{\omega(\mathbf{q}s)}{V}, \tag{3.56}$$

and a mode independent Grüneisen parameter as

$$\gamma = \frac{\sum_{\mathbf{q}s}\gamma(\mathbf{q}s)C_v(\mathbf{q}s)}{\sum_{\mathbf{q}s}C_v(\mathbf{q}s)}. \tag{3.57}$$

By this method we may define

$$\frac{\mathbf{q}\mathbf{q}'\mathbf{q}''}{\sqrt{\omega(\mathbf{q}s)\omega(\mathbf{q}'s')\omega(\mathbf{q}''s'')}}\left|A^{ss's''}_{\mathbf{q}\mathbf{q}'\mathbf{q}''}\right| = \frac{2\rho|\gamma|}{\bar{c}}\sqrt{\omega(\mathbf{q}s)\omega(\mathbf{q}'s')\omega(\mathbf{q}''s''}, \tag{3.58}$$

where $\bar{c}$ is the average acoustic phonon speed. With this substitution it is possible to define the scattering rate in terms of the material Grüneisen constant.

$$\begin{aligned}\tau^{-1}_{\mathbf{q}s} =& \frac{\hbar\pi}{\rho NV}\frac{|\gamma|^2}{\bar{c}^2}\sum_{\mathbf{q}'s'\mathbf{q}''s''}\omega(\mathbf{q}s)\omega(\mathbf{q}'s')\omega(\mathbf{q}''s'') \\ &\left[\frac{\bar{n}_{\mathbf{q}'s'}(\bar{n}_{\mathbf{q}''s''}+1)}{(\bar{n}_{\mathbf{q}s}+1)}\ \delta_{G,-q-q'+q''}\ \delta(\omega(\mathbf{q}s)+\omega(\mathbf{q}'s')-\omega(\mathbf{q}''s''))\right. \\ &\left.+\frac{1}{2}\frac{\bar{n}_{\mathbf{q}'s'}\bar{n}_{\mathbf{q}''s''}}{\bar{n}_{\mathbf{q}s}}\ \delta_{G,-q+q'+q''}\ \delta(\omega(\mathbf{q}s)-\omega(\mathbf{q}'s')-\omega(\mathbf{q}''s''))\right].\end{aligned} \tag{3.59}$$

This defines the quasi-anharmonic three phonon scattering rate. It is defined in terms of the measurable material property γ. However, since the assumption of homogeneity in three phonon interactions is not strictly accurate we allow the Grüneisen constant to act as an adjustable parameter. By using only a single such parameter, we can maintain a high statistical justification for the theory upon close modeling to experimental results[106].

3.3 Thermal Transport Summary

In this chapter thermal transport theory has been explored. Using the phonon Boltzmann transport equation and the single mode relaxation time approximation an expression is developed for the thermal conductivity. Different contributions to the scattering rate are then derived. Scattering rates are derived from three mechanisms. One source of scattering in a crystal finite size occurs at its natural boundaries. This boundary scattering is explored and an expression derived in section 3.2.1. A second source of scattering form the presence of isotopes and other

mass defects. A theory for randomly distributed isotopes is developed in section 3.2.2 and an equation for the mass defect scattering rate is derived. A third, and arguably most important, scattering mechanism is the three phonon interaction. In section 3.2.3 an expression for the three phonon scattering rate is derived using the average Grüneisen constant as an adjustable parameter. All expressions are derived to be applicable to data obtained through *ab initio*DFT.

Chapter 4

TMDC Heterostructures

> *" 'Normal science' means research firmly based upon one or more past scientific achievements, achievements that some particular scientific community acknowledges for a time as supplying the foundation for its further practice."*
>
> — Thomas S. Kuhn
>
> The Structure of Scientific Revolutions, 1962

4.1 Introduction

Two-dimensional (2D), or atomically thin, materials offer a high degree of customisability through their arrangement into van der Waals heterostructures. This is desirable because it allows a wide range of fixed material parameters to be tailored by the interface physics. This in turn leads to new properties [107], which are a result of the combined heteorostructure. These van der Waals heterostructures are breaking new ground in applications such as high ZT thermoelectrics [47, 108], highly efficient photodetectors [109] and photovoltaic cells [49]. A further unique feature

of heterostructures that has caught considerable attention are interlayer excitons, particularly in transition metal dichalcogenide (TMDC) heterostructures for optoelectronics [110, 111, 112, 113, 114]. This is in part due to the spatial separation of electron-hole pairs [50]. The fundamental physics driving these applications would benefit from having a predictive approach allowing one to estimate the key properties of the heterostructure such as the band gap and a more detailed understanding of the interface physics is determined by the band alignment and interactions of the constituents. The interface physics of these 2D heterostructures has been of intense focus, with several measurements [49, 50, 110, 111, 112, 115, 116, 117, 118, 119, 120, 121, 122, 123] and theoretical calculations [114, 124, 125]. However, given the greater than 5000 2D materials and hence 16 million combinations [126], a predictive approach made using only the properties of the constituents is vital.

Fundamentally, the band alignment of two-dimensional heterostructures is of great interest. However, different approaches have been adopted to explain band alignment in these systems. Many use Anderson's rule, despite being a macroscale approach, directly or implicitly for TMDCs to determine the band alignments [49, 50, 116, 117, 123, 124, 127], and it has even been reported that Anderson's rule is exact for these systems [117]. Conversely, those working with 3D materials, or conventional heteostructures, have long cited that Anderson's rule fails for these systems [128, 129, 130]. The origin of this contradiction provides an opportunity to develop a fuller understanding of band alignment in all these structures. Unlike in macroscale interfaces, where the materials can be expected to adopt their bulk properties far from the interface, these 2D materials are typically one nanometer in thickness meaning such bulk methodologies would be expected to fail.

Anderson suggested (as well as Schottky Mott) that band alignment depended purely on the relative work-function/affinities of the two constituents. However, relatively few experimental systems have validated this approach. This model was expanded [131] upon thereafter to include the effect of charge states at the inter-

face. These states are a result of (a) the formation of new states due to chemical bonding between the two systems and (b) a requirement for charge neutrality caused by the induced field created from the resultant electron affinities of the two systems [132]. These charge states include interface (or metal) induced gap states, IIGS (or MIGS) [133, 134]. Predicting the energies of these states, and the shape of the electrostatic field induced across the interface is non-trivial due to the atomic bonding and system geometry. The recent exploration [49, 50, 116, 117, 123, 124] of weakly interacting two-dimensional materials offer a chance to revisit the understanding of band alignment in these systems, as unlike in the 3D case, dangling bonds are not present at the surface and new bonds are not formed between the layers, nor is substantial reconstruction present [135]. Effectively, these TMDC heterostructures are the closest real world likenesses to Anderson's original thought experiment, where the band alignment results from bringing two separate systems close together from infinity with minimal interaction [128]. These interactions (such as IIGS) should be more clearly identifiable in such systems and thus provides a window to enhancing our understanding how the band alignment is governed.

In this chapter we explain how band alignment in TMDC heterostructures is governed, providing insight into why Anderson's rule appears exact in some cases and fails in others. We determine how these differences arise based on the interactions of the atomic wave functions and the induced electric field due to the difference in the hole affinities of the constituents. From this, we derive analytical expressions that can be applied to predict the bandgap in TMDC van der Waals heterostructures. Our methodology comes from a combination of first principles density functional theory and analytical modelling based upon tight binding. The final expression given provides a method to estimate the band alignment of these heterostructures, alleviating the necessity of large scale numerical simulations. Finally, we discuss how the theory accounts for strain and Moiré systems and how such a theory could be extended to all 2D heterostructures.

4.2 Methodology

To investigate 2D TMDC heterostructures and their interactions, we employ an analytical model developed using tight binding and *ab initio* methods. This model utilises density functional theory to calibrate and validate it. For our *ab initio* calculations, we use the PBE [77] and HSE06 [70] functionals with PAW pseudopotentials [136] and Grimme-D3 [137] correction as implemented in VASP [138]. For our density functional calculations, a plane-wave cutoff of 900 eV is used to accurately capture the confinement effects. Simulations with cutoffs of 600 eV and below showed changes in the electronic structure, which converged at 600 eV and higher. For our consideration of the Monkhorst-Pack grid [91] used in the simulations, we applied a minimum of 15 × 15 × 15 for bulk TMDCs and a 15 × 15 × 1 (or greater) Monkhorst-Pack grid for monolayer TMDCs. For Moiré cells, a k-point density greater than 12 × 12 × 1 per monolayer constituent cell, is maintained. Bulk TMDCs consisted of two 3-atom individual layers in the 2H structure. Similarly, our monolayers consisted of a single layer of 3 atoms in H structure. Our heterostructures are formed from two of these primitive cells with H-type stacking. To generate Moire structures we used ARTEMIS[139]. This allows the generation of supercells with a lattice matching of 12 MoS_2 cells to 13 CrS_2 cells with an angle ∼16.1°, and 19 MoS_2 cells to 16 HfS_2 cells with an angle ∼23.4° between their respective primary lattice vectors. The structures began with an interatomic distance smaller than the average of the two bulks and were allowed to relax. In all the systems considered, we used a 15 Å vacuum gap between monolayer and bilayers to avoid spurious interactions with periodic replicas. All structures are relaxed using the conjugate gradient algorithm to within 0.001 eV/Å. Also, to avoid the effect of electric fields across the vacuum created by the charge transfer involved in the heterostructures, we created mirror image structures which were compared with to ensure the electric field effects were negligible in all cases. The bilayer structures maintain their lack of inversion symmetry and therefore band splitting due to spin

orbit coupling (SOC) still occurs [41, 42]. However, here SOC is neglected as it is an intralayer effect [140] with no influence on the interlayer coupling [141] and has no direct effect on the band alignment. All relevant systems have been examined with SOC to confirm this conclusion.

4.3 Results and discussion

4.3.1 Band structure of TMDC heterostructures

A broad set of TMDCs are investigated using the PBE functional. In Fig. 4.1 we can observe the full bandstructure of 9 TMDC heterostructures compared to their individual constituents. For many of the heterostructures the overlay bands appear to match there constituents almost exactly. The fact that this similarity is so strong could help explain why Anderson's rule is so commonly used in literature[49, 50, 116, 117, 123, 124, 127]. Despite this however, there are key differences that can be identified between the bands of the heterostructure and the constituents. Two clear alterations to the bands occur when a heterostucture is formed. Firstly, there is a static shift in some of the bands and, secondly, there is an interaction that drives up the valence band maximum at the Brillouin zone center (Γ). These two changes are the only significant adaptation to the Anderson's rule prediction. The limited variation and consistency of these subtle effects in the bandstructure make truer bandgap prediction for TMDC heterostructures attainable.

As discussed in chapter 2 the HSE06 hybrid functional can be considered generally more accurate in the prediction of bandstructures. Therefor we examine in further detail the two sub-cases considered using HSE06. We present in Fig. 4.2 the band alignment of WSe_2/MoS_2 and MoS_2/CrS_2, and we show that, whilst Anderson's rule is a reasonable estimate, it is not precisely held. This is just as was

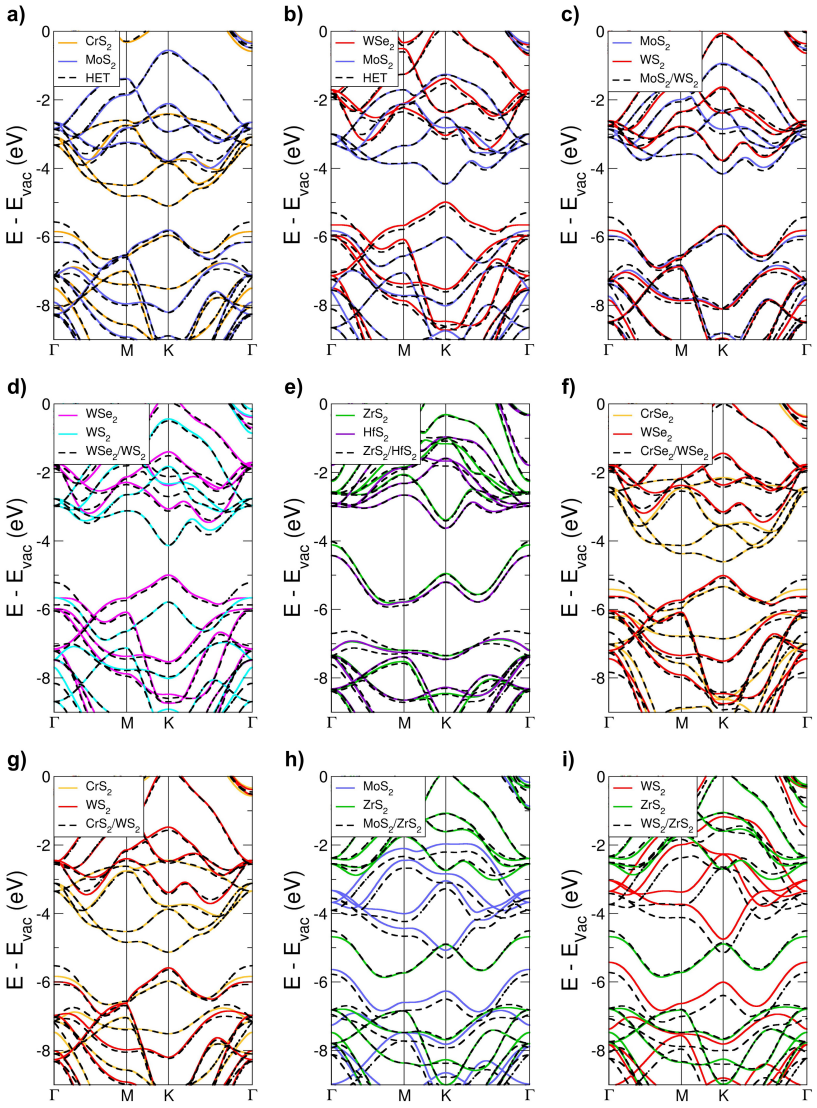

Figure 4.1. The overlay band structures of all 9 studied heterobilayers. From a) to i) they are a) CrS_2/MoS_2, b) WSe_2/MoS_2, c) MoS_2/WS_2, d) WSe_2/WS_2, e) ZrS_2/HfS_2, f) $CrSe_2/WSe_2$, g) CrS_2/WS_2, h) MoS_2/ZrS_2, i) WS_2/ZrS_2. Each panel consists of the band structure of the heterostructure, the individual constituents and these are aligned by reference to the vacuum level. The BZ coordinates for the special k-points are $\Gamma = 0$, $M = \frac{1}{2}\vec{a}^*$ and $K = \frac{1}{3}\vec{a}^* + \frac{1}{3}\vec{b}^*$

found using the PBE functional. The results in Fig. 4.2 show that the deviation from Anderson's rule is 0.07 eV (8.0%) for WSe_2/MoS_2 and 0.12 eV (11.9%) for MoS_2/CrS_2.

TMDC heterostructures are typically incommensurate and thus the creation of a periodic unit cell inevitably results in strain. The two heterobilayers WSe_2/MoS_2 and MoS_2/CrS_2, are laterally strained resulting in a 1.90% compression on WSe_2 and 1.92% expansion on MoS_2, for the WSe_2/MoS_2 heterobilayer, and a 2.14% compression on MoS_2 and 2.53% expansion on CrS_2, for the MoS_2/CrS_2 heterobilayer. This is due to the aforementioned incommensurability and thus the creation of a periodic unit cell inevitably results in strain. Despite this, it is still possible to distinguish interlayer and strain effects. Our calculations show the effects of strain can be treated as decoupled from the interlayer interactions.We further discuss the effects of strain on our theory later.

4.3.2 Band alignment theory

The bandstructures in Fig. 4.1 and 4.2 show two consistent deviations from Anderson's rule. As such, two factors are needed to correct for these deviations. These corrections are (i) ΔE_Γ, the change in the valence band energy at Γ created due to interlayer interaction (An IIGS effect) and (ii) ΔE_{IF}, the energy shift in all the bands of the constituent with the smallest hole affinity created due to the induced field.

First we discuss the role of IIGS, that is the change in the bandstructure due to interlayer interactions. Adjacent layers interact through weak transient bonding resulting in small distortions to the existing bands. The net (zone center) distortions, $\Delta E_\Gamma - \Delta E_{\mathrm{IF}}$ and ΔE_Γ are labeled in Fig. 4.2a and 4.2b respectively. The heterobilayer, WSe_2/MoS_2, has a ΔE_Γ value of 0.43 eV while for MoS_2/CrS_2 it is

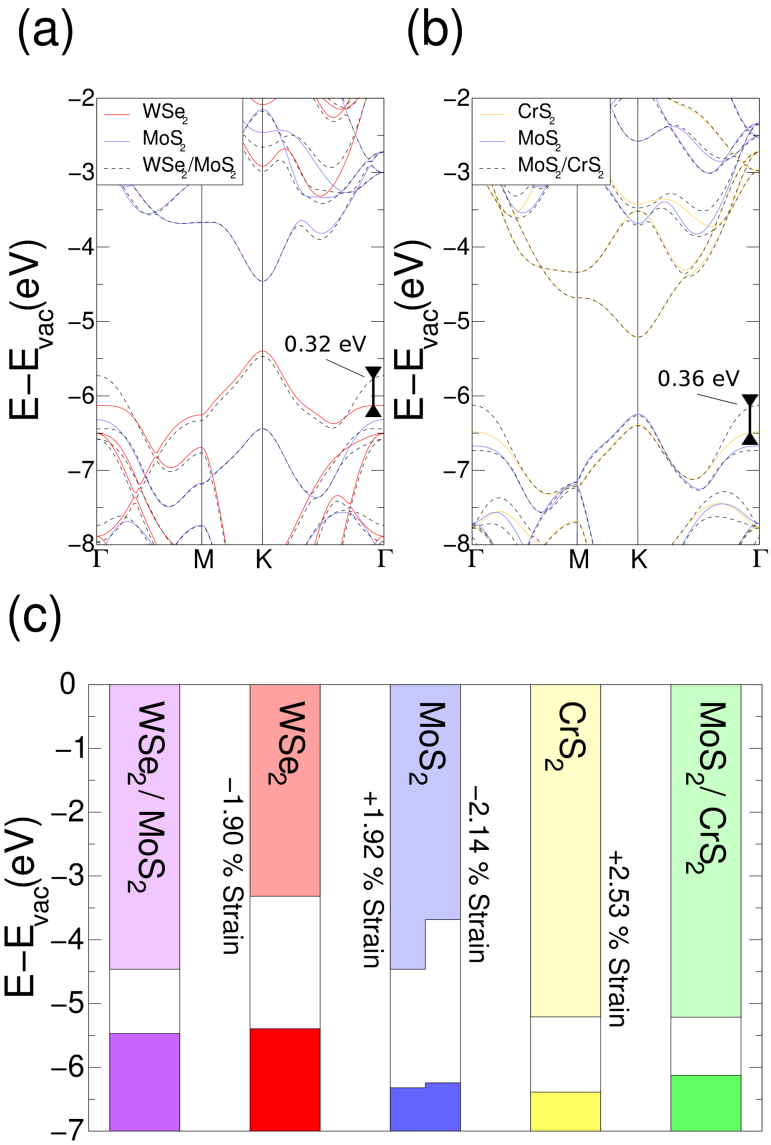

Figure 4.2. (a) The electronic dispersion of the heterostructure WSe_2/MoS_2 (black dashed) overlaying the electronic dispersions of the two constituents WSe_2 (red) and MoS_2 (blue). (b) Dispersion of the heterostructure MoS_2/CrS_2 (black dashed) overlaying the electronic dispersions of the MoS_2 (blue) and CrS_2 (yellow). (c) Band edge diagram of heterostructures and their constituents showing VBM and CBM. All energies are plotted relative to the vacuum energy and calculated with the HSE06 functional.

equal to 0.36 eV. In the WSe_2/MoS_2 ΔE_Γ does not raise the valence band at Γ above the height of the valence band at K. Similarly, one can observe that the induced shift in the heterobilayer bands due to band alignment, ΔE_{IF}, is equal to 0.11 eV, for WSe_2/MoS_2 and acts on the WSe_2 bands. In the MoS_2/CrS_2 case, the value of ΔE_{IF} is very small, resulting in the MoS_2 bands being shifted by 0.03 eV in the heterobilayer. This shift is driven by an induced field created from the relative positions of the two constituents' valence bands. It is interesting that our results show that correction due to charge transfer resulting from the band offset is non-linear, as has been suggested in previous works [142]. This, in turn, suggests that the electric field does not follow the simple quadratic form normally considered for a heterojunction.

4.3.2.1 Induced field correction, ΔE_{IF}

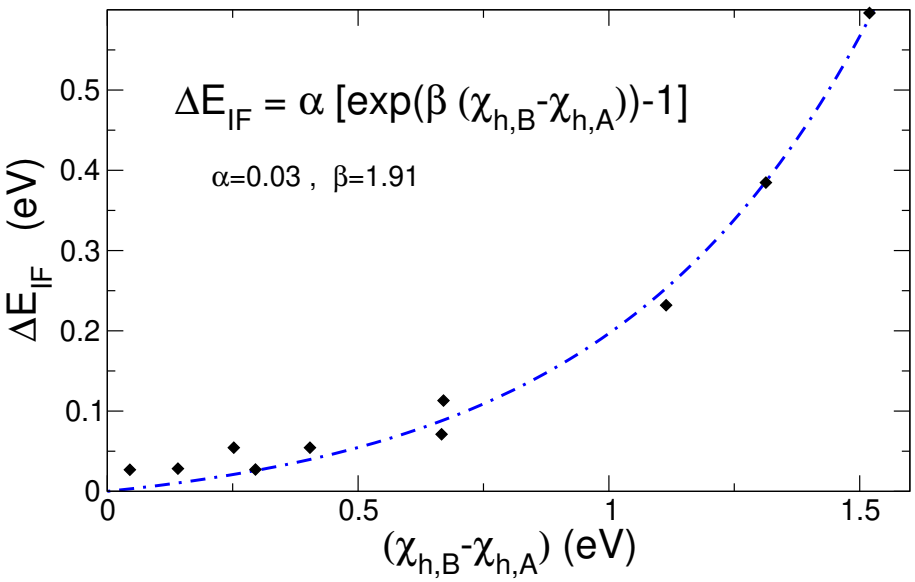

Figure 4.3. The relationship between the valence band offset ($\chi_{h,\mathrm{B}} - \chi_{h,\mathrm{A}}$) and the resultant shift in the band energies (ΔE_{IF}). The inset gives the equation and parameters for the empirical fit (blue dashed line).

The shift in band alignment due to the field induced from the band offset can be described as ΔE_{IF}. The simulation data for ΔE_{IF} is plotted against the VBM offset ($\chi_{h,\mathrm{B}} - \chi_{h,\mathrm{A}}$) in Fig. 4.3. ΔE_{IF} is defined as the average band shift for all

k-points along the band edge from M to K. Figure 4.3 shows the empirical fit

$$\Delta E_{\mathrm{IF}} = \alpha \left(\exp\left(\beta \left(\chi_{h,\mathrm{B}} - \chi_{h,\mathrm{A}} \right) \right) - 1 \right), \tag{4.1}$$

where α and β are 0.03 eV and 1.91 Å/eV, respectively. we define material A as having the smaller hole affinity, $\chi_{h,\mathrm{A}}$, compared to the hole affinity of material B, $\chi_{h,\mathrm{B}}$. The form of Eq. 4.1 both agrees with the data and obeys the condition ΔE_{IF} for identical layers (i.e. a bilayer system consisting of a single material).

The shift, ΔE_{IF}, is similar to the description of band bending in conventional heterostructures created by a charge transfer that occurs due to the VBM offset, which induces an electric field. However, the functional form of the electric field is not simply described. It's effect is to change the relative energy of the bands in each layer such that local electron affinity is preserved. The resultant electric field also changes the vacuum energy in that region. By defining the highest local potential energy as the vacuum, we observe that the lower valence band material (negatively charged, so higher vacuum energy) is aligned with the hetero-bands and the other layer has shifted bands. This shift is the term we describe as ΔE_{IF}. As expected, this induced field does not change the size of the band gap of either constituent as has been observed in monolayer systems [143].

The effect of ΔE_{IF} on the bands is constant however how it effects the bandgap depends on the band alignment. In Type II band alignment (where the two bandgaps partially overlap), the effect of ΔE_{IF} will be to increase the bandgap since the VBM will drop lower. In the case of Type I band alignment (where one constituents bandgap lies completely within the other material), the heterobilayers will have an unchanged bandgap because both the VBM and conduction band minima (CBM) change together. Hence, from Eq. 4.1 it is possible to determine the shift, ΔE_{IF}, based only on the properties of the monolayer constituents.

4.3.2.2 Layer hybridization correction, ΔE_Γ

We have explored one of the identified consistent deviations from Anderson's rule, and a second corrective term, arising from the overlap of the atomic wavefunctions between layers, is required, which we describe as ΔE_Γ. This shift can be seen in Fig. 4.2a and 4.2b at Γ, as well as many of the bandsructures in Fig. 4.1. This shift will usually, but not always, affect the bandgap, depending on where the VBM is located in the Brillouin zone. When the valence band at Γ, $E_{\mathrm{VB}}(\mathbf{k} = \Gamma)$, is below the VBM, E_{VBM}, by an amount greater than ΔE_Γ, then the bandgap will not be affected. As is the case in Fig. 4.2b, we find that, typically, $\Delta E_\Gamma > \big(E_{\mathrm{VBM}} - E_{\mathrm{VB}}(\mathbf{k} = \Gamma)\big)$ and thus it reduces the bandgap of the heterostructure.

The ΔE_Γ term comes from the weak overlap of the orbitals of the two constituent layers. To examine this behaviour, we have calculated the magnitude of ΔE_Γ using first principles simulations by varying the interlayer spacing, d, in bulk TMDCs, as shown in Fig. 4.4. Analysis of the projected density of states suggests that the magnitude of ΔE_Γ is controlled by the overlap of the $\langle d_{z^2}|d_{z^2}\rangle$ and $\langle p_z|d_{z^2}\rangle$ (which is a function of d). The sharp discontinuity corresponds to the switch between energy configurations, i.e. from $\langle d_{z^2}|d_{z^2}\rangle$ to $\langle p_z|d_{z^2}\rangle$. To confirm this, we have developed a tight binding model [144, 145, 146], calibrated from our first principles findings. In this model, we have shown that, whilst the in-layer components consist of d_{xy} and $d_{x^2-y^2}$, we only need to consider the interactions of the p_z and d_{z^2} orbitals between layers to replicate the behaviour of ΔE_Γ. In agreement with previous work we dismiss the weaker π and δ bonding as insignificant interlayer contributions [147]. These results show that ΔE_Γ is driven by the bonding and antibonding interaction of the p_z and d_{z^2} orbitals between layers. Generally, the tight binding approach clearly shows that the p_z-d_{z^2} (d_{z^2}-d_{z^2}) dominates in the high (low) separation regimes. We note, however for HfX_2 and ZrX_2 the behavior is controlled by $\langle p_z|p_z\rangle$, which becomes metallic at low separations. This is due to these nanostructures effectively

having their d-orbitals depleted to form the TMDC structure. Furthermore, the splitting is no longer meaningful beyond the point that the nanostructure becomes metallic.

Following our tight binding model (see appendix D), we derive a simplified form for ΔE_Γ by directly considering the overlap of $\langle d_{z^2}|p_z\rangle$ or $\langle d_{z^2}|d_{z^2}\rangle$. This suggests ΔE_Γ should take the form

$$\Delta E_\Gamma = e^{-\lambda \Delta d} \sum_{i=0}^{n+n'-3} \eta_i (\Delta d)^i, \tag{4.2}$$

where Δd is the change in separation from the bulk interlayer spacing, defined as $d - d_0$, with d_0 being the bulk interlayer spacing and d the interlayer spacing of the hetero-/homo-bilayer. λ and η_i are constants, which differ for the p_z-d_{z^2} or d_{z^2}-d_{z^2} regimes with n and n' being principle quantum numbers. One can estimate the value of λ and η_i using the 2H-TMDCs (η_i the p_z-d_{z^2} regime and where η_i' denotes the d_{z^2}-d_{z^2} regime). Hence, we have evaluated ΔE_Γ for many 2H-TMDCs at different spacings (d), using the PBE functional, as shown in Fig. 4.4. From these results, we determine that $\lambda = 1.3$ Å^{-1} ($\lambda' = 0.5$ Å^{-1}) with the exception of the those 2D layered materials which are p_z-p_z dominated (ZrS_2 and HfS_2) where $\lambda = 0.75$ Å^{-1}. The values of η_i for Eq. 4.2 are given in Fig. 4.4. The first two terms are sufficient to make the error of Eq. 4.2 negligible ($\sim 10^{-5}$ eV) compared with the simulation data.

The remaining parameters are material-dependent and can now be evaluated using the appropriate values for λ and η_i and the interlayer distance. The interlayer distance can be approximated as the average of the distances between the layers in the two bulk constituents. Now, one only has to consider the higher VBM material, and use Eq. 4.2 with that materials parameters and the average interlayer spacing to estimate ΔE_Γ.

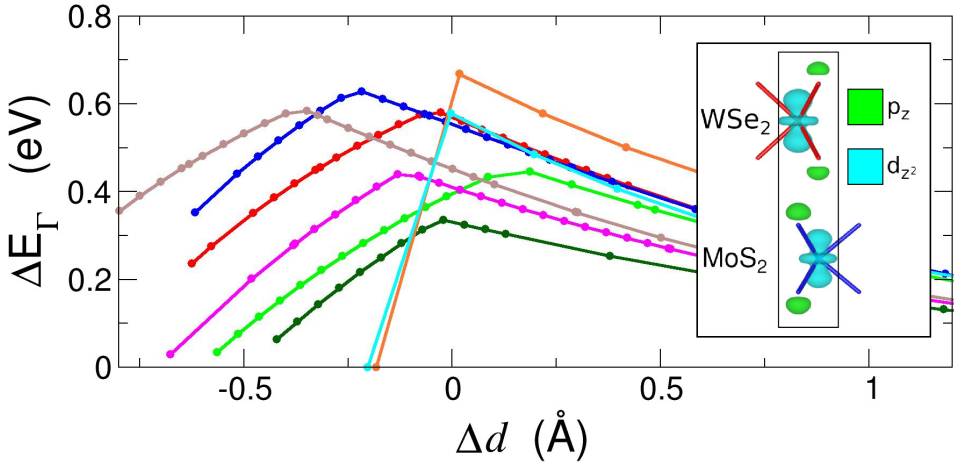

MoS$_2$	η_0= 0.570	η_1= 0.348	η'_0= 0.608	η'_1= 0.695
MoSe$_2$	η_0= 0.498	η_1= 0.366	η'_0= 0.395	η'_1= 0.657
WS$_2$	η_0= 0.553	η_1= 0.370	η'_0= 0.750	η'_1= 0.795
WSe$_2$	η_0= 0.451	η_1= 0.230	η'_0= 0.714	η'_1= 0.597
CrS$_2$	η_0= 0.410	η_1= 0.233	η'_0= 0.504	η'_1= 0.716
CrSe$_2$	η_0= 0.330	η_1= 0.231	η'_0= 0.352	η'_1= 0.716
ZrS$_2$	η_0= 0.673	η_1= 0.0404	----------	----------
HfS$_2$	η_0= 0.574	η_1=-0.0635	----------	----------

Figure 4.4. (Top) The relation between ΔE_Γ and Δd. (Bottom) The tabulated fitting parameters that reproduce the simulation data, corresponding to those in eq. 4.2 for η_0 (eV) and η_1 (eV/Å). Both ZrS_2 and HfS_2 are metallic for $d \leq 6$ Å and therefore have no η'_i values.

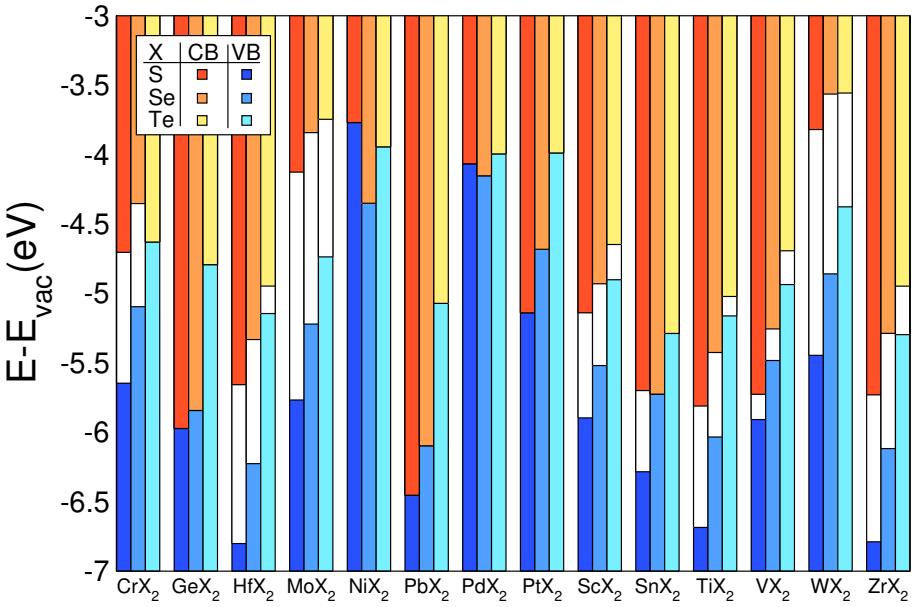

Figure 4.5. Conduction and valence band edges calculated within PBE for the 2D TMDCs. The colored bar edges represent the valence bands (shades of blue/cyan) and the conduction bands (shades of red/yellow) for each monolayer; All energies are taken with respect to the vacuum level. Due to the band gap underestimate by PBE, the electron affinities are overestimated.

4.3.2.3 Bandgap prediction

Having evaluated the corrections to Anderson's rule, we propose a corrected form which calculates the band offsets using only information about the monolayer constituents. We present the key properties, the band edges, of the monolayer constituents in Fig. 4.5.

The two corrections explored in this work can be implemented on top of an Anderson's approach. It is first necessary to evaluate whether the system is Type I, Type II or III. This is determined from the electron and hole affinities, χ_e and χ_h respectively. By defining material A using the condition $\chi_{h,A} > \chi_{h,B}$, it is possible to define the type of heterostructure following the normal convention, i.e. Type I alignment if $\chi_{e,B} > \chi_{e,A}$, Type III if $\chi_{e,A} > \chi_{h,B}$, Type II otherwise. The ΔE_{IF} correction will only affect the bandgap for Type II band alignments. It is also necessary to determine to what extent ΔE_{Γ} will affect the bandgap. As discussed earlier, ΔE_{Γ} must be larger than $(E_{\mathrm{VBM}} - E_{\mathrm{VB}}(\Gamma))$, to alter the bandgap, and

Hetero	ΔE_{VB} (eV)	ΔE_{Γ} (eV)	ΔE_{IF} (eV)	d (Å)	Bandgap (eV)			Error	
					DFT	**Anderson's**	**Corrected**	**Anderson's**	**Corrected**
CrS_2/MoS_2	0.045	0.378	0.003	6.15	0.465	0.700	0.343	50.71%	20.90%
WSe_2/MoS_2	0.670	0.537	0.078	6.37	0.647	0.521	0.641	19.41%	7.36%
MoS_2/WS_2	0.141	0.342	0.009	6.22	1.260	1.505	1.107	19.51%	4.27%
WSe_2/WS_2	0.666	0.536	0.077	6.37	0.936	0.858	0.941	8.33%	0.09%
ZrS_2/HfS_2	0.295	0.656	0.023	6.22	0.696	1.021	0.683	46.67%	1.89%
$CrSe_2/WSe_2$	0.404	0.102	0.035	6.48	0.468	0.398	0.438	15.00%	7.54%
CrS_2/WS_2	0.252	0.371	0.019	6.17	0.393	0.451	0.301	14.85%	15.43%
MoS_2/ZrS_2	1.114	0.594	0.083	6.18	0.000	0.000	0.000	-	-
WS_2/ZrS_2	1.313	0.340	0.113	6.22	0.000	0.000	0.000	-	-
Average								24.93%	8.21%
Standard deviation								16.70%	7.48%

Table 4.1. Tabulated values of TMDC heterobilayers quantitatively comparing the original and corrected Anderson's bandgap predictions to the DFT PBE bandgap values. The values of ΔE_{Γ} and ΔE_{IF} are calculated using Eq. 1 and Eq. 2, respectively. Here ΔE_{VB} equals $E_{\mathrm{VBM}} - E_{\mathrm{VB}}(\mathbf{k} = \Gamma)$ and d is the interlayer spacing. The error values of the corrected method are directly compared to those obtained using Anderson's rule. Heterobilayers in this table without provided error values have Type III band alignment and, are therefore, metallic.

generally this is the case. This requires the difference in energies for the valence band at Γ, $E_{\mathrm{VB}}(\Gamma)$, and the valence band maxima (normally at K), E_{VBM}. We implement the positive part function, which express the bandgap reduction due to ΔE_{Γ} as

$$E'_{\Gamma} = \frac{\Delta E_{\Gamma} - (E_{\mathrm{VBM}} - E_{\mathrm{VB}}(\Gamma))}{2} + \frac{|\Delta E_{\Gamma} - (E_{\mathrm{VBM}} - E_{\mathrm{VB}}(\Gamma))|}{2}. \tag{4.3}$$

Hence, we can evaluate the bandgap of the heterostructure. For Type I, it is expressed as

$$E_g = \chi_{e,B} - \chi_{h,B} - E'_{\Gamma}, \tag{4.4}$$

and for Type II

$$E_g = \chi_{e,B} - \chi_{h,A} + \Delta E_{\mathrm{IF}} - E'_{\Gamma}, \tag{4.5}$$

and for Type III E_G=0. This approach reduces the mean error in predicting the bandgap of a heterostructure using Anderson's rule (approximately 25%) to less than 10%.

A complete quantitative comparison between the *ab initio* simulation data (from Fig. 4.1) and the predictive bandgap theory is included in Table 4.1. It shows that the corrected values of Anderson's rule have a reduced error on average. The greatest reduction is given by ZrS_2/HfS_2 and the only system for which the corrected prediction is worse is CrS_2/WS_2. The average error in bandgap prediction falls below 10% when applying the corrections. Conversely Anderson's rule has an average error above 24%. This demonstrates the advantages of applying the corrected theory over the current Anderson's rule approach. Furthermore, with the standard deviation of the corrected rule being approximately half that of Anderson's rule, there is significantly more reliability that the corrected rule will, for a given heterostructure pairing, provide a reasonable bandgap prediction.

Corrected rule bandgaps can be calculated by applying Eq.4.3, Eq.4.4 and Eq.4.5 alongside the Table 4.1 values for ΔE_{VB}, ΔE_{Γ}, ΔE_{IF} and Anderson's bandgap. When the heterobilayer is of Type I band alignment, the Anderson's rule prediction for the bandgap is equivalent to $(\chi_{e,\mathrm{B}} - \chi_{h,\mathrm{B}})$ from Eq. 4.4. When the heterobilayer is of Type II band alignment, Anderson's rule is $(\chi_{e,\mathrm{B}} - \chi_{h,\mathrm{A}})$ from Eq. 4.5. The value of d is the interlayer distance, however, the average of the constituents can be used with a mean error of 1.87%. Calculation of the bandgaps depends on using the appropriate equation for the respective band alignment; CrS_2/MoS_2 and CrS_2/WS_2 are of Type I, MoS_2/ZrS_2 and WS_2/ZrS_2 are of Type III and all others are of Type II.

4.3.3 Discussion of Moiré and strain effects on band alignment

Thus far all discussions have included strained TMDCs with no rotation between layers. This is a product of the one-to-one cell matching. The assumption that the effects of strain are additive to the effects of interlayer interaction is reasonable.

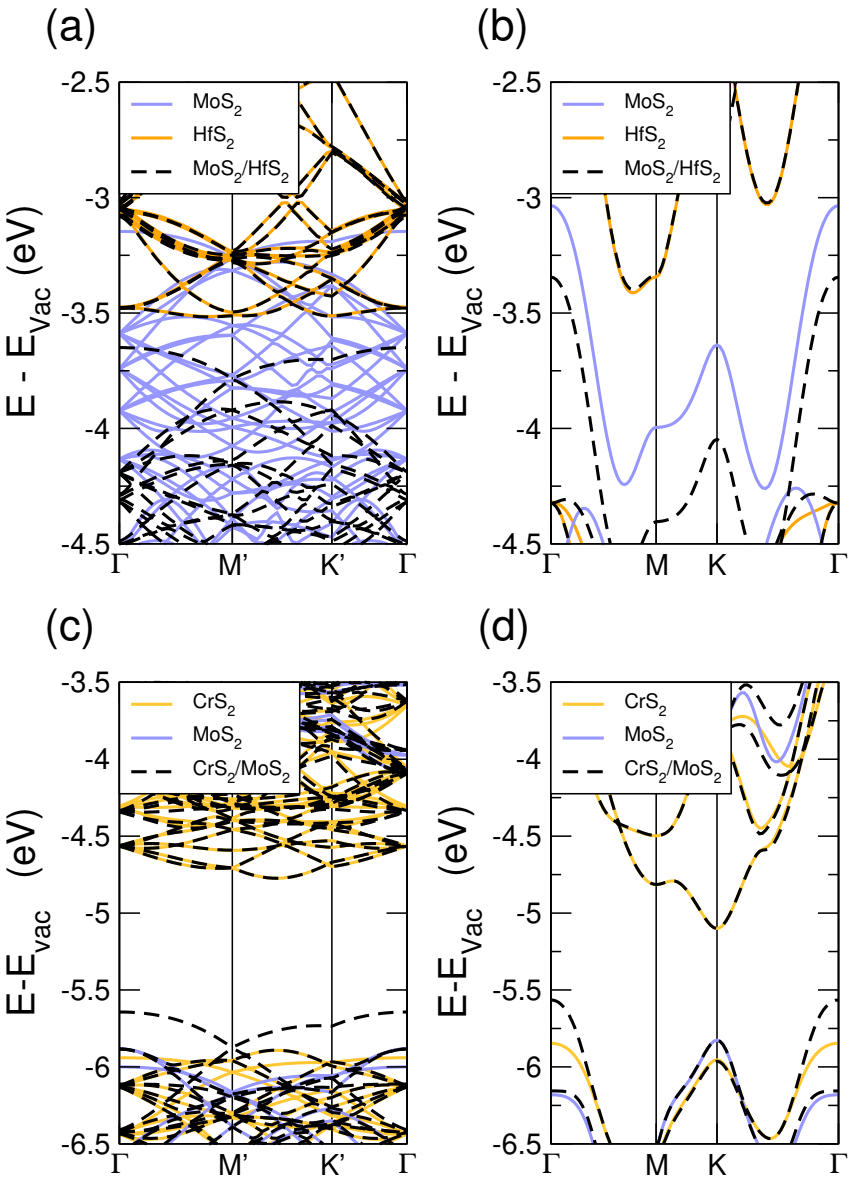

Figure 4.6. (a & b) An overlay bandstructure showing the constituent bands (blue & orange) overlayed by the heterobilayer bands (black dashed) with (a) showing the Moiré structure and (b) showing the one-to-one cell matching for MoS_2/HfS_2. (c & d) Constituent bands (blue & gold) with heterobilayer bands (black dashed) overlayed. (c) showing the Moiré structure and (d) showing a one-to-one cell matching for CrS_2/MoS_2. The BZ coordinates for the special k-points M and K are defined by the unit cell reciprocal lattice vectors ($M = \frac{1}{2}\vec{a}^*$ and $K = \frac{1}{3}\vec{a}^* + \frac{1}{3}\vec{b}^*$). The M′ and K′ special k-points are defined equivalently but using the supercell reciprocal lattice vectors.

The basis of this assumption is that if a strained TMDC constitutes part of the heterostructure then that constituent is not MX_2 but is instead strained MX_2. At first, this would appear to undermine the empirical bandgap prediction presented in this report as it would require exact knowledge of the strain characteristics of each TMDC, both when in a heterostructure and when in isolation. This would, once again, require the application of density functional theory and hence one might as well calculate the heterostructure itself. However, real world TMDCs tend to form heterostructures with incommensurate lattice matching resulting in a Moiré lattice pattern. A greater concern of Moiré structures is how rotated lattices will affect the interlayer interaction.

Through the examination of Moiré lattice heterostructures, testing the assumption that strain is additive with the interlayer interaction is easily done, since the Moiré structures are effectively without strain (average strain $< 1\%$). It is also possible to investigate the effects of rotation. For this purpose two heterostructures have been examined. Calculations for MoS_2/HfS_2 and CrS_2/MoS_2 Moiré structures were performed using the same methodology as the lattice matched heterostructures.

It can be observed from Fig. 4.6a & 4.6b that the both Moiré and lattice matched systems have a significant ΔE_{IF}. However comparison between the two requires careful consideration of their relative strains. Because the strain on the constituents changes between the two systems it is necessary to test them against our identified trend instead of against each other. In the case of MoS_2/HfS_2 Moiré structure the value of ΔE_{IF} is 0.596 eV for a band offset of 1.520 eV, this deviates from Eq. 4.1 by 0.07 eV. The one-to-one MoS_2/HfS_2 heterobilyer results in $\Delta E_{\mathrm{IF}} =$ 0.346 eV, for a band offset of 1.284 eV, deviating from Eq. 4.1 by 0.02 eV. This demonstrates that Moiré twisting and strain do not effect the validity of Eq. 4.1.

It is expected that ΔE_{IF} is preserved as it does not depend on the local structure. It depends on the relative VBM heights across each layer. The effect on

ΔE_Γ however is dependent on the local atomic positioning between the two layers. The nature of an incommensurate Moiré lattice is that it will, at some point, pass through all local configurations. By this logic, the vertical atomic alignment giving rise to the $\langle d_{z^2}|p_z\rangle$ interaction must occur within the structure. If this interaction is present anywhere in the system, it will represent the band with the highest energies at Γ.

Figure 4.6c and 4.6d show the effect of Moiré twisting and strain on ΔE_Γ. In spite of the changing strain on the systems, the change in ΔE_Γ is less than 0.02 eV. This change is a direct result of the strain of the components and not the angle twist. Hence, the Moiré lattice has no important effect on the band alignment rule for the minimal gap presented in Eqs. 4.4 and 4.5. However, a significant features that arises from the Moiré twisting is the band folding. Due to the reduced periodicity, the symmetry breaking bands become folded back across the Brillouin zone. This would mean for optical processes there would be more direct transitions. This could be observed through a reduction in thermalization during electro/photo luminescence.

In considering TMDC heterostructures, often strain is the first practical concern. These effects have been thoroughly explored over the last decade [109, 118, 145, 148, 149, 150, 151, 152], which provides a guide to incorporating the effects of strain into the above methodology. An effective tight binding model proposed by Pearce *et al.*[145] provided a fundamental description of how strain influences the electronic response at key points in the band structure. In addition, several groups have applied first principles techniques to explore the role of strain. Johari and Shenoy [149], in 2012, gave an exploration of lateral strain effects in MoX_2 and WX_2 (where X= S, Se, Te) using first principles. These results can be used to determine the bandgap changes of these constituents for strains of up to 10%. Rasmussen and Thygesen [151] provide details for in-plane strains of up to 2%, covering all feasible TMDC structures, which can be used to extract the bandgap behaviour.

The effects of strain have also been explored extensively by Kang and Kwon [153] computationally showing how the bandgap with the PBE approximation for differing values of strain for various TMDC sulphides and selenides (M= Mo, W, Ti, Cr, V, Nb, Ta, Hf, Zr) and show that the trends hold when considered using the GW method. Whilst experiment has shown that these structures can sustain higher strains than conventional materials [152] (up to 10%). However, heterostructures formed from 2D materials show much lower or no strain [117, 118, 119, 120, 121, 122], due to the weak interlayer interaction meaning that there is no pinning of adjacent layer positions. If one wishes to include the effects of strain in the theory discussed, then one could consider the results presented in the above works and use these to scale the band gap, and then apply the corrective terms, ΔE_{Γ} and ΔE_{IF}. In these cases, we expect that ΔE_{Γ} and ΔE_{IF} would be overestimates, but not sufficiently different to prevent a reasonable estimate of the band gap, which can be confirmed by comparison of our results with Lu *et al.* [154]. Our results have indicated that strains of less than 5% have minimal impact on the theory presented.

4.3.4 Discussion

Experimental evidence for ΔE_{Γ} and ΔE_{IF} relies on optical techniques, where one has to be careful to separate excitonic effects. However, recent measurements by Wu *et al.* [122] of WSe_2/WS_2 show that the heterostructure has a clear reduction in bandgap compared to the result expected from Anderson's rule. In their report it is suggested that this is an issue with the accuracy of their measurements, but we suggest here that the reduction is due to ΔE_{Γ}. Similarly, Aretouli *et al.* [119] report a miscellaneous reduction in the bandgap of $HfSe_2/MoSe_2$, which is evidence of the effect of ΔE_{Γ}. Indirect evidence of this is also observed in the exciton behaviour in heterostructures[155], as the effect of ΔE_{Γ} is to increase the energy of the valence band at Γ and thus decrease its effective mass, resulting in the exciton

lifetime increased. The case of MoS_2/WSe_2 is the most discussed case [117, 120, 121], however it is an unhelpful candidate for experimental comparison due to the predicted correction term being negligible (see Fig. 4.2a,c). This prediction is, however, consistent with experimental results, which would suggest for this particular pairing, Anderson's rule is obeyed [117].

The expressions Eq. 4.4 and Eq. 4.5 have interesting implications for TMDC heterostructures and for 2D materials in general. Firstly, the the effective mass (and transport properties) of the valence band depends on ΔE_Γ and hence on the interaction between layers. This factor will always increase the curvature (and thus mobility) of the valence band, and this provides a mechanism to enhance the transport characteristics of the heterostructure over the constituents. Conversely, the conduction band is almost identical (see Fig. 4.2) to the constituent that has the highest electron affinity.

The particular orbital overlap here is unique to H-TMDCs, but due to all orbital interactions following similar forms as Eq. 4.2, the shift from ΔE_Γ will be universal with values of λ and η_i changing, which implies that one could expect external pressure applied perpendicularly to create a pressure sensitive bandgap for all 2D heterostuctures, under the condition that this shift results in Eq. 4.3 being non-zero. The interaction in ΔE_Γ also clearly explains the transition between direct and indirect behaviour between TMDC monolayers and the bulk in terms of a simple analytically described interaction.

Type III 2D heterostructures offer an intriguing possibility compared to bulk heterostructures. Normally, when considering a heterostructure, one considers the system being in equilibrium with the bulk materials properties, forming a triangular well. In this case, as both layers are less than a nanometer thick, one can expect that one 2D layer will effectively have an empty valence band and the other will have a significantly filled conduction band. This would result in both layers being

metallic, but with electron and hole conduction localised to different layers.

4.4 Summary

In conclusion, we have demonstrated and explained the failure of Anderson's rule and how it can be corrected to more accurately predict 2D heterostructure bandgaps. We have shown that due to ΔE_{Γ} any constructed heterostructure is likely to exhibit an indirect bandgap and that the effective mass will always decrease. Furthermore we have provided expressions to give the band alignments in terms of the material properties of the constituents and their separation. The theory could be readily extended to other 2D heterostructures with some minor adjustments to ΔE_{Γ} and ΔE_{IF}. The approach presents a method which avoids the need for advanced calculation when estimating the properties of TMDC heterostructures. This expands the possibilities for exploring the optoelectronic properties of various heterostructures to the broader community.

Chapter 5

Thermal Attenuation In 2D Heterostructures

"We're all concerned about sustainable energy. If we could recycle waste heat to generate energy, we could use it for something useful."

— Mildred Dresselhaus

5.0.1 Introduction

Research interest in 2D materials has remained strong for over a decade, with work presented on topics ranging from superconductivity[156] through ultra-high[157] and ultra-low[158] thermal conductivity to exceptional photo-detection[109]. The promise of 2D materials is widely understood, however, much of the focus is on optoelectronic properties[49, 50, 110, 111, 112, 113, 114, 115, 116, 117, 118, 119, 120, 121, 122, 123]. Fewer published works focus on thermal properties but, those that do, tend to approach them from the thermoelectric perspective[159]. Fewer works, still, have investigated thermal transport in 2D heterostructures[141, 160].

Thermal management is of vital importance in most devices[11]. Computer processor units, in particular, face a high level thermal toll due to the scale of current transistor components[4]. In this context 2D layered materials are looked at, mostly, for their high conductivity but have potential advantages in both heat dissipation and thermal insulation[160, 161]. On the other hand heterostructures with low thermal conductivity have significant research potential in the field of thermoelectricity[158, 162, 163, 164, 165, 166]. Two dimensional materials have been a strong focus for thermoelectrics research following the innovative work of Dresselhaus *et al.*[54]. They demonstrated that 2D materials offer a method for enhancing the density of states and for increasing the electron mobility, thus, enhancing the Seebeck coefficient. Furthermore 2D materials offer a greater degree of phonon boundary scattering, than their 3D counterparts, reducing thermal conductivity. Both increasing the Seebeck coefficient and decreasing the thermal conductivity, have the effect of improving the thermoelectric efficiency[54].

The TMDCs have been extensively studied using both theoretical [88, 167, 168, 169, 170, 171] experimental methods [108, 158, 172, 173, 174, 175, 176, 177, 178, 179, 180, 181, 182]. The most studied TMDC is MoS_2 [172, 173, 174, 175, 176, 177, 178, 179]. Thermal conductivity measurements of MoS_2 range from 84 $WK^{-1}m^{-1}$ measured by the optothermal Raman technique[108] down to 24 $WK^{-1}m^{-1}$ measured by resistance thermometer micro-device at room temperature[172] with other measurements on differently grown samples lying between [178]. This wide range can be attributed to layer number, growth (CVD or exfoliation) and measurement technique. Aiyiti *et al.*[175] characterise both the crystalline and amorphous phase of MoS_2 and are accurately able to identify amorphous phase transition demonstrating the reliability of this study. The thermal conductivity is measured from ~ 30 to ~ 350 K with a room temperature value of 34 $WK^{-1}m^{-1}$. The work of Chang *et al.*[180] is a study not focused on MoS_2. Instead it is focused on SnS_2 for thermoelectric applications. A room temperature thermal conductivity of 3.6 $WK^{-1}m^{-1}$

is derived using the laser flash method. They conclude that despite the low thermal conductivity SnS_2 shows poor thermoelectric properties due to low electrical conductivity.

Theoretical approaches, to thermal conductivity, have solved the Boltzmann transport equation, incorporating three phonon[167, 168, 171] and discussing four phonon contributions[88], while other studies rely on isotope[170] or boundary scattering[169] only. These theoretical studies support the the evidence that all explored TMDCs exist in the anharmonic regime at room temperature. Glebko *et al.*[171] obtain thermal conductivities for TiS_2, ZrS_2 and HfS_2 by solving the phonon Boltzmann transport equation with three phonon and boundary scattering. They calculate the mode-dependent Grüneisen parameters directly from the third-order force constants. Their calculations for TiS_2 thermal conductivity give a room temperature value of 6.1 $WK^{-1}m^{-1}$ fitting neatly within the experimental range, 4.5 $WK^{-1}m^{-1}$[181] to 6.4 $WK^{-1}m^{-1}$[182]. While the reported studies have investigated the thermal properties of individual TMDCs, the majority of their heterostructures, presented here, remain unexplored.

If one fabricates a van der Waals (vdW) heterostructure the lattice mismatch induces strain (be it local or homogenous), which influences the local harmonic potential present, which in turn effectively changes the forces between atoms. This effect changes the phonon dispersion relations and this in turn changes the thermal properties of the heterostructure. Furthermore a vdW heterostructure can be influenced by their relative angle and by stacking sequence, with effects such as those observed in graphene[183, 184]. The great appeal of 2D vdW heterostructures lies with the potential to develop, novel emergent material properties, that go beyond either of the constituents.

Recent work by Zhang *et al.*[185] using classical molecular dynamics on 2D heterostructures has shown that the in-plain thermal conductivity has, approxi-

mately, the average value of the two constituent materials. At room temperature the heterostructure has a thermal conductivity of 24.8 $WK^{-1}m^{-1}$, while the two constituents, MoS_2 and $MoSe_2$ have 32.9 and 24.8 $WK^{-1}m^{-1}$, respectively. Investigations on graphene substrates[186] show the thermal conductivity is not the average. In this report, Zhang *et al.* demonstrate the conductivity changes with stacking order with the variance in results being $\sim 9\%$ for a sample length of 400 nm. This in turn demonstrates a significant interlayer coupling effect. Lastly Ma *et al.*[187] performed conductivity calculations using a Boltzmann transport equation (LBTE) methodology for a single heterobilayer of $MoS_2/MoSe_2$ and found similar results to Zhang *et al.*[185]. It is noted that a recent review has stated that high convergence is necessary to be sure 1st principle results are accurate, and these results have yet to be verified (theoretically or experimentally)[188]

In this work, we will develop a quasi-anharmonic model of thermal transport based on *ab initio* first principles results. This theory will be applied to the transition metal dichalcogenides (TMDCs) and, where possible, to heterostructures of those same constituent materials. The phonon dispersion relations for the heterostructures are reviewed and compared to their constituents. From these dispersion relations, we present the heat capacities of these systems and discuss the connection between the heterostructures and their constituents. From this, we then present results for the thermal conductivities. We explore the role of various scattering mechanisms and how these affect the constituents and their heterostructures appropriately. Lastly we will use our quasi-anharmonic model to calculate the thermal conductivity for homostructures and heterostructures and compare their relative values against temperature.

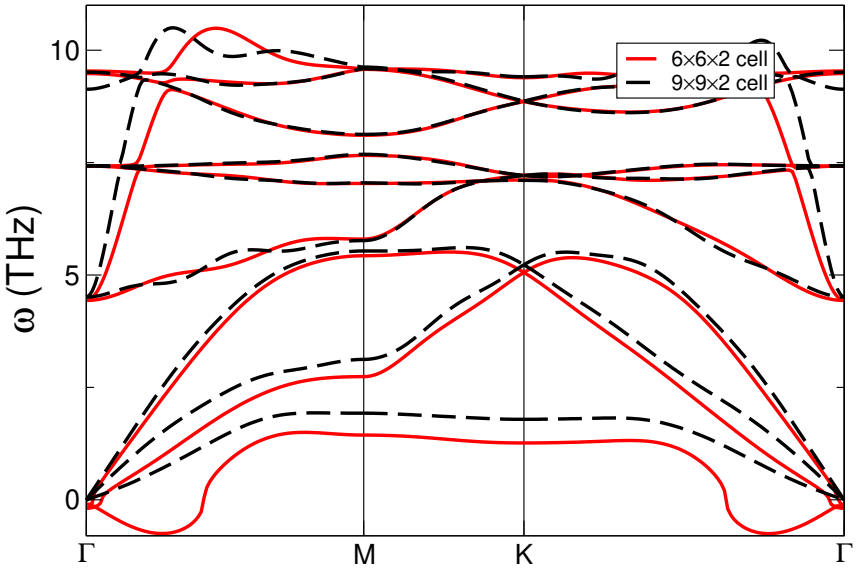

Figure 5.1. A demonstration of spurious instability in 2D materials. Figure shows the phonon bandstructure of ZrS_2 computed with a 6×6×2 (red solid line) and with a 9×9×2 supercell.

5.1 Methodology

5.1.1 *ab initio* calculation

We calculate the thermal properties of TMDCs bulks and their superlattices. To do this, we employ density functional theory (DFT) as implemented in the Vienna *ab initio* simulation package (VASP)[138]. We use the PBE [77] functional with VASP library of PAW pseudopotentials [136] and Grimme-D3 [137] vdW correction. All systems were geometrically relaxed to within phonon accuracy, with forces lower that 10^{-3} eV/Å for each atom and an energy cutoff of 700 eV. Phonons were calculated using the frozen phonon method, as implemented in phonopy[62]. All structures are modelled in the TMDC T-phase, with the exception of MoS_2. MoS_2 is considered in both the T and H phases. We consider five TMDC systems, MoS_2, HfS_2, SnS_2, $SnSe_2$ and ZrS_2. These constituent materials are calculated with supercells sufficient to prevent spurious negatives in the long wavelength limit of the ZA mode, which can be expected to be significant in thermal conductivity calculations. The existence of spurious negative frequencies in the ZA mode of 2D materials is a recognised

phenomena[188, 189] caused by convergence criteria and other issues. Here, we show that these can be overcome by considering larger supercells, as seen from figure 5.1, which shows that imaginary frequencies in the ZA mode can be prevented from occurring in the calculation by increasing the supercell size. Other than MoS_2 and ZrS_2, which required supercells of $3 \times 3 \times 1$ and $9 \times 9 \times 2$ respectively, a supercell of $6 \times 6 \times 2$ was found to be sufficient. All thermal properties calculation used a Monkhorst-Pack grid [91] equivalent to at least 864 ($12 \times 12 \times 6$) k-points per primitive cell with the exception of ZrS_2 which has an equivalent 164 ($9 \times 9 \times 2$) k-points per primitive cell. All heterostructures use a $2 \times 2 \times 6$ k-point mesh regardless of supercell size.

Thermal conductivity calculations are performed for the heterostructures of HfS_2/SnS_2, $HfS_2/SnSe_2$, HfS_2/ZrS_2, $SnS_2/SnSe_2$, SnS_2/ZrS_2, MoS_2/HfS_2, MoS_2/SnS_2 and lastly MoS_2/ZrS_2. We also calculated the phonon dispersion relations of $MoS_2/SnSe_2$ and $SnSe_2/ZrS_2$ and found that these systems were unstable (i.e. possessed imaginary phonon modes) within the limits of our computational resources. Five of the heterostructures are calculated with a 1-to-1 cell matching in the T phase; HfS_2/SnS_2, $HfS_2/SnSe_2$, HfS_2/ZrS_2, $SnS_2/SnSe_2$ and SnS_2/ZrS_2. Of these five HfS_2/SnS_2 and $HfS_2/SnSe_2$ used a supercell for phonon calculations of $6 \times 6 \times 1$ while the others used $6 \times 6 \times 2$ providing the equivalent of 36 q-points and 72 q-points per constituent cell respectively. Thermal conductivity calculations are performed on an interpolated $9 \times 9 \times 9$ q-point mesh.

To generate Moiré structures we used the ARTEMIS[139] package (see chapter 6). Three heterostructures require a lattice matched Moiré structure to be phonon stable. A lattice matching of 10 MoS_2 to 9 HfS_2 is used to make the MoS_2/HfS_2 heterostructure and 4 MoS_2 cells to 3 SnS_2 and 3 ZrS_2 cells to form MoS_2/SnS_2 and MoS_2/ZrS_2 heterostructures respectively. These are shown in Fig. 5.2. When taking into account the Moiré rotations, each of these materials has an effective supercell consisting of 36 ($6 \times 6 \times 1$) constituent primitive cells for phonon cal-

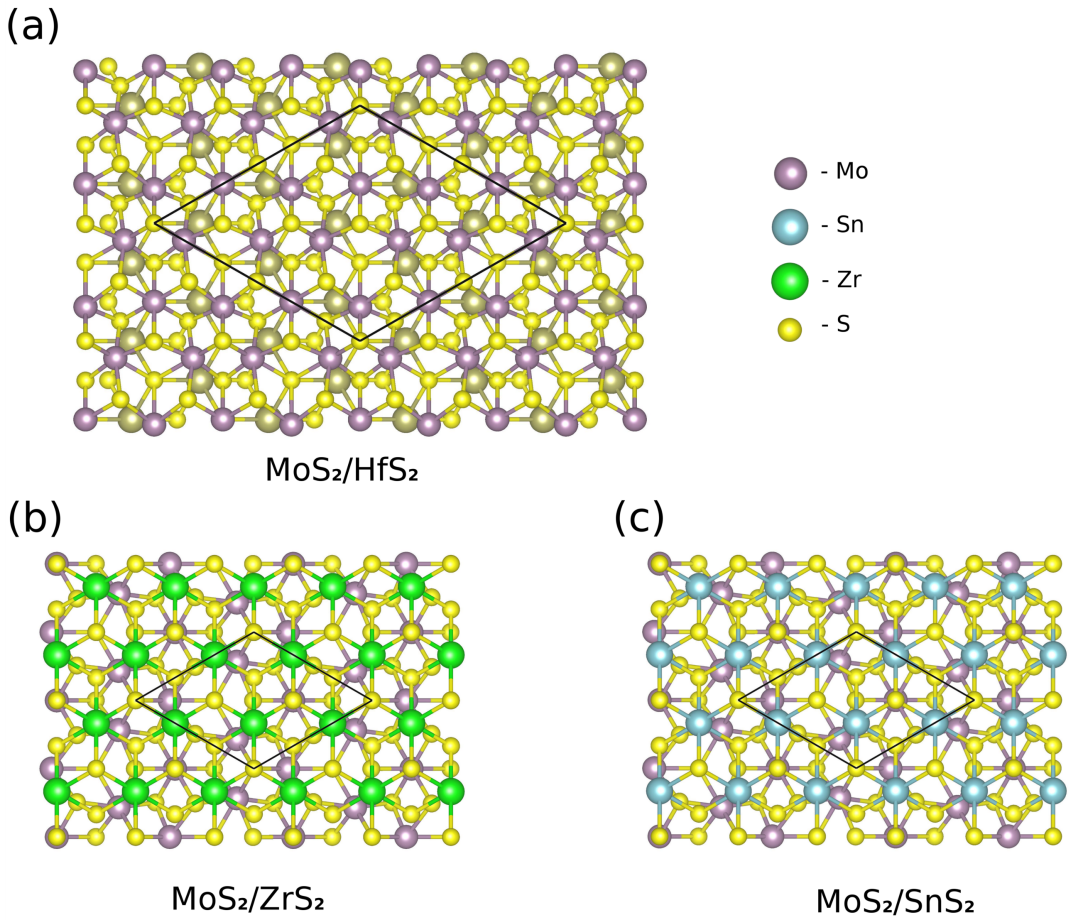

Figure 5.2. (a) Shows the Moiré lattice matching between 10 MoS_2 primitive cells and 9 HfS_2 primitive cells, along side a legend denoting the different atomic species. (b) Shows the 4 to 3 primitive cell matching between MoS_2 and ZrS_2, and (c) shows the 4 to 3 primitive cell matching between MoS_2 and SnS_2.

culations. Thermal conductivity calculations are performed on interpolated q-point meshes which give greater than or equal to 729 q-points per constituent primitive cell.

Previously, we have discussed how instabilities due to supercell limitaions can be normally overcome using a larger unit cell. However, for larger systems such as these, this is not currently possible with current computational resources. To alleviate this issue, one can consider both the continuum model and the diatomic linear chain[84], which both show that the acoustic branch is dominated by the heavy component of a two mass (density) system. Specifically for the Moiré heterostructure MoS_2/SnS_2, one requires a supercell that is considerably larger than the previously discussed supercells in order to compute the phonons. However, based on the insight from the previous models, we show that a reasonable agreement comes from using the acoustic branch of the heavier of the two constituents (which is demonstrated in Fig.5.3 for the HfS_2/SnS_2 and $SnS_2/SnSe_2$ heterostructure and its constituents). This allows us to replace the the lowest mode of MoS_2/SnS_2 with the ZA mode of SnS_2 when calculating the thermal conductivity and allows us to consider far larger cells thermal conductivity than had been previously considered possible.

5.1.2 Thermal conductivity calculations

The theory of the thermal conductivity and how it is calculated is outlined in Chapter 3. Here, we provide a brief discussion of the computational considerations for calculating the thermal conductivity. The first question one might examine when calculating thermal conductivity (particularly anharmonic contributions) is why we have not followed a parameterless fit, following the ideas suggested by Togo *et al*[64]. Whilst many approaches for high temperatures now rely on the parameterless 3-phonon calculations from first principles, here this is not possible due to the large interaction space (i.e. the multiple phonon branch interactions that one needs to

consider in superlattice and Moire structures) which are beyond current computational limits. Furthermore, such an approach would not be guaranteed to succeed as systems which possess phase transformations (such as H to T for MoS_2[190]) cannot be simply treated within the realms of most frozen phonon approaches [191]. As such, we adopt an approach which allows us to examine these systems based upon the principle of only fitting three parameters for the constituents, namely, l (see eq. (3.4)), g (see eq.3.28) and γ (see eq (3.59)). These parameters are fitted to the experimental data using a least squares method. As can be seen, the results of these parameter fits are within reason for a real sample, and provide guidance as to the choice of parameters for the heterostructure. We consider two different parameterisations for each heterostructures. The first result is highly conservative and based on the principle of taking the parameters which would indicate the highest conductivity. i,e. the least amount of scattering. This ideally provides an upper bound to our calculations. The second is based upon the average of the two materials' parameters following an normalised approach.

Basic physical principles were followed in order to fit the parameters for the conductivity of the constituents. Wherever possible the scattering boundary length, l, was assigned from experimental measurements (this is the case for MoS_2, from Aiyiti *et al.*[175]). When this was not possible, l was constrained to an experimental range i.e. SnS_2 was constrained to grain size measurements 8×10^{-8} and 4×10^{-5} from Chang *et al.*[180]. To set the Grüneisen parameter (eq. 3.59) the fitting was constrained such that its value must be greater than zero and less than one. Similar constraints were placed on the the mass defect scaling parameter, which was held between 1 and 10.

The parameters used to model each constituent are detailed in table 5.1. For 2H-MoS_2 the scattering length , l, is set from experimental measurements, while both g and γ are fitted to Aiyiti *et al.*[175]. The constituent materials SnS_2 and $SnSe_2$ are highly similar and hence can be expected to have the same parameters

	2H-MoS_2	SnS_2	$SnSe_2$	HfS_2	ZrS_2
l=	3.00×10^{-6}	2.12×10^{-7}	2.12×10^{-7}	2.11×10^{-6}	1.13×10^{-6}
g=	7.52	1.00	1.00	0.00	0.00
γ=	8.04×10^{-2}	7.34×10^{-1}	7.34×10^{-1}	4.17×10^{-1}	5.61×10^{-1}

Table 5.1. The parameterisation for each constituent. l is the scattering length, g is the mass defect scaling parameter and γ is the Grüneisen constant. MoS_2 is fitted to Aiyiti *et al.*[175], SnS_2 and $SnSe_2$ are fitted to Chang *et al.*[180], while both HfS_2 and ZrS_2 are fitted to theoretical data from Glebko *et al.*[171].

to close approximation. The data SnS_2 is fitted to is from Chang *et al.*[180]. Both HfS_2 and ZrS_2 are fitted to theoretical data from Glebko *et al.*[171]. Following the method of Glebko we set the isotope scattering to zero for these materials.

5.2 Results

5.2.1 Phonon bandstructures

Figure 5.3 shows the phonon band structure of HfS_2, SnS_2, and HfS_2/SnS_2 (a) and SnS_2, $SnSe_2$ and $SnS_2/SnSe_2$ (b). Due to the weak interaction of the van der waal force, the overlay shows the phonon modes of the heterostructure appear highly similar to those of the constituents[107]. As can be seen from the Figure, the constituents (shwon in red and blue) possess the standard LA (longitudinal acoustic), TA (transverse acoustic)and the ZA (z-axis transverse acoustic) q^2-like mode expected in 2D materials. The heterostructure shows these same modes, with an additional set of low-lying optical modes that closely map onto the acoustic modes of the lower mass constituent (except near Γ). A linear scaling effect can be observed in the heterostructure frequencies, most notably in $SnS_2/SnSe_2$. This linear effect can be attributed to the strain interaction adjusting the lattice constant of the constituent layers. The acoustic group velocities are similarly scaled by this effect.

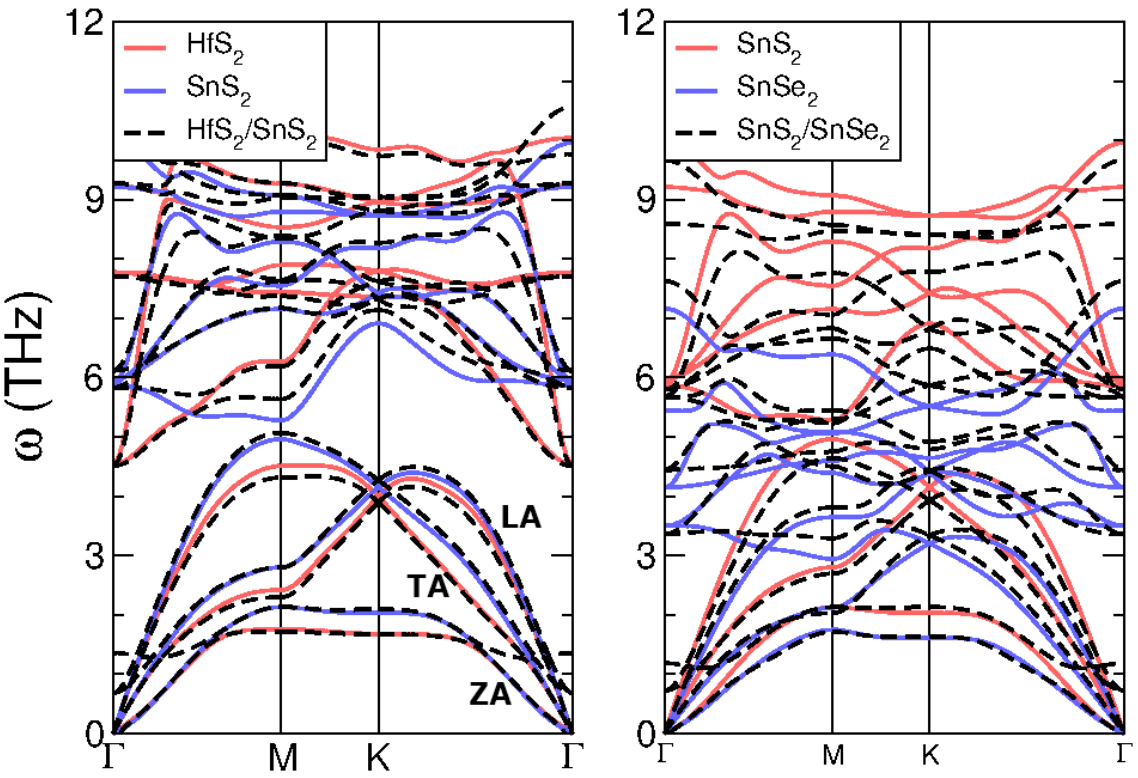

Figure 5.3. The coloured lines (red & blue) denoting the constituent bands, display the standard LA (longitudinal acoustic, steepest mode), TA (transverse acoustic, middle mode)and the ZA (z-axis transverse acoustic, shallowest mode) q^2-like mode expected in 2D materials.

For most bulk systems, the acoustic modes which are expected to most contribute to the thermal conductivity, especially at low temperature. As expected, the heterostructure phonon dispersion relations also present the LA, TA and ZA modes. At the zone center three acoustic modes of the constituents generally overlay with the six acoustic/pseudo-acoustic modes of the heterostructure. Close the Γ-point (before the pseudo-acoustic modes are present) the true acoustic modes follow the constituent with the greater mass density. The origin of the three pseudo-acoustic modes come from the weak interaction between the different material layers. A unit cell can only support three true acoustic modes, each associated with the uniform vibration of atoms in the three principle directions. For there to be more than three acoustic modes it would require the oscillation of atoms in different layers to be completely uncoupled. The examples shown in figure 5.3 exhibit weak coupling and therefor show only three acoustic-like bands near Γ and six away from the zone center. Near the zone edge the heterostructure bands overlay those of both of the constituents. The higher optical modes are more distorted than the lower modes. This distortion is a result of the constituents adopting a matching lattice, which results in a strain. The amount of distortion of the heterostructure optical modes compared to the constituents hence increases with increasing frequency.

Our calculations showed the 1T MoS2 TMDC possessed imaginary phonon modes and was unstable. However, when 1T-MoS2 is combined with other TMDC layers, it forms a stable (no imaginary) phonon band structure. This result cannot be explained simply as a result of the strain on the system as an equivalently strained 1T-MoS_2 system still possesses imaginary modes. Similarly, we found that heterostructures made from $MoS_2/SnSe_2$ and $SnSe_2/ZrS_2$ were phonon unstable, despite the constituents possessing no imaginary modes. Enlarged supercells of up to 5×5 where used to confirm this instability.

5.2.2 Specific heat

We have calculated the specific heat capacity due to phonon modes as a function of temperature for the TMDC constituents (MoS2, HfS2, SnS2, SnSe2 and ZrS2) and their heterostructures (where stable). Figure 5.4 shows the specific heat capacity as a function of temperature for each heterostructure and its constituents. As expected these systems all tend to the Debye limit and the heat capacity is the average of the two constituents. The heat capacity varies as T^2 for these two dimensional materials, as one would expect from a simple analysis of a 2D continuum phonon model. In addition, at high temperatures they tend to the Dulong Petit (or free particle) model.

The implications of the specific heat capacity results for the thermal conductivity are two fold: (i) the thermal conductivity of the system would be the average of the two bulk materials if the scattering rate is constant, and (ii) the thermal conductivity at low temperatures can be expected to vary as T^2.

5.3 Thermal Conductivity

The thermal conductivity of the heterostructures and their constituents is first calculated and discussed for the MoS_2/SnS_2 superlattice. The results of our calculations and the fit of the constituents to experiment are shown in figure. 5.5. The experimental data used to model MoS_2 was taken from Aiyiti *et al.*[175] while the data used to model SnS_2 was taken from Chang *et al.*[180]. Our results indicate good agreement with experiment and show a drop in the thermal conductivity of the superlattice compared to the constituents. They also show the expected T^2 dependence for the conductivity at low temperatures and the $1/T$ dependence at high temperatures. Our results indicate a small amount of defect scattering in the two constituents and a Grüneisen parameter of 0.0804 and 0.734 for MoS_2 and SnS_2 respectively, which

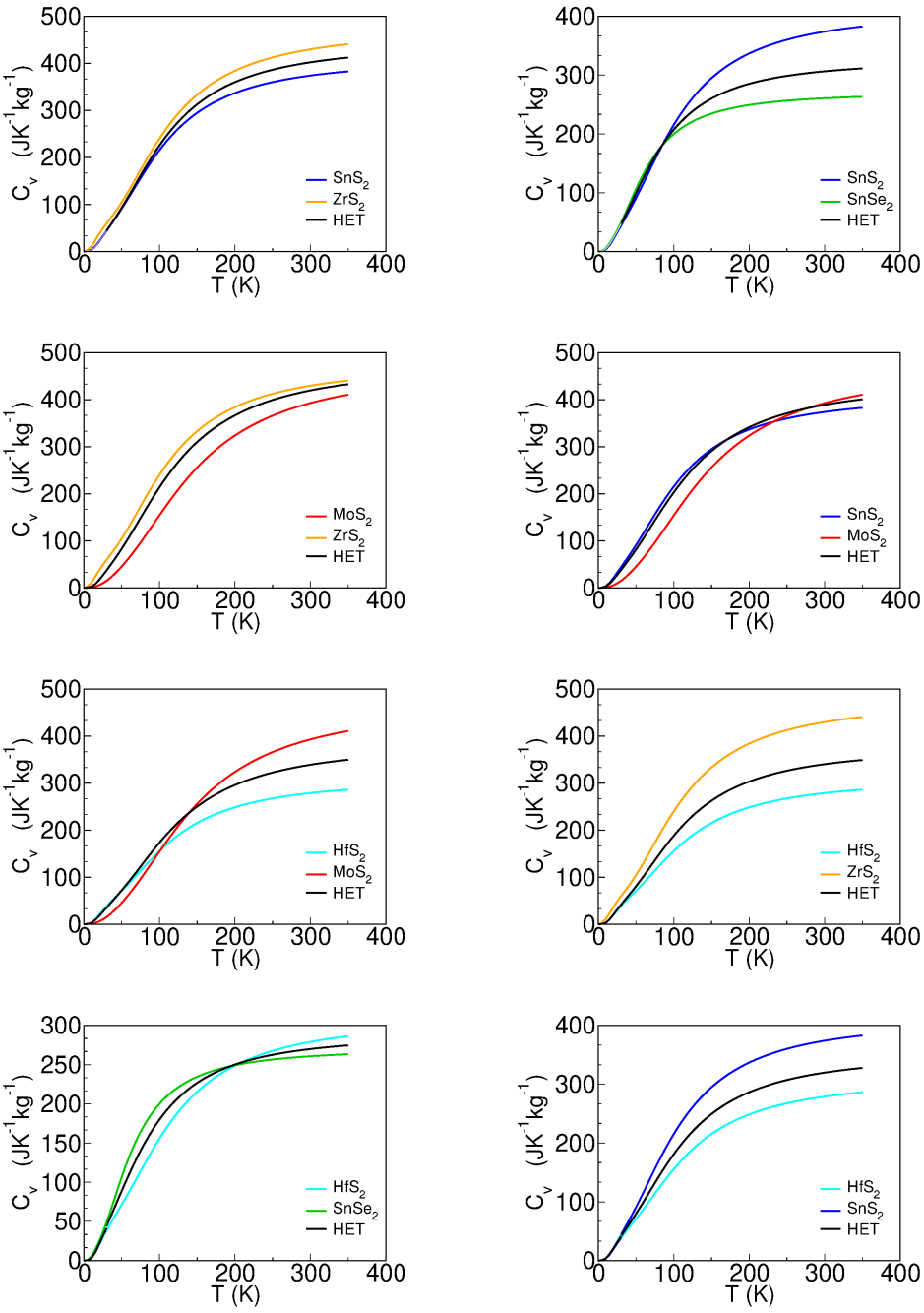

Figure 5.4. The specific heat capacity curves of heterostructures (Black lines) shown relative to their constituent layers specific heat capacity curves (coloured lines).

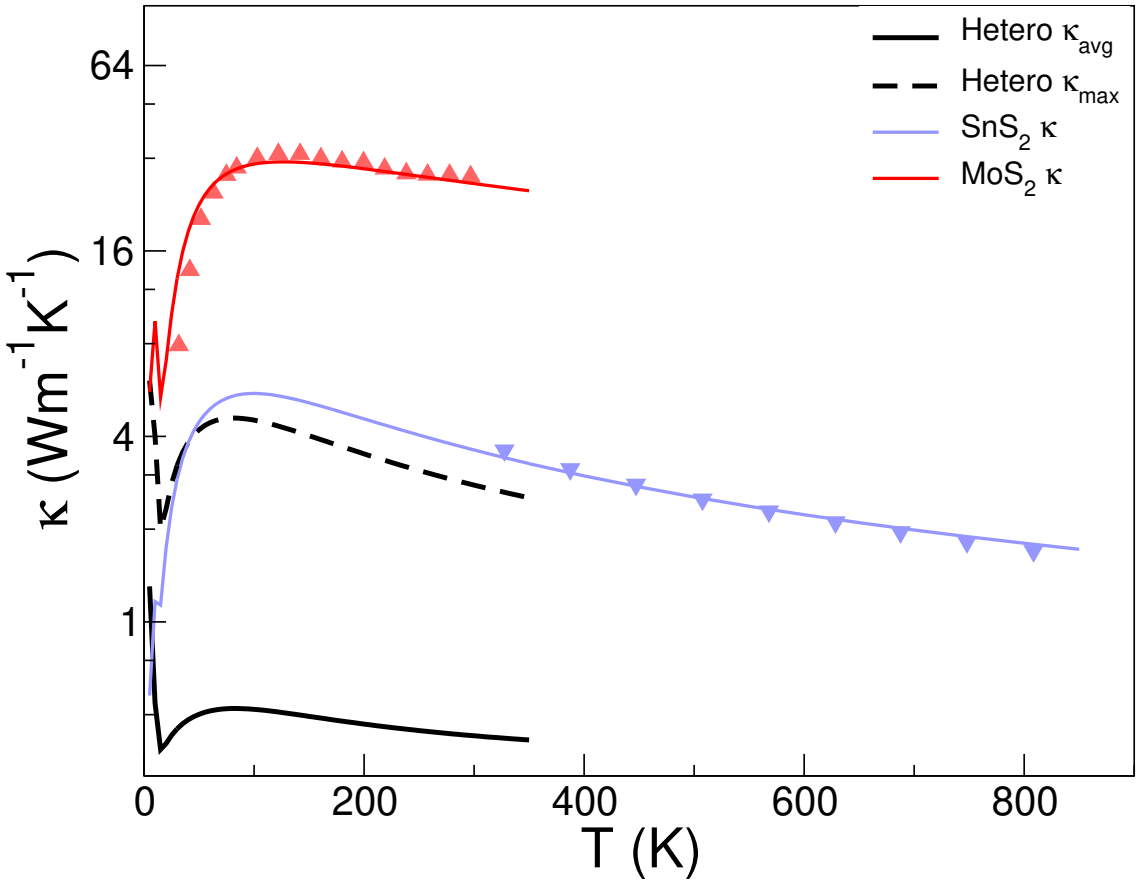

Figure 5.5. In plane thermal conductivity plots for SnS_2 (solid blue line) and 2H-MoS_2 (solid red line) are plotted against there experimental data sets. 2H-MoS_2 exp. data from Aiyiti *et al.*[175] is plotted in red triangles and SnS_2 exp. data from Chang *et al.*[180] is plotted in inverted blue triangles. The figure also shows the maximum prediction for the 1T-MoS_2/1T-SnS_2 heterostructure thermal conductivity (dashed black) and average prediction (solid black).

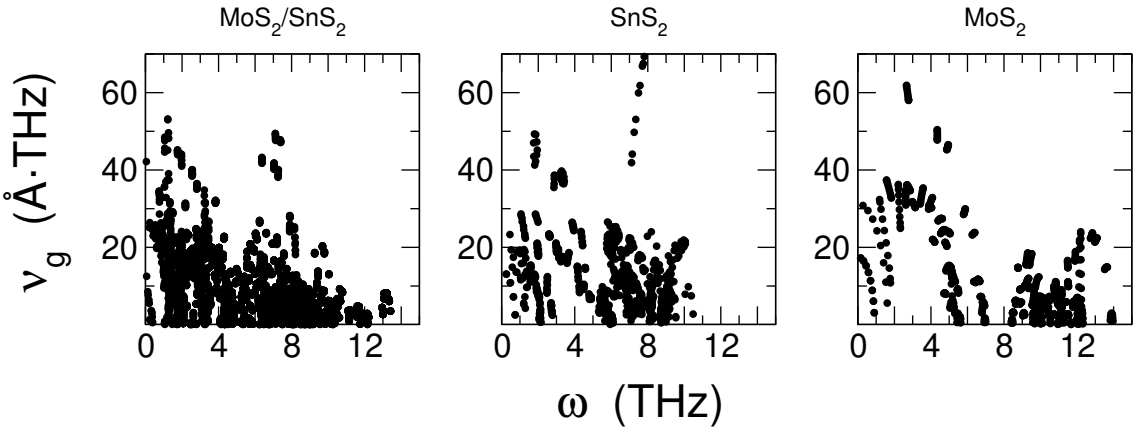

Figure 5.6. The frequency group velocity graphs for the heterostructure, MoS_2/SnS_2 (Left), and it's two constituents, SnS_2 (Middle) and MoS_2 (Right). The heterostructure shows a small reduction in group velocities compared to it's two constituents.

fits within the physical values one would expect for this constant. The two fits for the heterostructures show that our conservative "least scattering" approach still has a lower thermal conductivity than the constituents. This drop in thermal conductivity originates from increased number of allowed phonon transitions. The out of plane component of the wave-vector results in little change in the dispersion, this means that several allowed phonon transitions (see Eq. 3.59) for 3-phonon scattering are possible, resulting in a substantially higher scattering rate. Whilst the group velocity of these modes are lower, this change is very minor, especially at low frequencies which dominate thermal transport, as can be seen in figure 5.6. The "least scattering" approach does not meet the constituent conductivity, to increase the thermal conductivity of the heterostructure to that of the bulk constituents would required a parameter fit with exceptionally low Grüneisen parameter or a lower scattering rate from mass defects than the minimum associated from isotope scattering.

In comparison to other methods of thermal conductivity reduction the heterostructuring is very competitive. Alloying is another, more traditional, method for reducing the thermal conductivity that has been explored in TMDC structures[192]. It is found that for an alloy of MoS_2 and $MoSe_2$ the maximum thermal conductivity reduction is 6.64 times. This value is well within the range of thermal conductivity

reduction shown in (at 100 K) in figure 5.7. The largest and smallest reductions are 39.13 and 3.866 times, respectively. The unique electrical properties provided by heterostructuring make this approach highly attractive for future consideration.

The data in figures 5.5 and 5.7 show anomalies in the conductivity at low temperature. Our corrections at the Brillouin zone edge offer improvements but are not granular enough to facilitate the accurate modeling of scattering at extremely low temperatures outside of the intended range of the code. By correcting the group velocity we improve the overall scattering rates. At very low temperatures scattering can become under estimated due to the fact that very few q-points are contributing to the calculation. This can result in thermal transport being dominated by lowest zone center q-point at temperatures below $\sim$ 10 Kelvin. Such errors are best accounted for by increasing the density of q-points evaluated in the calculation.

Normally artificially low scattering will occur due to the corrections in 1 q-point in $9 \times 9 \times 9$ (729) q-points. This however will also allow these modes to carry heat at higher temperatures when boundary scattering not the primary scattering mechanism controlling thermal conductivity. For this reason we restrict all of our comments and analysis to the region above 30 Kelvin.

The thermal conductivity of eight heterostructures and their constituents (MoS_2, SnS_2, $SnSe_2$, HfS_2 and ZrS_2) are calculated as a function of temperature. These results are presented in Fig. 5.7. As noted for MoS_2/SnS_2, these superlattices all show a reduced thermal conductivity as a function of temperature when compared to their bulks. The most surprising of these superlattices is the $SnS_2/SnSe_2$ superlattice. However, due to the difference in the S and Se atomic masses, this results in several additional phonon branches (see Fig. 5.3) as well as the low-lying optical branches, which considerably enhance the scattering rate. This trend holds for all heterostructures investigated. We note that our results show the least promise for MoS_2/SnS_2 and $HfS_2/SnSe_2$,as our estimate for the highest thermal conductivity of

the superlattice closely approaches the lower of the two constituents. However, most promisingly, for thermoelectric and thermal management applications, MoS_2/ZrS_2 and HfS_2/MoS_2,show a significant reduction in the thermal conductivity. The conductivity for constituents SnS_2 and $SnSe_2$ represent an interesting case since both use the same parameter set. The TMDCs SnS_2 and $SnSe_2$ have a crossing in there conductivity demonstrating the importance of bandstructure over parameterization in determining the conductivity. In this case $SnSe_2$ has a reduced boundary scattering at low temperature due to reduced group velocity, however, the more clustered bands, with many overlapping acoustic and optical modes, drastically increase the three phonon scattering at high temperature. This leads to the conductivity curves observed in Fig. 5.7 with $SnSe_2$ being greater at lower temperature and SnS_2 becoming greater as temperature increases.

The drop in the thermal conductivity in superlattices of TMDCs is supported by previous studies into superlattice results. As noted for Si/Ge superlattices [193] the drop in thermal conductivity due to increased phonon interaction space is to be expected. Furthermore, phonon scattering rates are shown to be the driving mechanism behind the reduced thermal conductivity, since the specific heat capacities are shown to adopt an approximate average of the two constituents. Similarly, the phonon velocity reduction due to phononic gaps results in only a small decrease [167] in the thermal conductivity. In addition, in this consideration, no additional scattering mechanisms were considered to include interfaces scattering [84, 193]. such scattering mechanisms, would result in a further decrease in the thermal conductivity, resulting in a higher performance for applications (such as thermoelectrics) where low thermal conductivity is key.

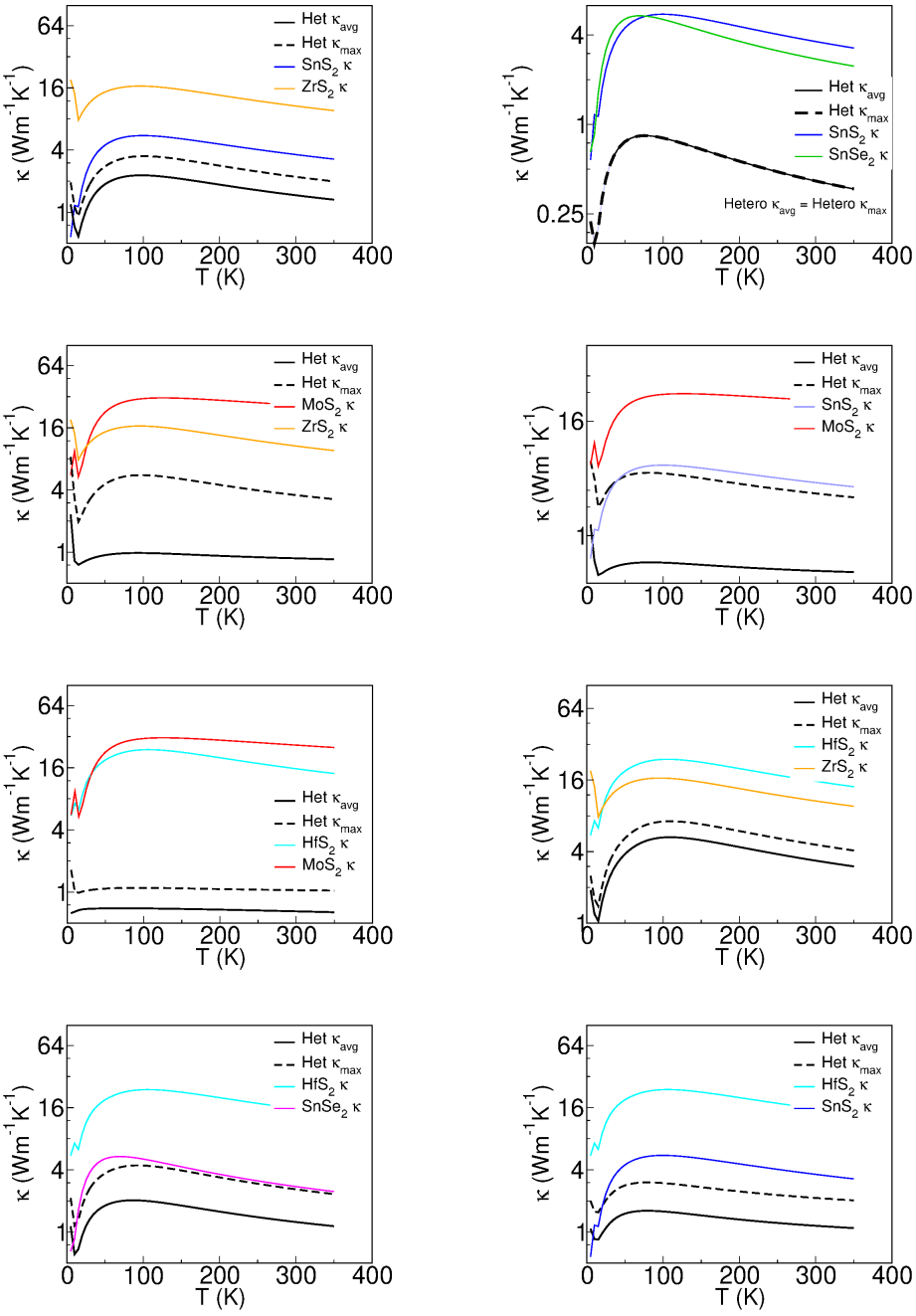

Figure 5.7. In plane thermal conductivity plots for constituents (solid coloured lines) and there heterostructure (black lines). Both the maximum prediction (dashed black) and average prediction (solid black) for the heterostructure are plotted.

5.4 Summary

In conclusion we have shown that the thermal conductivity of a TMDC heterostructure will (almost always) be lower than either constituent. Whilst this result agrees with previous results for superlattice systems, the already ultralow thermal conductivity of TMDCs due their layered character makes these systems very exciting for thermoelectric applications. By being conservative with our parameter fitting, we have shown that for a wide range of possible conductivities these superlattices will possess low thermal conductivity, even in the least optimal case. We define a region of thermal conductivities using generous parameter allocation to define maximum conductivity values. This approach significantly improves the confidence in our conclusions. This therefore provides a route for artificially reducing heat flow in 2D layered materials. Such advancements are highly attractive for 2D thermoelectrics applications, where careful application of band alignments can simultaneously enhance electrical conductivity [194] and reduce thermal conductivity.

Chapter 6

ARTEMIS

"God made the bulk, the surface was invented by the devil"

— W. Pauli [195]

"Interface is the device"

— H. Kroemer [196]

6.1 Introduction

Heterostructures and metal-semiconductor interfaces display several unique features, such as Andersons- and Schottky-like band alignment [129, 194, 197, 198, 199, 200, 201], thermal barrier effects [96, 202, 203], atomic reconstructions [204, 205, 206, 207], and nanometer scale metamaterials [193, 208]. The modelling of these features is generally based upon atomic scale approaches, which require an accurate interface structure, or a close approximation, such that atomic simulations can find the ground state. However, the complexity of the interface is vast, due to the issues of lattice matching, surface termination, intermixing, the large size of the unit cells, poor initial guesses and reaction kinetics, which can be further hindered by unintended

human biases. The electronic properties are sometimes considered using Anderson's rule, but atomic scale physics and measurements has shown repeatedly that this rule is invalid [209, 210, 211] and hence to accurately predict the band alignment requires the interface structure. Similarly, thermal boundary resistance is governed by the structure and make up of the interface [96, 202]. Thus the need for an accurate atomic structure is high. In addition, interfaces can yield unique physical phenomena such as quantum wells, new material phases [212, 213, 214, 215] and conductivity between insulators [16, 17, 216], all of which require accurate modelling. All these issues are compounded by the fact that experimental characterisation of an interface is exceptionally difficult. The best characterisations such as Transmission Electron Microscopy [217, 218], X-ray-diffraction [219, 220] , and others [221, 222, 223] can only provide hints as to the structure, the range of intermixing, and which surface reconstruction formed the interface.

The last 40 years has seen significant interest in methods to define, identify and consider the properties of interfaces and, in particular, for examining and calculating the most favourable interface between two materials. Starting in 1984, Zur *et al.* [224] presented a method of lattice matching that lay the foundation for subsequent methods [225, 226, 227, 228]. Raclariu *et al.* [225] implemented Zur's method for lattice matching, and applied a nearest neighbour method to estimate the optimum position of the two materials with respect to each other. Mathew *et al.* [226] developed a series of scripts with capabilities to predict the structure of surface structures according to Wulff construction, and also match interfaces using Zur's lattice matching algorithm. Daniele and Jelver *et al.* [227, 228] implement the method by Zur and extend it by introduction the elastic tensors of the two individual crystals in order to determine the energy cost of performing a lattice match. Whilst these methodologies involve lattice matching, little focus is placed on the surface stoichiometry the materials at this interface and the potential fo diffusion of the two materials across the interface.

Another approach to interface prediction involves random structure searches [229, 230]. The methodology involves generating an interface and randomly moving the atoms within a region around the interface; the generated structures are then modelled using first-principles methods in order to determine the most energetically favourable configuration. However, this process has, thus far, been limited to grain boundaries of a single material, simplying circumventing the need for lattice matching. The use of this method is to model diffusion of materials across the interface, which cannot be captured by first-principles relaxation methods alone (due to the large energy barriers involved in relaxing such a system).

There has been little focus on joining these two approaches of lattice matching and random-structure generation, mainly due to the significant number of systems that one would need to explore before finding the true interface for a pair of materials. The software package presented here attempts to go beyond the previous methods by fully exploring the surface stoichiometry of slabs, developing a method to more accurately predict the optimum position of two materials with respect to each other, and developing a methodology for investigating diffusion alongside the lattice matching method.

ARTEMIS is a software package designed to produce a set of interface structures between two bulk materials. From these interfaces, one can then use either empirical or *ab initio* software to refine the structure, rank the stability of the various potential interfaces by energy, and then calculate the desired properties. The workflow for producing the interface structures follows a logical progression allowing the user to modify settings as they wish. ARTEMIS estimates the optimum interface separation and includes the capability to both shift and intermix interfaces. In addition, the software allows the user to submit existing interface structures and use the software for both post processing and further reconstructions/interface generation. These tools aid in a more thorough exploration of the interface and thus reduces human bias. The software is being continuously developed and the latest

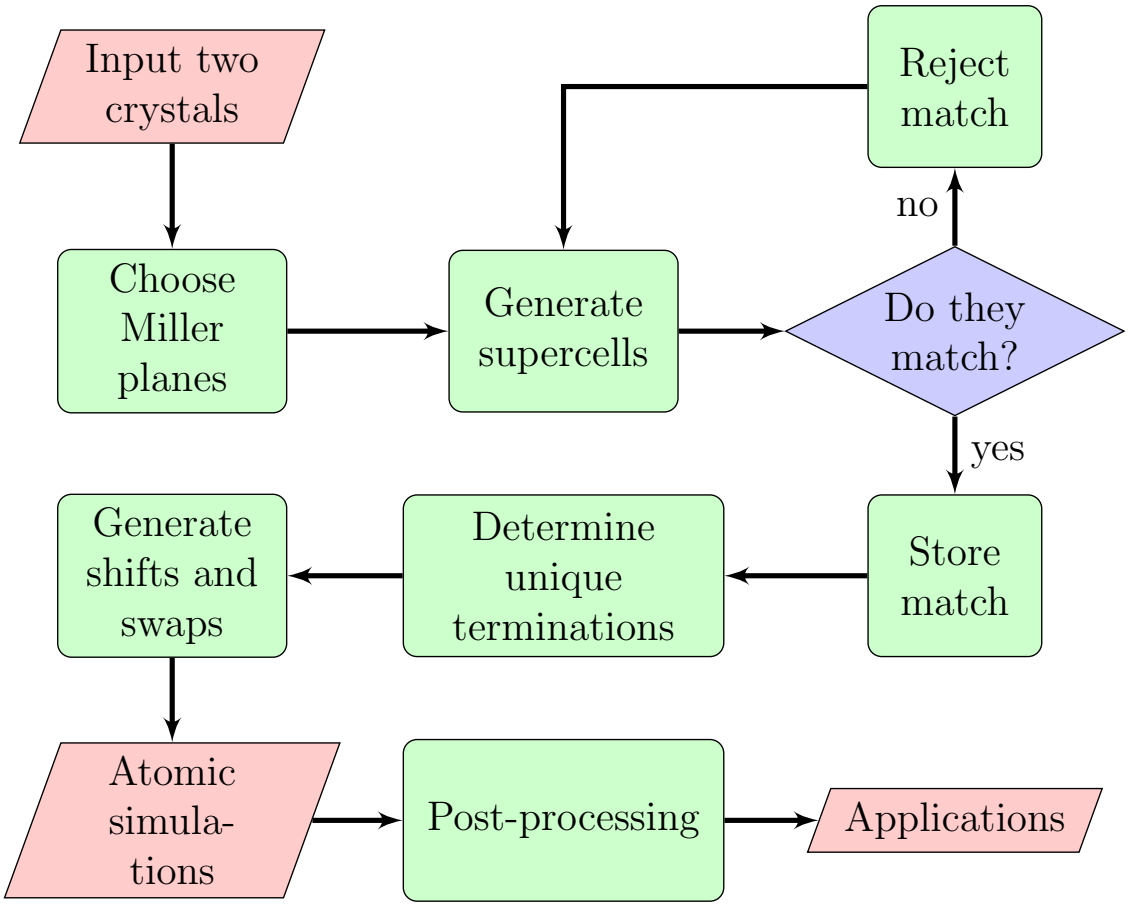

Figure 6.1. An overview of the workflow process of ARTEMIS, outlining its key stages.

version can be obtained from `http://www.artemis-materials.co.uk/`.

6.2 ARTEMIS: overview

The ARTEMIS software package generates interfaces as outlined in Figure 6.1. It takes two parents crystals and then considers a set of Miller planes over which to search for matches. On each plane, it generates supercells for both materials and determines whether they match each other, as detailed in Section 6.2.1. When successful matches are found, unique terminations of those Miller planes are used to generate interfaces. The two slabs of materials are then shifted (displaced) with respect to each other, both parallel and perpendicular to the interface, and in the

process, a set of shifted interface structures are generated. Output structure files are then written for each configuration for use in atomic simulation software packages. The software also has the option to take in pregenerated interface structures and perform further shifts or intermixings on them.

The ARTEMIS software package is written in Fortran, using a set of default Fortran functions and in-house developed functions and subroutines and is developed to read and output in the Quantum Espresso, CASTEP and VASP structure file formats.

Built into the ARTEMIS code is a help function accessible via the use of flags. This help function details the possible tags for use in the code's input file. Also, ARTEMIS can be run using flags, though the recommended method of running is using the input file.

6.2.1 Lattice matching

In order to construct an interface between two crystals, one needs to consider how one would match the lattices of the two structures. The first objective is create a set of interfaces between the two parent crystals that minimises the potential strain caused by mismatch between them. The second is to identify the interfaces with minimal supercell area so as to reduce the total number of atoms in each structure. This second objective allows for more feasible computational simulation of the structures using various atomic scale approaches.

Here, we outline the algorithms for lattice matching and, how, within this routine, Miller planes are generated, unique surface terminations are identified and vector matching is performed. A schematic of this scheme can be seen in Figure 6.2a. The approach developed here is similar to that developed by Zur *et al.* [224] and Jelver *et al.* [228].

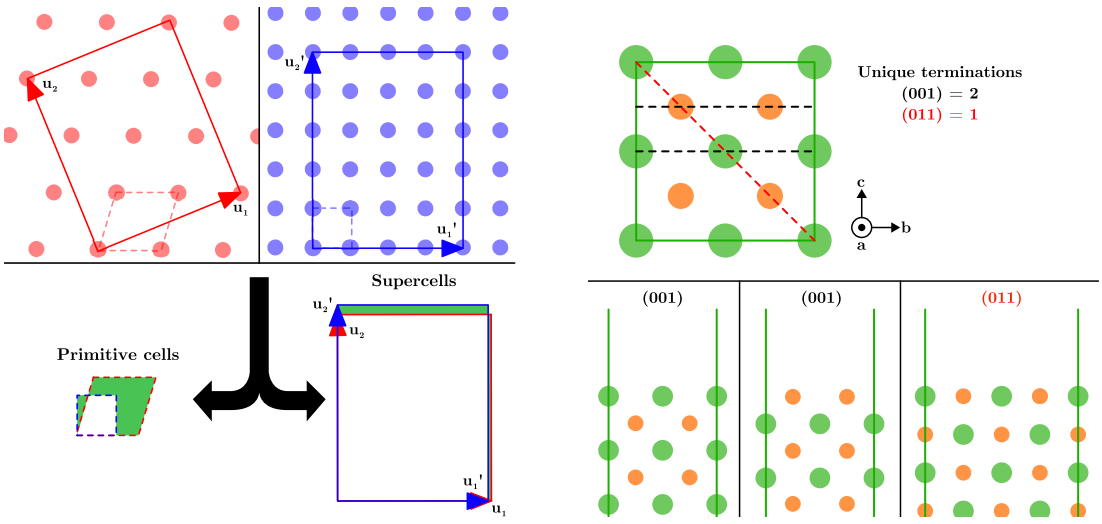

(a) Rotations (b) Terminations

Figure 6.2. Schematics outlining two main stages of lattice matching. (a) Rotations (supercells) of two surfaces can lead to better matching and, hence, less strain. The top two panels depict the lattice of two crystal surfaces, along with the primitive and a supercell for each lattice. The bottom panel displays the poor matching (highlighted in green) of the two primitive cells and the better matching of the chosen supercells. (b) Potential surface terminations of the crystal for the (0 0 1) and the (0 1 1). Top panel shows the different potential cleavage planes. The bottom left and bottom middle panel depict the two unique surface terminations for the (0 0 1) Miller plane. The bottom right panel depicts the unique surface terminations for the (0 1 1) plane.

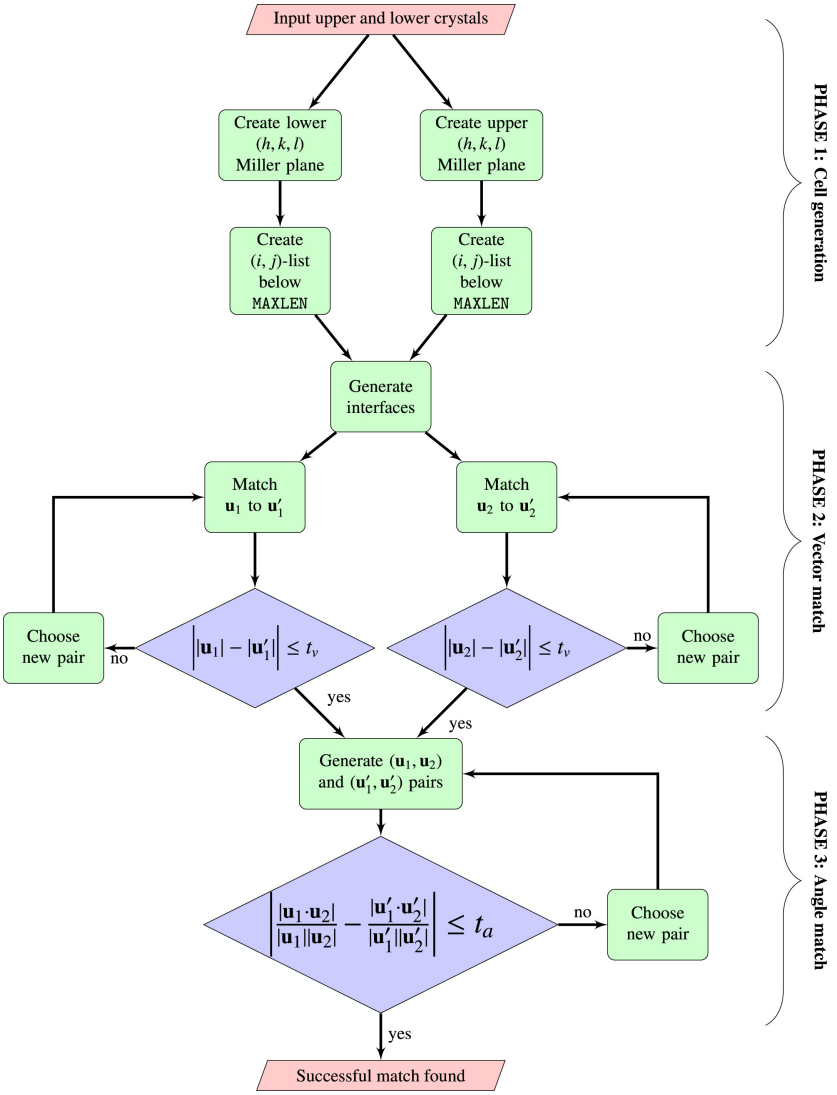

Figure 6.3. Workflow of the lattice matching method implemented in ARTEMIS. The method is split into three phases labelled cell generation, vector match and angle match. t_v and t_a correspond to the `TOL_VEC` and `TOL_ANG` input file tags, respectively.

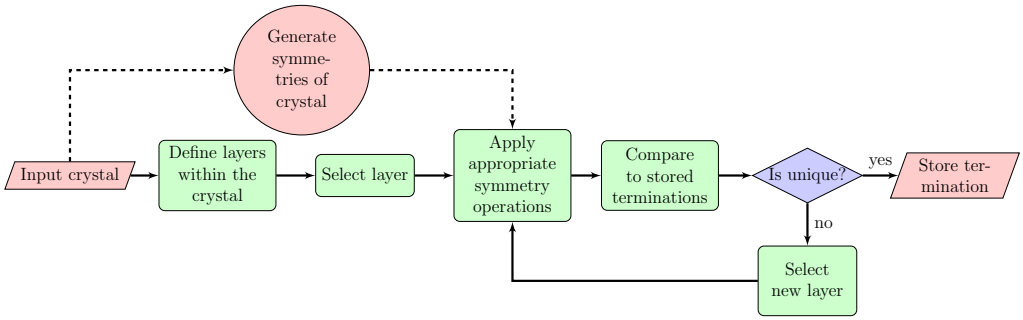

Figure 6.4. Surface identification workflow diagram. The process by which ARTEMIS identifies unique surface terminations.

Figure 6.3 represents the workflow of the lattice matching method. To begin with, we define our two crystals. These input lattice crystals are defined by lattice vectors $(\mathbf{a}_1, \mathbf{a}_2, \mathbf{a}_3)$ and $(\mathbf{a}'_1, \mathbf{a}'_2, \mathbf{a}'_3)$. Vectors relating to the upper crystal will be defined by a prime ($'$) in this section, with all other vectors being related to the lower crystal. For both crystals, a set of Miller planes are generated to be considered for the lattice matching. Planes are constructed such that (h, k, l) obeys the condition of $-10 \leq h, k, l \geq 10$. Symmetry operations of the crystals are then applied to their respective Miller planes in order to reduce these sets to the unique Miller planes. The two Miller plane sets are then cycled over, determining the lattice vectors for each plane in turn. The shortest surface lattice vectors of each plane, $\mathbf{b}_1$, $\mathbf{b}_2$ ($\mathbf{b}'_1$, $\mathbf{b}'_2$), are obtained using the Lenstra-Lenstra-Lovász lattice basis reduction algorithm [231]. (As LLL-reduction only applies to integer vectors, this is performed on the two columns of the transformation matrix that will act on lattice vectors $\mathbf{b}_1$ and $\mathbf{b}_2$.) For each Miller plane, integer quantities of the two surface vectors are then combined to generate a list of lattice vectors that span this plane, *i.e.* $\mathbf{u} = i\mathbf{b}_1 + j\mathbf{b}_2$. These lattice vectors are then generated with the condition $|\mathbf{u}| \leq$ `MAXLEN` (`MAXLEN`, default = 20 Å). The list of lattice vectors obtained for the two parent crystals are then compared to find matching pairs of $(\mathbf{u}_1, \mathbf{u}'_1)$ and $(\mathbf{u}_2, \mathbf{u}'_2)$. These pairs are obtained when the magnitude of $\mathbf{u}_1$ ($\mathbf{u}_2$) matches the magnitude of $\mathbf{u}'_1$ ($\mathbf{u}'_2$) to within the user-defined tolerance (`TOL_VEC`, default = 5 %). The list of lattice vector pairs defined above are then cycled through to find potential lattice matches. By joining

two lattice vector pairs, it can be determined whether the angle between $\mathbf{u}_1$ and $\mathbf{u}_2$ matches that of $\mathbf{u}'_1$ and $\mathbf{u}'_2$ to within a tolerance defined by `TOL_ANG` (`TOL_ANG`, default = 1°). Pairs matching this criteria are then stored as a suitable lattice match. The set is then ordered by their vector and angular mismatch. A weighting is applied to favour matches of a smaller area, as such matches are more likely to be modellable). The user can define the number of most favourable lattice matches to be generated (`NMATCH`, default = 5).

6.2.2 Surface Terminations

A method is implemented in ARTEMIS to distinguish the atomic layers within each material (with respect to the surface plane) and thus allowing for unique terminations to be defined. However, in doing so, non-physical surfaces can be generated and care must be taken, especially for 2D materials.

In order to define unique surface terminations, we first need to specify what constitutes a *layer*. We define distinct atomic layers within a crystal as regions parallel to the chosen Miller direction that are separated by vacuum gaps of greater than `LAYER_SEP` (`LAYER_SEP`, default = 1 Å). This definition creates atomic layers appropriate to the chosen Miller direction, with the caveat that high atomic density regions remain grouped. Cleaving through such high-density regions is forbidden as this would be expected to result in a high cleavage energy (akin to cutting through a large number of bonds). Using this technique alone to create layers can result in two different layers being defined which are symmetrically equvialent. To determine if a layer is unique, we consider whether there exists a symmetry operation that matches the layer to another layer within the set (excluding mirror symmetries in the Miller direction); if a symmetry operation matches two layers in such a way, then one of these is discarded. From this set, the top atom for each of these layers is then defined as a unique surface termination. This process is performed for both crystals for each

Miller plane being considered. The result is a set of unique surface terminations for each crystal. Figure 6.2b depicts potential terminations of a crystal structure based on the choice of Miller plane and the workflow can be seen in Figure 6.4.

The ideal end goal of the surface termination finding process is to generate two symmetrically equivalent interfaces. This is intended to prevent the creation of spurious electric fields, and model a single unique interface per simulation. However, ARTEMIS does allow the user to create asymmteric interfaces if they wish. The initial thickness of each slab is defined by the number of symmetrically equivalent layers, perpendicular to the Miller plane, within the parent crystal. The user can define the number of equivalent layers to be contained within the lower (upper) slab using the parameter `LW_SLAB_THICKNESS` (`UP_SLAB_THICKNESS`).

A notable exceptions this process occurs when a material displays neither S_n nor C_{nh} symmetries [232]($n = 1, ..., 6$) in the Miller plane. This condition prevents asymmetrically equivalent surfaces from existing for such a crystal. For materials of this nature, such as fresnoite [214], ARTEMIS will create two unique interfaces in the system and, therefore, users have the option to change the surface termination of each slab. This is done using the `LW_SURFACE` (`UP_SURFACE`) tags. These same parameters can be also be used for symmetric structures if the user wishes.

6.2.2.1 Layered 2D Materials

The case of 2D materials presents a couple of unique problems. Because layered materials have weak van der Waals forces between their 2D sheets, cleavage does not occur in the same manner as in other crystals. Cleavage in layered materials occurs preferentially along the van der Waals gap. Any surface termination that occurs in the plane of the layers must coincide with the van der Waals gap or else it will be unphysical. The second problem with surface terminations in layered structures is that equivalent surfaces should not include symmetries that require

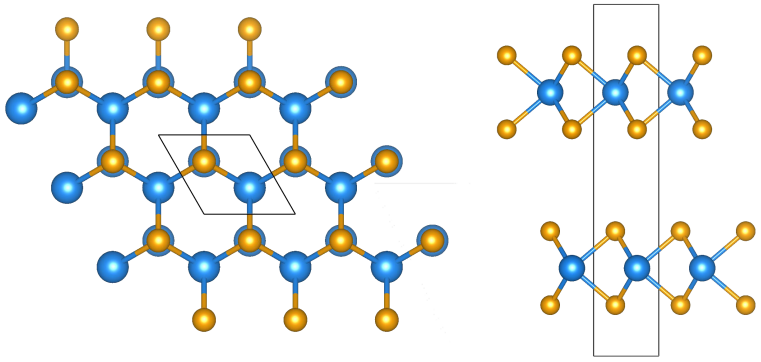

Figure 6.5. The 2H structure of the Transition metal dichalcogenides.

interlayer coordination. However, the default symmetry analysis will include this. When considering the 2H structure of the transition metal dichalcogenides (shown in fig. 6.5) it is clear that each layer is equivalent to each other. When considering the complete structure, however, it shows a different space group for even ($P\bar{3}m1$, #164) and odd ($P\bar{6}m2$, #187) number of layers[233]. The default symmetry operations will therefore prevent an odd number of layers from being generated from a parent structure with an even number of layers. In short the surface termination procedure is preserving the stacking order of the layered material.

2D structures may present difficulties due to stacking order and preferential cleavage plains, the rules that govern their interface generation are relatively simple. Both of these problems are solved by identifying the direction of the layering and removing the symmetry equivalence condition on layers. We include an input parameter `LW_LAYERED` to account for this condition. If `LW_LAYERED` (`UP_LAYERED`) is set to true, then only stoichiometric surface terminations are considered for the lower (upper) material. This ensures that only full layers are generated (i.e. cleaving occurs along the van der Waals gap) and that the generation does not erroneously replicate stacking order.

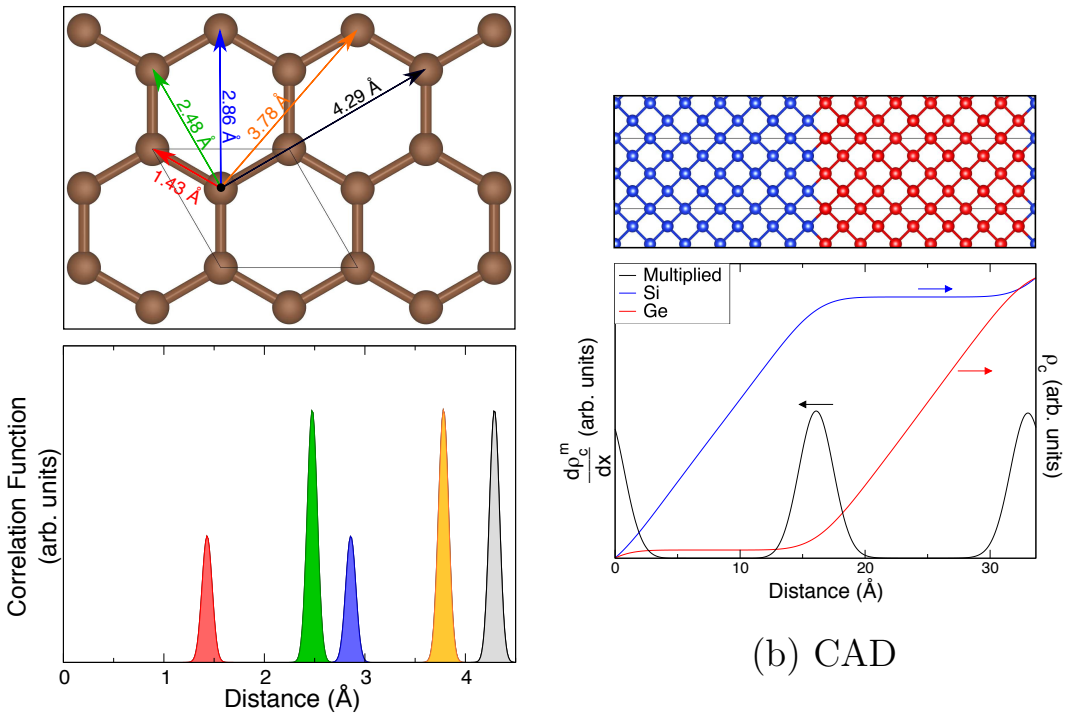

(a) DON

(b) CAD

Figure 6.6. The two methods implemented in ARTEMIS for interface identification. (a) Density of neighbours (DON), with a graphene monolayer used as an example. Top panel depicts the five shortest unique bond lengths of graphene. Bottom panel displays the radial distribution of bond lengths as gaussian peaks, where the height of peak relates to the number of that bond length present. (b) Cumulative atomic density (CAD), with an Si/Ge interface used as an example. Top panel shows the structure of the chosen interface. Bottom panel graph plots the species-dependent cumulative atomic density (ρ_c) and its derivative ($d\rho_c^m/dx$). The arrows on the graph indicate which data relates to which axis.

6.2.3 Interface Identification

Both to examine existing structures that have been made by other users and to allow reruns on existing interface structures, ARTEMIS includes a subroutine capable of reading a structure and identifying the interfaces within it. The code has the capability to perform interface manipulations on pregenerated interface structures. To begin with, we define the direction perpendicular to the interface as the 'interface direction'. To locate the interfaces in the pregenerated structures, ARTEMIS identifies the interface direction using a process we name DON and location of the

interfaces along this axis are identified using CAD. These two processes are discussed below.

6.2.3.1 DON - Density of neighbours

In order to determine the interface direction, correlation functions are employed to determine the axis of greatest dissimilarity. To do so, we start by generating a species-dependent density of neighbours (sDON). The DON is an angle-independent description of the distance of atoms akin to the nearest neighbour profile used to characterise amorphous materials [234] and Figure 6.6a gives a visual description of how it works. For each atom in the structure, a DON is generated in order to describe their local environments. The sDON and DON are given

$$\mathrm{sDON}_{s,i}(p,\Delta r) = \sum_{j}^{n_{\mathrm{atom},p}} e^{-\frac{(\Delta r - |\mathbf{r}_{s,i}-\mathbf{r}_{p,j}|)^2}{2\sigma^2}}, \tag{6.1}$$

$$\mathrm{DON}_{s,i}(\Delta r) = \sum_{p}^{n_{\mathrm{spec}}} \mathrm{sDON}_{s,i}(p,\Delta r), \tag{6.2}$$

where $\mathbf{r}_{s,i}$ and Δr are the location of and the distance from atom i in species s, respectively. n_{spec} is the total number of species in the system, $n_{\mathrm{atom},p}$ defines the number of atoms associated with species p, and $\sigma = 0.05$ Å. The sDON of each atom is then compared, with all the other atoms in order to determine the *similarity* of that one atom to the rest of the structure (with a heavier weighting placed on the atoms nearby, offering a description for the similarity of the local environment). We define this similarity, *sim* as

$$\mathrm{sim}_{s,i} = \sum_{x}^{x_{\mathrm{cutoff}}} \sum_{j}^{n_{\mathrm{atom},s}} \mathrm{mDON}_{s,i,j}(x) e^{-\frac{|\mathbf{r}_{s,i}-\mathbf{r}_{s,j}|}{r_0}}, \tag{6.3}$$

where $x_{\text{cutoff}} = 4$ Å, $r_0 = 1$ Å and

$$\text{mDON}_{s,i,j}(\Delta r) = \sum_{p}^{n_{\text{spec}}} \min\Big(\text{sDON}_{s,i}(p, \Delta r), \text{sDON}_{s,j}(p, \Delta r)\Big). \tag{6.4}$$

Then we compare the range of these similarity values associated with each axis and define this range as the *dissimilarity*,

$$\text{disim}_{\alpha} = \max\Big(|\text{sim}_{s,i} - \text{sim}_{s,j}| f(\mathbf{r}_{s,i}(\alpha) - \mathbf{r}_{s,j}(\alpha))\Big)_{s,i,j}, \tag{6.5}$$

with

$$f(x) = \begin{cases} 1, & |x| \leq 1 \text{ Å} \\ 0, & \text{otherwise,} \end{cases} \tag{6.6}$$

where $\alpha = 1, 2, 3$ refer to the $\mathbf{a}_1'', \mathbf{a}_2'', \mathbf{a}_3''$ axes, respectively. The axis with the smallest *dissimilarity* determines the interface direction, defined as β. Having determined the interfacial axis, the locations along this axis of the two interfaces needs to be found.

6.2.3.2 CAD - Cumulative atomic density

After having defined the interface direction (β), we now need to determine the interface location along that axis. The use of this method can be seen in Figure 6.6b. Firstly, the species-dependent cumulative atomic density profile (CAD) for the interfacial axis is calculated from

$$\mathrm{CAD}_\beta(s, \Delta r_\beta) = \sum_{x=0}^{\Delta r_\beta} \sum_{i}^{n_{\mathrm{atom},s}} e^{-\frac{(x - r_{\beta,s,i})^2}{2\sigma^2}}, \tag{6.7}$$

where $\sigma = 2$ Å, $r_{\beta,s,a}$ is the β^{th} element of the position vector of $\mathrm{atom}_{s,a}$ and Δr_β defines the position along the β^{th} axis. The derivative at each point is then determined for each species. Finally, all of the species-dependent cumulative atomic density derivative profiles are multiplied together and the two greatest maxima of this function are defined as the two interfaces of the system (as the structures are periodic, two interfaces are present in a cell).

$$\mathrm{multiCADD}_\beta(\Delta r_\beta) = \left| \prod_{s}^{n_{\mathrm{spec}}} \frac{d}{dx} \mathrm{CAD}_\beta(s, \Delta r_\beta) \right|. \tag{6.8}$$

The CAD process identifies the two interfaces within the cell as the two locations with greatest $\mathrm{multiCADD}_\beta(\Delta r_\beta)$. The location of these interfaces along the interface direction are stored as $x_{\mathrm{intf},1}$ and $x_{\mathrm{intf},2}$. This method works for nearly all interfaces with the exception of planar defects where material effectively has a stacking fault.

6.2.4 Interface Manipulation

Matching two crystals lattice vectors is the first stage of making an interface. However, as discussed previously, many other factors need to be considered. Chief among these factors are sources of stress in the structure. These can originate from the misalignment of the two materials, or from broken bonds or a lack of intermixing across the interface. In this section, we outline the various methods available within ARTEMIS to generate structures with different interface alignments (shifts) and to include atomic diffusion (in the form of atomic swaps). These structures are generated so that the user can examine the energy space dependence on these factors

and assess the various interfaces and their favourability.

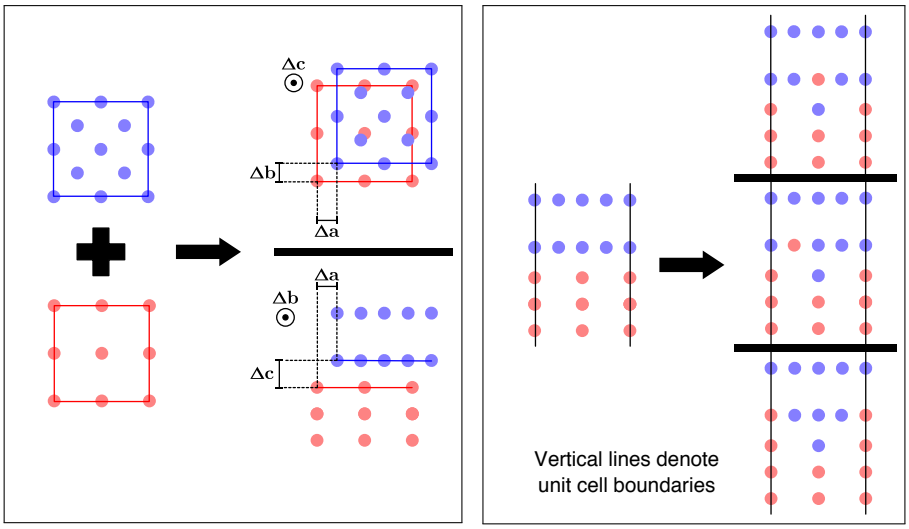

(a) Shifts (b) Swaps

Figure 6.7. Schematic outlining shifting (alignment) and swapping (intermixing) used to relieve interface strain. (a) Shifts, The left panel shows two crystal surfaces. The top right panel depicts the shifts in the interface plane, whilst the bottom right panel highlights shifts parallel to the interface direction. (b) Swaps. The left panel depicts a non-intermixed interface. The three unique swap structures are shown in the right panel as top, middle and bottom, with the structures being separated by the bold black bars. The vertical black lines denote the boundaries of the unit cell; as such, any atoms lying on a black line are repeated on the opposite black line.

6.2.4.1 Shifting

We define the shifting of material A with respect to material B as the 'interfacial alignment'. Interface alignment is the first step in reducing stress. When determining shifts, it is important to consider the bonds that have been cleaved through in order form a surface from a crystal. Here, these *cut* (broken) bonds are termed as missing bonds. Having matched lattice vectors, one needs next to consider the correct alignment of the basis of the two separate structures in order to best accommodate for these missing bonds at the interface. A depiction of interfacial aligment can be seen in Figure 6.7a.

A set of methods are available in ARTEMIS to manipulate *interface alignment*,

via generating and performing sets of shifts, $\boldsymbol{\delta}$. A shift is defined as a displacement of one surface with respect to the other. These methods are selected using the `ISHIFT` tag. `ISHIFT` = 0 allows for user-defined shift values, 1 uses random shifts, 2 matches the average interfacial bond to the two materials' bulk bonds, 3 and 4 attempt to predict a set of descriptive bonds. In particular, `ISHIFT` = 3, 4 represents ARTEMIS at its most comprehensive, generating a set of interfaces with different shift values. The number of shifted structures generated per lattice match is determined by `NSHIFT` (`NSHIFT`, default = 5).

`ISHIFT` = 0 allows the user to specify the tag `SHIFT` = a b c, where a, b and c are the manual shifts defined by the user and each can be any real number.

`ISHIFT` = 1 creates `NSHIFT` number of random shifts of the interface structure.

`ISHIFT` = 2 ensures that the average minimum separation between atoms either side of the interface best matches to the mean of the two parent crystals' averaged bond lengths.

`ISHIFT` = 3 begins using the `ISHIFT` = 2 methodology and then produces a set of `NSHIFT` shifts parallel to the interface plane, whilst maintaining its interfacial separation (the spacing parallel to the interface direction). By fixing the interface separation to that determined by `ISHIFT` = 2, a new set of shifts (parallel to the interface) are generated that allow for the average interface bond to most and least match to the average bulk bonds (best, worst, second best, second worst, etc.). These set of shifts are intended to be descriptive of the energetic space of potential interface shifts, which allows the user to determine how drastically the energy can change depending on the alignment for chosen systems.

`ISHIFT` = 4 is a method of shifting which attempts to match the bond lengths across the interface to the missing bulk bond lengths of the surface atoms. By determining the shortest missing bond of the surface atoms of each crystal (and the

number of those bonds missing for each of them), the opposite crystal's structure can be used to supplement these absent bonds. This is similar to the broken-bond rule for metal surfaces, which assumes that the cleaving energy is directly related to the number of broken bonds for the metal's surface. Thus our method here assumes that the most energetically favourable alignment of two surfaces is to compensate for the greatest number of missing bonds [235, 236].

To determine the missing bonds for `ISHIFT` = 4, we generate for each individual atom within each component slab a DON. We then subtract the individual DONs from their Wyckoff bulk (i.e. ideal) counterparts. This produces a nearest neighbour profile which highlights the missing bonds of each atom. These missing bonds are characterised by both their bond length and the number of such missing bonds. We then store the value of the shortest missing bond for each atom for later reference, where the shortest bond of an atom must be smaller than `MBOND_MAXLEN` (`MBOND_MAXLEN`, default = 4 Å).

Next, the two slabs are placed on top of each other such that the top of the lower slab's surface and the bottom of the upper slab's surface occur at the same point (i.e. zero separation). No initial shift is applied either parallel or perpendicular to the interface plane. In order to determine a set of suitable shifts, the code evaluates a bond ideality factor, $D_{\mathbf{s}}$, for each possible shift ($\boldsymbol{\delta}$) and generates `NSHIFT` number of structures using the shifts with the smallest bond ideality factors. In the case of a perfectly matching interface, the bond ideality factor has a value of zero. The value of $D_{\mathbf{s}}$ is given as

$$D_{\boldsymbol{\delta}} = d_{\boldsymbol{\delta},lu} + d_{\boldsymbol{\delta},ul} \tag{6.9}$$

where

$$d_{\boldsymbol{\delta},lu} = \sum_{m}^{l} \left[\left| N_m - \sum_{n}^{u} f(|\mathbf{r}_m + \boldsymbol{\delta} - \mathbf{r}'_n| - b_m) \right| + \sum_{n}^{u} g\left(\frac{|\mathbf{r}_m + \boldsymbol{\delta} - \mathbf{r}'_n| - b_m}{b_m} \right) \right]. \tag{6.10}$$

$d_{\boldsymbol{\delta},lu}$ quantifies how well slab u compensates for the missing bonds in the surface of slab l, which is generally distinct from $d_{\boldsymbol{\delta},ul}$. Here, l and u are the sets of missing bonds for atoms from the lower and upper slabs, respectively. N_m is the total number of missing bonds for atom m, $\mathbf{r}_m$ is the location of atom m and $\mathbf{r}'_n$ is the location of atom n. b_m is the length of the missing bond for atom m. We also include a pair of weighting functions,

$$f(x) = \frac{1 - \tanh(9(|x| - 1/4))}{2} \tag{6.11}$$

and

$$g(x) = \begin{cases} \frac{8}{3} |\tan(\pi x/2)|, & x < 0 \\ 0, & \text{otherwise.} \end{cases} \tag{6.12}$$

where the $f(x)$ function weights the set of shifts towards ones that compensate for the surface atoms' missing bonds, whilst $g(x)$ helps to prevent shifts that place atoms too close to one another. The specific forms of the two functions, $f(x)$ and $g(x)$, are used in order to satisfy the three following conditions. Firstly, $f(x)$ and $g(x)$ should be at their maximum and minimum, respectively, when a bond across the interface perfectly matches the missing bond length. Second, $f(x)$ should decrease with increasing disagreement between the interface bond and missing bond lengths. Finally, $g(x)$ should go to infinity when an interface bond goes to zero. The exact

parameterization and function used was selected mimic a softened top-hat function that would return a value of ≈ 0.5 when the bond length changed from the ideal length by 0.5 Å. This is based on an assumption that a deviation of 0.5 Åis at the destructive limit of a typical bond. It is reasoned that this be treated as "half stabilising" as it would provide a compensating bond but only when the rest of the structure supports it. The exact parameterization of the function can be improved in the future by testing against broader data sets. This could provide a promising application for machine learning since there are few parameters and much data.

To further validate the above approach, `ISHIFT` = 4 can be used between two identical bulk crystals. This methodology identifies appropriate shifts to reproduce a crystal's bulk bonds (to within 0.1 Å) across the interface and has been tested on numerous bulks containing either single or multiple species.

6.2.4.2 Intermixing

In order to enable exploration of diffusion across the interface, sets of structures are generated in which atoms from either material are intermixed (swapped), as demonstrated in Figure 6.7b. Intermixing is introduced to serve two main purposes. Firstly, we previously observed [205] that the intermixing both reduces strain and produces interface structures more favourable than the initial abrupt boundary model. The second is that by introducing disorder it allows for interfaces involving more elaborate reconstructions to be explored, such as the GaAs $\beta(2\times4)$ surface [105, 237].

The concentration of intermixing is governed by the `SWAP_DENSITY` tag (units of $Å^2$) and the number of uniquely intermixed structures generated per shift is determined by `NSWAP`. Each set of swaps in a structure are generated randomly, excluding symmetrically equivalent swaps. New swaps are performed until the `SWAP_DENSITY` has been reached. By default, intermixing is turned off (`ISWAP` = 0). To turn on random intermixing, set `ISWAP` = 1. To use the physics-based swapping procedure,

set `ISWAP` = 2.

`ISWAP` = 1 is purely a random swapping routine, based upon the user specifying a depth (`SWAP_DEPTH`, default = 3 Å), and the swapping density (`SWAP_DENSITY`, default = 0.05 Å^2). ARTEMIS then randomly swaps atoms either side of the interface to create a more graded interface.

`ISWAP` = 2 is based upon the observation [205] that the amount of intermixing exponentially decays with distance. As such, we use the following function to weight the chance of swapping

$$s(x) = e^{-\frac{x-x_{\text{intf}}}{2\sigma^2_{\text{swap}}}} \tag{6.13}$$

where x_{intf} is the location of the interface and σ_{swap} defines the decay of the probability of atoms further from the interface being swapped (`SWAP_SIGMA`, default = 0.05 Å). This function mimics the behaviour seen in reference [205] by selecting atoms to swap with an exponential weighting towards selecting atoms closer to the interface.

For a system where the two interfaces are symmetrically equivalent, any swaps performed across one interface are then mirrored to the opposite interface. In doing so, each generated structure still has two interfaces in the unit cell, with those two still interfaces being symmetrically equivalent. In doing so, this will prevent the introduction of spurious electric fields into the system.

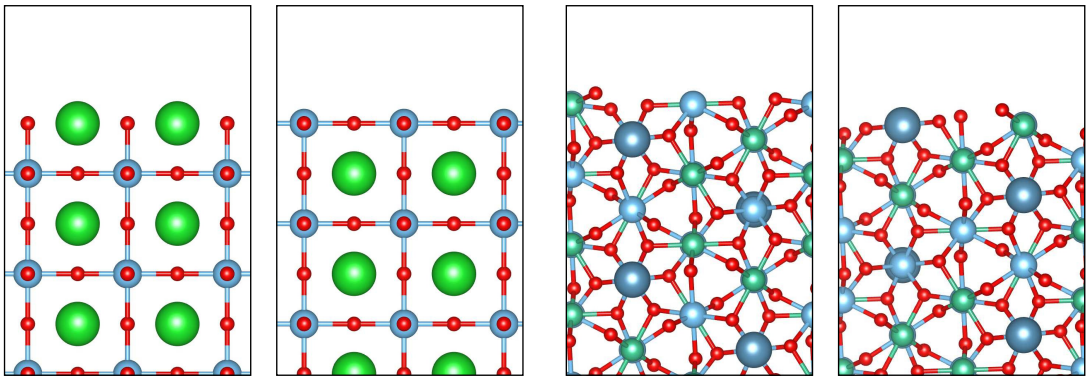

(a) $BaTiO_3$ (0 0 1) (b) $CaCu_3Ti_4O_{12}$ (1 2 1)

Figure 6.8. The two unique surface planes as identified by ARTEMIS for (a) the (0 0 1) Miller plane of $BaTiO_3$ and (b) the (1 2 1) Miller plane of $CaCu_3Ti_4O_{12}$.

6.3 Test Cases

6.3.1 Surface terminations

Using the `LSURF_INFO` tag, users can get the surface terminations of the lower (upper) parent crystal along the Miller plane specified by the `LW_MILLER` (`UP_MILLER`) tag. The surface is generated using the 1×1 unit cell reconstruction with the shortest lattice vectors on that plane. The number of symmetrically equivalent layers in the lower (upper) slab is specified using the `LW_SLAB_THICKNESS` (`UP_SLAB_THICKNESS`) tag.

The surface termination identification method used in ARTEMIS has been tested on a large set of structures. In Figure 6.8, the unique surfaces identified by ARTEMIS are shown for $BaTiO_3$ and $CaCu_3Ti_4O_{12}$ for the (0 0 1) and the (1 2 1) Miller planes, respectively. For all of the test cases, ARTEMIS generates the surfaces using the smallest lattice vectors parallel to the surface.

For the (0 0 1) Miller plane, the $BaTiO_3$ crystal is shown to have two unique surfaces, the AO-rich and the BO_2-rich surfaces (where a perovskite's chemical formula is given as ABO_3). These are the two most common surfaces of perovskites,

with the BO_2 being the most commonly studied [238, 239, 240, 241, 242, 243].

In the case of examples similar to the $CaCu_3Ti_4O_{12}$ (1 2 1) Miller plane, more care needs to be taken. As can be seen in Figure 6.8b, surface terminations are less clearly identifiable and, as such, defining surfaces is more difficult. Still, two unique surface terminations are identified, with these being chosen due to possessing the largest interplanar spacing.

Surface terminations have been generated for the two-atom primitive cell of silicon using the (1 0 1) Miller plane. It is found to properly identify the well-known surface (0 0 1) termination with the [1 1 0] and [1 $\bar{1}$ 0] in-plane lattice vectors [244, 245, 246].

6.3.2 Interface Identification

Interface identification is tested on a set of sample structures as shown in Figure 6.9. As can be seen, ARTEMIS identifies the interface in all cases. These four interface structures are used to exhibit different structural features an interface may have (only the $CaCu_3Ti_4O_{12}$/CuO structure has been relaxed, all others are generated examples for testing). The Si/Ge system is used as an example of structurally identical regions that differ only by species. The graphite/TiO_2 system shows an interface between 2D layered and a 3D bulk crystals. The $CaCu_3Ti_4O_{12}$/CuO system demonstrates a chemically diverse and disordered interface. Finally, the graphite/diamond interface demonstrates a transition between two phases of the same material. In each structural scenario, the interface is successfully identified.

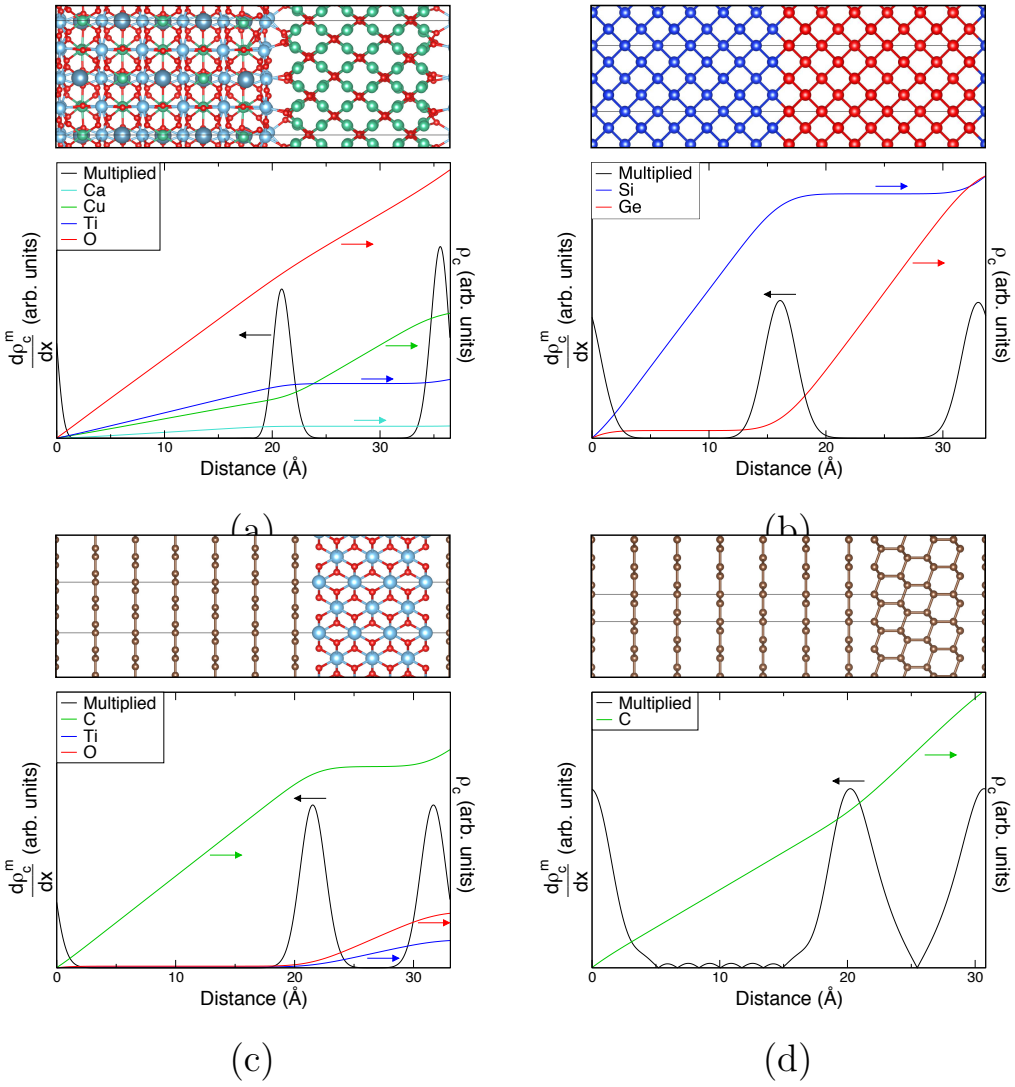

Figure 6.9. Interface identification performed on four structures. Cumulative atomic density derivative plots shown for (a) $CaCu_3Ti_4O_{12}$/CuO, (b) Si/Ge, (c) graphite/TiO_2 and (d) graphite/diamond interfaces. The arrows on the graphs indicate which data relates to which axis. These interfaces have been used to display four different qualities interfaces can exhibit. For all plots, the righthand axis denotes the cumulative density for each species in the system, whilst the lefthand axis denotes the 1st-order derivative of the species-multiplied cumulative atomic density (multiCADD).

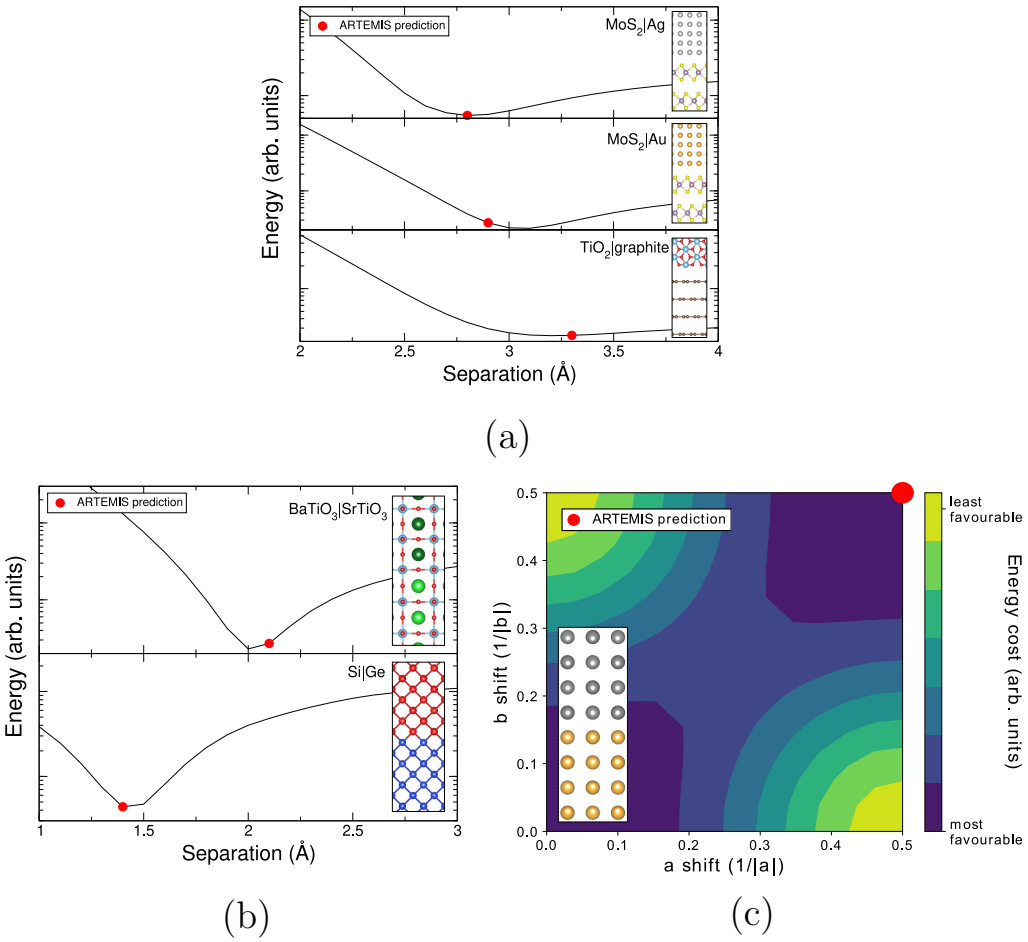

Figure 6.10. The relationship between energy and the alignment of the two parent crystals. (a) & (b) show the relation between energy and the interface seperation for 2D/3D and 3D/3D interfaces, resepectively. The optimum separation as estimated by ARTEMIS for each interface structure is is denoted by the red dots. The energies are obtained using the VASP density functional theory software package. (c) displays the energy cost of different shifts parallel to the interface plane for an Au/Ag interfacial structure. The optimum shift as estimated by ARTEMIS for each interface structure is is denoted by the red dot. The inset displays the Au/Ag interface structure used to display the effect of shifting on the interface energy.

6.3.3 Shifting

Here, the `ISHIFT` = 4 interface alignment setting is tested and presented on three 2D layered/3D bulk (Figure 6.10a) and two 3D bulk/3D bulk (Figure 6.10b) interface structures. To test this method, we generate a set of 20 interface separations within the range shown on the separation axes for each structure and calculate the energy for each. The interface separation predicted by ARTEMIS is then indicated on these lines by a red dot. We find that, in all cases, the default interface separation prediction is close to the most energetically favourable separation (to within 0.2 Å in these cases shown). This initial estimate of the separation of the two slabs means that the structure can be relaxed to its optimum distance using external first-principles software packages. This suggests the method of `ISHIFT` = 4 discussed in Section 6.2.4.1 is an appropriate method for interface separation estimation.

For shifts parallel to the interface, a test case of an Au/Ag interface has been chosen. The chosen Miller planes are (0 0 1) for both parent crystals. The energetic space of the in-plane shifts is shown in Figure 6.10c, with the shift predicted by ARTEMIS being labelled with a red dot. The shift determined by ARTEMIS is found to be the most favourable alignment for this metal-metal interface. Currently, this method has only been found to automatically identify the most favourable parallel shift for interfaces between simple, single-species crystals. For more complicated structures, the number of required structures (as generated by `ISHIFT`= 4) increases and the user needs to consider each case. However, it should be emphasised that interface separation predicted by ARTEMIS is generally found within the first iteration.

All energies reported in this subsection are obtained using density functional theory as implemented in the Vienna Ab initio Simulation Package (VASP). The energy for each shifted structure has been obtained by performing self-consistent field calculations on the generated, unrelaxed, structures. The calculations have

been performed using the PBE GGA functional with PAW pseudopotentials and an energy convergence of 10^{-7} eV. k-point grids of $3 \times 3 \times 2$ have been used for each structure.

6.4 Inputs and outputs

The code requires either one or two material structure files (depending on whether the user is supplying a preconstructed interface or two bulk materials) and one ARTEMIS input file.

If the user has supplied two material structure files for the purposes of generating an interface between them, then Sections 6.2.1 and 6.2.4 are used. If a preconstructed interface structure file is supplied, then Sections 6.2.3 and 6.2.4 are used.

The ARTEMIS input file has a set of cards and tags that can be explored and understood by using the built-in help function

```
./bin/artemis --help all
```

This will print all potential tags to the terminal, with a brief description of each. For further information on tag `[TAGNAME]`, use the command

```
./bin/artemis --search [TAGNAME]
```

With this, users can find the full set of tags available in the latest release version of ARTEMIS.

6.5 Summary

We have devloped a software package, ARTEMIS, for the generation of potential interfaces between any two materials; here the parent materials can be single-species or mutli-species, layered or bulk. The generated interface structure files can be output in a set of different formats that allow ease of use for DFT calculations using either QuantumEspresso, CASTEP or VASP, with an aim output in file formats for large-scale empirical calculations in the future. Through the use of the ARTEMIS software, users can more easily automate the task of interface generation and identification; for example, sets of interfacial alignments and intermixings can be easily generated, allowing for more thorough studies of potential interfaces between two parent crystals and their energy landscapes. With the lattice matching method able to scan over large sets of Miller planes, users can quickly identify low-strain matches which would otherwise take a lot of time to find. The test cases outlined in Section 6.3 show how the `ISHIFT` $= 4$ method can help in identifying the most favourable interface separation. ARTEMIS is under continuous development at the University of Exeter, with the intent of adding additional features, tools and methodologies for predicting the structure and properties of interfaces.

Chapter 7

Fresnoite: Interface Material Study

"Shut up and calculate!"

—David Mermin

What's Wrong with this Pillow?, 1989

7.1 Introduction

Due to the high permittivity exhibited by $BaTiO_3$ (BTO) (over 5000 at 1 kHz) [247, 248], it is seen as a material with great potential for device applications, such as capacitors [249], energy storage devices [250], phased array radar [251] and random access memory [252]. Recent literature has looked into the potential to form composites that can exhibit both the high permittivity found in BTO whilst also displaying the low dielectric loss of materials such as silica, SiO_2 (SO) [253, 254, 255]. To this end, BTO/SiO_2 core-shell composites have recently been made that exhibit the high breakdown voltage of SiO_2 whilst maintaining the colossal permittivity of

the BTO [256, 257, 258], giving them greater promise for use in supercapacitors. However, it has been shown that, during growth, a layer of fresnoite, $Ba_2TiSi_2O_8$ (BTSO), forms across a diffusion length into either material at the interface [259, 260]. These core-shell structures have been shown to exhibit both desired properties experimentally, yet theoretical studies of BTO/SO interfaces do not mirror these results [234, 261]. BTO/BTSO interfaces are, therefore, potentially responsible for the properties of such a structure. Furthermore, as many manufacturing processes for BTO involve growth on silica wafers, intermediate fresnoite layers can form during the process [259]. Clearly the properties of BTSO needs to be understood before the interface can be explored.

Successful growth of large BTSO crystals, as well as the characterisation of its piezoelectric and dielectric properties were reported in the 1970s [262]. BTSO has the space group P4bm, experimental lattice parameters of $a = 8.529$ Å and $c = 5.211$ Å, and displays a melting temperature of 1445 °C [263]. The tetrahedral TiO_5 structure present in fresnoite makes it highly polar [264], causing it to exhibit piezoelectricity [265, 266], nonlinear optical properties [262, 267] and ferroelectricity [268]. Due to the highly polar structure, modelling surfaces of fresnoite becomes rather challenging as most potential cleavage planes form non-stoichiometric and charged surfaces. For modelling purposes, this creates a net electric field across the structure, which is unphysical.

In order to fully understand the electronic and elastic characteristics of materials [269], such as BTSO, density functional theory (DFT) calculations are necessary. Very little literature is currently available on first principles calculations for BTSO, with only one paper partially exploring its electronic properties via the generalised gradient approximation (GGA) of DFT [270]. It is therefore unclear whether such results can be fully reliable as it is well known that GGA significantly underestimates the band gap of semiconductors, as well as electron

localisation[271]. Our choice of the Heyd-Scuseria-Ernzerhof (HSE06) hybrid functional[272] is due to its improved accuracy for electron localisation and band gap values [271]. An alternate approach would be to consider GW calculations, however, it has been recently shown [273, 274, 275] that for systems without a defect, HSE06 calculations accurately capture the bulk properties as well as GW calculations, for a lower computational cost. Hence our approach here is focused on application of HSE06.

In this work, we perform *ab initio* first principle calculations on the bulk fresnoite structure. We study the electronic properties, comparing GGA and hybrid functionals and their effects on the band structure, band gap and charge distribution. We also present the bulk elastic properties and the Raman modes to investigate the stability criteria of fresnoite. For the elastic properties, we compare and contrast with the properties of BTO and SO.

7.2 Methodology

First principles calculations are performed using the plane-wave DFT software package VASP [276, 277, 278]. The Perdew-Burke-Ernzerhof (PBE) [279] and projector-augmented-wave method [280] is used for GGA calculations. For hybrid DFT calculations, the HSE06 method [281] is applied. The valence electrons for each atomic species are considered as follows: $5s^2 5p^6 6s^2$ for Ba, $3s^2 3p^2$ for Si, $3p^6 3d^4 4s^2$ for Ti and $2s^2 2p^4$ for O.

In order to optimise the structure of BTSO, the internal atomic coordinates are fully relaxed using PBE-DFT until the residual Hellmann-Feynman forces acting on every atom became smaller than 0.01 eV/Å. The theoretical lattice constants are then found for both PBE and HSE06 whilst maintaining the experimental ratio of a/c, which is done to better compare with experimental data. The structural

optimisation was carried out using an energy cutoff of 600 eV and a $4 \times 4 \times 6$ Monkhorst-Pack k-point mesh [282]. To better understand the localisation of electrons within fresnoite, Bader charge analysis [283] is performed on BTSO and BTO using both functionals.

Planewave DFT codes sometimes use aggressive pseudopotentials where only the valence electrons will be modeled directly. This can lead to the misattribution of charge to ionic cores. Bader charge analysis uses a second order turning points in the charge density which form zero flux surfaces dividing the atomic cores[283]. The charge within the each closed surface can then be attributed to each ion. Aggressive pseudopotentials can result in the valence charge density decaying into the atomic cores and preventing the identification of turning points only present in the total charge density. In these cases it is important to include the core charge density in addition to the valence charge or else the turning points cannot be established and charge may be erroneously designated.

For the calculation of the dielectric and elastic tensors, as well as the Raman frequencies of the fresnoite structure, a higher accuracy is required. An energy cutoff of 650 eV is used along with a $6 \times 6 \times 8$ Γ-centred Monkhorst-Pack k-point mesh to sample the Brillouin zone for these calculations, which are obtained through use of density functional perturbation theory (DFPT) [284, 285] using the PBE functional for the Raman and dielectric properties and the finite difference method [286] using PBE for the elastic properties.

Figure 7.1 displays the crystal structure of BTSO. Ba and Si are in Wyckoff position $4(c)$, whilst Ti is in $2(a)$. Whilst the other atomic species each display only one type, oxygen displays four distinct types, with O(1) in Wyckoff position $2(b)$, O(2) in $4(c)$, O(3) in general $8(d)$ and O(4) in $2(a)$.

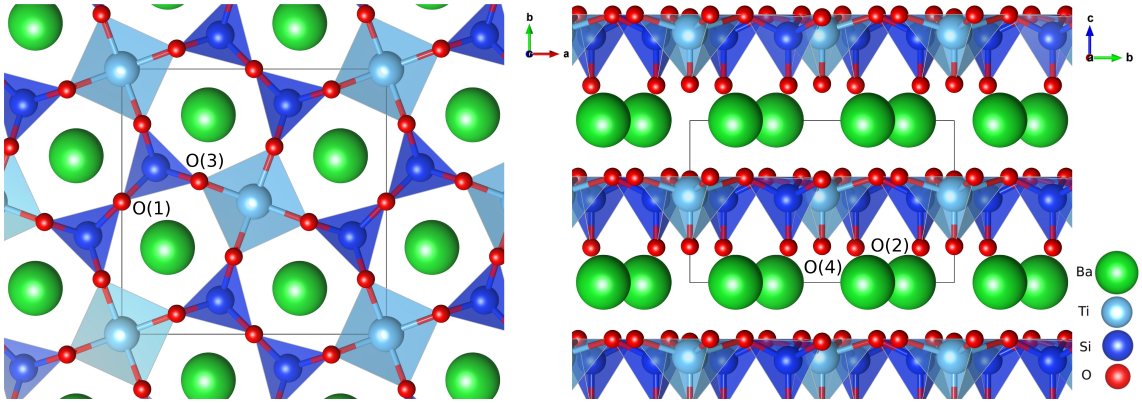

Figure 7.1. The crystal structure of $Ba_2TiSi_2O_8$ seen from (a) the [001] and (b) [100] planes, with the unit cell being outlined in both. The TiO_5 pentahedrons and SiO_4 tetrahedrons are highlighted, where O(4) and O(2) are located at the bottom of them, respectively.

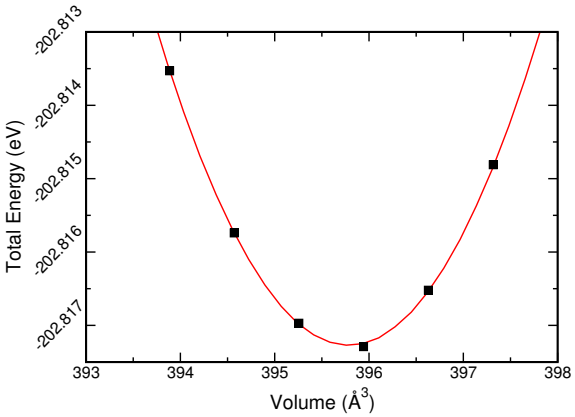

Figure 7.2. Calculated results using the PBE functional of the total energy vs. volume for fresnoite $Ba_2TiSi_2O_8$.

7.3 Results and discussions

7.3.1 Mechanical properties

The elastic properties of fresnoite are presented in table 7.1. The tetragonal structure of BTSO breaks symmetry between the C_{11} and C_{33} elastic constants. We find that our results agree well with the experimental values for direct deformation. From figure 7.2, one can extract the bulk modulus, B, through use of the equation

$$B = V_0 \frac{\partial^2 E}{\partial V^2}, \tag{7.1}$$

where V is volume, E is energy and V_0 is the volume at zero pressure. In this case, the value of 131.73 GPa is obtained for the single crystal. This value lies between that of BTO (175 GPa) [287] and quartz silica (37.2 GPa) [288, 289]. Values for polycrystalline elastic moduli can also be obtained from the elastic tensor via the Voigt-Reuß-Hill approach [290] . For BTSO, we find values of the bulk, shear and Young's moduli are 85.06 GPa, 35.57 GPa and 94.60 GPa, respectively. For single-phase BTO, we show a Young's modulus of 247 GPa, in good agreement with literature [291]. From these results, we find that polycrystalline BTSO is more flexible than that of BTO. The difference between the two values of bulk modulus for BTSO are due to the difference between single crystal and polycrystalline structures. The bulk modulus shows that the system becomes more susceptible to deformation when under pressure with increasing SO content. The mechanical stability of a system is defined using the Born stability criteria [292]. This criteria specifics that a crystal is mechanical stable when no phonon modes have an imaginary frequency which would lead to displacements causing an amplifying force rather than a returning force. The elastic constants, presented in table 7.1, show the system is stable, according to these criteria.

By comparing the value of C_{11} for BTSO to that of BTO and SO, the elasticity along the [100] direction is found to be the average of the two. Whereas, for the elasticity along the [001] direction, we find fresnoite to be lower than that of both BTO and SO; through the inclusion of Si and O in BTSO, the direct deformation in c becomes close to the value found in pure SO.

The O(4)–Ti–O(3) bond angles are found to be 106.4°, whereas the O(2)–Si–O(3) and O(2)–Si–O(1) bond angles are 115.4° and 110.7°, respectively. In comparison, the bond angle for O–Ti–O in BTO is 90°, and the angle for O–Si–O is 109.5°

Table 7.1. Theoretical and experimental elastic moduli, C_{ij} (in units of GPa) for $Ba_2TiSi_2O_8$, $BaTiO_3$ and quartz SiO_2. Where the elastic constants are defined in their usual notations.

	C_{11}	C_{12}	C_{13}	C_{33}	C_{44}	C_{66}
$Ba_2TiSi_2O_8$ [a]	180.57	84.06	45.25	102.56	23.47	66.74
$Ba_2TiSi_2O_8$ [b]	165.5	57.7	43.6	99.9	31.7	69.4
$BaTiO_3$ [a]	280.52	102.65	101.34	271.62	120.23	120.76
SiO_2 [c]	81.1	8.3	7.5	104.8	49.7	36.4

[a] This work, calculated using PBE

[b] Expt. [267]

[c] Local density approximation. [293]

in quartz silica. The larger Ti–O bonding angle found in fresnoite suggests that the Si–O bonding is dominant; whilst the larger Si–O bonding angle than in SO is likely caused by the large ionic Ba–O bonds in fresnoite.

Raman frequencies are obtained for BTSO and the system is shown to be dynamically stable as it exhibits no modes below 0 cm^{-1}. Through factor group analysis, BTSO is shown to have 47 Raman-active modes, split into $11A_1$, $6B_1$, $10B_2$ and $20E$ modes, where the 20 E modes are doubly degenerate. The strongest peak exhibited in Raman spectra, found at around 876 cm^{-1} [294, 295], is found in our analysis. We see good agreement in the vibrations that give rise to these modes. For example, the bands between 600–700 cm^{-1} are due to Si–O(1)–Si stretching; whereas the bands between 800-925 cm^{-1} are due to SiO_3 stretching. We find that two bands around 854 cm^{-1} are due to symmetric and antisymmetric stretching of the Ti–O(4) bonds. Bands are found at 864 cm^{-1} and 890 cm^{-1} that correspond to symmetric and antisymmetric stretching modes of the SiO_3 groups.

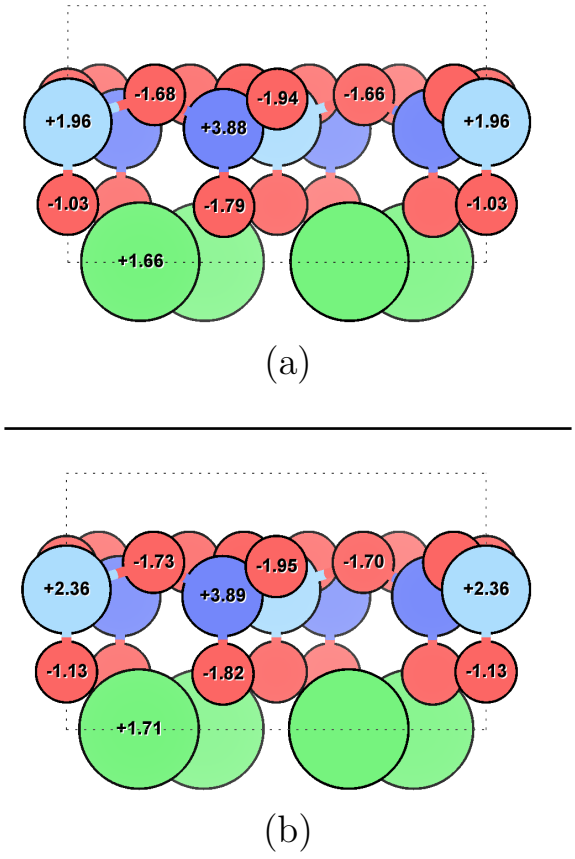

Figure 7.3. Bader charge analysis of $Ba_2TiSi_2O_8$ performed using the (a) PBE and (b) HSE06 functionals. The numbers depict the amount of charge gained by each atom when compared to the isotropic charge of the respective atomic species.

Table 7.2. Raman-activate phonon frequencies (cm^{-1}) for $Ba_2TiSi_2O_8$. Calculated using PBE.

Mode number	A_1	B_1	B_2	E
	Frequency (cm^{-1})			
1	108.567599	38.214216	86.308234	49.934423
2	125.590279	159.280804	136.882766	75.346482
3	211.314167	324.568544	139.348692	107.981567
4	246.963528	346.949356	254.622529	114.743744
5	268.205099	448.681377	388.125932	152.840538
6	446.527377	854.019813	423.117658	176.465284
7	555.008999		544.006739	188.182915
8	628.996167		638.728551	206.664157
9	853.603009		889.963443	255.529978
10	915.104215		961.793413	298.740370
11	994.884744			322.380920
12				351.945957
13				364.979379
14				451.223322
15				514.336224
16				545.658933
17				824.997166
18				864.366343
19				932.125583
20				975.193524

7.3.2 Electronic properties

To better understand the electronic and polar properties, we first examine the charge distribution. By performing Bader charge analysis, we are able to find a more accurate picture of the localisation of electrons across the unit cell. In figure 7.3, we present the charge distribution across the fresnoite unit cell for both the PBE and HSE06 functionals. In the system, strong oxidation occurs to the barium atoms, causing them to display strong ionic bonding with nearby oxygen atoms. This is typical of barium in oxides and is very similar in its behaviour to BTO (tab. 7.3). Bader analysis shows very little charge on the silicon atoms and further analysis of the charge density suggests this is due to covalent bonding between them and their neighbouring oxygen. Although titanium shows partial ionic bonding between

Table 7.3. Bader analysis of the tetragonal unit cell of $BsTiO_3$ using the PBE and HSE06 functionals. Here, O(1) are the two O that lie in the Ti plane and O(2) the O atom that lies in the Ba plane.

Functional	Electrons gained			
	Ba	Ti	O(1)	O(2)
PBE	-1.640	-2.085	+1.235	+1.256
HSE06	-1.696	-2.307	+1.322	+1.360

neighbouring oxygen atoms, it exhibits more covalent-like bonding than the barium, with the charge being shared between both the Ti and O atoms.

Comparison of the HSE06 and PBE functionals shows that the charge localisation broadly remains the same. Small charge redistribution is seen on the barium, and no charge redistribution occurs on the silicon. Significant charge redistribution is instead seen on the titanium and oxygen atoms. Overall, these results are expected as charge is generally found to be more delocalised with GGA functionals than the HSE06 functional.

The HSE06 functional calculations show slightly stronger oxidation occurring to the Ba atoms than the PBE functional. In general, Bader charge analysis reveals the Ba has a positive charge. In PBE calculations, this value is +1.657, whereas in HSE06, the value is +1.699, indicating the ionic bonding is stronger in the real system than a PBE calculation would suggest. Although no change of charge is found on the silicon atoms, their neighbouring oxygen atoms see slight charge redistribution. O(2), O(1) and O(3) all exhibit an increase in charge comparing HSE06 with PBE. Similarly, silicon atoms show slightly increased ionicity and decreased covalency. In comparison, O(4) and Ti atoms all show significant differences in charges between the two functionals. Overall, an increased localisation of charge doesn't change covalent bonds much; whereas ionic bonding is shown to depend quite heavily on the choice of functional. This stronger ionisation is also visible in the band structures seen in figure 7.4; the increased ionisation results in a larger band gap.

When comparing BTSO and BTO, we find that barium and titanium show similar charge characteristics, regardless of choice of functional. Through the introduction of silica to form BTSO, electron distribution across the oxygens is radically changed. Oxygens neighbouring silicon atoms gain roughly 1.8 electrons each - whereas O(4) gain only 1.07 electron. In both systems, Ti atoms ionise roughly 2.3 electrons each. Due to the polar nature of BTSO, Ti atoms undergo ionic bonding with oxygen in the Si-Ti plane, and more covalent-like bonding to oxygens near the Ba plane. This polar structure is also present with the Si atoms, but to a much smaller extent.

For HSE06, the in-plane bond lengths of Ti–O(4) are found to be 1.68Å, which is shorter than the in-plane bonds in BTO (1.99Å in-plane and 2.01Å in-tetragonal-plane). Along with the average loss of 0.3 electrons for O(4) compared to BTO, this indicates the TiO bonds in fresnoite are more covalent-like. Because SO is dominant in this region, the TiO bonds orientated in the [001] direction are decreased, preventing O(4) from extending further.

7.3.3 Band structure and density of states

In figure 7.4, we present BTSO's band structure and density of states. We compare also the PBE and HSE06 results. The first clear result is that using PBE gives a value of 3.79 eV for the band gap of fresnoite, whereas the hybrid functional method of HSE06 gives the band gap as 5.717 eV (tab. 7.4). By comparison, the experimental band gaps of $BaTiO_3$ and quartz are 3.2 eV [296] and 8.9 eV [297], respectively, showing that inclusion of SO in BTSO significantly increases the band gap.

BTSO is shown to have an indirect band gap of 5.717 eV along the Γ–M direction, with a second indirect gap of 0.330 eV appearing above the first two

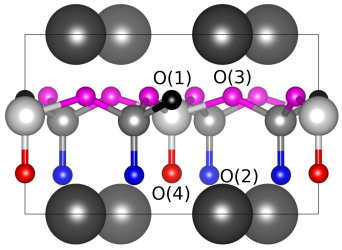

(a) Atomic structure.

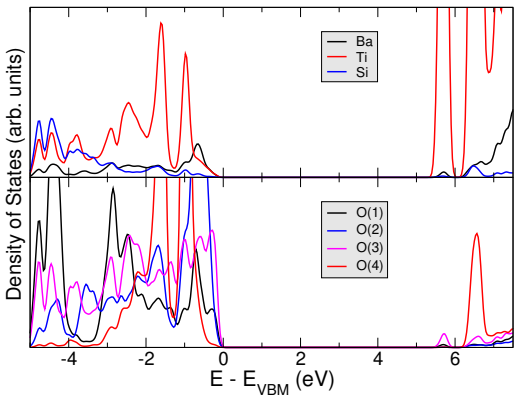

(b) PDOS of atoms (HSE06).

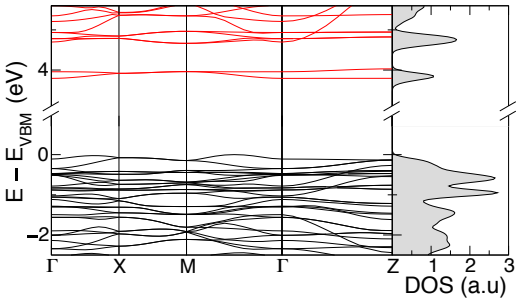

(c) Band structure (PBE).

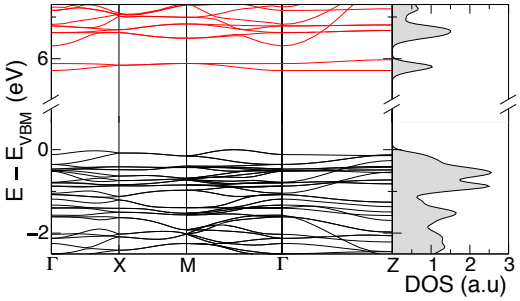

(d) Band structure (HSE06).

Figure 7.4. (Colour online) (b) Projected density of states (PDOS) for BTSO calculated using the HSE06 functional. (a) distinguishes between the four oxygen atoms, where their various colours match those of the states found in the PDOS in (b). The band structure and total density of states for $Ba_2TiSi_2O_8$ using the PBE (c) and HSE06 (d) functionals. All energies are given with respect to the valence band maximum.

Table 7.4. Theoretical and experimental lattice parameters, cohesive energy and band gap for $Ba_2TiSi_2O_8$ and tetragonal $BaTiO_3$ unit cells.

	Method	Lattice parameter (Å)		Cohesive energy (eV/atom)	E_g (eV)
		a	c		
$Ba_2TiSi_2O_8$	PBE[a]	8.6500	5.2918	-6.297	3.793
	HSE06[a]	8.56500	5.2398	-6.989	5.717
	Expt.[b]	8.529	5.211		
$BaTiO_3$	PBE[a]	4.03	4.048	-6.331	1.788
	HSE06[a]	3.98	3.998	-5.978	3.114
	Expt.	3.998[c]	4.018[c]	6.314[d]	3.2[c]

[a] This work
[b] Reference [263]
[c] Reference [296]
[d] Reference [300]

conduction bands. This suggests that BTSO can display not only a broadband response between the conduction band and valence band, but also a small optical response within the conduction band. This optical transition in the conduction band will look similar to that of defect transitions. Figure 7.4 shows that the electronic contribution due to the oxygen create the valence band edge of BTSO, whilst the titanium orbitals are dominant in the conduction band. Strong hybridisation of the O(4) orbitals with the Ti orbitals can be seen in figure 7.4(b), in which both atoms display very similar features near to the band edges. This structure of the titanium orbitals being dominant in the conduction band, oxygen orbitals being the main contributor to the valence band edge and barium orbitals filling the lower valence band is similarly present in BTO [287, 298, 299].

By comparing figure 7.3(b) and figure 7.4(b), the weaker localisation of charge on the O(4) atoms (when compared to the other O atoms in the system) is, again, attributed to a stronger covalent-like bonding between the Ti atoms above, as evidenced by the hybridisation of the O(4)-2p and Ti-3d orbitals. One of the largest differences between the two band structures in figure 7.4 is the downward shift of a band near the conduction band edge. This band splitting and increased dispersion of the O(4)-2p and Ti-3d orbitals is a result of the charge redistribution in this

bond between the two functionals. Due to this splitting, the anti-crossings present in these bands also increase with use of HSE06. As expected, there is no significant change of the bands within the valence region between functionals.

The BTSO HSE06 band structure displays a strong difference between the band edges and the sub bands. Whilst the valence band maximum (VBM) and conduction band minimum (CBM) states are relatively dispersionless, the sub bands show significant dispersion. Large anisotropy in the system is also present in the bands; we find both the band edges along Γ–Z display almost entirely flat bands, whereas the other directions display more dispersion - with a maximum band variation of 0.17 eV. Across the entire Brillouin zone, we find that two Ti electronic bands at the CBM are separated from the rest of the conduction band and act like a defect in the band structure, with very little dispersion. We describe this state as defect-like as the difference in the energies of minima-maxima of the band is under 0.001 eV, which means the electron mobilities are expected to be very low along Γ–Z unless excited to the second set of conduction bands. This is due to the low percentage of Ti in the structure, constituting approximately 20% of the potential Si/Ti sites. The conduction band is, therefore, highly sensitive to the titanium and its surrounding environment.

Finally, we present the effective masses of the electrons and holes (m_e^* and m_h^*, respectively) at the CBM and VBM when using the HSE06 functional. Due to the curvature, the values for $m_{e,h}^*$ depend on the total range of the Brillouin zone considered. The value ranges represent us approximating the band edge within 15% or 25% of the Brillouin zone near to the band edge in the quadratic regime. It is found that holes travelling along the Γ–M direction display an m_h^* of 2.1–2.3 m_e. Whereas electrons at the conduction band edge exhibit an effective mass, m_e^*, of 4.7–5.7 m_e along Γ–M. By comparison, we notice the conduction band edge along Γ–Z displays an almost completely flat band. This suggests very little conduction along this direction with an effective mass of approximately 300 m_e. However, this

value is difficult to quantify in a meaningful manner as we attempt to fit a nearly flat band to a quadratic. But we can confidently state a minimum value of at least 147 m_e.

7.4 Conclusion

Electronic and mechanical properties of $Ba_2TiSi_2O_8$, have been obtained and compared using the generalised gradient approximation and hybrid functional methods. The Ti-3d state is found to dominate the conduction band edge, whilst the O-2p is the main contributor to the valence band edge. With use of a hybrid functional, the band gap is corrected from 3.79 eV to 5.72 eV. The hybrid functional shows overall stronger ionic bonding and weaker covalent bonding within the structure; both the barium and titanium atoms are found to show stronger ionic bonding than with the GGA functional. The calculated value of 131.73 GPa for the bulk modulus sits between the values for $BaTiO_3$ and SiO_2. Theoretical values for Raman frequencies of the system allow us to show the system to be mechanically stable, as well as the origin of the vibrational modes. The elastic tensor values we obtain agree strongly with those found in experiment, showing the system to be highly anisotropic, as expected. Both the electronic and elastic properties of fresnoite show it to be a highly anisotropic system, with little dispersion visible in its band edges along Γ–Z and significant differences between the elastic moduli along the [100] and [001] directions. We believe that the more accurate HSE06 electronic structure of BTSO will give a better understanding of the optical and electron transport properties as well as providing better understanding of its chemical structure, which will be helpful for further work on systems like fresnoite which occur at interfaces.

7.5 Special Acknowledgements

Here is made a special thanks to Ned Taylor who provided recalculated plots of the original work, published by myself (with Ned Taylor and Steven Hepplestone) Mater. Res. Express 4 125904 (2017). The work was recalculated, to higher accuracy, and did not show changes, significant enough, to alter any conclusions. The recalculated data includes figures 7.3a, 7.3b, 7.4b 7.4c and 7.4d.

Chapter 8

Closing Remarks

"So long, and thanks for all the fish"

— Douglas Adams

8.1 Summary

The research presented here, identifies thermal and electronic trends in 2D heterostructures and develops a rigorous methodology for calculation of interface structures. Chapter 1 provides the reader with the necessary context to understand the relevance and importance of this work. The link is made between common devices and the materials and interfaces from which they are constructed. Lastly, 2D materials and their heterostructures are described.

Chapter 2 and 3 present and derive the theories used throughout the thesis. In chapter 2, the fundamental theories of DFT are derived and defined. The reason why many body *ab initio* methods are needed is described and the Hohenberg-Kohn and Kohn-Sham theorems are derived, under the adiabatic approximation, thus defining

DFT. This theory provides vital background for chapters 4, 5, 6 and 7. Chapter 2 further demonstrates that the frozen phonon method may, using the Hellmann-Feynman forces to determine the force constants, calculate the dynamical matrix and hence, a full phononic dispersion relation. This theory applies in chapters 5 and 7. Chapter 3 explores the phonon Boltzmann transport equation and uses the single mode relaxation time approximation to derive an expression for the thermal conductivity. The derived thermal transport model is applied to TMDCs and their heterostructures in chapter 5.

In chapter 4, we have demonstrated and explained the failure of Anderson's rule in 2D heterostructures. We also demonstrate how 2D heterostructure bandgap predictions can be improved using two physically based corrections to Anderson's rule ΔE_Γ and ΔE_{IF}. We have shown that ΔE_Γ affects the bandstructure such that for any constructed heterostructure the effective mass will always decrease and is likely to exhibit an indirect bandgap. Furthermore we have provided expressions to give the band alignments in terms of knowable material properties. It is discussed how theory could be readily extended to other 2D heterostructures by adjustments to corrective terms ΔE_Γ and ΔE_{IF}. This insight allows for a method which avoids the need for advanced calculation when estimating the properties of TMDC heterostructures. This in turn expands the possibilities for exploring the optoelectronic properties of various heterostructures to the broader research community. This work presents and describes a set of interactions in 2D heterostructures. These interactions are generalised and provide a fundamental understanding of 2D heterostructure interfaces.

While chapter 4 explores Electrical properties of the 2D heterostructure interfaces, chapter 5 considers their thermal properties. In chapter 5 we have shown that the thermal conductivity of a TMDC heterostructure will be lower than either constituent. We have shown that this is consistent even when considering a wide range of possible conductivities. To bound this region a generous parameter allo-

cation is used to define maximum conductivity values. This approach significantly improves the confidence in our conclusions. It also provides a route for artificially reducing heat flow in 2D layered materials. Such advancements are highly attractive for 2D thermoelectrics applications, where careful application of band alignments can simultaneously enhance electrical conductivity and reduce thermal conductivity. This work demonstrates a clear and consistent trend in 2D heterostructure interfaces with regards to thermal transport.

In chapter 6, the focus of the thesis turns from trends in heterostructure interfaces to the development of methodologies for their calculation. In this chapter a software package, ARTEMIS, is developed for the generation of potential interfaces between any two materials; 3D as well as 2D. The two parent materials can be single-species or multi-species, layered or bulk. Interface structures are the primary output of this code and can be printed in a range of formats that allow easy use in DFT calculations, performed using either QuantumEspresso, CASTEP or VASP. Through the use of the ARTEMIS software more thorough studies of potential interfaces between two parent crystals and their energy landscapes may be conducted. With the lattice matching method employed in this software, users can quickly identify low-strain matches by scanning over large sets of Miller planes. The code has been developed with post processing tools for pregenerated interface structures to allow users to further study an already tested interface. These tools include interface identification, interface alignment and intermixing. Collectively the functions of this code provide a rigorous methodology for the investigation of interface structures and heterostructures.

A shortcoming of ARTEMIS, (in its current version) is that there is no straight forward way to calculate interfacial materials although the intermixing methods can approach this. However, due to interactions with their local environment, such inter-grain materials need not adhere to the stoichiometry of the host crystal or crystals. The study of the surface vacancy energies and random structure searches can be

used. However, any confidence in these results still calls for experimental justification. For known interfacial materials such as $Ba_2TiSi_2O_8$ (known as fresnoite) an extensive study can be performed. In chapter 7, the electronic and mechanical properties of $Ba_2TiSi_2O_8$, have been obtained and compared using the generalised gradient approximation and hybrid functional methods. It is demonstrated that for insulating inter-grain materials hybrid functionals can result in significant change. The hybrid functional corrected the bandgap from 3.79 eV to 5.72 eV and shows overall stronger ionic bonding and weaker covalent bonding within the structure. The calculated value of 131.73 GPa for the bulk modulus sits between the values for $BaTiO_3$ and SiO_2. Theoretical values for Raman frequencies of the system show it to be mechanically stable, and provide the measurable vibrational modes. The elastic tensor values show the system to be highly anisotropic. The electronic structure calculated by the more accurate HSE06 functional, will give a better understanding of the optical and electron transport properties and provide better understanding of the chemical structure. This investigation will be helpful for further work on similar inter-grain systems.

Each chapter in this thesis serves the purpose of identifying general trends across heterostructures and interfaces or developing sound methodologies for the investigation of these structures. The first chapter provides context for this work while the following chapters describe the underlying theories used throughout. The first half of this thesis is concerned with the identification of trends, and the second, with the development of methodologies. This body of research invites further study, both continuing with the themes of the thesis and beyond.

8.2 Future Work

As is the nature of research, much of the work collected here opens the door for new investigative research. The work presented in chapter 4 derives a tool for the prediction of band alignments in heterostructures. This work could be extended by the application of this theory to a set of potential TMDC heterostructures. Using existing experimental or high throughput theoretical data for 2D materials (and TMDCs in particular) the band edges can be accurately predicted. These low cost predictions may be used to identify heterostructures for high efficiency photovoltaics. This investigation would require deeper knowledge of the interlayer excitations (layered materials have stronger excitonic effects due to reduced Coulomb screening[301]) and an understanding of the selection rules at play, which, in most cases, forbid the K to K transition in homostructures of 2H TMDCs. However, the study in chapter 4 demonstrates that the bandgap prediction is sound even for Moiré lattices which break the symmetry underlying the known selection rules. Furthermore, interlayer excitons have received much research attention with some work deriving expressions for exciton binding energies[302]. These same principles may be considered for screening materials for photo catalysis. This would require the calculation of surface molecules corresponding to the hydrogen evolution reaction.

The work presented in chapter 5 demonstrates a reduction in the thermal conductivity of heterostructures relative to their constituents. This reduction in thermal transport has clear benefits for thermoelectric applications. However, any potential benefits must be tested against the change in electrical conductivity and the Seebeck coefficient. Electrical conductivity calculations (and Seebeck coefficient) can be performed using the same Boltzmann transport methodology as the phonon transport model. Typically such calculations use a constant relaxation time approach, as implemented in the BoltzTraP code[63], but because a full phonon calculation has already been done on these systems, the electron-phonon scatter-

ing could be calculated for each electronic state. A second area of this study that warrants further investigation is the homogenised Grüneisen constant. The spatial separation of phonons in the two respective layers can be expected to result in lower interlayer coupling than the intralayer coupling. The significance of the asymmetry in the mode dependent Grüneisen constant could influence the thermal conductivity. A full phonon calculation, using the third order force constants to compute the phonon coupling constants matrix, would be the ultimate theoretical test of these results.

The electronic and thermal work on TMDC heterostructures in chapters 4 & 5 each provide some basic understanding of the coupling of electrons or phonons across van der Waals layers. A staggered TMDC heterostructure could lead to effective thermoelectric performance. Both thermal and electronic transport across layers has been investigated. A staggered TMDC heterostructure would include intralayer transport through the layers with interlayer transport in an overlap region. The thermal and electronic interlayer transport are governed by the electronic and phononic coupling respectively. The ratio of the interlayer couplings can be directly linked to an enhancement or reduction in the thermoelectric figure of merit. A highly simplistic thermoelectric model might relate an interface figure of merit, ZT', to the figure of merit of the constituents, ZT, as a basic equation $ZT' = f(R_p^e)ZT$, where $f(R_p^e)$ is a function of the ratio of electronic to phononic coupling. Such structures are experimentally viable and could provide advancements in the field of thermoelectric devices.

Chapter 6 explores the automated generation of interface structures. The lattice-matching procedure may be improved by incorporating relative strain between the crystals. When lattice-matching, the fitting will not, in general, have an integer ratio of lattice vectors. By consideration of the elastic tensor for each crystal an optimal strain may be estimated for any interface. Each lattice-matching can be expressed as an integer set of vectors plus a strain term. Strain is related to energy

density by the equation $U = \frac{1}{2}C_{ijkl}\epsilon_{ij}\epsilon_{kl}$, where ϵ is stress and C_{ijkl} is the elastic tensor. If the elastic tensor is calculated for each crystal then the strain may be optimised to minimise the energy of the interface. The elastic tensor is calculated through the same perturbation theory approach as zone center phonon calculations. This provides a second area for improvement of ARTEMIS. A γ point phonon calculation would serve two purposes. The first, is to determine the mechanical stability of the interface. If the phonon calculation returns imaginary modes then the interface is unstable and cannot form. The second purpose for such a calculation is to provide clear evidence that the calculations are performed to sufficient convergence.

8.3 Closing Remarks

The themes of this thesis are to identify trends in 2D heterostructures and to establish a clear and consistent methodology for calculation of interface structures such as heterostructures. As part of this body of work I have identified characteristic interactions at TMDC interfaces and used this to develop a general rule that describes the trend for the electronic band alignment in TMDC heterobilayers. I have also presented a study on the behaviour of thermal transport along an interface and established the trend that conductivity is reduced from either constituent. I have jointly developed the *ab initio* Restructuring Tool Enabling the Modeling of Interface Structures (ARTEMIS), this represents a significant contribution to the existing library of structure tools for atomistic modeling. For those cases that fall outside of the capabilities of this code a case study (on fresnoite) has been performed. The goals of this thesis have been met. I have delivered on the objectives of identifying trends in heterostructure interfaces and have provided a methodology for interface calculation with examples for exploring extended interface problems.

Appendices

Appendix A

Single Mode Relaxation Time Approximation

A.1 Linearised Boltzmann Transport Equation

First, we begin with the phonon Boltzmann transport equation. We assume there exists a distribution function n_λ which gives the occupation number of state λ (where $\lambda = \mathbf{q}s$). We balance the rate of change by thermal diffusion with that of the scattering to achieve a steady state.

$$\frac{\partial n_\lambda}{\partial t}\Big|_{scatt} = \nu(\lambda) \cdot \nabla T \frac{\partial n_\lambda}{\partial T}, \tag{A.1}$$

where ν is the group velocity, T is the temperature and n is the occupation. We may attempt to express this in terms of deviations from equilibrium. We can see that in equilibrium ($\bar{n}_\lambda$) none of the states experience time evolution.

$$\frac{\partial \bar{n}_\lambda}{\partial t} = 0 \tag{A.2}$$

hence using a first order expansion,

$$\begin{aligned}\frac{\partial n_\lambda}{\partial t} &= -\frac{\partial(n_\lambda - \bar{n}_\lambda)}{\partial t} \\ &\approx -\frac{(n_\lambda - \bar{n}_\lambda)}{\tau_\lambda}\end{aligned} \tag{A.3}$$

and so we may define

$$-\nu(\lambda)\cdot\nabla T\frac{\partial n_\lambda}{\partial T} = \frac{(n_\lambda - \bar{n}_\lambda)}{\tau_\lambda} \tag{A.4}$$

Now we must define the occupations in terms of deviations from equilibrium. In order to do this, we expand the occupation number to second order, about equilibrium. A non-equilibrium distribution function may be defined as

$$n_\lambda = \left(\exp\left(\frac{\hbar\omega_\lambda}{k_B T} - \xi_\lambda\right) - 1\right)^{-1} \tag{A.5}$$

The second order Taylor series is expanded about equilibrium ($\omega_\lambda = \xi_\lambda k_B T/\hbar + \omega_\lambda$), giving

$$\begin{aligned}n_\lambda &\approx \bar{n}_\lambda + \frac{\exp\left(\frac{\hbar\omega_\lambda}{k_B T}\right)}{\left(\exp\left(\frac{\hbar\omega_\lambda}{k_B T}\right) - 1\right)^2}(-\xi_\lambda) \\ &= \bar{n}_\lambda + \xi_\lambda\bar{n}_\lambda(\bar{n}_\lambda + 1)\end{aligned} \tag{A.6}$$

Where we call ξ the deviation from equilibrium which we assume to be small. We can now also use this to define

$$\frac{\partial n_\lambda}{\partial t} = -\frac{\xi_\lambda\bar{n}_\lambda(\bar{n}_\lambda + 1)}{\tau_\lambda} \tag{A.7}$$

We may now define the scattering rate for an arbitrary interaction. Here, we examine general inelastic collisions.

$$-\frac{\partial n_\lambda}{\partial t} = \sum_{\lambda'\lambda''\lambda'''} P_{\lambda\lambda'}^{\lambda''\lambda'''} - P_{\lambda''\lambda'''}^{\lambda\lambda'}, \tag{A.8}$$

where P_i^f is a transition probability from an initial to a final state. We may better understand the probabilities by expressing their initial and final states for $P_{\lambda\lambda'}^{\lambda''\lambda'''}$.

$$|i\rangle = |n_\lambda, n_{\lambda'}, n_{\lambda''}, n_{\lambda'''}\rangle \tag{A.9}$$

$$|f\rangle = |n_\lambda - 1, n_{\lambda'} - 1, n_{\lambda''} + 1, n_{\lambda'''} + 1\rangle \tag{A.10}$$

It follows that such an interaction expressed in terms of creation and annihilation operators would be,

$$\begin{aligned} a_\lambda a_{\lambda'} a^\dagger_{\lambda''} a^\dagger_{\lambda'''} |i\rangle = \\ n_\lambda n_{\lambda'}(n_{\lambda''}+1)(n_{\lambda'''}+1)\,|f\rangle\,. \end{aligned} \tag{A.11}$$

We may therefore define the transition probabilities as

$$P_{\lambda\lambda'}^{\lambda''\lambda'''} = n_\lambda n_{\lambda'}(n_{\lambda''}+1)(n_{\lambda'''}+1)Q_{\lambda\lambda'}^{\lambda''\lambda'''} \tag{A.12}$$

$$P_{\lambda''\lambda'''}^{\lambda\lambda'} = (n_\lambda+1)(n_{\lambda'}+1)n_{\lambda''}n_{\lambda'''}Q_{\lambda''\lambda'''}^{\lambda\lambda'} \tag{A.13}$$

where Q_i^f is the intrinsic scattering rate and due to the principle of micro reversibility it is unchanged by an inversion of transition direction ($Q_{\lambda''\lambda'''}^{\lambda\lambda'} = Q_{\lambda\lambda'}^{\lambda''\lambda'''}$). We may therefore express equation A.8 as

$$-\frac{\partial n_\lambda}{\partial t} = \sum_{\lambda'\lambda''\lambda'''} [n_\lambda n_{\lambda'}(n_{\lambda''}+1)(n_{\lambda'''}+1) - (n_\lambda+1)(n_{\lambda'}+1)n_{\lambda''}n_{\lambda'''}]Q_{\lambda\lambda'}^{\lambda''\lambda'''} \tag{A.14}$$

Now, using equation A.6 we may express the scattering rate in terms of the equilib-

rium distribution ($\bar{n}_\lambda$) and the deviations from it (ξ_λ). This gives

$$
\begin{aligned}
-\frac{\partial n_\lambda}{\partial t} = & \sum_{\lambda'\lambda''\lambda'''} Q_{\lambda\lambda'}^{\lambda''\lambda'''} \\
& \big[(\bar{n}_\lambda + \xi_\lambda \bar{n}_\lambda(\bar{n}_\lambda + 1))(\bar{n}_{\lambda'} + \xi_{\lambda'}\bar{n}_{\lambda'}(\bar{n}_{\lambda'} + 1)) \\
& (\bar{n}_{\lambda''} + \xi_{\lambda''}\bar{n}_{\lambda''}(\bar{n}_{\lambda''} + 1) + 1)(\bar{n}_{\lambda'''} + \xi_{\lambda'''}\bar{n}_{\lambda'''}(\bar{n}_{\lambda'''} + 1) + 1) \\
& - (\bar{n}_\lambda + \xi_\lambda \bar{n}_\lambda(\bar{n}_\lambda + 1) + 1)(\bar{n}_{\lambda'} + \xi_{\lambda'}\bar{n}_{\lambda'}(\bar{n}_{\lambda'} + 1) + 1) \\
& (\bar{n}_{\lambda''} + \xi_{\lambda''}\bar{n}_{\lambda''}(\bar{n}_{\lambda''} + 1))(\bar{n}_{\lambda'''} + \xi_{\lambda'''}\bar{n}_{\lambda'''}(\bar{n}_{\lambda'''} + 1)).\big]
\end{aligned}
\tag{A.15}
$$

Upon expansion we follow the approximation already applied. By assuming only small deviations from equilibrium, we can neglect all terms with higher order deviations. We therefore keep only terms containing a single ξ. We now expand equation A.15, as follows:

$$
\begin{aligned}
-\frac{\partial n_\lambda}{\partial t} = & \sum_{\lambda'\lambda''\lambda'''} Q_{\lambda\lambda'}^{\lambda''\lambda'''} \\
& \big[\ \bar{n}_\lambda \bar{n}_{\lambda'}(\bar{n}_{\lambda''} + 1)(\bar{n}_{\lambda'''} + 1) \\
& + \xi_\lambda \bar{n}_\lambda(\bar{n}_\lambda + 1)\bar{n}_{\lambda'}(\bar{n}_{\lambda''} + 1)(\bar{n}_{\lambda'''} + 1) \\
& + \bar{n}_\lambda \xi_{\lambda'}\bar{n}_{\lambda'}(\bar{n}_{\lambda'} + 1)(\bar{n}_{\lambda''} + 1)(\bar{n}_{\lambda'''} + 1) \\
& + \bar{n}_\lambda \bar{n}_{\lambda'}\xi_{\lambda''}\bar{n}_{\lambda''}(\bar{n}_{\lambda''} + 1)(\bar{n}_{\lambda'''} + 1) \\
& + \bar{n}_\lambda \bar{n}_{\lambda'}(\bar{n}_{\lambda''} + 1)(\xi_{\lambda'''}\bar{n}_{\lambda'''}(\bar{n}_{\lambda'''} + 1)) \\
& - (\bar{n}_\lambda + 1)(\bar{n}_{\lambda'} + 1)\bar{n}_{\lambda''}\bar{n}_{\lambda'''} \\
& - \xi_\lambda \bar{n}_\lambda(\bar{n}_\lambda + 1)(\bar{n}_{\lambda'} + 1)\bar{n}_{\lambda''}\bar{n}_{\lambda'''} \\
& - (\bar{n}_\lambda + 1)\xi_{\lambda'}\bar{n}_{\lambda'}(\bar{n}_{\lambda'} + 1)\bar{n}_{\lambda''}\bar{n}_{\lambda'''} \\
& - (\bar{n}_\lambda + 1)(\bar{n}_{\lambda'} + 1)\xi_{\lambda''}\bar{n}_{\lambda''}(\bar{n}_{\lambda''} + 1)\bar{n}_{\lambda'''} \\
& - (\bar{n}_\lambda + 1)(\bar{n}_{\lambda'} + 1)\bar{n}_{\lambda''}(\xi_{\lambda'''}\bar{n}_{\lambda'''}(\bar{n}_{\lambda'''} + 1))\big]
\end{aligned}
\tag{A.16}
$$

This may be considerably simplified by defining,

$$
Q_{\lambda\lambda'}^{\lambda''\lambda'''}\bar{n}_\lambda \bar{n}_{\lambda'}(\bar{n}_{\lambda''} + 1)(\bar{n}_{\lambda'''} + 1) = \bar{P}_{\lambda\lambda'}^{\lambda''\lambda'''} \tag{A.17}
$$

and, because in equilibrium transition, probabilities must balance

$$\bar{P}^{\lambda''\lambda'''}_{\lambda\lambda'} = \bar{P}^{\lambda\lambda'}_{\lambda''\lambda'''} \tag{A.18}$$

We may now rewrite equation A.16 as

$$\begin{aligned} -\frac{\partial n_\lambda}{\partial t} = \sum_{\lambda'\lambda''\lambda'''} & \\ & \bar{P}^{\lambda''\lambda'''}_{\lambda\lambda'}[1+\xi_\lambda(\bar{n}_\lambda+1)+\xi_{\lambda'}(\bar{n}_{\lambda'}+1)+\xi_{\lambda''}\bar{n}_{\lambda''}+\xi_{\lambda'''}\bar{n}_{\lambda'''}] \\ & -\bar{P}^{\lambda\lambda'}_{\lambda''\lambda'''}[1+\xi_\lambda\bar{n}_\lambda+\xi_{\lambda'}\bar{n}_{\lambda'}+\xi_{\lambda''}(\bar{n}_{\lambda''}+1)+\xi_{\lambda'''}(\bar{n}_{\lambda'''}+1)] \end{aligned} \tag{A.19}$$

and hence as,

$$-\frac{\partial n_\lambda}{\partial t} = \sum_{\lambda'\lambda''\lambda'''} \bar{P}^{\lambda''\lambda'''}_{\lambda\lambda'}\Big(\xi_\lambda+\xi_{\lambda'}-\xi_{\lambda''}-\xi_{\lambda'''}\Big) \tag{A.20}$$

This is the process of linearising the scattering rate and is part the methodology of the single mode relaxation time (SMRT). The final step in the application of SMRT is to reduce all but the phonons of state λ to equilibrium (i.e. $\xi_{\lambda'} = \xi_{\lambda''} = \xi_{\lambda'''} = 0$). Equation A.7 can then be applied to obtain a value for the scattering rate.

A.2 Three Phonon

The example of the three phonon scattering rate is provided. The scattering rate may be written for the three phonon process as

$$\frac{\partial n_\lambda}{\partial t} = \sum_{\lambda'\lambda''}\left[\Big(P^{\lambda'}_{\lambda\lambda''}-P^{\lambda\lambda''}_{\lambda'}\Big)+\frac{1}{2}\Big(P^{\lambda'\lambda''}_{\lambda}-P^{\lambda}_{\lambda'\lambda''}\Big)\right] \tag{A.21}$$

This may be linearised following the methodology outlined in the previous section to give,

$$\frac{\partial n_\lambda}{\partial t} = \sum_{\lambda'\lambda''}\left[P^{\lambda'}_{\lambda\lambda''}(\xi_\lambda+\xi_{\lambda'}-\xi_{\lambda''})+\frac{1}{2}P^{\lambda'\lambda''}_{\lambda}(\xi_\lambda-\xi_{\lambda'}-\xi_{\lambda''})\right] \tag{A.22}$$

Now the single mode relaxation time approximation can be applied ($\xi_{\lambda'} = \xi_{\lambda''} = 0$)

$$\frac{\partial n_\lambda}{\partial t} = \sum_{\lambda'\lambda''} \left[P^{\lambda'}_{\lambda\lambda''}\xi_\lambda + \frac{1}{2} P^{\lambda'\lambda''}_{\lambda}\xi_\lambda \right] \tag{A.23}$$

From here the equation A.7 can substituted in to obtain,

$$\tau^{-1}_{\mathbf{q}s} = \frac{1}{\bar{n}_{\mathbf{q}s}(\bar{n}_{\mathbf{q}s}+1)} \sum_{\mathbf{q}'s'\mathbf{q}''s''} \bar{P}^{\mathbf{q}''s''}_{\mathbf{q}s\mathbf{q}'s'} + \frac{1}{2}\bar{P}^{\mathbf{q}'s'\mathbf{q}''s''}_{\mathbf{q}s}, \tag{A.24}$$

The scattering rate is now in terms of only equilibrium properties.

Appendix B

Brillouin Zone Integration Scheme

Periodic functions of a crystal often require an integration over the Brillouin zone. Such summations are needed for charge density, energy and scattering rates; indeed this applies to any continuous property of the solid. We can define a periodic function $f(\mathbf{k})$ and its average over the Brillouin zone as

$$\bar{f} = V_0 \int_{BZ} f(\mathbf{k}) d^3\mathbf{k}, \tag{B.1}$$

where V_0 is the unit cell volume (equivalent to one over the k-space volume). The periodic function $f(\mathbf{k})$ may be expanded as a Fourier series.

$$f(\mathbf{k}) = \sum_{\vec{T}} f(\vec{T}) e^{\mathrm{i}\mathbf{k}\cdot\vec{T}} \tag{B.2}$$

where $\vec{T}$ are the translation vectors of the crystal and $f(\vec{T})$ are Fourier coefficients. The contribution of higher order values of $\vec{T}$ are reduced exponentially. This is analogous to the manner in which integrations of successive orders of plane waves return smaller values. Due to the fact that the higher orders have diminishing returns, equation B.2 may be truncated to a finite sum.

The integration in equation B.1 can be carried out numerically as

$$\bar{f} = \sum_{i=1}^{N} w_i f(\mathbf{k}_i) + \mathcal{R}, \tag{B.3}$$

where w_i is the i'th weighting factor, (this is included for summations over the irreducible Brillouin zone), $f(\mathbf{k}_i)$ is the value of the function at the i'th k-point and $\mathcal{R}$ is the remainder. The remainder my be treated as small for appropriate k-point samplings. The method proposed by Monkhorst and Pack [91] is the predominant approach for Brillouin zone integration schemes. It give a uniform set of points determined by a simple formula and is valid for any crystal.

$$\mathbf{k}_{n_1,n_2,n_3} \equiv \sum_{\alpha}^{3} \frac{2n_\alpha - N_\alpha - 1}{2N_\alpha} \mathbf{G}_\alpha, \tag{B.4}$$

where N_α is the total number of k-points along the direction of the reciprocal lattice vector $\mathbf{G}_\alpha$ and $n_\alpha = 1, 2, ..., N_\alpha$. This k-point set exactly integrates a function of $N_\alpha \vec{T}_\alpha$ Fourier components.

Appendix C

2D Phonon Specific Heat

The specific heat at constant volume is defined as the rate of change of internal energy with temperature.

$$C_V = \left.\frac{\partial U}{\partial T}\right|_V, \tag{C.1}$$

where the internal energy can be defined under the Debye model as,

$$U = \int_0^{\omega_D} D(\omega)\ \hbar\omega\ \bar{n}\ d\omega, \tag{C.2}$$

where $D(\omega)$ is the phonon density of states, $\hbar\omega$ is the phonon energy and $\bar{n}$ is the Bose-Einstein distribution. In order to evaluate the specific heat in 2 dimensions it is necessary to define the 2D density of states.

In two dimensions the q-area occupied by a single state is $\left(\frac{2\pi}{L}\right)^2$. We now equate the total number of states in the form of an integral over the density of states with respect to angular frequency and an q-space integral over the states per

q-area.

$$\begin{aligned} N = \int D(\omega) d\omega &= \int D(q) dq_x dq_y \\ &= \int \left(\frac{L}{2\pi}\right)^2 dq_x dq_y. \end{aligned} \tag{C.3}$$

Changing from cartisian to polar area element gives,

$$D(\omega) d\omega = \frac{L^2 q}{2\pi} dq, \tag{C.4}$$

where we drop the integral.

The Debye dispersion relation is used can be used to define the density of states in terms of frequency.

$$\omega = \nu q, \tag{C.5}$$

giving,

$$D(\omega) = \frac{L^2 \omega}{2\pi \nu^2}. \tag{C.6}$$

This is the 2D density of states.

Substituting Eq. C.6 into Eq. C.2 and writing out the Bose-Einstein distribution in full gives

$$U = \int_0^{\omega_D} \left(\frac{L^2 \omega}{2\pi \nu^2}\right) \hbar\omega \left(e^{\hbar\omega/k_B T} - 1\right)^{-1} d\omega \tag{C.7}$$

This can be simplified using the substitution $x = \hbar\omega/k_B T$ and expressing the upper bound on the integration as $x = \Theta/T$ where $\Theta = \hbar\omega_D/k_B$ thus replicating the upper bound of $\omega = \omega_D$. This results in the new expression

$$U = 2\left(\frac{L^2 k_B^2}{4\pi \nu^2 \hbar^2}\right) k_B T^3 \int_0^{\Theta/T} \left(\frac{x^2}{e^x - 1}\right) dx. \tag{C.8}$$

By imposing the low temperature limit the integral may be evaluated as,

$$\int_0^\infty \left(\frac{x^2}{e^x - 1}\right) dx = 2\zeta(3) \approx 2.404... \tag{C.9}$$

We may simplify the expression C.8 further by evaluating the integral for the total number of available states

$$N = \int_0^{\omega_D} D(\omega) d\omega = \int_0^{\omega_D} \frac{L^2 \omega}{2\pi\nu^2} d\omega = \frac{L^2 \omega_D^2}{4\pi\nu^2}. \tag{C.10}$$

Using the Debye temperature we may define the relationship,

$$\frac{N}{\Theta^2} = \frac{L^2 k_B^2}{4\pi\nu^2\hbar^2}. \tag{C.11}$$

Substituting Eq. C.9 and Eq. C.11 into equation C.8 gives,

$$U = 4Nk_BT\left(\frac{T}{\Theta}\right)^2 \zeta(3). \tag{C.12}$$

With this definition of the phonon internal energy the the 2D phonon specific heat at constant volume can be defied as,

$$C_V = \left.\frac{\partial U}{\partial T}\right|_V = 12Nk_B\left(\frac{T}{\Theta}\right)^2 \zeta(3). \tag{C.13}$$

This expression shows the typical T^2 dependency expected of 2D materials.

Appendix D

TMDC Tight Binding Model

D.1 The Hamiltonian

We construct a tight binding Hamiltonian to investigate the nature of the interlayer interaction. The work of Fang *et. al.*[147] and Liu *et al.*[146] discussed the interactions between d-orbitals and how they are mediated by the p-orbitals. Fang *et. al.*[147] specifically draw attention to the importance of the interlayer interaction between the d_{z^2} and p_z orbitals.

The model presented here for the interlayer interaction demonstrates that the ΔE_Γ splitting (see chapter 4) is driven by an interaction between the M-ion d_{z^2} orbitals and p_z orbitals of the X-ions within an adjacent layer. The bilayer Hamiltonian ($\mathcal{H}_{BL}$) takes the form

$$\mathcal{H}_{BL} = \begin{pmatrix} \mathcal{H}_M & \mathcal{H}_I \\ \mathcal{H}_I^\dagger & \mathcal{H}_M \end{pmatrix}, \tag{D.1}$$

where $\mathcal{H}_M$ is the monolayer TMDC Hamiltonian and $\mathcal{H}_I$ is the interlayer Hamiltonian.

The monolayer Hamiltonian is constructed from the d-orbitals of the M-ion and the p_z orbitals of the two X-ions. The basis states are $\phi_\alpha = \{p_z^t, p_z^b, d_{z^2}, d_{x^2-y^2}, d_{xy}\}$, where the p_z orbitals of the top and bottom X-ions are denoted p_z^t and p_z^b respectively. The full monolayer Hamiltonian is written,

$$\mathcal{H}_M = \begin{pmatrix} \mathcal{H}_p & \mathcal{H}_{pd} \\ \mathcal{H}_{dp} & \mathcal{H}_d \end{pmatrix} = \begin{pmatrix} h_1 & h_{12} & h_{13} & 0 & 0 \\ h_{21} & h_2 & h_{23} & 0 & 0 \\ h_{31} & h_{32} & h_3 & h_{34} & h_{35} \\ 0 & 0 & h_{43} & h_4 & h_{45} \\ 0 & 0 & h_{53} & h_{54} & h_5 \end{pmatrix} \tag{D.2}$$

Here the p-orbital Hamiltonian is formed of h_{11}, h_{22} and h_{12} and the d-orbital block is formed of h_{33}, h_{44}, h_{55}, h_{34}, h_{35} and h_{45} as well as their Hermitian conjugates. As can be seen from equation D.2 the p-orbital block interacts with the d-orbitals via the $\langle p_z^t | d_{z^2} \rangle$ and $\langle p_z^b | d_{z^2} \rangle$ interactions (corresponding to h_{13} & h_{23}). These interaction terms are necessary if the d_{z^2} orbitals of adjacent layers are to interact via the p-orbitals. The matrix elements of the monolayer Hamiltonian are:

$$h_1 = \varepsilon_p$$

$$h_2 = \varepsilon_p$$

$$h_{12} = V_{z-z}\cos(\delta_{\mathrm{x}} c) + \mathrm{i} V_{z-z}\sin(\delta_{\mathrm{x}} c)$$

$$h_3 = 2[\cos(2a) + \cos(a)\cos(b)]V_{z^2-z^2} + \varepsilon_{z^2}$$

$$h_4 = 2\cos(2a)V_{xy-xy} + (V_{xy-xy} + 3V_{yx-yx})\cos(a)\cos(b) + \varepsilon_{xy}$$

$$h_5 = 2\cos(2a)V_{yx-yx} + (3V_{xy-xy} + V_{yx-yx})\cos(a)\cos(b) + \varepsilon_{xy}$$

$$h_{34} = -2\sqrt{3}\,\sin(a)\sin(b)V_{z^2-yx} + 2\mathrm{i}[\sin(2a) + \sin(a)\cos(b)]V_{z^2-xy}$$

$$h_{35} = 2[\cos(2a) - \cos(a)\cos(b)]V_{z^2-yx} + 2\mathrm{i}\sqrt{3}\,\cos(a)\sin(b)V_{z^2-xy}$$

$$h_{45} = \sqrt{3}\,(V_{yx-yx} - V_{xy-xy})\sin(a)\sin(b) + 4\mathrm{i}\,\sin(a)[\cos(a) - \cos(b)]V_{xy-yx}$$

$$h_{13} = V_{z^2-z}\; e^{\mathrm{i}\delta_i c}\left[e^{\mathrm{i}a}e^{\mathrm{i}b/3} + e^{-\mathrm{i}a}e^{\mathrm{i}b/3} + e^{-\mathrm{i}2b/3}\right]$$

$$h_{23} = V_{z^2-z}\ e^{-\mathrm{i}\delta_i c}\left[e^{\mathrm{i}a}e^{\mathrm{i}b/3} + e^{-\mathrm{i}a}e^{\mathrm{i}b/3} + e^{-\mathrm{i}2b/3}\right]$$

All index inversions are Hermitian conjugates ($h^{\dagger}_{xy} = h_{yx}$). There are three on-site energy parameters $\{\varepsilon_p, \varepsilon_{z^2}, \varepsilon_{xy}\}$ and 8 bond energies, $\{V_{z-z}$, $V_{z^2-z^2}$, V_{xy-xy}, V_{yx-yx}, V_{z^2-yx}, V_{z^2-xy}, V_{xy-yx}, $V_{z^2-z}\}$, δ_i is the interlayer distance and δ_{x} is the intralayer X-ion to X-ion separation. The variables a, b and c are defined $1/2k_x$, $\sqrt{3}/2k_y$ and k_z, respectively. It must be noted that in the 2D regime $k_z = c = 0$.

The interlayer Hamiltonian presented here is designed to facilitate an interaction between the d_{z^2} orbitals of layers 1 and 2 both directly and indirectly. The ΔE_{Γ} splitting is shown to occur due to the interaction between the d_{z^2} orbitals of the M-ions in adjacent layers[144, 145, 303]. Here we define a bilayer with layer 1 sitting above layer 2, the upper X-ion is labeled "t" and the lower X-ion as "b"; the full set of basis states for the bilayer Hamiltonian are $\phi_\alpha = \{p_z^{1t}, p_z^{1b}, d^1_{z^2}, d^1_{x^2-y^2}, d^1_{xy}, p_z^{2t}, p_z^{2b}, d^2_{z^2}$ $, d^2_{x^2-y^2}, d^2_{xy}\}$. The simple direct interaction is driven by the overlap $\left\langle d^1_{z^2}\middle|d^2_{z^2}\right\rangle$ while the indirect interaction is mediated by the p_z orbitals of the X-ions and takes the form of two overlaps, $\left\langle d^1_{z^2}\middle|p_z^{2t}\right\rangle$ and $\left\langle d^2_{z^2}\middle|p_z^{1b}\right\rangle$. The opposite interactions ($\left\langle d^1_{z^2}\middle|p_z^{2b}\right\rangle$ and $\left\langle d^2_{z^2}\middle|p_z^{1t}\right\rangle$) are neglected in the bilayer case.

The interlayer Hamiltonian can written as,

$$\mathcal{H}_I = \begin{pmatrix} 0 & 0 & 0 & 0 & 0 \\ 0 & 0 & h^{12}_{23} & 0 & 0 \\ h^{12}_{31} & 0 & h^{12}_{33} & 0 & 0 \\ 0 & 0 & 0 & 0 & 0 \\ 0 & 0 & 0 & 0 & 0 \end{pmatrix}, \tag{D.3}$$

where the superscript index represents the layer and the subscript index represents the atomic orbital. The direct interaction between the d-orbitals is governed by the h^{12}_{33} element. The indirect interaction is governed by h^{12}_{23} and h^{12}_{31}. The matrix elements of the interlayer interaction Hamiltonian are listed:

ε_p	ε_{z^2}	ε_{xy}	V_{z-z}	$V_{z^2-z^2}$	V_{xy-xy}	V_{yx-yx}	V_{z^2-yx}	V_{z^2-xy}	V_{xy-yx}	V_{z^2-z}
-3.0	1.046	2.104	-0.1	-0.184	0.218	0.057	0.507	0.401	0.338	0.300

Table D.1. The set of parameter values used to produce test bandstructures. Where possible the parameter values are taken from Liu *et al.*[303].

$$h_{33}^{12} = 2\mathrm{I}_0\cos(c)[2\cos(a)\cos(b/3) + \cos(2b/3)] + 2\mathrm{i}\mathrm{I}_0\cos(c)[2\cos(a)\sin(b/3) + \sin(2b/3)]$$

$$h_{23}^{12} = \mathrm{I}_1\cos((\delta_i - \tfrac{\delta_x}{2})c) - \mathrm{i}\mathrm{I}_1\sin((\delta_i - \tfrac{\delta_x}{2})c)$$

$$h_{31}^{12} = \mathrm{I}_1 cos((\delta_i - \tfrac{\delta_x}{2})c) + \mathrm{i}\mathrm{I}_1 sin((\delta_i - \tfrac{\delta_x}{2})c)$$

The interlayer matrix elements reveal 2 interaction parameters I_0 and I_1. The parameter I_0 determines the strength of the direct d_{z^2} interaction; setting this parameter to zero prevents the direct interaction between d_{z^2} orbitals. The parameter I_1 controls the strength of the interactions between p_z and d_{z^2} orbitals.

D.2 Band Splitting

The bilayer Hamiltonian is used to produce a selection of bandstructures. One bandstructure is generated with no interlayer interaction, a second is generated with a direct interaction between d_{z^2} orbitals and a third is generated using an indirect

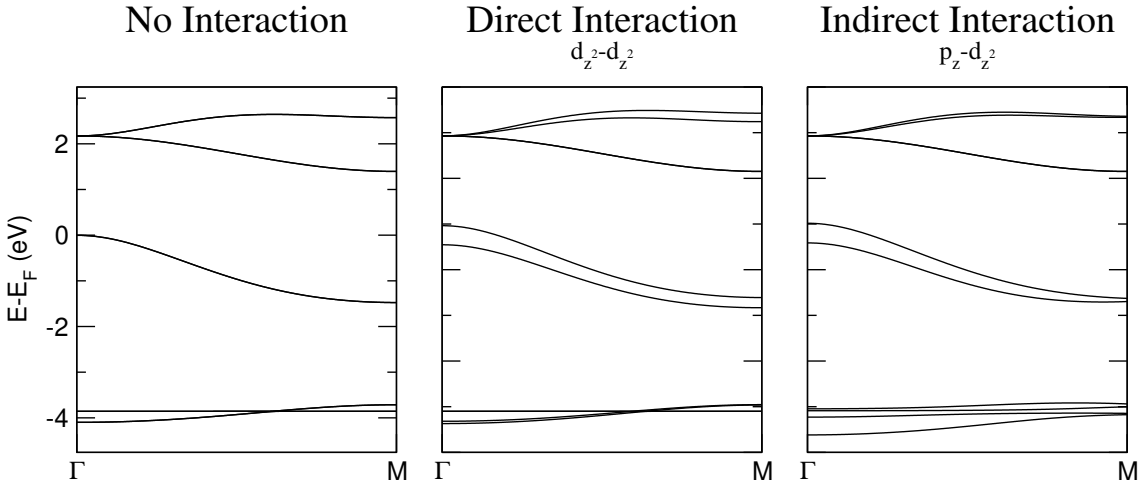

Figure D.1. Caption

interaction mediated by the p_z orbitals. The set of parameter values unrelated to the interlayer interaction are given in table D.1. There are 3 sets of interlayer interaction strengths, they are: $\{\mathrm{I}_0 = 0.00, \mathrm{I}_1 = 0.00\}$ for no interaction, $\{\mathrm{I}_0 = 0.05, \mathrm{I}_1 = 0.00\}$ for the direct interaction and $\{\mathrm{I}_0 = 0.00, \mathrm{I}_1 = 0.50\}$ for the indirect interaction. The splitting for each interaction is shown in figure D.1.

The three bandstructures (see fig. D.1) demonstrate that the indirect interaction properly replicates the Γ point splitting in the valence band due to the direct interaction.

Appendix E

Acknowledgement of funding and resources

Via our membership of the UK's HEC Materials Chemistry Consortium, which is funded by EPSRC, United Kingdom (EP/L000202, EP/R029431), this work used the ARCHER UK National Supercomputing Service (http://www.archer.ac.uk). This work also used the Isambard 2 UK National Tier-2 HPC Service (http://gw4.ac.uk/isambard/) operated by GW4 and the UK Met Office, and funded by EPSRC (EP/T022078/1). Also, the author acknowledges there funding from the EPSRC, United Kingdom (EP/L015331/1).

Bibliography

[1] Gordon E Moore. "Cramming more components onto integrated circuits". In: *Electronics* 38.8 (1965), pp. 114–117.

[2] Office for National Statistics. "Internet access – households and individuals, Great Britain: 2018". In: (2018). URL: ons.gov.uk/peoplepopulationandcommunity/householdcharacteristics/homeinternetandsocialmediausage/bulletins/internetaccesshouseholdsandindividuals/2018.

[3] T. Coughlin. "Impact of COVID-19 on the Consumer Electronics Market". In: *IEEE Consumer Electronics Magazine* 10.1 (2021), pp. 58–59. DOI: 10.1109/MCE.2020.3016753.

[4] "Emerging challenges and materials for thermal management of electronics". In: *Materials Today* 17.4 (2014), pp. 163–174. ISSN: 1369-7021. DOI: https://doi.org/10.1016/j.mattod.2014.04.003.

[5] Yasushi Nanishi. "The birth of the blue LED". In: *Nature Photonics* 8.12 (2014), pp. 884–886.

[6] C. E. Kohlhase and P. A. Penzo. "Voyager mission description". In: *Space Science Reviews* 21.2 (1977), pp. 77–101. ISSN: 1572-9672. DOI: 10.1007/BF00200846. URL: https://doi.org/10.1007/BF00200846.

[7] Hee Seok Kim et al. "Relationship between thermoelectric figure of merit and energy conversion efficiency". In: *Proceedings of the National Academy of Sciences* 112.27 (2015), pp. 8205–8210.

[8] Dario Narducci et al. *Hybrid and fully thermoelectric solar harvesting*. Vol. 268. Springer, 2018.

[9] Mildred S Dresselhaus et al. "New directions for low-dimensional thermoelectric materials". In: *Advanced materials* 19.8 (2007), pp. 1043–1053.

[10] Jiangtao Wei et al. "Review of current high-ZT thermoelectric materials". In: *Journal of Materials Science* 55.27 (Sept. 2020), pp. 12642–12704. ISSN: 1573-4803. DOI: 10.1007/s10853-020-04949-0. URL: https://doi.org/10.1007/s10853-020-04949-0.

[11] L. T. Yeh. "Review of Heat Transfer Technologies in Electronic Equipment". In: *Journal of Electronic Packaging* 117.4 (Dec. 1995), pp. 333–339. ISSN: 1043-7398. DOI: 10.1115/1.2792113. eprint: https://asmedigitalcollection.asme.org/electronicpackaging/article-pdf/117/4/333/5801274/333_1.pdf. URL: https://doi.org/10.1115/1.2792113.

[12] Z S Gelmanova et al. "Electric cars. Advantages and disadvantages". In: *Journal of Physics: Conference Series* 1015 (2018), p. 052029. DOI: 10.1088/1742-6596/1015/5/052029. URL: https://doi.org/10.1088/1742-6596/1015/5/052029.

[13] R. C. Chu et al. "Review of cooling technologies for computer products". In: *IEEE Transactions on Device and Materials Reliability* 4.4 (2004), pp. 568–585. DOI: 10.1109/TDMR.2004.840855.

[14] Yabo Gao et al. "Toward Single-Layer Uniform Hexagonal Boron Nitride–Graphene Patchworks with Zigzag Linking Edges". In: *Nano Letters* 13.7 (July 2013), pp. 3439–3443. ISSN: 1530-6984. DOI: 10.1021/nl4021123. URL: https://doi.org/10.1021/nl4021123.

[15] Zheng Liu et al. "In-plane heterostructures of graphene and hexagonal boron nitride with controlled domain sizes". In: *Nature Nanotechnology* 8.2 (Feb.

2013), pp. 119–124. ISSN: 1748-3395. DOI: 10.1038/nnano.2012.256. URL: https://doi.org/10.1038/nnano.2012.256.

[16] H. Y. Hwang et al. "Emergent phenomena at oxide interfaces". In: *Nature Materials* 11.2 (2012), pp. 103–113. ISSN: 1476-4660. DOI: 10.1038/nmat3223. URL: https://doi.org/10.1038/nmat3223.

[17] Ned T Taylor et al. "The Fundamental Mechanism Behind Colossal Permittivity in Oxides". In: *Adv. Mater.* 31.51 (2019), p. 1904746. ISSN: 0935-9648. DOI: 10.1002/adma.201904746.

[18] Wei Sun Leong, Hao Gong, and John T. L. Thong. "Low-Contact-Resistance Graphene Devices with Nickel-Etched-Graphene Contacts". In: *ACS Nano* 8.1 (2014), pp. 994–1001. ISSN: 1936-0851. DOI: 10.1021/nn405834b. URL: https://doi.org/10.1021/nn405834b.

[19] K. S. Novoselov et al. "Two-dimensional atomic crystals". In: *Proceedings of the National Academy of Sciences* 102.30 (2005), pp. 10451–10453. ISSN: 0027-8424. DOI: 10.1073/pnas.0502848102. eprint: https://www.pnas.org/content/102/30/10451.full.pdf. URL: https://www.pnas.org/content/102/30/10451.

[20] Zhili Zhu et al. "Multivalency-driven formation of Te-based monolayer materials: a combined first-principles and experimental study". In: *Physical review letters* 119.10 (2017), p. 106101.

[21] M E Dávila et al. "Germanene: a novel two-dimensional germanium allotrope akin to graphene and silicene". In: *New Journal of Physics* 16.9 (2014), p. 095002. DOI: 10.1088/1367-2630/16/9/095002. URL: https://doi.org/10.1088/1367-2630/16/9/095002.

[22] K S Novoselov et al. "Two-dimensional gas of massless Dirac fermions in graphene". In: *Nature* 438.7065 (2005), pp. 197–200. ISSN: 0028-0836.

[23] Matthew J. Allen, Vincent C. Tung, and Richard B. Kaner. "Honeycomb Carbon: A Review of Graphene". In: *Chemical Reviews* 110.1 (2010), pp. 132–145. ISSN: 0009-2665. DOI: 10.1021/cr900070d. URL: https://doi.org/10.1021/cr900070d.

[24] Seongjun Park. "The puzzle of graphene commercialization". In: *Nature Reviews Materials* 1.11 (2016), p. 16085. ISSN: 2058-8437. DOI: 10.1038/natrevmats.2016.85. URL: https://doi.org/10.1038/natrevmats.2016.85.

[25] Li Lin, Hailin Peng, and Zhongfan Liu. "Synthesis challenges for graphene industry". In: *Nature Materials* 18.6 (2019), pp. 520–524. ISSN: 1476-4660. DOI: 10.1038/s41563-019-0341-4. URL: https://doi.org/10.1038/s41563-019-0341-4.

[26] S. Ghosh et al. "Extremely high thermal conductivity of graphene: Prospects for thermal management applications in nanoelectronic circuits". In: *Applied Physics Letters* 92.15 (2008), p. 151911. ISSN: 0003-6951. DOI: 10.1063/1.2907977. URL: https://doi.org/10.1063/1.2907977.

[27] R. R. Nair et al. "Fine Structure Constant Defines Visual Transparency of Graphene". In: *Science* 320.5881 (2008), pp. 1308–1308. ISSN: 0036-8075. DOI: 10.1126/science.1156965. eprint: https://science.sciencemag.org/content/320/5881/1308.full.pdf. URL: https://science.sciencemag.org/content/320/5881/1308.

[28] Sukosin Thongrattanasiri, Frank H. L. Koppens, and F. Javier Garcia de Abajo. "Complete Optical Absorption in Periodically Patterned Graphene". In: *Phys. Rev. Lett.* 108 (4 2012), p. 047401. DOI: 10.1103/PhysRevLett.108.047401. URL: https://link.aps.org/doi/10.1103/PhysRevLett.108.047401.

[29] C. R. Dean et al. "Boron nitride substrates for high-quality graphene electronics". In: *Nature Nanotechnology* 5.10 (Oct. 2010), pp. 722–726. ISSN:

1748-3395. DOI: 10.1038/nnano.2010.172. URL: https://doi.org/10.1038/nnano.2010.172.

[30] Xiaomu Wang and Fengnian Xia. "Stacked 2D materials shed light". In: *Nature Materials* 14.3 (Mar. 2015), pp. 264–265. DOI: 10.1038/nmat4218. URL: https://doi.org/10.1038/nmat4218.

[31] I. Meric et al. "Graphene Field-Effect Transistors Based on Boron–Nitride Dielectrics". In: *Proceedings of the IEEE* 101.7 (2013), pp. 1609–1619. DOI: 10.1109/JPROC.2013.2257634.

[32] Rui Dong and Irma Kuljanishvili. "Review Article: Progress in fabrication of transition metal dichalcogenides heterostructure systems". In: *Journal of Vacuum Science & Technology B* 35.3 (2017), p. 030803. ISSN: 2166-2746. DOI: 10.1116/1.4982736. URL: https://doi.org/10.1116/1.4982736.

[33] Anubhav Jain et al. "Commentary: The Materials Project: A materials genome approach to accelerating materials innovation". In: *APL Materials* 1.1 (July 2013), p. 011002. DOI: 10.1063/1.4812323. URL: https://doi.org/10.1063/1.4812323.

[34] Tawinan Cheiwchanchamnangij and Walter R. L. Lambrecht. "Quasiparticle band structure calculation of monolayer, bilayer, and bulk MoS_2". In: *Phys. Rev. B* 85 (20 May 2012), p. 205302. DOI: 10.1103/PhysRevB.85.205302. URL: https://link.aps.org/doi/10.1103/PhysRevB.85.205302.

[35] Kin Fai Mak et al. "Atomically Thin MoS_2: A New Direct-Gap Semiconductor". In: *Phys. Rev. Lett.* 105 (13 Sept. 2010), p. 136805. DOI: 10.1103/PhysRevLett.105.136805. URL: https://link.aps.org/doi/10.1103/PhysRevLett.105.136805.

[36] Hao-Wei Guo et al. "Stacking of 2D Materials". In: *Advanced Functional Materials* 31.4 (2021), p. 2007810. DOI: https://doi.org/10.1002/adfm.202007810. eprint: https://onlinelibrary.wiley.com/doi/pdf/10.

1002/adfm.202007810. URL: https://onlinelibrary.wiley.com/doi/abs/10.1002/adfm.202007810.

[37] Juan Xia et al. "Phase evolution of lithium intercalation dynamics in 2H-MoS2". In: *Nanoscale* 9.22 (2017), pp. 7533–7540. ISSN: 2040-3364. DOI: 10.1039/C7NR02028G. URL: https://doi.org/10.1039/C7NR02028G.

[38] Alexander V Kolobov and Junji Tominaga. *Two-dimensional transition-metal dichalcogenides*. Vol. 239. Springer, 2016.

[39] Qing Hua Wang et al. "Electronics and optoelectronics of two-dimensional transition metal dichalcogenides". In: *Nature Nanotechnology* 7.11 (Nov. 2012), pp. 699–712. ISSN: 1748-3395. DOI: 10.1038/nnano.2012.193. URL: https://doi.org/10.1038/nnano.2012.193.

[40] Shiang Fang et al. "Ab initio tight-binding Hamiltonian for transition metal dichalcogenides". In: *Physical Review B* 92.20 (2015), p. 205108.

[41] Aaron M Jones et al. "Spin-layer locking effects in optical orientation of exciton spin in bilayer WSe 2". In: *Nature Physics* 10.2 (2014), pp. 130–134. ISSN: 17452481. DOI: 10.1038/nphys2848.

[42] H B Xiao et al. "Influence of oxygen vacancy on the electronic structure of CaCu3Ti4O12 and its deep-level vacancy trap states by first-principle calculation". In: *J. Appl. Phys.* 111.6 (2012), p. 63713. ISSN: 00218979. DOI: 10.1063/1.3697899.

[43] Arunima K. Singh et al. "Computational Screening of 2D Materials for Photocatalysis". In: *The Journal of Physical Chemistry Letters* 6.6 (Mar. 2015), pp. 1087–1098. DOI: 10.1021/jz502646d. URL: https://doi.org/10.1021/jz502646d.

[44] Tianyi Wang et al. "MoS2-Based Nanocomposites for Electrochemical Energy Storage". In: *Advanced Science* 4.2 (Feb. 2017), p. 1600289. ISSN: 2198-3844.

DOI: 10.1002/advs.201600289. URL: https://doi.org/10.1002/advs.201600289.

[45] Yi-Chen Wu and Wei-Ren Liu. "Few-layered MoSe2 ultrathin nanosheets as anode materials for lithium ion batteries". In: *Journal of Alloys and Compounds* 813 (2020), p. 152074. ISSN: 0925-8388. DOI: https://doi.org/10.1016/j.jallcom.2019.152074. URL: https://www.sciencedirect.com/science/article/pii/S0925838819333201.

[46] L. Britnell et al. "Field-Effect Tunneling Transistor Based on Vertical Graphene Heterostructures". In: *Science* 335.6071 (Feb. 2012), p. 947. DOI: 10.1126/science.1218461. URL: https://doi.org/10.1126/science.1218461.

[47] Guangqian Ding et al. "Engineering of charge carriers: Via a two-dimensional heterostructure to enhance the thermoelectric figure of merit". In: *Nanoscale* 10.15 (2018), pp. 7077–7084. ISSN: 20403372. DOI: 10.1039/c7nr09029c.

[48] Augustin J. Hong et al. "Graphene Flash Memory". In: *ACS Nano* 5.10 (Oct. 2011), pp. 7812–7817. ISSN: 1936-0851. DOI: 10.1021/nn201809k. URL: https://doi.org/10.1021/nn201809k.

[49] Jongtae Ahn et al. "Transition metal dichalcogenide heterojunction PN diode toward ultimate photovoltaic benefits". In: *2D Materials* 3.4 (2016). ISSN: 20531583. DOI: 10.1088/2053-1583/3/4/045011.

[50] Frank Ceballos et al. "Ultrafast charge separation and indirect exciton formation in a MoS 2 -MoSe 2 van der waals heterostructure". In: *ACS Nano* 8.12 (2014), pp. 12717–12724. ISSN: 1936086X. DOI: 10.1021/nn505736z.

[51] H. U. Din et al. "Rashba spin splitting and photocatalytic properties of GeC$-$*M*SSe (*M* = Mo, W) van der Waals heterostructures". In: *Phys. Rev. B* 100 (16 Oct. 2019), p. 165425. DOI: 10.1103/PhysRevB.100.165425. URL: https://link.aps.org/doi/10.1103/PhysRevB.100.165425.

[52] Phan Thi Kim Loan et al. "Graphene/MoS2 Heterostructures for Ultrasensitive Detection of DNA Hybridisation". In: *Advanced Materials* 26.28 (July 2014), pp. 4838–4844. ISSN: 0935-9648. DOI: 10.1002/adma.201401084. URL: https://doi.org/10.1002/adma.201401084.

[53] M. O. Li et al. "Two-Dimensional Heterojunction Interlayer Tunneling Field Effect Transistors (Thin-TFETs)". In: *IEEE Journal of the Electron Devices Society* 3.3 (2015), pp. 200–207. DOI: 10.1109/JEDS.2015.2390643.

[54] MS Dresselhaus et al. "Low-dimensional thermoelectric materials". In: *Physics of the Solid State* 41.5 (1999), pp. 679–682.

[55] Chris J. Pickard and R. J. Needs. "Ab initiorandom structure searching". In: *Journal of Physics: Condensed Matter* 23.5 (2011), p. 053201. ISSN: 0953-8984. DOI: 10.1088/0953-8984/23/5/053201. URL: https://doi.org/10.1088/0953-8984/23/5/053201.

[56] L. H. Thomas. "The calculation of atomic fields". In: *Mathematical Proceedings of the Cambridge Philosophical Society* 23.5 (1927), pp. 542–548. DOI: 10.1017/S0305004100011683.

[57] Gyaneshwar P Srivastava. *Theoretical modelling of semiconductor surfaces: microscopic studies of electrons and phonons*. World Scientific, 1999.

[58] Paul AM Dirac. "Note on exchange phenomena in the Thomas atom". In: *Mathematical proceedings of the Cambridge philosophical society*. Vol. 26. 3. Cambridge University Press. 1930, pp. 376–385.

[59] Pierre Hohenberg and Walter Kohn. "Inhomogeneous electron gas". In: *Physical review* 136.3B (1964), B864.

[60] Paolo Giannozzi. *Numerical methods in quantum mechanics*. 2013. URL: http://www.fisica.uniud.it/~giannozz/Didattica/MQ/LectureNotes/mq.pdf.

[61] Richard M Martin. *Electronic structure: basic theory and practical methods*. Cambridge university press, 2004.

[62] A Togo and I Tanaka. "First principles phonon calculations in materials science". In: *Scr. Mater.* 108 (2015), pp. 1–5.

[63] Georg KH Madsen and David J Singh. "BoltzTraP. A code for calculating band-structure dependent quantities". In: *Computer Physics Communications* 175.1 (2006), pp. 67–71.

[64] Atsushi Togo, Laurent Chaput, and Isao Tanaka. "Distributions of phonon lifetimes in Brillouin zones". In: *Physical Review B* 91.9 (2015), p. 094306.

[65] Erwin Schrödinger. "An undulatory theory of the mechanics of atoms and molecules". In: *Physical review* 28.6 (1926), p. 1049.

[66] Max Born and Robert Oppenheimer. "Zur quantentheorie der molekeln". In: *Annalen der physik* 389.20 (1927), pp. 457–484.

[67] J. F. Janak. "Proof that $\frac{\partial E}{\partial n_i} = \epsilon$ in density-functional theory". In: *Phys. Rev. B* 18 (12 1978), pp. 7165–7168. DOI: 10.1103/PhysRevB.18.7165. URL: https://link.aps.org/doi/10.1103/PhysRevB.18.7165.

[68] V. I. Anisimov et al. "Density-functional theory and NiO photoemission spectra". In: *Phys. Rev. B* 48 (23 1993), pp. 16929–16934. DOI: 10.1103/PhysRevB.48.16929. URL: https://link.aps.org/doi/10.1103/PhysRevB.48.16929.

[69] John P. Perdew and Mel Levy. "Physical Content of the Exact Kohn-Sham Orbital Energies: Band Gaps and Derivative Discontinuities". In: *Phys. Rev. Lett.* 51 (20 1983), pp. 1884–1887. DOI: 10.1103/PhysRevLett.51.1884. URL: https://link.aps.org/doi/10.1103/PhysRevLett.51.1884.

[70] Jochen Heyd, Gustavo E Scuseria, and Matthias Ernzerhof. "Hybrid functionals based on a screened Coulomb potential". In: *Journal of Chemical Physics* 118.18 (2003), pp. 8207–8215. ISSN: 00219606. DOI: 10.1063/1.1564060.

[71] F Aryasetiawan and O Gunnarsson. "TheGWmethod". In: *Reports on Progress in Physics* 61.3 (1998), pp. 237–312. DOI: 10.1088/0034-4885/61/3/002. URL: https://doi.org/10.1088/0034-4885/61/3/002.

[72] Mel Levy, John P. Perdew, and Viraht Sahni. "Exact differential equation for the density and ionization energy of a many-particle system". In: *Phys. Rev. A* 30 (5 1984), pp. 2745–2748. DOI: 10.1103/PhysRevA.30.2745. URL: https://link.aps.org/doi/10.1103/PhysRevA.30.2745.

[73] Andreas Görling. "Density-functional theory for excited states". In: *Phys. Rev. A* 54 (5 1996), pp. 3912–3915. DOI: 10.1103/PhysRevA.54.3912. URL: https://link.aps.org/doi/10.1103/PhysRevA.54.3912.

[74] J. P. Perdew and Alex Zunger. "Self-interaction correction to density-functional approximations for many-electron systems". In: *Phys. Rev. B* 23 (10 1981), pp. 5048–5079. DOI: 10.1103/PhysRevB.23.5048. URL: https://link.aps.org/doi/10.1103/PhysRevB.23.5048.

[75] John P. Perdew and Yue Wang. "Accurate and simple analytic representation of the electron-gas correlation energy". In: *Phys. Rev. B* 45 (23 1992), pp. 13244–13249. DOI: 10.1103/PhysRevB.45.13244. URL: https://link.aps.org/doi/10.1103/PhysRevB.45.13244.

[76] Jianmin Tao et al. "Climbing the Density Functional Ladder: Nonempirical Meta–Generalized Gradient Approximation Designed for Molecules and Solids". In: *Phys. Rev. Lett.* 91 (14 2003), p. 146401. DOI: 10.1103/PhysRevLett.91.146401. URL: https://link.aps.org/doi/10.1103/PhysRevLett.91.146401.

[77] John P Perdew, Kieron Burke, and Matthias Ernzerhof. "The stability of ionic crystal surfaces. Journal of Physics C: Solid State Physics, 12(22), 4977." In: *Physical Review Letters* 77.18 (1996), pp. 3865–3868. ISSN: 10797114. DOI: 10.1103/PhysRevLett.77.3865. arXiv: 0927-0256(96)00008 [10.1016].

[78] Alejandro J. Garza and Gustavo E. Scuseria. "Predicting Band Gaps with Hybrid Density Functionals". In: *The Journal of Physical Chemistry Letters* 7.20 (2016), pp. 4165–4170. DOI: 10.1021/acs.jpclett.6b01807. URL: https://doi.org/10.1021/acs.jpclett.6b01807.

[79] John P. Perdew, Matthias Ernzerhof, and Kieron Burke. "Rationale for mixing exact exchange with density functional approximations". In: *The Journal of Chemical Physics* 105.22 (1996), pp. 9982–9985. DOI: 10.1063/1.472933. eprint: https://doi.org/10.1063/1.472933.

[80] K. Kim and K. D. Jordan. "Comparison of Density Functional and MP2 Calculations on the Water Monomer and Dimer". In: *The Journal of Physical Chemistry* 98.40 (1994), pp. 10089–10094. ISSN: 0022-3654. DOI: 10.1021/j100091a024.

[81] P. J. Stephens et al. "Ab Initio Calculation of Vibrational Absorption and Circular Dichroism Spectra Using Density Functional Force Fields". In: *The Journal of Physical Chemistry* 98.45 (1994), pp. 11623–11627. ISSN: 0022-3654. DOI: 10.1021/j100096a001. URL: https://doi.org/10.1021/j100096a001.

[82] M. Shishkin and G. Kresse. "Implementation and performance of the frequency-dependent *GW* method within the PAW framework". In: *Phys. Rev. B* 74 (3 2006), p. 035101. DOI: 10.1103/PhysRevB.74.035101. URL: https://link.aps.org/doi/10.1103/PhysRevB.74.035101.

[83] Kurt Binder et al. *Monte Carlo methods in statistical physics*. Springer-Verlag, New York, 1979.

[84] Gyaneshwar P Srivastava. *The physics of phonons*. Bristol: Adam Hilger, 1990. ISBN: 0852741537.

[85] Paolo Giannozzi et al. "Ab initio calculation of phonon dispersions in semiconductors". In: *Phys. Rev. B* 43 (9 1991), pp. 7231–7242. DOI: 10.1103/

PhysRevB.43.7231. URL: https://link.aps.org/doi/10.1103/PhysRevB.43.7231.

[86] R. P. Feynman. "Forces in Molecules". In: *Phys. Rev.* 56 (4 1939), pp. 340–343. DOI: 10.1103/PhysRev.56.340. URL: https://link.aps.org/doi/10.1103/PhysRev.56.340.

[87] BH Bransden and CJ Joachain. *Quantum Mechanics ,Second edition*. Pearson Education),(Original work published 1989), 2000.

[88] Iorwerth O Thomas and GP Srivastava. "Anharmonic, dimensionality and size effects in phonon transport". In: *Journal of Physics: Condensed Matter* 29.50 (2017), p. 505703.

[89] JM Ziman and Paul W Levy. "Electrons and phonons". In: *Physics Today* 14.11 (1961), p. 64.

[90] Peter Carruthers. "Theory of thermal conductivity of solids at low temperatures". In: *Reviews of Modern Physics* 33.1 (1961), p. 92.

[91] James D Pack and Hendrik J Monkhorst. "Special points for Brillonin-zone integrations". In: *Physical Review B* 16.4 (1977), pp. 1748–1749. ISSN: 01631829. arXiv: arXiv:1011.1669v3.

[92] Rudolf Peierls. "Zur theorie der galvanomagnetischen effekte". In: *Zeitschrift für Physik* 53.3-4 (1929), pp. 255–266.

[93] R Berman. "The thermal conductivity of dielectric solids at low temperatures". In: *Advances in Physics* 2.5 (1953), pp. 103–140.

[94] HBG Casimir. "Note on the conduction of heat in crystals". In: *Physica* 5.6 (1938), pp. 495–500.

[95] Joseph Callaway. "Model for lattice thermal conductivity at low temperatures". In: *Physical Review* 113.4 (1959), p. 1046.

[96] S. P. Hepplestone and G. P. Srivastava. "Lattice dynamics and thermal properties of phononic semiconductors". In: *Phys. Rev. B - Condens. Matter Mater. Phys.* 84.11 (2011), pp. 1–13. ISSN: 10980121. DOI: 10.1103/PhysRevB.84.115326.

[97] PG Klemens. "The thermal conductivity of dielectric solids at low temperatures (theoretical)". In: *Proceedings of the Royal Society of London. Series A. Mathematical and Physical Sciences* 208.1092 (1951), pp. 108–133.

[98] PG Klemens. "The scattering of low-frequency lattice waves by static imperfections". In: *Proceedings of the Physical Society. Section A* 68.12 (1955), p. 1113.

[99] Eric J. Skoug and Donald T. Morelli. "Role of Lone-Pair Electrons in Producing Minimum Thermal Conductivity in Nitrogen-Group Chalcogenide Compounds". In: *Phys. Rev. Lett.* 107 (23 2011), p. 235901. DOI: 10.1103/PhysRevLett.107.235901. URL: https://link.aps.org/doi/10.1103/PhysRevLett.107.235901.

[100] Shin-ichiro Tamura. "Isotope scattering of dispersive phonons in Ge". In: *Physical Review B* 27.2 (1983), p. 858.

[101] John R De Laeter et al. "Atomic weights of the elements. Review 2000 (IUPAC Technical Report)". In: *Pure and applied chemistry* 75.6 (2003), pp. 683–800.

[102] Damien Tristant et al. "Phonon anharmonicity in few-layer black phosphorus". In: *ACS nano* 13.9 (2019), pp. 10456–10468.

[103] Carlos A Polanco et al. "Defect-limited thermal conductivity in MoS 2". In: *Physical Review Materials* 4.1 (2020), p. 014004.

[104] Enamul Haque, Claudio Cazorla, and M Anwar Hossain. "First-principles prediction of large thermoelectric efficiency in superionic Li 2 SnX 3 (X= S, Se)". In: *Physical Chemistry Chemical Physics* 22.2 (2020), pp. 878–889.

[105] G. Srivastava and S. Jenkins. "Atomic geometry and bonding on the GaAs(001)-$\beta 2(2 \times 4)$ surface from *ab initio* pseudopotential calculations". In: *Phys. Rev. B - Condens. Matter Mater. Phys.* 53.19 (1996), pp. 12589–12592. ISSN: 1550235X. DOI: 10.1103/PhysRevB.53.12589.

[106] Simon Vaughan. *Scientific inference: Learning from data*. Cambridge University Press, 2013.

[107] K. S. Novoselov et al. "2D materials and van der Waals heterostructures". In: *Science* 353.6298 (2016). ISSN: 0036-8075. DOI: 10.1126/science.aac9439.

[108] Xiuwen Zhang et al. "Intrinsic Transparent Conductors without Doping". In: *Phys. Rev. Lett.* 115.17 (2015), pp. 1–6. ISSN: 10797114. DOI: 10.1103/PhysRevLett.115.176602. arXiv: 1506.08884.

[109] Adolfo De Sanctis et al. "Strain-engineered inverse charge-funnelling in layered semiconductors". In: *Nature Communications* 9.1 (2018). ISSN: 20411723. DOI: 10.1038/s41467-018-04099-7.

[110] Bastian Miller et al. "Long-Lived Direct and Indirect Interlayer Excitons in van der Waals Heterostructures". In: *Nano Letters* 17.9 (2017), pp. 5229–5237. ISSN: 1530-6984. DOI: 10.1021/acs.nanolett.7b01304.

[111] Søren Ulstrup et al. "Ultrafast Band Structure Control of a Two-Dimensional Heterostructure". In: *ACS Nano* 10.6 (2016), pp. 6315–6322. ISSN: 1936086X. DOI: 10.1021/acsnano.6b02622.

[112] Pasqual Rivera et al. "Interlayer valley excitons in heterobilayers of transition metal dichalcogenides". In: *Nature nanotechnology* 13.11 (2018), pp. 1004–1015. ISSN: 17483395. DOI: 10.1038/s41565-018-0193-0.

[113] Ashish Arora et al. "Interlayer excitons in a bulk van der Waals semiconductor". In: *Nature Communications* 8.1 (2017), p. 639. ISSN: 2041-1723. DOI: 10.1038/s41467-017-00691-5.

[114] Engin Torun et al. "Interlayer and intralayer excitons in MoS2/WS2 and MoSe2/WSe2 heterobilayers". In: *Physical Review B* 97.24 (2018), p. 245427. ISSN: 24699969. DOI: 10.1103/PhysRevB.97.245427.

[115] Heather M. Hill et al. "Band Alignment in MoS2/WS2 Transition Metal Dichalcogenide Heterostructures Probed by Scanning Tunneling Microscopy and Spectroscopy". In: *Nano Letters* 16.8 (2016), pp. 4831–4837. ISSN: 15306992. DOI: 10.1021/acs.nanolett.6b01007.

[116] Woosuk Choi et al. "Twist-Angle-Dependent Optoelectronics in a Few-Layer Transition-Metal Dichalcogenide Heterostructure". In: *ACS Applied Materials and Interfaces* 11.2 (2019), pp. 2470–2478. ISSN: 19448252. DOI: 10.1021/acsami.8b15817.

[117] Ming-Hui Chiu et al. "Band Alignment of 2D Transition Metal Dichalcogenide Heterojunctions". In: *Advanced Functional Materials* 27.19 (2017), p. 1603756. ISSN: 1616301X. DOI: 10.1002/adfm.201603756.

[118] Eunhye Koo et al. "Growth Order-Dependent Strain Variations of Lateral Transition Metal Dichalcogenide Heterostructures". In: *ACS Applied Electronic Materials* 1.1 (2019), pp. 113–121.

[119] K. E. Aretouli et al. "Two-dimensional semiconductor HfSe2 and MoSe2/HfSe2 van der Waals heterostructures by molecular beam epitaxy". In: *Applied Physics Letters* 106.14 (2015), p. 143105. DOI: 10.1063/1.4917422.

[120] Ming-Hui Chiu et al. "Spectroscopic Signatures for Interlayer Coupling in MoS2–WSe2 van der Waals Stacking". In: *ACS Nano* 8 (2014), p. 9649. DOI: 10.1021/nn504229z.

[121] Ming-Hui Chiu et al. "Determination of band alignment in the single-layer MoS2/WSe2 heterojunction". In: *Nature Communications* 6 (2015), p. 7666. DOI: 10.1021/ncomms8666.

[122] Xueping Wu et al. "Vapor growth of WSe2/WS2 heterostructures with stacking dependent optical properties". In: *Nano Research* 12.12 (2019), pp. 3123–3128. ISSN: 1998-0000. DOI: 10.1007/s12274-019-2564-8.

[123] Wenjia Wang et al. "Investigation of the band alignment at MoS2/PtSe2 heterojunctions". In: *Applied Physics Letters* 114.20 (2019), p. 201601. ISSN: 00036951. DOI: 10.1063/1.5097248.

[124] Ke Xu et al. "The role of Anderson's rule in determining electronic, optical and transport properties of transition metal dichalcogenide heterostructures". In: *Physical Chemistry Chemical Physics* 20.48 (2018), pp. 30351–30364. ISSN: 14639076. DOI: 10.1039/c8cp05522j.

[125] Bin Amin, Nirpendra Singh, and Udo Schwingenschlögl. "Heterostructures of transition metal dichalcogenides". In: *Physical Review B* 92.7 (2015), p. 075439.

[126] Nicolas Mounet et al. "Two-dimensional materials from high-throughput computational exfoliation of experimentally known compounds". In: *Nature Nanotechnology* 13.3 (2018), pp. 246–252. ISSN: 17483395. DOI: 10.1038/s41565-017-0035-5.

[127] A Chaves et al. "Bandgap engineering of two-dimensional semiconductor materials". In: *npj 2D Materials and Applications* 4.1 (2020), pp. 1–21.

[128] Winfried Mönch. *Semiconductor surfaces and interfaces*. Vol. 26. Springer Science & Business Media, 2013.

[129] Kris T. Delaney, Nicola A. Spaldin, and Chris G. Van De Walle. "Theoretical study of Schottky-barrier formation at epitaxial rare-earth-metal/semiconductor interfaces". In: *Phys. Rev. B - Condens. Matter Mater. Phys.* 81.16 (2010), pp. 1–11. ISSN: 10980121. DOI: 10.1103/PhysRevB.81.165312.

[130] M Aldegunde et al. "Multi-scale simulations of a Mo/n+-GaAs Schottky contact for nano-scale III-V MOSFETs". In: *Semiconductor Science and Technology* 29.5 (2014), p. 054003. DOI: 10.1088/0268-1242/29/5/054003.

[131] Volker Heine. "Theory of Surface States". In: *Phys. Rev.* 138 (6A 1965), A1689–A1696. DOI: 10.1103/PhysRev.138.A1689. URL: https://link.aps.org/doi/10.1103/PhysRev.138.A1689.

[132] Herbert Kroemer. "Problems in the theory of heterojunction discontinuities". In: *C R C Critical Reviews in Solid State Sciences* 5.4 (1975), pp. 555–564. DOI: 10.1080/10408437508243512. eprint: https://doi.org/10.1080/10408437508243512. URL: https://doi.org/10.1080/10408437508243512.

[133] E. Louis, F. Yndurain, and F. Flores. "Metal-semiconductor junction for (110) surfaces of zinc-blende compounds". In: *Phys. Rev. B* 13 (10 1976), pp. 4408–4418. DOI: 10.1103/PhysRevB.13.4408. URL: https://link.aps.org/doi/10.1103/PhysRevB.13.4408.

[134] C Tejedor and F Flores. "A simple approach to heterojunctions". In: *Journal of Physics C: Solid State Physics* 11.1 (1977), pp. L19–L23. DOI: 10.1088/0022-3719/11/1/005. URL: https://doi.org/10.1088%2F0022-3719%2F11%2F1%2F005.

[135] Andre K Geim and Irina V Grigorieva. "Van der Waals heterostructures". In: *Nature* 499.7459 (2013), pp. 419–425.

[136] G Kresse and D Joubert. "From ultrasoft pseudopotentials to the projector augmented-wave method". In: *Physical Review B* 59.3 (1999), pp. 1758–1775. ISSN: 0163-1829. DOI: 10.1103/PhysRevB.59.1758.

[137] Stefan Grimme et al. "A consistent and accurate ab initio parametrization of density functional dispersion correction (DFT-D) for the 94 elements H-Pu". In: *Journal of Chemical Physics* 132.15 (2010), p. 130901. ISSN: 00219606. DOI: 10.1063/1.3382344.

[138] G. Kresse and J. Furthmüller. "Efficiency of ab-initio total energy calculations for metals and semiconductors using a plane-wave basis set". In: *Computational Materials Science* 6.1 (1996), pp. 15–50. ISSN: 09270256. DOI: 10.1016/0927-0256(96)00008-0.

[139] Ned Thaddeus Taylor et al. "ARTEMIS: Ab initio restructuring tool enabling the modelling of interface structures". In: *Computer Physics Communications* 257 (2020), p. 107515.

[140] Duy Le et al. "Spin-orbit coupling in the band structure of monolayer WSe2". In: *Journal of Physics Condensed Matter* 27.18 (2015), p. 182201. ISSN: 1361648X. DOI: 10.1088/0953-8984/27/18/182201.

[141] Yajun Zhang, M. P. K. Sahoo, and Jie Wang. "Tuning the band gap and polarization of BaSnO ¡sub¿3¡/sub¿ /SrSnO ¡sub¿3¡/sub¿ superlattices for photovoltaic applications". In: *Phys. Chem. Chem. Phys.* 19.10 (2017), pp. 7032–7039. ISSN: 1463-9076. DOI: 10.1039/C6CP06042K.

[142] Winfried Mönch. "Explanation of the barrier heights of graphene Schottky contacts by the MIGS-and-electronegativity concept". In: *Journal of Applied Physics* 120.10 (2016), p. 104501.

[143] Tian Tian et al. "Electronic polarizability as the fundamental variable in the dielectric properties of two-dimensional materials". In: *Nano Letters* (2020). DOI: 10.1021/acs.nanolett.9b02982.

[144] K V Shanavas and S Satpathy. "Effective tight-binding model for MX2 under electric and magnetic fields". In: *Physical Review B - Condensed Matter and Materials Physics* 91.23 (2015), p. 235145. ISSN: 1550235X. DOI: 10.1103/PhysRevB.91.235145.

[145] Alexander J Pearce, Eros Mariani, and Guido Burkard. "Tight-binding approach to strain and curvature in monolayer transition-metal dichalcogenides".

In: *Physical Review B* 94.15 (2016). ISSN: 24699969. DOI: 10.1103/PhysRevB.94.155416.

[146] Yang Liu et al. "Dielectric properties of giant permittivity NaCu3Ti3NbO12ceramics". In: *Ceram. Int.* 39.8 (2013), pp. 9201–9206. ISSN: 02728842. DOI: 10.1016/j.ceramint.2013.05.023.

[147] Shiang Fang et al. "Ab initio tight-binding Hamiltonian for transition metal dichalcogenides". In: *Physical Review B - Condensed Matter and Materials Physics* 92.20 (2015), p. 205108. ISSN: 1550235X. DOI: 10.1103/PhysRevB.92.205108.

[148] Sangyeon Pak et al. "Strain-Mediated Interlayer Coupling Effects on the Excitonic Behaviors in an Epitaxially Grown MoS2/WS2 van der Waals Heterobilayer". In: *Nano Letters* 17.9 (2017). PMID: 28832158, pp. 5634–5640. DOI: 10.1021/acs.nanolett.7b02513.

[149] Priya Johari and Vivek B. Shenoy. "Tuning the Electronic Properties of Semiconducting Transition Metal Dichalcogenides by Applying Mechanical Strains". In: *ACS Nano* 6.6 (2012). PMID: 22591011, pp. 5449–5456. DOI: 10.1021/nn301320r.

[150] H. Peelaers and C. G. Van de Walle. "Effects of strain on band structure and effective masses in MoS_2". In: *Phys. Rev. B* 86 (24 2012), p. 241401. DOI: 10.1103/PhysRevB.86.241401.

[151] Filip A. Rasmussen and Kristian S. Thygesen. "Computational 2D Materials Database: Electronic Structure of Transition-Metal Dichalcogenides and Oxides". In: *The Journal of Physical Chemistry C* 119.23 (2015), pp. 13169–13183. DOI: 10.1021/acs.jpcc.5b02950.

[152] Simone Bertolazzi, Jacopo Brivio, and Andras Kis. "Stretching and Breaking of Ultrathin MoS2". In: *ACS Nano* 5.12 (2011). PMID: 22087740, pp. 9703–9709. DOI: 10.1021/nn203879f.

[153] Seoung-Hun Kang and Young-Kyun Kwon. "Strain effects on phase transitions in transition metal dichalcogenides". In: *Current Applied Physics* 19.6 (2019), pp. 690–696.

[154] Ning Lu et al. "MoS2/MX2 heterobilayers: bandgap engineering via tensile strain or external electrical field". In: *Nanoscale* 6 (5 2014), pp. 2879–2886. DOI: 10.1039/C3NR06072A.

[155] Pasqual Rivera et al. "Observation of long-lived interlayer excitons in monolayer MoSe 2–WSe 2 heterostructures". In: *Nature communications* 6.1 (2015), pp. 1–6.

[156] Satoru Ichinokura et al. "Superconducting calcium-intercalated bilayer graphene". In: *Acs Nano* 10.2 (2016), pp. 2761–2765.

[157] Alexander A Balandin et al. "Superior thermal conductivity of single-layer graphene". In: *Nano letters* 8.3 (2008), pp. 902–907.

[158] Aamir Shafique, Abdus Samad, and Young-Han Shin. "Ultra low lattice thermal conductivity and high carrier mobility of monolayer SnS 2 and SnSe 2: a first principles study". In: *Physical Chemistry Chemical Physics* 19.31 (2017), pp. 20677–20683.

[159] R. Abinaya et al. "Interface driven energy-filtering and phonon scattering of polyaniline incorporated ultrathin layered molybdenum disulphide nanosheets for promising thermoelectric performance". In: *Journal of Colloid and Interface Science* 584 (2021), pp. 295–309. ISSN: 0021-9797. DOI: https://doi.org/10.1016/j.jcis.2020.09.061.

[160] Xue-Kun Chen, Yu-Jia Zeng, and Ke-Qiu Chen. "Thermal Transport in Two-Dimensional Heterostructures". In: *Frontiers in Materials* 7 (2020), p. 427. ISSN: 2296-8016. DOI: 10.3389/fmats.2020.578791.

[161] Yuxi Wang et al. "Thermal properties of two dimensional layered materials". In: *Advanced Functional Materials* 27.19 (2017), p. 1604134.

[162] D Dragoman and M Dragoman. "Giant thermoelectric effect in graphene". In: *Applied Physics Letters* 91.20 (2007), p. 203116.

[163] Yiming Zhou and Li-Dong Zhao. "Promising thermoelectric bulk materials with 2D structures". In: *Advanced Materials* 29.45 (2017), p. 1702676.

[164] DD Fan et al. "MoS2 nanoribbons as promising thermoelectric materials". In: *Applied physics letters* 105.13 (2014), p. 133113.

[165] Guo Huai-Hong et al. "Theoretical study of thermoelectric properties of MoS2". In: *Chinese Physics B* 23.1 (2013), p. 017201.

[166] Hasan Babaei, JM Khodadadi, and Sanjiv Sinha. "Large theoretical thermoelectric power factor of suspended single-layer MoS2". In: *Applied Physics Letters* 105.19 (2014), p. 193901.

[167] "Control of thermal conductivity with species mass in transition-metal dichalcogenides". In: *Journal of Applied Physics* 123.13 (Apr. 2018), p. 135703. ISSN: 0021-8979. DOI: 10.1063/1.5017034. URL: http://dx.doi.org/10.1063/1.5017034%20http://aip.scitation.org/doi/10.1063/1.5017034.

[168] Daniel O. Lindroth and Paul Erhart. "Thermal transport in van der Waals solids from first-principles calculations". In: *Physical Review B* 94.11 (2016), pp. 1–11. ISSN: 24699969. DOI: 10.1103/PhysRevB.94.115205.

[169] Koichi Nakamura. "First-principles simulation on thermoelectric properties of transition metal dichalcogenide monolayers". In: *Japanese Journal of Applied Physics* 57.6 (2018). ISSN: 13474065. DOI: 10.7567/JJAP.57.06HE04.

[170] Guangqian Ding et al. "Thermoelectric properties of monolayer MSe2 (M = Zr, Hf): Low lattice thermal conductivity and a promising figure of merit". In: *Nanotechnology* 27.37 (2016). ISSN: 13616528. DOI: 10.1088/0957-4484/27/37/375703.

[171] Nina Glebko and Antti J Karttunen. "Lattice thermal conductivity of TiS 2, ZrS 2, and HfS 2: Periodic trends studied by dispersion-corrected hybrid density functional methods". In: *Physical Review B* 100.2 (2019), p. 024301.

[172] Yunshan Zhao et al. "Studying thermal transport in suspended monolayer molybdenum disulfide prepared by a nano-manipulator-assisted transfer method". In: *Nanotechnology* 31.22 (2020). ISSN: 13616528. DOI: 10.1088/1361-6528/ab7647.

[173] Insun Jo et al. "Basal-plane thermal conductivity of few-layer molybdenum disulfide". In: *Applied Physics Letters* 104.20 (2014). ISSN: 00036951. DOI: 10.1063/1.4876965. URL: http://dx.doi.org/10.1063/1.4876965.

[174] Puqing Jiang et al. "Probing Anisotropic Thermal Conductivity of Transition Metal Dichalcogenides MX2 (M = Mo, W and X = S, Se) using Time-Domain Thermoreflectance". In: *Advanced Materials* 29.36 (Sept. 2017), p. 1701068. ISSN: 15214095. DOI: 10.1002/adma.201701068. URL: http://doi.wiley.com/10.1002/adma.201701068.

[175] Adili Aiyiti et al. "Thermal conductivity of suspended few-layer MoS 2". In: *Nanoscale* 10.6 (2018), pp. 2727–2734.

[176] Yifei Yu et al. "In-Plane and Interfacial Thermal Conduction of Two-Dimensional Transition-Metal Dichalcogenides". In: *Physical Review Applied* 13.3 (2020), p. 1. ISSN: 23317019. DOI: 10.1103/PhysRevApplied.13.034059. URL: https://doi.org/10.1103/PhysRevApplied.13.034059.

[177] Jung Jun Bae et al. "Thickness-dependent in-plane thermal conductivity of suspended MoS2 grown by chemical vapor deposition". In: *Nanoscale* 9.7 (2017), pp. 2541–2547. ISSN: 20403372. DOI: 10.1039/c6nr09484h.

[178] Rusen Yan et al. "Thermal conductivity of monolayer molybdenum disulfide obtained from temperature-dependent Raman spectroscopy". In: *ACS Nano* 8.1 (2014), pp. 986–993. ISSN: 19360851. DOI: 10.1021/nn405826k.

[179] Jarosaw Judek et al. "High accuracy determination of the thermal properties of supported 2D materials". In: *Scientific Reports* 5 (2015), pp. 1–11. ISSN: 20452322. DOI: 10.1038/srep12422.

[180] Yi Chang et al. "Synthesis process and thermoelectric properties of the layered crystal structure SnS 2". In: *Journal of Materials Science: Materials in Electronics* 31.7 (2020), pp. 5425–5433.

[181] Chunlei Wan et al. "Flexible n-type thermoelectric materials by organic intercalation of layered transition metal dichalcogenide TiS2". In: *Nature Materials* 14.6 (2015), pp. 622–627. ISSN: 1476-4660. DOI: 10.1038/nmat4251. URL: https://doi.org/10.1038/nmat4251.

[182] H. Imai, Y. Shimakawa, and Y. Kubo. "Large thermoelectric power factor in TiS_2 crystal with nearly stoichiometric composition". In: *Phys. Rev. B* 64 (24 2001), p. 241104. DOI: 10.1103/PhysRevB.64.241104. URL: https://link.aps.org/doi/10.1103/PhysRevB.64.241104.

[183] Yuan Cao et al. "Unconventional superconductivity in magic-angle graphene superlattices". In: *Nature* 556.7699 (2018), pp. 43–50.

[184] Yuan Cao et al. "Correlated insulator behaviour at half-filling in magic-angle graphene superlattices". In: *Nature* 556.7699 (2018), pp. 80–84.

[185] Jingchao Zhang et al. "Phonon thermal properties of transition-metal dichalcogenides MoS2 and MoSe2 heterostructure". In: *The Journal of Physical Chemistry C* 121.19 (2017), pp. 10336–10344.

[186] Zhongwei Zhang et al. "Hexagonal boron nitride: a promising substrate for graphene with high heat dissipation". In: *Nanotechnology* 28.22 (2017), p. 225704. DOI: 10.1088/1361-6528/aa6e49.

[187] Jiang-Jiang Ma et al. "First-principles calculations of thermal transport properties in MoS 2/MoSe 2 bilayer heterostructure". In: *Physical Chemistry Chemical Physics* 21.20 (2019), pp. 10442–10448.

[188] Lucas Lindsay et al. "Perspective on ab initio phonon thermal transport". In: *Journal of Applied Physics* 126.5 (2019), p. 050902. ISSN: 0021-8979. DOI: 10.1063/1.5108651. URL: https://doi.org/10.1063/1.5108651.

[189] V Zólyomi, ND Drummond, and VI Fal'Ko. "Electrons and phonons in single layers of hexagonal indium chalcogenides from ab initio calculations". In: *Physical Review B* 89.20 (2014), p. 205416.

[190] Xiaorong Gan et al. "2H/1T Phase Transition of Multilayer MoS2 by Electrochemical Incorporation of S Vacancies". In: *ACS Applied Energy Materials* 1.9 (2018), pp. 4754–4765. DOI: 10.1021/acsaem.8b00875. URL: https://doi.org/10.1021/acsaem.8b00875.

[191] I Pallecchi et al. "Review on thermoelectric properties of transition metal dichalcogenides". In: *Nano Futures* 4.3 (2020), p. 032008.

[192] Xiaokun Gu and C.Y. Zhao. "Thermal conductivity of single-layer MoS2(1-x)Se2x alloys from molecular dynamics simulations with a machine-learning-based interatomic potential". In: *Computational Materials Science* 165 (2019), pp. 74–81. ISSN: 0927-0256. DOI: https://doi.org/10.1016/j.commatsci.2019.04.025. URL: https://www.sciencedirect.com/science/article/pii/S0927025619302356.

[193] S. P. Hepplestone and G. P. Srivastava. "Theory of interface scattering of phonons in superlattices". In: *Phys. Rev. B - Condens. Matter Mater. Phys.* 82.14 (2010), pp. 1–6. ISSN: 10980121. DOI: 10.1103/PhysRevB.82.144303.

[194] Francis H Davies et al. "Band alignment of transition metal dichalcogenide heterostructures". In: *Physical Review B* 103.4 (2021), p. 045417.

[195] Bjørn Jamtveit and Paul Meakin, eds. *Growth, Dissolution and Pattern Formation in Geosystems*. Dordrecht: Springer Netherlands, 1999. ISBN: 978-90-481-4030-5. DOI: 10.1007/978-94-015-9179-9.

[196] Herbert Kroemer. "Nobel Lecture: Quasielectric fields and band offsets: teaching electrons new tricks". In: *Reviews of Modern Physics* 73.3 (2001), pp. 783–793. ISSN: 0034-6861. DOI: 10.1103/RevModPhys.73.783.

[197] R. L. Anderson. "Germanium-Gallium Arsenide Heterojunctions [Letter to the Editor]". In: *IBM Journal of Research and Development* 4.3 (1960), pp. 283–287. ISSN: 0018-8646. DOI: 10.1147/rd.43.0283.

[198] David O. Scanlon et al. "Band alignment of rutile and anatase TiO2". In: *Nat. Mater.* 12.9 (2013), pp. 798–801. ISSN: 14761122. DOI: 10.1038/nmat3697.

[199] Rebecca Saive et al. "Study of the interface in a GaP/Si heterojunction solar cell". In: *IEEE J. Photovoltaics* 8.6 (2018), pp. 1568–1576. ISSN: 21563381. DOI: 10.1109/JPHOTOV.2018.2861724.

[200] N F Mott. "Note on the contact between a metal and an insulator or semiconductor". In: *Math. Proc. Cambridge Philos. Soc.* 34.4 (1938), pp. 568–572. ISSN: 0305-0041. DOI: 10.1017/S0305004100020570.

[201] John Bardeen. "Surface states and rectification at a metal semi-conductor contact". In: *Phys. Rev.* 71.10 (1947), pp. 717–727. ISSN: 0031899X. DOI: 10.1103/PhysRev.71.717.

[202] S.-M. Lee, David G. Cahill, and Rama Venkatasubramanian. "Thermal conductivity of Si–Ge superlattices". In: *Appl. Phys. Lett.* 70.22 (1997), pp. 2957–2959. ISSN: 0003-6951. DOI: 10.1063/1.118755.

[203] L. Wang et al. "Effect of interface on the thermal conductivity of thermal barrier coatings: A numerical simulation study". In: *Int. J. Heat Mass Transf.* 79 (2014), pp. 954–967. ISSN: 00179310. DOI: 10.1016/j.ijheatmasstransfer.2014.08.088.

[204] Richard M. Martin. "Atomic reconstruction at polar interfaces of semiconductors". In: *J. Vac. Sci. Technol.* 17.5 (1980), pp. 978–981. ISSN: 0022-5355. DOI: 10.1116/1.570651.

[205] S. P. Hepplestone and P. V. Sushko. "Effect of metal intermixing on the Schottky barriers of Mo(100)/GaAs(100) interfaces". In: *J. Appl. Phys.* 116.19 (2014). ISSN: 10897550. DOI: 10.1063/1.4902009.

[206] Fang Liu et al. "Temperature-Induced Atomic Reconstruction At $Au/MgAl_2O_4$ Interfaces". In: *Adv. Mater. Interfaces* 5.12 (2018), pp. 2–7. ISSN: 21967350. DOI: 10.1002/admi.201701664.

[207] Hyobin Yoo et al. "Atomic and electronic reconstruction at the van der Waals interface in twisted bilayer graphene". In: *Nat. Mater.* 18.5 (2019), pp. 448–453. ISSN: 14764660. DOI: 10.1038/s41563-019-0346-z. arXiv: 1804.03806.

[208] Tingjun Wu and Peng Gao. "Development of perovskite-type materials for thermoelectric application". In: *Materials (Basel).* 11.6 (2018), pp. 1–32. ISSN: 19961944. DOI: 10.3390/ma11060999.

[209] J. F. Wager. "Transparent electronics: Schottky barrier and heterojunction considerations". In: *Thin Solid Films* 516.8 (2008), pp. 1755–1764. ISSN: 00406090. DOI: 10.1016/j.tsf.2007.06.164.

[210] S Gariglio et al. "Superconductivity at the LaAlO3/SrTiO3 interface". In: *Journal of Physics Condensed Matter* 21.16 (2009), p. 3. ISSN: 09538984. DOI: 10.1088/0953-8984/21/16/164213.

[211] M. Ribeiro, L. R.C. Fonseca, and L. G. Ferreira. "First-principles calculation of the AlAs/GaAs interface band structure using a self-energy-corrected local density approximation". In: *Epl* 94.2 (2011). ISSN: 02955075. DOI: 10.1209/0295-5075/94/27001.

[212] U-Chan Chung et al. "Interface Investigation in Nanostructured $BaTiO_3$/Silica Composite Ceramics". In: *J. Am. Ceram. Soc.* 93.3 (2010), pp. 865–874. ISSN: 00027820. DOI: 10.1111/j.1551-2916.2009.03474.x.

[213] Georg Schusteritsch, Steven P. Hepplestone, and Chris J. Pickard. "First-principles structure determination of interface materials: The Ni_xInAs nickelides". In: *Phys. Rev. B - Condens. Matter Mater. Phys.* 92.5 (2015), pp. 1–7. ISSN: 1550235X. DOI: 10.1103/PhysRevB.92.054105.

[214] Ned Thaddeus Taylor, Francis Huw Davies, and S P Hepplestone. "First principles electronic and elastic properties of fresnoite $Ba_2TiSi_2O_8$". In: *Mater. Res. Express* 4.12 (2017), p. 125904. ISSN: 2053-1591. DOI: 10.1088/2053-1591/aa99e8.

[215] B. Hinterleitner et al. "Thermoelectric performance of a metastable thin-film Heusler alloy". In: *Nature* 576.7785 (2019), pp. 85–90. ISSN: 14764687. DOI: 10.1038/s41586-019-1751-9.

[216] A Ohtomo and H Y Hwang. "A high-mobility electron gas at the LAO/STO heterointerface." In: *Nature* 427.6973 (2004), pp. 423–426. ISSN: 0028-0836. DOI: 10.1038/nature04773.

[217] W. H. Zou et al. "TEM and HREM study of the interphase interface structure of Ti_3Ni_4 precipitates and parent phase in an aged TiNi shape memory alloy". In: *Mater. Sci. Eng. A* 219.1-2 (1996), pp. 142–147. ISSN: 09215093. DOI: 10.1016/S0921-5093(96)10418-4.

[218] Lianfeng Zou et al. "In situ atomic-scale imaging of the metal/oxide interfacial transformation". In: *Nat. Commun.* 8.1 (2017), pp. 1–8. ISSN: 20411723. DOI: 10.1038/s41467-017-00371-4.

[219] E. D. Specht et al. "X-ray-diffraction measurement of interface structure in GaAs/Si(001)". In: *Phys. Rev. B* 43.15 (1991), pp. 12425–12430. ISSN: 0163-1829. DOI: 10.1103/PhysRevB.43.12425. arXiv: arXiv:1011.1669v3.

[220] Haydn Chen. "Surface/interface X-ray diffraction". In: *Mater. Chem. Phys.* 43.2 (1996), pp. 116–125. ISSN: 02540584. DOI: 10.1016/0254-0584(95)01618-5.

[221] D. A. Bonnell et al. "Direct measurement of local properties of interfaces with scanning tunneling microscopy". In: *Acta Metall. Mater.* 40.SUPPL. (1992), pp. 161–171. ISSN: 09567151. DOI: 10.1016/0956-7151(92)90276-K.

[222] N. I. Plusnin. "Application of AES and EELS for surface/interface characterization". In: *J. Electron Spectros. Relat. Phenomena* 137-140.SPEC. ISS. (2004), pp. 161–164. ISSN: 03682048. DOI: 10.1016/j.elspec.2004.02.091.

[223] Michael J. Zachman et al. "Emerging Electron Microscopy Techniques for Probing Functional Interfaces in Energy Materials". In: *Angew. Chemie - Int. Ed.* (2019), pp. 1384–1396. ISSN: 15213773. DOI: 10.1002/anie.201902993.

[224] A. Zur and T. C. McGill. "Lattice match: An application to heteroepitaxy". In: *Journal of Applied Physics* 55.2 (1984), pp. 378–386. ISSN: 0021-8979. DOI: 10.1063/1.333084.

[225] A. M. Raclariu et al. "A fast method for predicting the formation of crystal interfaces and heterocrystals". In: *Computational Materials Science* 108.PA (2015), pp. 88–93. ISSN: 09270256. DOI: 10.1016/j.commatsci.2015.05.023.

[226] Kiran Mathew et al. "MPInterfaces: A Materials Project based Python tool for high-throughput computational screening of interfacial systems". In: *Comput. Mater. Sci.* 122 (2016), pp. 183–190. ISSN: 09270256. DOI: 10.1016/j.commatsci.2016.05.020.

[227] Stradi Daniele et al. "Method for determining optimal supercell representation of interfaces". In: *J. Phys. Condens. Matter* 29.18 (2017), p. 185901.

[228] Line Jelver et al. "Determination of low-strain interfaces via geometric matching". In: *Phys. Rev. B* 96.8 (2017), pp. 1–7. ISSN: 24699969. DOI: 10.1103/PhysRevB.96.085306.

[229] Alvin L.S. Chua et al. "A genetic algorithm for predicting the structures of interfaces in multicomponent systems". In: *Nature Materials* 9.5 (2010), pp. 418–422. ISSN: 14764660. DOI: 10.1038/nmat2712.

[230] Georg Schusteritsch and Chris J. Pickard. "Predicting interface structures: From SrTiO3 to graphene". In: *Phys. Rev. B - Condens. Matter Mater. Phys.* 90.3 (2014), pp. 1–7. ISSN: 1550235X. DOI: 10.1103/PhysRevB.90.035424. arXiv: 1407.2153.

[231] A. K. Lenstra, H. W. Lenstra, and L. Lovász. "Factoring polynomials with rational coefficients". In: *Math. Ann.* 261.4 (1982), pp. 515–534. ISSN: 14321807. DOI: 10.1007/BF01457454.

[232] I Novak. "Molecular isomorphism". In: *Eur. J. Phys.* 16.4 (1995), pp. 151–153. ISSN: 0143-0807. DOI: 10.1088/0143-0807/16/4/001. arXiv: 0143-0807/16/4/001 [10.1088].

[233] Jenaina Ribeiro-Soares et al. "Group theory analysis of phonons in two-dimensional transition metal dichalcogenides". In: *Physical Review B* 90.11 (2014), p. 115438.

[234] Anna V Kimmel and Peter V Sushko. "Mechanisms of formation of chemical bonding and defect formation at the a-SiO_2/$BaTiO_3$ interfaces." In: *J. Phys. Condens. Matter* 27.47 (2015), p. 475006. ISSN: 1361-648X. DOI: 10.1088/0953-8984/27/47/475006.

[235] I. Galanakis et al. "Broken-bond rule for the surface energies of noble metals". In: *Europhys. Lett.* 58.5 (2002), pp. 751–757. ISSN: 02955075. DOI: 10.1209/epl/i2002-00413-7. arXiv: 0105207 [cond-mat].

[236] Y. Y. Sun et al. "Rule for structures of open metal surfaces". In: *Phys. Rev. Lett.* 93.13 (2004), pp. 1–4. ISSN: 00319007. DOI: 10.1103/PhysRevLett.93.136102.

[237] John E Northrup and Sverre Froyen. "Structure of GaAs(001) surfaces: The role of electrostatic interactions". In: *Phys. Rev. B* 50.3 (1994), pp. 2015–2018. ISSN: 0163-1829. DOI: 10.1103/PhysRevB.50.2015.

[238] S. Piskunov, E. A. Kotomin, and E. Heifets. "The electronic and atomic structure of $SrTiO_3$, $BaTiO_3$, and $PbTiO_3$(0 0 1) surfaces: Ab initio DFT/HF hybrid calculations". In: *Microelectron. Eng.* 81.2-4 (2005), pp. 472–477. ISSN: 01679317. DOI: 10.1016/j.mee.2005.03.049.

[239] S. Piskunov et al. "Hybrid DFT calculations of the atomic and electronic structure for ABO_3 perovskite (0 0 1) surfaces". In: *Surf. Sci.* 575.1-2 (2005), pp. 75–88. ISSN: 00396028. DOI: 10.1016/j.susc.2004.11.008.

[240] R. I. Eglitis. "Ab initio calculations of $SrTiO_3$, $BaTiO_3$, $PbTiO_3$, $CaTiO_3$, $SrZrO_3$, $PbZrO_3$ and $BaZrO_3$ (001), (011) and (111) surfaces as well as F centers, polarons, KTN solid solutions and Nb impurities therein". In: *Int. J. Mod. Phys. B* 28.17 (2014). ISSN: 17936578. DOI: 10.1142/S0217979214300096.

[241] R. I. Eglitis and A. I. Popov. "Systematic trends in (0 0 1) surface ab initio calculations of ABO_3 perovskites". In: *J. Saudi Chem. Soc.* 22.4 (2018), pp. 459–468. ISSN: 13196103. DOI: 10.1016/j.jscs.2017.05.011.

[242] Yueh Lin Lee and Dane Morgan. "*Ab initio* defect energetics of perovskite (001) surfaces for solid oxide fuel cells: A comparative study of $LaMnO_3$ versus $SrTiO_3$ and $LaAlO_3$". In: *Phys. Rev. B - Condens. Matter Mater. Phys.* 91.19 (2015). ISSN: 1550235X. DOI: 10.1103/PhysRevB.91.195430.

[243] Joshua J. Brown et al. "Oxygen Vacancy Defect Migration in Titanate Perovskite Surfaces: Effect of the A-Site Cations". In: *J. Phys. Chem. C* 122.26 (2018), pp. 14590–14597. ISSN: 19327455. DOI: 10.1021/acs.jpcc.8b03322.

[244] S. Jenkins and G. Srivastava. "Structure and energetics of segregated and nonsegregated Ge(001)/Si(2×1)". In: *Phys. Rev. B - Condens. Matter Mater.*

Phys. 57.15 (1998), pp. 8794–8796. ISSN: 1550235X. DOI: 10.1103/PhysRevB.57.8794.

[245] R J Dixon et al. "Structure and stability of the Si(001) $c(4 \times 4)$-Sb surface". In: *Phys. Rev. B* 57.20 (1998), R12701–R12704. ISSN: 0163-1829. DOI: 10.1103/PhysRevB.57.R12701.

[246] R. H. Miwa and G. P. Srivastava. "Energetic stability, equilibrium geometry, and electronic properties of Bi-induced Si (001) - $(2 \times n)$ surfaces". In: *Phys. Rev. B - Condens. Matter Mater. Phys.* 74.3 (2006), pp. 1–6. ISSN: 10980121. DOI: 10.1103/PhysRevB.74.035301.

[247] B. Wul. "Dielectric Constants of Some Titanates". In: *Nature* 156.3964 (1945), p. 480. ISSN: 0028-0836. DOI: 10.1038/156480a0.

[248] Pedro Duran et al. "Densification behaviour, microstructure development and dielectric properties of pure BaTiO3 prepared by thermal decomposition of (Ba, Ti)-citrate polyester resins". In: *Ceram. Int.* 28 (2002), pp. 283–292.

[249] Z. Q. Shi, Q. X. Jia, and W. A. Anderson. "High-Performance barium titanate capacitors with double layer structure". In: *J. Electron. Mater.* 20.11 (1991), pp. 939–944. ISSN: 0361-5235. DOI: 10.1007/BF02816036.

[250] Jinghui Gao et al. "Enhancing dielectric permittivity for energy-storage devices through tricritical phenomenon". In: *Sci. Rep.* 7.January (2017), p. 40916. ISSN: 2045-2322. DOI: 10.1038/srep40916.

[251] D.C. Collier. "Ferroelectric phase shifters for phased array radar applications". In: *ISAF '92 Proc. Eighth IEEE Int. Symp. Appl. Ferroelectr.* IEEE, 1992, pp. 199–201. ISBN: 0-7803-0465-9. DOI: 10.1109/ISAF.1992.300662.

[252] J F Scott. "Applications of modern ferroelectrics." In: *Science* 315.February (2007), pp. 954–959. ISSN: 0036-8075. DOI: 10.1126/science.1129564.

[253] Eduard A. Stefanescu et al. "Multifunctional fiberglass-reinforced PMMA-BaTiO3 structural/dielectric composites". In: *Polymer (Guildf).* 52.9 (2011), pp. 2016–2024. ISSN: 00323861. DOI: 10.1016/j.polymer.2011.02.050.

[254] Z Wang and Jk Nelson. "Dielectric properties of electrospun barium titanate fibers/graphene/silicone rubber composites". In: *Annu. Rep. Conf. Electr. Insul. Dielectr. Phenom.* (2011), pp. 640–643. DOI: 10.1109/CEIDP.2011.6232738.

[255] Enis Tuncer et al. "Electrical properties of epoxy resin based nano-composites". In: *Nanotechnology* 18.2 (2006), p. 025703. ISSN: 0957-4484. DOI: 10.1088/0957-4484/18/2/025703.

[256] D. Nuzhnyy et al. "High-Frequency Dielectric Spectroscopy of BaTiO3 Core - Silica Shell Nanocomposites: Problem of Interdiffusion". In: *J. Adv. Dielectr.* 01.3 (2011), pp. 309–317. ISSN: 2010-135X. DOI: 10.1142/S2010135X11000367.

[257] Chongjun Xu et al. "A new route to fabricate barium titanate with high permittivity". In: *Ceram. Int.* 40.7 (2014), pp. 10927–10931. ISSN: 02728842. DOI: 10.1016/j.ceramint.2014.03.090.

[258] Wuttichai Reainthippayasakul. "Silica-coated BaTiO3/P(VDF-CTFE) nanocomposites for electrical energy Storage". PhD thesis. Pennsylvania State University, 2014.

[259] John P George et al. "Preferentially oriented BaTiO3 thin films deposited on silicon with thin intermediate buffer layers." In: *Nanoscale Res. Lett.* 8.1 (2013), p. 62. ISSN: 1931-7573. DOI: 10.1186/1556-276X-8-62.

[260] U-C. Chung et al. "Evidence of diffusion at BaTiO3/silicon interfaces". In: *Thin Solid Films* 520.6 (2012), pp. 1997–2000. ISSN: 00406090. DOI: 10.1016/j.tsf.2011.09.055.

[261] G. Pilania, K. Slenes, and R. Ramprasad. "First principles study of the interface between silicone and undoped/doped BaTiO3". In: *J. Appl. Phys.* 113.6 (2013). ISSN: 00218979. DOI: 10.1063/1.4791755.

[262] C R Robbins. "Synthesis and Growth of Fresnoite (Ba2TiSi2O8) from a TiO2 Flux and Its Relation to the System BaTi03-Si02". In: *J. Res. Natl. Bur. Std.* 74.April (1970), pp. 229–232.

[263] S. A. Markgraf et al. "X-ray structure refinement and pyroelectric investigation of fresnoite, Ba2TiSi2O8". In: *Ferroelectrics* 62.1 (1985), pp. 17–26. ISSN: 0015-0193. DOI: 10.1080/00150198508017914.

[264] P. B. Moore and J. Louisnathan. "Fresnoite: Unusal Titanium Coordination". In: *Science (80-.).* 156.3780 (1967), pp. 1361–1362. ISSN: 0036-8075. DOI: 10.1126/science.156.3780.1361.

[265] Masakazu Kimura, Yoshio Fujino, and Tsutomu Kawamura. "New piezoelectric crystal: Synthetic fresnoite (Ba2Si 2TiO8)". In: *Appl. Phys. Lett.* 29.4 (1976), pp. 227–228. ISSN: 00036951. DOI: 10.1063/1.89045.

[266] Masakazu Kimura. "Elastic and piezoelectric properties of Ba ¡sub¿2¡/sub¿ Si ¡sub¿2¡/sub¿ TiO ¡sub¿8¡/sub¿". In: *J. Appl. Phys.* 48.7 (1977), pp. 2850–2856. ISSN: 0021-8979. DOI: 10.1063/1.324092.

[267] S. Haussühl et al. "Growth and physical properties of fresnoite Ba2TiSi2O8". In: *J. Cryst. Growth* 40.2 (1977), pp. 200–204. ISSN: 00220248. DOI: 10.1016/0022-0248(77)90006-9.

[268] M C Foster et al. "Fresnoite: A new ferroelectric mineral". In: *J. Appl. Phys.* 85.4 (1999), pp. 2299–2303. ISSN: 00218979. DOI: 10.1063/1.369541.

[269] Y. Mogulkoc et al. "The structural, electronic, elastic, vibration and thermodynamic properties of GdMg". In: *Solid State Sci.* 16 (2013), pp. 168–174. ISSN: 12932558. DOI: 10.1016/j.solidstatesciences.2012.10.014.

[270] Nayoung Song et al. "Polar phase transitions and physical properties in fresnoite A2TiSi2O8 (A= Ba, Sr) by first principles calculations". In: *J. Solid State Chem.* 242 (2016), pp. 136–142. ISSN: 1095726X. DOI: 10.1016/j.jssc.2016.06.016.

[271] Dmitrij Rappoport et al. "Approximate Density Functionals: Which Should I Choose?" In: *Encycl. Inorg. Chem.* Chichester, UK: John Wiley & Sons, Ltd, 2009, pp. 159–172. ISBN: 9780470862100. DOI: 10.1002/0470862106.ia615. arXiv: 0505109 [physics].

[272] Jochen Heyd, Gustavo E. Scuseria, and Matthias Ernzerhof. "Hybrid functionals based on a screened Coulomb potential". In: *J. Chem. Phys.* 118.18 (2003), pp. 8207–8215. ISSN: 00219606. DOI: 10.1063/1.1564060.

[273] Christoph Freysoldt et al. "First-principles calculations for point defects in solids". In: *Rev. Mod. Phys.* 86.1 (2014), pp. 253–305. ISSN: 15390756. DOI: 10.1103/RevModPhys.86.253.

[274] Matteo Gerosa et al. "Electronic structure and phase stability of oxide semiconductors: Performance of dielectric-dependent hybrid functional DFT, benchmarked against GW band structure calculations and experiments". In: *Phys. Rev. B - Condens. Matter Mater. Phys.* 91.15 (2015), pp. 1–15. ISSN: 1550235X. DOI: 10.1103/PhysRevB.91.155201. arXiv: 1508.02174.

[275] Baochang Wang et al. "A Comparison Between Hybrid Functional, GW Approach and the Bethe Salpether Equation: Optical Properties of High Pressure Phases of TiO2". In: *Sci. Adv. Mater.* 6.6 (2014), pp. 1170–1178. ISSN: 19472935. DOI: 10.1166/sam.2014.1883.

[276] G. Kresse and J. Hafner. "Ab initio molecular dynamics for liquid metals". In: *Phys. Rev. B* 47.1 (1993), pp. 558–561. ISSN: 01631829. DOI: 10.1103/PhysRevB.47.558.

[277] G. Kresse and J. Furthmüller. "Efficient iterative schemes for ab initio total-energy calculations using a plane-wave basis set". In: *Phys. Rev. B* 54.16 (1996), pp. 11169–11186. ISSN: 0163-1829. DOI: 10.1103/PhysRevB.54.11169.

[278] G. Kresse and J. Furthmüller. "Efficiency of ab-initio total energy calculations for metals and semiconductors using a plane-wave basis set". In: *Comput. Mater. Sci.* 6.1 (1996), pp. 15–50. ISSN: 09270256. DOI: 10.1016/0927-0256(96)00008-0.

[279] John P. Perdew, Kieron Burke, and Matthias Ernzerhof. "Generalized Gradient Approximation Made Simple". In: *Phys. Rev. Lett.* 77.18 (1996), pp. 3865–3868. ISSN: 0031-9007. DOI: 10.1103/PhysRevLett.77.3865.

[280] G. Kresse. "From ultrasoft pseudopotentials to the projector augmented-wave method". In: *Phys. Rev. B* 59.3 (1999), pp. 1758–1775. ISSN: 1098-0121. DOI: 10.1103/PhysRevB.59.1758.

[281] Oleg A. Vydrov et al. "Importance of short-range versus long-range Hartree-Fock exchange for the performance of hybrid density functionals". In: *J. Chem. Phys.* 125.7 (2006), p. 074106. ISSN: 0021-9606. DOI: 10.1063/1.2244560.

[282] James D. Pack and Hendrik J. Monkhorst. ""special points for Brillouin-zone integrations"-a reply". In: *Phys. Rev. B* 16.4 (1977), pp. 1748–1749. ISSN: 01631829. DOI: 10.1103/PhysRevB.16.1748. arXiv: arXiv:1011.1669v3.

[283] Richard F. W. Bader. "A quantum theory of molecular structure and its applications". In: *Chem. Rev.* 91.5 (1991), pp. 893–928. ISSN: 0009-2665. DOI: 10.1021/cr00005a013.

[284] Stefano Baroni and Raffaele Resta. "Ab initio calculation of the macroscopic dielectric constant in silicon". In: *Phys. Rev. B* 33.10 (1986), pp. 7017–7021. ISSN: 0163-1829. DOI: 10.1103/PhysRevB.33.7017.

[285] Na Sai, Karin M. Rabe, and David Vanderbilt. "Theory of structural response to macroscopic electric fields in ferroelectric systems". In: *Phys. Rev. B - Condens. Matter Mater. Phys.* 66.10 (2002), pp. 1041081–10410817. ISSN: 01631829. DOI: 10.1103/PhysRevB.66.104108. arXiv: 0205442 [cond-mat].

[286] Yvon Le Page and Paul Saxe. "Symmetry-general least-squares extraction of elastic data for strained materials from ¡i¿ab initio¡/i¿ calculations of stress". In: *Phys. Rev. B* 65.10 (2002), p. 104104. ISSN: 0163-1829. DOI: 10.1103/PhysRevB.65.104104.

[287] S Piskunov et al. "Bulk properties and electronic structure of SrTiO3, BaTiO3, PbTiO3 perovskites: an ab initio HF/DFT study". In: *Comput. Mater. Sci.* 29.2 (2004), pp. 165–178. ISSN: 09270256. DOI: 10.1016/j.commatsci.2003.08.036. arXiv: 1004.2974.

[288] N Soga. "Temperature and Pressure Derivatives of Isotropic Sound Velocities of Alpha Quartz". In: *J. Geophys. Res.* 73.2 (1968), pp. 827–&. DOI: Doi10.1029/Jb073i002p00827.

[289] Paul Heyliger, Hassel Ledbetter, and Sudook Kim. "Elastic constants of natural quartz." In: *J. Acoust. Soc. Am.* 114.2 (2003), pp. 644–650. ISSN: 00014966. DOI: 10.1121/1.1593063.

[290] R Hill. "The Elastic Behaviour of a Crystalline Aggregate". In: *Proc. Phys. Soc. Sect. A* 65.5 (1952), pp. 349–354. ISSN: 0370-1298. DOI: 10.1088/0370-1298/65/5/307.

[291] H Colder et al. "Structural characterisation of BaTiO 3 thin films deposited on SrRuO 3 /YSZ buffered silicon substrates and silicon microcantilevers". In: *J. Appl. Phys.* 115.5 (2014), p. 053506. ISSN: 0021-8979. DOI: 10.1063/1.4863542.

[292] Félix Mouhat and Fran çois-Xavier Coudert. "Necessary and sufficient elastic stability conditions in various crystal systems". In: *Phys. Rev. B* 90 (22 2014),

p. 224104. DOI: 10.1103/PhysRevB.90.224104. URL: https://link.aps.org/doi/10.1103/PhysRevB.90.224104.

[293] Hajime Kimizuka et al. "Complete set of elastic constants of α -quartz at high pressure: A first-principles study". In: *Phys. Rev. B - Condens. Matter Mater. Phys.* 75.5 (2007), pp. 1–6. ISSN: 10980121. DOI: 10.1103/PhysRevB.75.054109.

[294] M. Gabelica-Robert and P. Tarte. "Vibrational spectrum of fresnoite (Ba2TiOSi2O7) and isostructural compounds". In: *Phys. Chem. Miner.* 7.1 (1981), pp. 26–30. ISSN: 03421791. DOI: 10.1007/BF00308197.

[295] S A Markgraf, S K Sharma, and A S Bhalla. "Raman study of fresnoite-type materials: Polarized single crystal, crystalline powders, and glasses". In: *J. Mater. Res.* 8 (1993), pp. 635–648. ISSN: 0884-2914. DOI: 10.1557/JMR.1993.0635.

[296] S. H. Wemple. "Polarization fluctuations and the optical-absorption edge in BaTiO3". In: *Phys. Rev. B* 2.7 (1970), pp. 2679–2689. ISSN: 01631829. DOI: 10.1103/PhysRevB.2.2679.

[297] T. H. DiStefano and D. E. Eastman. "The band edge of amorphous SiO2 by photoinjection and photoconductivity measurements". In: *Solid State Commun.* 9.24 (1971), pp. 2259–2261. ISSN: 00381098. DOI: 10.1016/0038-1098(71)90643-0.

[298] Ph. Ghosez, X. Gonze, and J. -P. Michenaud. "First-principles characterization of the four phases of barium titanate". In: *Ferroelectrics* 220.1 (1999), pp. 1–15. ISSN: 0015-0193. DOI: 10.1080/00150199908007992.

[299] D Bagayoko et al. "Ab initio calculations of the electronic structure and optical properties of ferroelectric tetragonal BaTiO 3". In: *J. Phys. Condens. Matter* 10 (1998), pp. 5645–5655.

[300] Renata M. Wentzcovitch, Alexandra Navrotsky, and Kenneth Reinhard Poeppelmeier. *Perovskite materials: symposium*. San Fancisco: Materials Research Society, 2002. ISBN: 9781558996540.

[301] Bairen Zhu, Xi Chen, and Xiaodong Cui. "Exciton Binding Energy of Monolayer WS2". In: *Scientific Reports* 5.1 (2015), p. 9218. ISSN: 2045-2322. DOI: 10.1038/srep09218. URL: https://doi.org/10.1038/srep09218.

[302] M Van der Donck and FM Peeters. "Interlayer excitons in transition metal dichalcogenide heterostructures". In: *Physical Review B* 98.11 (2018), p. 115104.

[303] Gui-Bin Liu et al. "Three-band tight-binding model for monolayers of group-VIB transition metal dichalcogenides". In: *Physical Review B* 88.8 (2013), p. 085433.